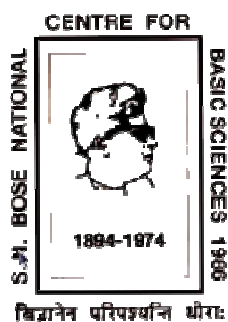


# **Spectroscopic Studies on Structure, Function and Dynamics of Biomolecules in Presence of Other Biologically Relevant Macromolecules**

**THESIS**  
**SUBMITTED FOR THE DEGREE OF**  
**DOCTOR OF PHILOSOPHY (SCIENCE)**  
**OF**  
**JADAVPUR UNIVERSITY**  
**2013**

**BY**  
**SURAJIT RAKSHIT**



**DEPARTMENT OF CHEMICAL, BIOLOGICAL AND**  
**MACROMOLECULAR SCIENCES,**  
**S. N. BOSE NATIONAL CENTRE FOR BASIC SCIENCES,**  
**BLOCK JD, SECTOR III, SALT LAKE,**  
**KOLKATA 700 098, INDIA**

सत्येन्द्र नाथ बसु राष्ट्रीय मौलिक विज्ञान केन्द्र  
SATYENDRA NATH BOSE NATIONAL  
CENTRE FOR BASIC SCIENCES

**CERTIFICATE FROM THE SUPERVISOR**

This is to certify that the thesis entitled "Spectroscopic Studies on Structure, Function and Dynamics of Biomolecules in Presence of Other Biologically Relevant Macromolecules" submitted by Mr. Surajit Rakshit, who got his name registered on June 24, 2010 for the award of **Ph.D. (Science) degree of Jadavpur University**, is absolutely based upon his own work under the supervision of Dr. Samir Kumar Pal and that neither this thesis nor any part of it has been submitted for any degree/diploma or any other academic award anywhere before.



1st October 2013

(Signature of Supervisor/date with official seal)

**Dr. SAMIR KUMAR PAL**  
Associate Professor,  
S. N. Bose National Centre,  
For Basic Sciences  
Government of India  
Block-JD, Sector-III, Salt Lake  
Kolkata-700098

ब्लॉक जे० डी०, सेक्टर-३, साल्ट लेक, कोलकाता ७०००९८, BLOCK-JD, SECTOR III, SALT LAKE, KOKATA - 700 098

दूरभाष/ Phones : 0091-(0)33-2335 5705-8, 2335 3057/61, 2335 0312/1313

ई-मेल/ E-mail : root@bose.res.in

Webpage : <http://www.bose.res.in>

Fax : 0091-(0)33-2335 3477

FUNDED BY THE DEPARTMENT OF SCIENCE & TECHNOLOGY, GOVT. OF INDIA

निष्ठिवद् विज्ञान और प्रौद्योगिकी विभाग भारत सरकार द्वारा

*To My Family*

## *Acknowledgements*

*A doctoral thesis is often described as a solitary endeavour; however the long list that follows definitely proves the opposite. So it is a pleasant task to express my thanks to all those who contributed in many ways to made this thesis possible and made it an unforgettable experience for me.*

*At this moment of accomplishment, first of all I pay homage to my guide, Dr. Samir Kumar Pal. This work would not have been possible without his guidance, support and encouragement. Under his guidance I successfully overcame many difficulties and learned a lot. I am especially grateful for his constant availability, great interest and innumerable helpful discussions for my work,*

*I would also like to thank Dr. Rajib Kumar Mitra, S. N. Bose National Centre for Basic Sciences, Kolkata, India; Dr. Achintya Singha, Bose Institute, India; Dr. Zaki Shakir Abdullah Seddigi, Umm Al-Qura University, Saudi Arabia; Prof. Gautam Basu, Bose Institute, India; Prof. Satyajit Mayor, National Centre for Biological Science (TIFR), India for fruitful collaborations.*

*I am really grateful to all the technical staffs especially Surajit da for helping me in the FTIR and DSC measurement during the entire course of work,*

*I am extremely thankful to Council of Scientific and Industrial Research (CSIR), Government of India, for providing the financial support through Junior Research Fellowship (JRF) for first two years and then through Senior Research Fellowship (SRF) for following years.*

*I am indebted to my many student colleagues for providing a stimulating and fun filled environment. My thanks go in particular to Dr. Pramod Kumar Verma with whom I started this work and many rounds of discussions on my project with him helped me a lot. I am ever indebted to Ranajay and I admire his distinguished helping nature. I would like to thank Dr. Amrita Chakraborty for her help in the computational work. My special appreciation goes to Nirmal, Subrata, Anupam for their friendship and encouragement. I am also thankful to Dr. Abhinandan Mahal, Soumik, Tanumoy, Soma, Samim, Nabarun, Susobhan, Siddhi, Dilip, Prasenjit and Soumendra da for providing a homely and cheerful environment, and also for assisting me in research.*

*I am also thankful to my batch mates specially Debasish, Saikat, Animesh and many more for their unconditional help whenever I needed. I am grateful to my childhood friends Sanajay, Uttam and Sukanta for their immense support during this whole tenure. Besides this, several people have knowingly and unknowingly helped me in the successful completion of this thesis.*

*Last but not the least, I would like to pay high regards to my beloved parents, for their devotions, sincere encouragement, support and inspiration throughout my research work that have made me more*

*courageous, dedicated and patient. I owe everything to them and they are the reasons for what I am today. I feel myself very fortunate to have them as parents, Jaydeb, Uttam, Biswajit as elder brothers, Mou as sister, Mousumi and Rumpa as sister-in-laws and Shruti as sweet niece. It is their unconditional love, well wishes and confidence on me that have made this thesis a success.*

*Dated:*

*Department of Chemical, Biological  
and Macromolecular Sciences,*

*S. N. Bose National Centre for Basic Sciences,*

*Block JD, Sec III, Salt Lake, Kolkata 700098, India.*

*(Surajit Rakshit)*

# Table of Contents

	<b>Page</b>
<b>Chapter 1: Introduction</b>	
1.1. Scope of the Spectroscopic Studies on Structure, Function and Dynamics of Biomolecules in Presence of Other Biologically Relevant Macromolecules	1
1.2. Objective	4
1.3. Summary of the Work Done	5
1.3.1. Structural and Dynamical Studies on the Solubilisation of Hydrophobic molecules in Bulk Water	5
1.3.1.1. Molecular Interaction, Co-solubilisation of Organic Pollutants and Ecotoxicity of a Potential Carcinogenic Fuel Additive MTBE in Water	5
1.3.2. Studies on Structure, Dynamics and Energetics of Water in Hydrophobic Environments	6
1.3.2.1. Effect of Hydrophobic Interaction on Structure, Dynamics and Reactivity of Water	6
1.3.3. Studies on the Role of Dynamics of Isolated Water Molecules in Proton Transfer Reaction in Biologically Important Hydrophobic/Confined Environments	7
1.3.3.1. Role of Solvation Dynamics in Excited State Proton Transfer of 1-Naphthol in Nanoscopic Water Clusters Formed in a Hydrophobic Solvent	7
1.3.3.2. Slow Solvent Relaxation Dynamics of Nanometer Sized Reverse Micellar Systems Through Tryptophan Metabolite, Kynurenine	7
1.3.4. Exploration of Structure and Function of a Protein in Macromolecular Crowding	8

	<b>Page</b>
1.3.4.1. Ultrafast Electron Transfer in Riboflavin Binding Protein in Macromolecular Crowding of Nano-Sized Micelle	8
1.3.5. Exploration of Environmental Dynamics and Enzymatic Activity in Nanoscopic Confinement	8
1.3.5.1. Modulation of Environmental Dynamics at the Active Site and Activity of an Enzyme Under Nanoscopic Confinement: Subtilisin Carlsberg in Anionic AOT Reverse Micelle	8
1.4. Plan of Thesis	9
References	10

## **Chapter 2: Experimental Techniques and Systems**

2.1. Steady-State and Dynamical Tools	16
2.1.1. Solvation Dynamics	16
2.1.1.1. Theory	16
2.1.1.2. Experimental Methods	21
2.1.2. Fluorescence Anisotropy	24
2.1.2.1. Theory	25
2.1.2.2. Experimental Methods	27
2.1.3. Arrhenius Theory of Activation Energy	29
2.1.4. Förster Resonance Energy Transfer (FRET)	30
2.1.5. Excited State Proton Transfer (ESPT)	33
2.1.6. Photoinduced Electron Transfer (PET)	34
2.1.6.1. Theory	34
2.1.6.2. Experimental Methods	34
2.2. Systems	35
2.2.1. Organized Assemblies (Biomimetics)	35
2.2.1.1. Reverse Micelle	35
2.2.1.2. Micelle	37

	<b>Page</b>
2.2.2. Proteins	38
2.2.2.1. Subtilisin <i>Carlsberg</i> (SC)	38
2.2.2.2. Riboflavin Binding Protein (RBP)	40
2.2.3. Molecular Probes	41
2.2.3.1. N-CBZ-Gly-Gly-Leu-p-Nitroanilide (CBZ-GGL-pNA)	41
2.2.3.2. Coumarin 500 (C500)	41
2.2.3.3. Kynurenine (KN)	43
2.2.3.4. 2'-(4-hydroxyphenyl)-5-[5-(4-methylpiperazine-1-yl) benzimidazo-2-yl-benzimidazole, Hoechst 33258	43
2.2.3.5. Tryptophan (Trp)	43
2.2.3.6. 4-(dicyanomethylene)-2-methyl-6-(p-dimethylaminostyryl) 4H-pyran (DCM)	43
2.2.3.7. Crystal Violet (CV)	44
2.2.3.8. Riboflavin (Rf)	44
2.2.3.9. 4',6-Diamidino-2-phenylindole (DAPI)	45
2.2.3.10. Benzoyl Chloride (BzCl)	45
2.2.3.11. 3-(Dansylamino)phenylboronic acid (DB)	45
References	46

### **Chapter 3: Instrumentation and Sample Preparation**

3.1. Instrumental Setup	54
3.1.1. Steady-State UV-Vis Absorption and Emission Measurement	54
3.1.2. Circular Dichroism (CD) Measurement	55
3.1.3. Time Correlated Single Photon Counting (TCSPC) Technique	57
3.1.4. Femtosecond-Resolved Fluorescence Upconversion Technique	58
3.1.5. Differential Scanning Calorimetry (DSC)	59
3.1.6. Dynamic Light Scattering (DLS) Measurement	60
3.1.7. Fourier Transform Infrared (FTIR) Measurement	63
3.1.8. Laser Raman Spectroscopy	64
3.1.9. Density and Sound Velocity Measurement	66

	<b>Page</b>
3.1.10. Viscosity Measurement	67
3.1.11. Refractive Indices Measurement	68
3.2. Sample Preparation	69
3.2.1. Chemicals Used	69
3.2.2. Preparation of Micellar Solution	69
3.2.3. Preparation of Reverse Micellar Solution	69
3.2.4. Preparation of DB-SC Complex	70
3.2.5. Measurement of Enzymatic Activity of Subtilisin Carlsberg (SC)	70
3.2.6. Cytotoxicity Assay Protocol	70
3.2.7. Computational Methods for Water-MTBE Interactions	70
3.2.8. Quantum Yield (QD) Calculation	71
References	72

#### **Chapter 4: Structural and Dynamical Studies on the Solubilisation of Hydrophobic Molecules in Bulk Water**

4.1. Introduction	74
4.2. Results and Discussion	75
4.2.1. Molecular Interaction, Co-solubilisation of Organic Pollutants and Ecotoxicity of a Potential Carcinogenic Fuel Additive MTBE in Water	75
4.3. Conclusion	90
References	91

#### **Chapter 5: Studies on Structure, Dynamics and Energetics of Water in Hydrophobic Environments**

5.1. Introduction	95
5.2. Results and Discussion	97
5.2.1. Effect of Hydrophobic Interaction on Structure, Dynamics and Reactivity of Water	97

	<b>Page</b>
5.2.1.1. MTBE in Water (MTBE/Water)	97
5.2.1.2. Water in MTBE (Water/MTBE)	103
5.3. Conclusion	113
References	115

## **Chapter 6: Studies on the Role of Dynamics of Isolated Water Molecules in Proton Transfer Reaction in Biologically Important Hydrophobic/Confined Environments**

6.1. Introduction	120
6.2. Results and Discussion	121
6.2.1. Role of Solvation Dynamics in Excited State Proton Transfer of 1-Naphthol in Nanoscopic Water Clusters Formed in a Hydrophobic Solvent	121
6.2.2. Slow Solvent Relaxation Dynamics of Nanometer Sized Reverse Micellar Systems Through Tryptophan Metabolite, Kynurenine	134
6.3. Conclusion	143
References	145

## **Chapter 7: Exploration of Structure and Function of a Protein in Macromolecular Crowding**

7.1. Introduction	149
7.2. Results and Discussion	151
7.2.1. Ultrafast Electron Transfer in Riboflavin Binding Protein in Macromolecular Crowding of Nano-Sized Micelle	151
7.3. Conclusion	162
References	164

	<b>Page</b>
<b>Chapter 8: Exploration of Environmental Dynamics and Enzymatic Activity in Nanoscopic Confinement</b>	
8.1. Introduction	167
8.2. Results and Discussion	168
8.2.1 Modulation of Environmental Dynamics at the Active Site and Activity of an Enzyme Under Nanoscopic Confinement: Subtilisin Carlsberg in Anionic AOT Reverse Micelle	168
8.3. Conclusion	184
References	185
<b>List of Publications</b>	189

# Chapter 1

## Introduction

### **1.1. Scope of the Spectroscopic Studies on Structure, Function and Dynamics of Biomolecules in Presence of Other Biologically Relevant Macromolecules:**

Biological macromolecules evolve and function within intracellular environments over billions of years. Still, understanding of the structure, function and dynamics of biomolecules *in vivo* remains unclear. Generally, to get the detailed knowledge of the rates, equilibria, and mechanism of biochemical reactions; studies of biochemical processes *in vitro* have usually been carried out in dilute buffer systems with low concentrations of biomolecules together with low molecular weight substrates, and cofactors as required. In contrast, in cellular environment protein and other biological macromolecules often co-exist in a medium containing high concentrations of macromolecules (50-400 g/l), which occupy a significant fraction of the total volume of the medium (about 40%) [1-4]. For example, the total concentration of protein and RNA inside a cell of *Escherichia coli* is in the range of 300-400 gL<sup>-1</sup> [2]. However, no individual macromolecular species is present at high concentration, but all species taken together occupy a significant fraction of the volume of the medium, such media are referred to as “crowded”. Moreover, in such crowded environment, biomolecules find themselves inside a small compartments or pores with dimensions comparable to the size of large macromolecules created by the cytoskeletal structures or by the central cage of the chaperonin proteins [5-7]. This situation is commonly known as “confinement”. Therefore, a significant fraction of the intracellular space is inaccessible to other macromolecules, as a result, effective concentration, or thermodynamic activity, or chemical potential of macromolecules increase by several orders of magnitude, and hence increase in the thermodynamic driving force for them to react [8]. Furthermore, diffusion coefficients of biomolecules in such a crowded environment are smaller than their values in a dilute solution. Hence, ligand

binding, protein-protein interactions, enzymatic activities, protein folding, and essentially all other biochemical processes are expected to be modified relative to their propensities in dilute solution by the high concentrations of macromolecules in cells.

Despite its relevance to biochemical reactions, macromolecular crowding is still an important but neglected aspect till last decades [7, 9, 10]. However, during recent decades it has been gradually recognized that crowding has substantial effect on a broad range of biochemical, biophysical and physiological processes, including nucleic acid and protein conformation and stability, protein-protein and protein-DNA association equilibria and kinetics (including protein crystallization, protein fibril formation and bundling), catalytic activity of enzymes and cell volume regulation. For example, protein-protein association rates are highly altered in the presence of crowding agents when compared to that in buffer solutions [11-18]. However, the behavior depends strongly on whether the solution is dilute, semidilute, or concentrated [12]. In addition macromolecular crowding has been demonstrated to significantly alter the activity of enzymes [19-25]. There are also many experimental and theoretical studies examining how crowding affects protein folding energetics, and the results mostly point to a modest stability effect [26-32]. Macromolecular crowding effects have also been extended to structural compression in nucleic acids [33-38]. However, despite numerous studies fundamental gaps remain in our understanding of the effects of macromolecular crowding on biomolecular system.

Molecular crowding is more accurately termed the excluded-volume effect, because of the mutual impenetrability of all the solute molecules in the medium. Therefore, crowded conditions can be mimicked experimentally by adding high concentrations of inert, water soluble synthetic or natural macromolecules, termed as crowding agent, to the system *in vitro* [9]. Generally, polyethylene glycol (PEG), ficoll, dextran, sodium dodecyl sulfate (SDS) or proteins (such as ovalbumin or hemoglobin) are used to simulate cellular crowding effects in the test tube [6]. However, even in these simplified model systems, monitoring the changes on the biomolecule of interest, to isolate the effect of crowding is experimentally challenging. Although a variety of NMR techniques have been used to characterize macromolecular motions and conformations within *in vitro* crowded solutions and also within living cells [34, 39]. Rivas et al. introduced a non-ideal sedimentation

equilibrium that allows the molar mass of a dilute trace macromolecule to be measured in the presence of other macromolecular species at concentrations up to several hundred milligrams per millilitre. This technique has allowed the direct observation of the significant enhancement of the self-association of dilute proteins (fibrinogen, tubulin and the bacterial cell-division FtsZ protein) in concentrated solutions of unrelated proteins and polymers [40, 41]. Fluorescence-based methods are another potentially powerful tools for studying the structural organization and dynamics of proteins in crowded solutions, due to the possibility of labeling only the tracer protein with extrinsic fluorescent dyes, which in this way can be easily distinguished from the crowding macromolecules [42]. However, so far there are few examples in which fluorescence assays have been applied to study crowding effects. For example, Minton et al. studied the dimerization of horse apomyoglobin in crowded medium by means of steady-state fluorescence anisotropy techniques [43].

In the present thesis, we have studied the macromolecular crowding and confinement effect on structure, function and dynamics of protein along with some model biochemical reaction. For example, we have studied the structure, dynamics and reactivity of water in presence of a hydrophobic solute, along with molecular interaction and co-solubilisation of other organic pollutants and ecotoxic effect of the solute in water. We have also studied the role of water dynamics in proton transfer process in nanoscopic water clusters formed in a hydrophobic/confined environments. Finally, we have studied the electron transfer (ET) dynamics of a flavoprotein to its cofactor in crowded environments. In another study, we have explored the environmental dynamics at the active site and the enzymatic activity of Subtilin *Carlsberg* (SC) in confined environments. The experimental tools used for studying the dynamical processes involve femto- and picosecond-resolved solvent relaxation dynamics. The different experimental techniques employed for the structural and functional characterization of the biomolecules includes steady-state UV-Vis absorption and fluorescence spectroscopy, differential scanning calorimetry (DSC), various time-resolved fluorescence spectroscopy, Fourier transform infrared spectroscopy (FTIR), Raman scattering, circular dichroism (CD) etc.

## 1.2. Objective:

The intercellular milieu is rich in diversity of both simple and complex molecules, and also quite crowded. This environmental constraint through different types of interfaces and crowding have energetic consequences that affect the stability and functionality/recognition of a biomolecule by modulating the structure, dynamics and the net content of the surrounding water shell. Therefore, understanding of water structure and dynamics and the role of water dynamics in biologically important proton transfer process, as well as stability and functionality of proteins in crowded/confinement environments is the sole objective of this thesis work. Protein folding is an inherently complex process involving a multiplicity of forces and interactions and has been a long-standing challenge to the scientific community. Dill and others have postulated that hydrophobicity serves as one of the most important driving forces for protein assembly [44-46]. However, the hydrophobic interaction imposed by a biomolecule on water is quite complex, and so forth to the presence of variety of polar and nonpolar side chains [47]. Therefore, to monitor hydrophobic interaction, we have designed a prototype reaction between water and an organic molecule that contains a hydrophobic backbone along with a hydrophilic group. Methyl *tert*-butyl ether (MTBE) is such an example of hydrophobic solute. The choice of MTBE also lies in the fact that, it is one of the most common gasoline oxygenates, has become a widespread contaminant in surface water and groundwater [48-54] due to its high water solubility ( $44 \text{ gL}^{-1}$  at  $20^\circ\text{C}$ ). The presence of MTBE in drinking water and groundwater resources causes different physical hazards. Moreover, there is also evidence that MTBE is a possible human carcinogen [55]. Thus, it is very important to investigate the water-MTBE molecular complexes in considerable details. In this regard, we have studied the interaction of water molecules with MTBE using various spectroscopic techniques. As a continuation of the above work, in another report, we have studied the effect of hydrophobic interaction on structure, dynamics and reactivity of water.

The isolated waters or its small clusters have a great impact on the understanding of dynamical behaviour of the water molecules in chemical and biological reactions e.g., proton transfer, electron transfer etc. Water dissolved in non-aqueous solvent (like dioxane, MTBE) forms very small cluster of 2-10 water molecules, which grows in size as the

content of water increases. This provides a rare opportunity for studying translational and rotational motions of water molecules without the effect of hydrogen bonding to the surrounding water molecules. We have observed a fast solvation dynamics in the very low free water concentration systems, which are due to the various modes of rotational relaxation of water molecules present in the isolated small water clusters.

The behavior of water in the cytoplasm is still much debated, especially within ion channels and protein cavities where water is found to be confined. In order to explore the confined water dynamics systematically, supramolecular assemblies like reverse micellar (RM) nanoscopic water droplets are excellent biomimetics. In this context, we have studied a detail photophysical characterization of Kynurenine (KN) in a model nonionic tetraethylene glycol monododecyl ether (Brij-30) RM. Apart from the environmental dynamics of RM using KN as solvation probe, our studies have also attempted to shed light on the probable binding position of KN in the micellar environment using Förster resonance energy transfer (FRET) technique.

In recent years significant efforts have been made to explore the effect of macromolecular crowding, in particular on proteins *in vitro* with regard to folding and denaturation; however, less is known about the biochemical reactions in crowded environments. In one of our work, we have studied electron transfer (ET) dynamics of riboflavin (Rf; vitamin B2) in Rf binding protein (RBP), in the presence of crowding environment of nanoscopic sodium dodecyl sulfate (SDS) micelles. Another consequences of crowding/confinement effect on structure, function and dynamics of protein is also evident from our recent study on Subtilisin *Carlsberg* in sodium bis(2-ethylhexyl) sulfosuccinate reverse micelle.

### **1.3. Summary of the Work Done:**

#### **1.3.1. Structural and Dynamical Studies on the Solubilisation of Hydrophobic Molecules in Bulk Water:**

**1.3.1.1. Molecular Interaction, Co-solubilisation of Organic Pollutants and Ecotoxicity of a Potential Carcinogenic Fuel Additive MTBE in Water [56]:** In this

work, we have studied the interaction of water molecules with a hydrophobic solvent, methyl *tert*-butyl ether (MTBE). Our study shows the change of bulk properties like densities, viscosities and refractive indices of binary mixtures of water and MTBE at temperatures from 10°C to 50°C and over the entire composition range, under atmospheric pressure using densimetry, viscometry and refractive index measurements. Dynamic light scattering (DLS) studies confirm the formation of micro-droplets (micelle-like) of MTBE in water, which is also supported by thermochemical studies of the binary eutectic melt of the system using DSC measurement. The negative value of the excess molar volumes and positive value of viscosity and refractive index deviations support interactions occurring through hydrogen bonding, which is also confirmed from FTIR and Raman spectroscopic studies. Co-solubilisation of other potential hazardous organic matters (anthracene, naphthalene, benzo[ $\alpha$ ]pyrene and 4-(dicyanomethylene)-2-methyl-6-(*p*-dimethylamino-styryl)-4H-pyran (DCM)) shows the enhanced magnitude of water pollution in presence of MTBE. Our studies also show the ecotoxic effect of MTBE in model eukaryotic microorganism yeast in aqueous environments.

### **1.3.2. Studies on Structure, Dynamics and Energetics of Water in Hydrophobic Environments:**

**1.3.2.1. Effect of Hydrophobic Interaction on Structure, Dynamics and Reactivity of Water [57]:** Here, we have studied the effect of hydrophobic interaction on structure, dynamics and reactivity of water. To explore the dynamical evolution of water in presence of hydrophobic molecule MTBE, femtosecond-resolved solvation dynamics techniques have been adopted. We have also used temperature dependent picosecond-resolved solvation dynamics in order to explore the magnitude of the intermolecular bonding energy in the water clusters, in presence of MTBE. Structural modification of water molecules in both water/MTBE and MTBE/water binary systems have been examined using FTIR and  $^1\text{H}$  NMR measurements. Using detailed *ab initio* calculations at the MP2 level, we have also attempted to predict the possible structures, energies and thermo-chemical parameters of corresponding MTBE-water molecular complexes in more details. The chemical reactivity of water further confirms the effect of the hydrophobic interaction on water molecules.

### **1.3.3. Studies on the Role of Dynamics of Isolated Water Molecules in Proton Transfer Reaction in Biologically Important Hydrophobic/ Confined Environments:**

**1.3.3.1. Role of Solvation Dynamics in Excited State Proton Transfer of 1-Naphthol in Nanoscopic Water Clusters Formed in a Hydrophobic Solvent [58]:** In this work, we have studied the role of solvation dynamics on the excited state proton transfer process of 1-naphthol (NpOH) in water-dioxane (DX) nano-clusters. The dynamics of proton transfer and solvent relaxation have been examined through picosecond-resolved fluorescence measurements. To ascertain the types of species present in the water-DX mixture, we have used picosecond-resolved area normalized emission spectroscopy (TRANES). The time resolved fluorescence Stokes shift method has been adopted to study the solvation dynamics of water in the nano-clusters. In order to compare the solvent relaxation dynamics as revealed by the probe NpOH, we have measured the solvation dynamics of water with another well-known solvation probe coumarin 500 (C500). To understand the energetics of the hydrogen bonded network in hydrophilic (water)-hydrophobic (DX) mixture, we have studied the excited state kinetics of both the probes at different temperatures. Similarity in both the results reveal the importance of hydrogen bonding interactions in the solvent relaxation process and thereby provides a strengthened connection between solvation dynamics and ESPT process.

**1.3.3.2. Slow Solvent Relaxation Dynamics of Nanometer Sized Reverse Micellar Systems Through Tryptophan Metabolite, Kynurenine [59]:** In this study, we report a detail photophysical characterization of KN in Brij-30 RM. We have employed DLS study for the structural characterization of the RM. Steady state, picosecond-resolved optical spectroscopy including polarization gated fluorescence anisotropy studies reveal the dynamics of the probe and solvent relaxation in the nanopool of water in the RM. In order to investigate the intermediate photoinduced species of the probe KN we have used TRANES. FRET studies of the probe to another surface bound acceptors, crystal violet (CV) and C500 confirm interfacial binding of the probe KN in the RM. In order to compare the dynamical information of the RM environments as revealed by the probe KN,

we have also used another well-known solvation probe Hoechst 33258 (a DNA minor groove binder) for the exploration of solvent relaxation in the restricted environments.

### **1.3.4. Exploration of Structure and Function of a Protein in Macromolecular Crowding:**

**1.3.4.1. Ultrafast Electron Transfer in Riboflavin Binding Protein in Macromolecular Crowding of Nano-Sized Micelle [60]:** In this work, we have studied the dynamics of ET of a flavoprotein to the bound cofactor, an important metabolic process, in a model molecular/macromolecular crowding environments. Rf and RBP are used as model cofactor and flavoprotein respectively. SDS, an anionic surfactant is used as a model crowding agent. A systematic study on the ET dynamics in various SDS concentrations, ranging from below critical micellar concentration (CMC), where the surfactants remain as monomeric form to above CMC, where the surfactants self-assemble to form nanoscopic micelle, explored the dynamics of ET in the model molecular and macromolecular crowding environments. With energy selective excitation in picosecond-resolved studies, we have followed temporal quenching of the tryptophan residue of the protein and Rf in the RBP-Rf complex in various degrees of molecular/macromolecular crowding. The structural integrity of the protein (secondary and tertiary structures), vitamin binding capacity of RBP has been investigated using various techniques including UV-Vis, CD spectroscopy and DLS studies in the crowding environments.

### **1.3.5. Exploration of Environmental Dynamics and Enzymatic Activity in Nanoscopic Confinement:**

**1.3.5.1. Modulation of Environmental Dynamics at the Active Site and Activity of an Enzyme Under Nanoscopic Confinement: Subtilisin Carlsberg in Anionic AOT Reverse Micelle [61]:** In this study, we have addressed the environmental dynamics at the active site and the enzymatic activity of SC in anionic AOT RM retaining the structural integrity of the protein. We have found that, the solvation dynamics at the active site of the enzyme becomes faster with increasing  $w_0$  ( $w_0 = [\text{water}]/[\text{surfactant}]$ ) values of the AOT RM. However, the enzymatic activity is found to be increased with increasing water content in the RM. The genesis of the observation appears to stem from the hydrolysis

characteristics of the reaction between CBZ-GGL-pNA and SC, where water acts as nucleophile. While, faster hydration dynamics at the active site of the enzyme with increasing water content causes an increase in local polarity around the active site due to the hydration of polar and charged groups. The increase in polarity increases the active site flexibility, which in turn facilitates the hydrolysis reaction. From temperature dependent solvation dynamics study, we have also calculated the activation energy that has to be overcome for full orientational freedom to the water molecules from bound to free-state.

## **1.4. Plan of Thesis:**

The plan of the thesis is as follows:

**Chapter 1:** This chapter gives a brief introduction to the scope and motivation behind the thesis work. A brief summary of the work done is also included in this chapter.

**Chapter 2:** This chapter provides an overview of the dynamical and steady-state tools, the structural aspects of biologically important systems (proteins, biomimetic etc) and probes used in the research.

**Chapter 3:** Details of instrumentation, data analysis and experimental procedures have been discussed in this chapter.

**Chapter 4:** In this chapter, we have discussed our work on interaction of water molecules with a hydrophobic solvent.

**Chapter 5:** Structure, dynamics and energetics of water in biologically relevant hydrophobic environments have been discussed.

**Chapter 6:** We will discuss the role of dynamics of isolated water molecules in proton transfer reaction in biologically important hydrophobic/confined environments.

**Chapter 7:** We have explored of structure and function of a protein in macromolecular crowding environments.

**Chapter 8:** Here, we have discussed the environmental dynamics and enzymatic activity of a protein in confined environments.

## References

- [1] A.B. Fulton, How crowded is the cytoplasm?, *Cell* 30 (1982) 345.
- [2] S.B. Zimmerman, S.O. Trach, Estimation of macromolecule concentrations and excluded volume effects for the cytoplasm of *Escherichia coli*, *J. Mol. Biol.* 222 (1991) 599.
- [3] S. Cayley, B.A. Lewis, H.J. Guttman, M.T. Record Jr, Characterization of the cytoplasm of *Escherichia coli* K-12 as a function of external osmolarity: Implications for protein-DNA interactions in vivo, *J. Mol. Biol.* 222 (1991) 281.
- [4] R.J. Ellis, A.P. Minton, Cell biology: Join the crowd, *Nature* 425 (2003) 27.
- [5] S.B. Zimmerman, A.P. Minton, Macromolecular crowding: Biochemical, biophysical and physiological consequences, *Annu. Rev. Biophys. Biomol. Struct.* 22 (1993) 27.
- [6] A.P. Minton, The influence of macromolecular crowding and macromolecular confinement on biochemical reactions in physiological media, *J. Biol. Chem.* 276 (2001) 10577.
- [7] R.J. Ellis, Macromolecular crowding: Obvious but underappreciated, *Trends Biochem. Sci.* 26 (2001) 597.
- [8] A. Minton, The effect of volume occupancy upon the thermodynamic activity of proteins: Some biochemical consequences, *Mol. Cell. Biochem.* 55 (1983) 119.
- [9] R.J. Ellis, Macromolecular crowding: An important but neglected aspect of the intracellular environment, *Curr. Opin. Struct. Biol.* 11 (2001) 114.
- [10] G.B. Ralston, Effects of "crowding" in protein solutions, *J. Chem. Educ.* 67 (1990) 857.
- [11] N. Kozer, G. Schreiber, Effect of crowding on protein-protein association rates: Fundamental differences between low and high mass crowding agents, *J. Mol. Biol.* 336 (2004) 763.
- [12] N. Kozer, Y.Y. Kuttner, G. Haran, G. Schreiber, Protein-protein association in polymer solutions: From dilute to semidilute to concentrated, *Biophys. J.* 92 (2007) 2139.
- [13] Y. Phillip, E. Sherman, G. Haran, G. Schreiber, Common crowding agents have only a small effect on protein-protein interactions, *Biophys. J.* 97 (2009) 875.

- [14] Y. Phillip, M. Harel, R. Khait, S. Qin, H.-X. Zhou, G. Schreiber, Contrasting factors on the kinetic path to protein complex formation diminish the effects of crowding agents, *Biophys. J.* 103 (2012) 1011.
- [15] Y. Phillip, V. Kiss, G. Schreiber, Protein-binding dynamics imaged in a living cell, *Proc. Natl. Acad. Sci. USA* 109 (2012) 1461.
- [16] B. van den Berg, R.J. Ellis, C.M. Dobson, Effects of macromolecular crowding on protein folding and aggregation, *EMBO J.* 18 (1999) 6927.
- [17] S. Zorrilla, G. Rivas, A.U. Acuña, M.P. Lillo, Protein self-association in crowded protein solutions: A time-resolved fluorescence polarization study, *Protein Sci.* 13 (2004) 2960.
- [18] N. Cole, G.B. Ralston, Enhancement of self-association of human spectrin by polyethylene glycol, *Int. J. Biochem.* 26 (1994) 799.
- [19] P.K. Verma, S. Rakshit, R.K. Mitra, S.K. Pal, Role of hydration on the functionality of a proteolytic enzyme  $\alpha$ -chymotrypsin under crowded environment, *Biochimie* 93 (2011) 1424.
- [20] A.P. Minton, J. Wilf, Effect of macromolecular crowding upon the structure and function of an enzyme: Glyceraldehyde-3-phosphate dehydrogenase, *Biochemistry* 20 (1981) 4821.
- [21] M. Jiang, Z. Guo, Effects of macromolecular crowding on the intrinsic catalytic efficiency and structure of enterobactin-specific isochorismate synthase, *J. Am. Chem. Soc.* 129 (2007) 730.
- [22] T. Vöpel, G.I. Makhatadze, Enzyme activity in the crowded milieu, *PLoS ONE* 7 (2012) e39418.
- [23] K. Totani, Y. Ihara, I. Matsuo, Y. Ito, Effects of macromolecular crowding on glycoprotein processing enzymes, *J. Am. Chem. Soc.* 130 (2008) 2101.
- [24] L. Homchaudhuri, N. Sarma, R. Swaminathan, Effect of crowding by dextrans and ficolls on the rate of alkaline phosphatase-catalyzed hydrolysis: A size-dependent investigation, *Biopolymers* 83 (2006) 477.
- [25] I. Pozdnyakova, P. Wittung-Stafshede, Non-linear effects of macromolecular crowding on enzymatic activity of multi-copper oxidase, *Biochim. Biophys. Acta* 1804 (2010) 740.

- [26] L. Stagg, S.Q. Zhang, M.S. Cheung, P. Wittung-Stafshede, Molecular crowding enhances native structure and stability of  $\alpha/\beta$  protein flavodoxin, *Proc. Nat. Acad. Sci. USA* 104 (2007) 18976.
- [27] L.M. Charlton, C.O. Barnes, C. Li, J. Orans, G.B. Young, G.J. Pielak, Residue-level interrogation of macromolecular crowding effects on protein stability, *J. Am. Chem. Soc.* 130 (2008) 6826.
- [28] X. Ai, Z. Zhou, Y. Bai, W.Y. Choy,  $^{15}\text{N}$  NMR spin relaxation dispersion study of the molecular crowding effects on protein folding under native conditions, *J. Am. Chem. Soc.* 128 (2006) 3916.
- [29] N. Tokuriki, M. Kinjo, S. Negi, M. Hoshino, Y. Goto, I. Urabe, T. Yomo, Protein folding by the effects of macromolecular crowding, *Protein Sci.* 13 (2004) 125.
- [30] K. Sasahara, P. McPhie, A.P. Minton, Effect of dextran on protein stability and conformation attributed to macromolecular crowding, *J. Mol. Biol.* 326 (2003) 1227.
- [31] D. Homouz, M. Perham, A. Samiotakis, M.S. Cheung, P. Wittung-Stafshede, Crowded, cell-like environment induces shape changes in aspherical protein, *Proc. Natl. Acad. Sci. USA* 105 (2008) 11754.
- [32] M.S. Cheung, D. Klimov, D. Thirumalai, Molecular crowding enhances native state stability and refolding rates of globular proteins, *Proc. Nat. Acad. Sci. USA* 102 (2005) 4753.
- [33] K.S. Harve, R. Lareu, R. Rajagopalan, M. Raghunath, Understanding how the crowded interior of cells stabilizes DNA/DNA and DNA/RNA hybrids—in silico predictions and in vitro evidence, *Nucleic Acids Res.* 38 (2010) 172.
- [34] H. Workman, P.F. Flynn, Stabilization of RNA oligomers through reverse micelle encapsulation, *J. Am. Chem. Soc.* 131 (2009) 3806.
- [35] B. Akabayov, S.R. Akabayov, S.J. Lee, G. Wagner, C.C. Richardson, Impact of macromolecular crowding on DNA replication, *Nat. Commun.* 4 (2013) 1615.
- [36] S. Nakano, H. Karimata, T. Ohmichi, J. Kawakami, N. Sugimoto, The effect of molecular crowding with nucleotide length and cosolute structure on DNA duplex stability, *J. Am. Chem. Soc.* 126 (2004) 14330.
- [37] C.H. Spink, J.B. Chaires, Effects of hydration, ion release, and excluded volume on the melting of triplex and duplex DNA, *Biochemistry* 38 (1998) 496.

- [38] R. Goobes, N. Kahana, O. Cohen, A. Minsky, Metabolic buffering exerted by macromolecular crowding on DNA–DNA interactions: Origin and physiological significance, *Biochemistry* 42 (2003) 2431.
- [39] M.M. Dedmon, C.N. Patel, G.B. Young, G.J. Pielak, FlgM gains structure in living cells, *Proc. Natl. Acad. Sci. USA* 99 (2002) 12681.
- [40] G. Rivas, J.A. Fernandez, A.P. Minton, Direct observation of the self-association of dilute proteins in the presence of inert macromolecules at high concentration via tracer sedimentation equilibrium: Theory, experiment, and biological significance, *Biochemistry* 38 (1999) 9379.
- [41] G. Rivas, J.A. Fernández, A.P. Minton, Direct observation of the enhancement of noncooperative protein self-assembly by macromolecular crowding: Indefinite linear self-association of bacterial cell division protein FtsZ, *Proc. Natl. Acad. Sci. USA* 98 (2001) 3150.
- [42] M.P. Brown, C. Royer, Fluorescence spectroscopy as a tool to investigate protein interactions, *Curr. Opin. Biotech.* 8 (1997) 45.
- [43] J. Wilf, A.P. Minton, Evidence for protein self-association induced by excluded volume Myoglobin in the presence of globular proteins, *Biochim. Biophys. Acta* 670 (1981) 316.
- [44] K.A. Dill, S. Bromberg, K. Yue, H.S. Chan, K.M. Ftebig, D.P. Yee, P.D. Thomas, Principles of protein folding—A perspective from simple exact models, *Protein Sci.* 4 (1995) 561.
- [45] S. Sun, R. Brem, H.S. Chan, K.A. Dill, Designing amino acid sequences to fold with good hydrophobic cores, *Protein Eng.* 8 (1995) 1205.
- [46] A. Zarrine-Afsar, S. Wallin, A.M. Neculai, P. Neudecker, P.L. Howell, A.R. Davidson, H.S. Chan, Theoretical and experimental demonstration of the importance of specific nonnative interactions in protein folding, *Proc. Natl. Acad. Sci. USA* 105 (2008) 9999.
- [47] F. Pizzitutti, M. Marchi, F. Sterpone, P.J. Rossky, How protein surfaces induce anomalous dynamics of hydration water, *J. Phys. Chem. B* 111 (2007) 7584.

- [48] J.F. Pankow, N.R. Thomson, R.L. Johnson, A.L. Baehr, J.S. Zogorski, The urban atmosphere as a non-point source for the transport of MTBE and other volatile organic compounds (VOCs) to shallow groundwater, *Environ. Sci. Technol.* 31 (1997) 2821.
- [49] J.E. Reuter, B.C. Allen, R.C. Richards, J.F. Pankow, C.R. Goldman, R.L. Scholl, J.S. Seyfried, Concentrations, sources, and fate of the gasoline oxygenate methyl tert-butyl ether (MTBE) in a multiple-use lake, *Environ. Sci. Technol.* 32 (1998) 3666.
- [50] C. Achten, A. Kolb, W. Püttmann, P. Seel, R. Gühr, Methyl tert-butyl ether (MTBE) in river and wastewater in Germany, *Environ. Sci. Technol.* 36 (2002) 3652.
- [51] P.J. Squillace, J.S. Zogorski, W.G. Wilber, C.V. Price, Preliminary assessment of the occurrence and possible sources of MTBE in groundwater in the United States, 1993–1994, *Environ. Sci. Technol.* 30 (1996) 1721.
- [52] P.J. Squillace, M.J. Moran, W.W. Lapham, C.V. Price, R.M. Clawges, J.S. Zogorski, Volatile organic compounds in untreated ambient groundwater of the United States, 1985–1995, *Environ. Sci. Technol.* 33 (1999) 4176.
- [53] A.L. Baehr, P.E. Stackelberg, R.J. Baker, Evaluation of the atmosphere as a source of volatile organic compounds in shallow groundwater, *Water Resour. Res.* 35 (1999) 127.
- [54] J. Klinger, C. Stieler, F. Sacher, H.J. Brauch, MTBE (methyl tertiary-butyl ether) in groundwaters: Monitoring results from Germany, *J. Environ. Monitor.* 4 (2002) 276.
- [55] F. Belpoggi, M. Soffritti, C. Maltoni, Methyl-tertiary-butyl ether (MTBE)—A gasoline additive—Causes testicular and lympho haematopoietic cancers in rats, *Toxicol. Ind. Health* 11 (1995) 119.
- [56] S. Rakshit, R. Saha, A. Singha, Z.S.A. Seddigi, S.K. Pal, Molecular interaction, co-solubilization of organic pollutants and ecotoxicity of a potential carcinogenic fuel additive MTBE in water, *J. Mol. Liq.* 180 (2013) 235.
- [57] S. Rakshit, R. Saha, A. Chakraborty, S.K. Pal, Effect of hydrophobic interaction on structure, dynamics, and reactivity of water, *Langmuir* 29 (2013) 1808.
- [58] S. Rakshit, R. Saha, P.K. Verma, S.K. Pal, Role of solvation dynamics in excited state proton transfer of 1-naphthol in nanoscopic water clusters formed in a hydrophobic solvent, *Photochem. Photobiol.* 88 (2012) 851.

- [59] S. Rakshit, N. Goswami, S.K. Pal, Slow solvent relaxation dynamics of nanometer sized reverse micellar systems through tryptophan metabolite, kynurenine, *Photochem. Photobiol.* 88 (2012) 38.
- [60] S. Rakshit, R. Saha, P.K. Verma, R.K. Mitra, S.K. Pal, Ultrafast electron transfer in riboflavin binding protein in macromolecular crowding of nano-sized micelle, *Biochimie* 94 (2012) 2673.
- [61] S. Rakshit, R. Saha, S.K. Pal, Modulation of environmental dynamics at the active site and activity of an enzyme under nanoscopic confinement: Subtilisin carlsberg in anionic AOT reverse micelle, *J. Phys. Chem. B* (2013) doi.org/10.1021/jp4061494.

# Chapter 2

## Experimental Techniques and Systems

In order to investigate the ultrafast processes involved in the course of study on structure, function and dynamics of biomolecules in presence of other biologically relevant macromolecules, different steady-state and dynamical tools have been employed. These include solvation dynamics, fluorescence anisotropy, solvolysis, Förster resonance energy transfer (FRET), densimetric-acoustic measurements, enzyme kinetics and determination of activation energy using Arrhenius theory. In this chapter, we have included a brief discussion about the above mentioned dynamical tools. Overviews of the various systems and the fluorescent probes used in the studies have also been provided.

### 2.1. Steady-State and Dynamical Tools:

**2.1.1. Solvation Dynamics:** Almost all biological macromolecules, proteins (enzymes) and DNAs are inactive in the absence of water. Hydration of a protein/enzyme/DNA is particularly important for their structural stability and function, especially their recognition by ligand molecules. This role of hydration in enzymatic activity and molecular recognition of biomolecules have recently been reviewed in a number of publications [1-4].

**2.1.1.1. Theory:** Solvation dynamics refer to the process of reorganization of solvent dipoles around a dipole created instantaneously or an electron/proton injected suddenly in a polar liquid. In order to understand the meaning and scope of solvation dynamics, let us first visualize the physical essence of the dynamical process involved for a solute molecule in a polar solvent [5-7]. A change in the probe's dipole is made at the time  $t = 0$ , by an excitation laser pulse. This dipole gives rise to an instantaneous electric field on the solvent molecules. The interaction of permanent dipoles of the solvent with the instantaneously created electric field shifts the free energy minimum of the solvent to a non-zero value of the polarization. The solvent motion is crucial (Figure 2.1). Since the probe is excited instantaneously (a Franck-Condon transition as far as the nuclear degrees of freedom are concerned), the solvent molecules at  $t = 0$  find themselves in a relatively high-energy

configuration. Subsequently, the solvent molecules begin to move and rearrange themselves to reach their new equilibrium positions (Figure 2.2). The nuclear motion involved can be broadly classified into rotational and translational motions.

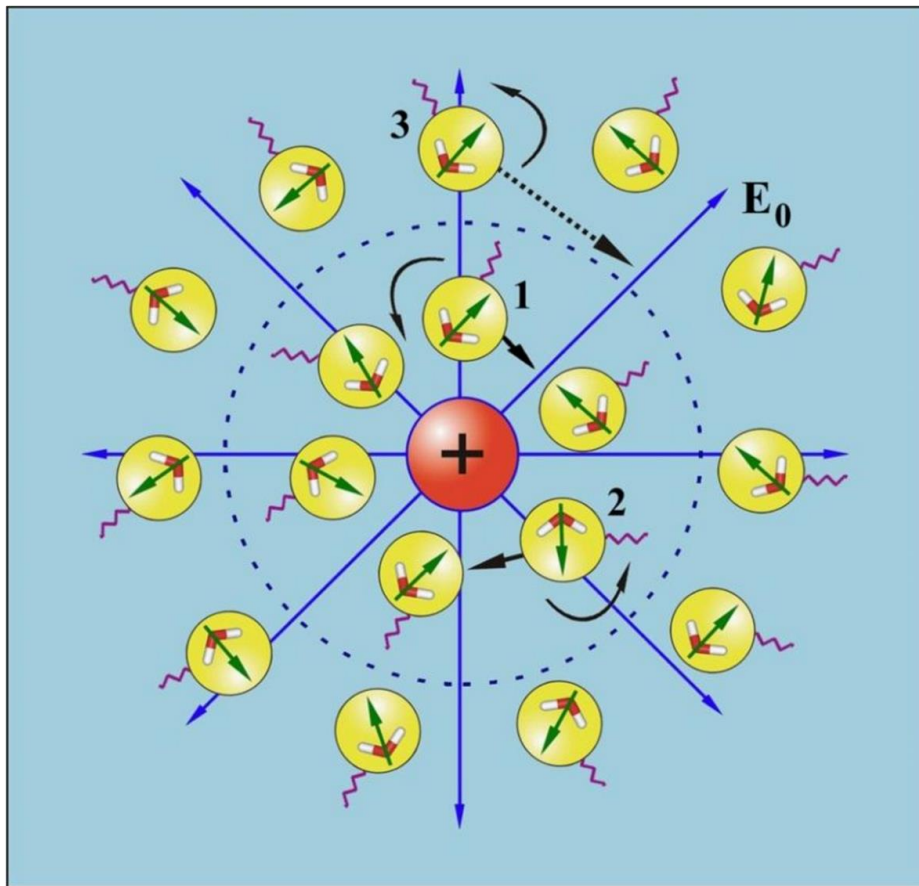


**Figure 2.1:** Schematic illustration of solvation of an ion (or dipole) by water. The neighboring molecules (numbered 1 and 2) can either rotate or translate to attain the minimum energy configuration. On the other hand, distant water molecule 3 can only rotate to attain minimum energy configuration. The field is shown as  $E_0$ . The springs connected to the molecules are meant to denote hydrogen bonding.

When the solvent is bulk water, rotational motion would also include hindered rotation and libration, while translation would include the intermolecular vibration due to the extensive hydrogen bonding. The two specific motions, libration and intermolecular vibration, are relatively high in frequency and are expected to play a dominant role in the initial part of solvation [8]. The molecular motions involved are shown schematically in Figure 2.1 and in Figure 2.3 we show a typical solvation time correlation function. For clarity, we approximate the motions responsible for the decay in different regions.

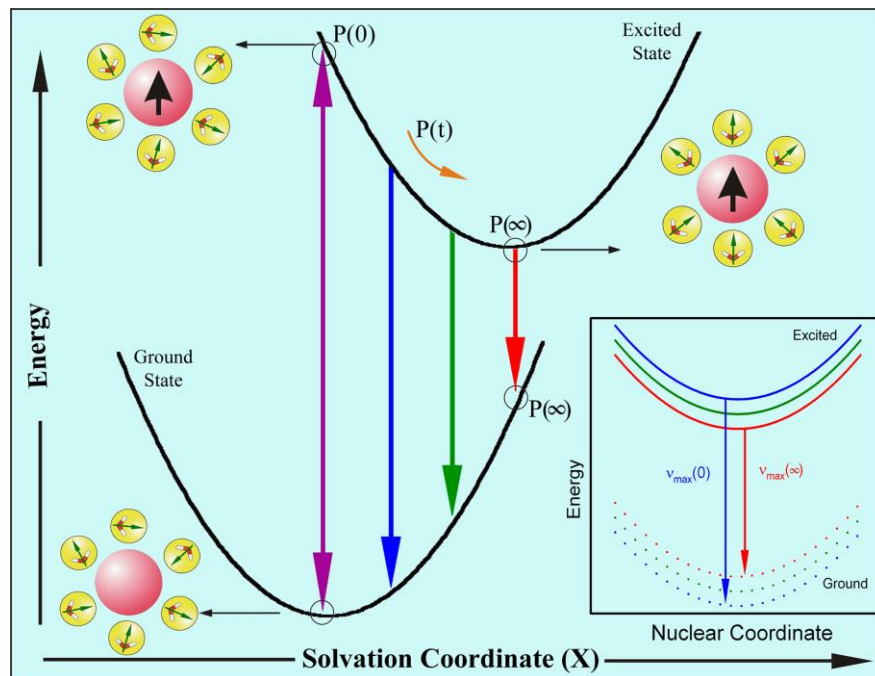


**Figure 2.2:** Schematic representation of the potential energy surfaces involved in solvation dynamics showing the water orientational motions along the solvation coordinate together with instantaneous polarization  $P$ . In the inset we show the change in the potential energy along the intramolecular nuclear coordinate. As solvation proceeds the energy of the solute comes down giving rise to a red shift in the fluorescence spectrum. Note the instantaneous  $P$ , e.g.,  $P(\infty)$ , on the two connected potentials.

A simple way to address the dynamics of polar solvation is to start with the following expression for the solvation energy,  $E_{\text{solv}}(t)$  [9],

$$E_{\text{solv}}(t) = -\frac{1}{2} \int d\mathbf{r} \mathbf{E}_0(\mathbf{r}) \cdot \mathbf{P}(\mathbf{r}, t) \quad (2-1)$$

where  $\mathbf{E}_0(\mathbf{r})$  is the instantaneously created, position-dependent electric field from the ion or the dipole of the solute and  $\mathbf{P}(\mathbf{r}, t)$  is the position and time-dependent polarization. The latter is defined by the following expression,

$$\mathbf{P}(\mathbf{r}, t) = \int d\Omega \boldsymbol{\mu}(\Omega) \rho(\mathbf{r}, \Omega, t) \quad (2-2)$$

where  $\boldsymbol{\mu}(\Omega)$  is the dipole moment vector of a molecule at position  $\mathbf{r}$ , and  $\rho(\mathbf{r}, \Omega, t)$  is the position, orientation and time-dependent density. Therefore, the time dependence of the solvation energy is determined by the time dependence of polarization that is in turn determined by the time dependence of the density. If the perturbation due to the probe on dynamics of bulk water is negligible, then the time dependence of polarization is dictated by the natural dynamics of the liquid.

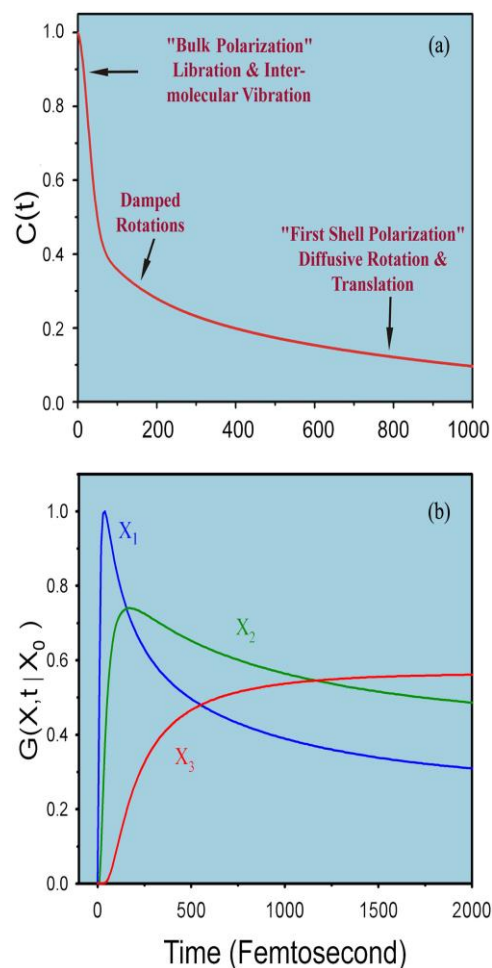


**Figure 2.3:** (a) A typical solvation time correlation function for water is shown here. The time correlation function exhibits three distinct regions: The initial ultrafast decay, an intermediate decay of about 200 fs and the last slow decay with time constant of 1 ps. The physical origin of each region is indicated on the plot itself; see text. (b) Green's function  $G(X,t|X_0)$  for population relaxation along the solvation coordinate ( $X$ ) is plotted against time in femtosecond. In  $G$ ,  $X_0$  is the initial position at  $t = 0$ . This figure shows the position and time dependence of the population fluorescence intensity. At early times (when the population is at  $X_1$ ) there is ultrafast rise followed by an ultrafast decay. At intermediate times (when the population is at  $X_2$ ) there is a rise followed by a slow decay as shown by the green line. At long times when the population is nearly relaxed (position  $X_3$ , red line) we see only a rise.

The theoretical analysis of the time-dependent density is usually carried out using a molecular hydrodynamic approach that is based on the basic conservation (density, momentum and energy) laws and includes the effects of intermolecular (both spatial and orientational) correlations. The latter provides the free energy surface on which solvation proceeds. The equation of motion of the density involves both orientational and translational motions of the solvent molecules. The details of the theoretical development

are reported in literature [5]; here we shall present a simple physical picture of the observed biphasic solvation dynamics.

Within linear response theory, the solvation correlation function is directly related to the solvation energy as,

$$C(t) = \frac{\langle \delta E(0) \cdot \delta E(t) \rangle}{\langle \delta E^2 \rangle} = \frac{\langle E(t) \rangle - \langle E(\infty) \rangle}{\langle E(0) \rangle - \langle E(\infty) \rangle} \quad (2-3)$$

where  $\delta E$  is the fluctuation of solvation energy from the average equilibrium value. Note that the equality in equation (2-3) indicates the direct relation for the average of the fluctuations over the equilibrium distribution (left) and the non-equilibrium function (right) which relates to observables; without  $\langle E(\infty) \rangle$  the correspondence is clear, and  $\langle E(\infty) \rangle$  is rigorously the result of the equilibrium term in the numerator and for normalization in the denominator.

The ultrafast component in the solvation time correlation function (Figure 2.3(a)), originates from the initial relaxation in the steep collective solvation potential. The collective potential is steep because it involves the total polarization of the system [5, 6]. This initial relaxation couples mainly to the hindered rotation (i.e., libration) and the hindered translation (i.e., the intermolecular vibration), which are the available high frequency modes of the solvent; neither long amplitude rotation nor molecular translation are relevant here. The last part in the decay of the solvation correlation function involves larger amplitude rotational and translational motions of the nearest neighbor molecules in the first solvation shell. In the intermediate time, one gets contributions from the moderately damped rotational motions of water molecules. In a sense, with the above description one recovers the famous Onsager's "inverse snow-ball" picture of solvation [10]. The slowest time constant is  $\sim 1$  ps, which is determined by the individual rotational and translational motions of the molecules in the "first solvation shell" nearly close to the probe. The femtosecond component is dominated by the high frequency hindered rotational and translational (vibration) polarization [8, 11, 12].

Figure 2.2 shows a schematic of the solvation potential and the orientational motions for the water molecules involved. From the shape of the potential, it can be seen

that the transient behavior for the population during solvation should be a decay function on the blue edge of the spectrum and a rise function on the red edge. These wavelength-dependent features can be explained nicely within a generalized model of relaxation in which a Gaussian wave packet relaxes on a harmonic surface. The relaxation is non-exponential and a Green's function can describe the approach of the wave packet along the solvation coordinate,  $X$ , to its equilibrium value. For the general non-Markovian case it is given by [13],

$$G(X, t|X_0) = \frac{1}{\sqrt{2\pi\langle X^2 \rangle [1 - C^2(t)]}} \exp \left[ -\frac{[X - X_0 C(t)]^2}{2\langle X^2 \rangle [1 - C^2(t)]} \right] \quad (2-4)$$

where  $\langle X^2 \rangle$  is the equilibrium mean square fluctuation of the polarization coordinate in the excited state surface,  $C(t)$  is the solvation correlation function described in equation (2-3) and  $X_0$  is the initial value of the packet on the solvation coordinate. Equation (2-4) describes the motion of the wave packet (polarization density) beginning at  $t = 0$  ( $X_0$ ) as a delta function and according to the solvation time correlation function. As  $t \rightarrow \infty$ ,  $C(t) \rightarrow 0$  and we recover the standard Gaussian distribution. Initially, ( $t \rightarrow 0$ ), the exponential is large, so the decay is ultrafast, but at long times, the relaxation slows down, ultimately to appear as a rise. In Figure 2.3(b), we present calculations of  $G(X, t|X_0)$  at different positions along the solvation coordinate giving decays at  $X_1$  and  $X_2$ , but with different time constants, and a rise at  $X_3$ , as demonstrated experimentally.

**2.1.1.2. Experimental Methods:** In order to study solvation stabilization of a probe in an environment, a number of fluorescence transients are taken at different wavelengths across the emission spectrum of the probe. As described earlier, blue and red ends of the emission spectrum are expected to show decay and rise, respectively in the transients. The observed fluorescence transients are fitted by using a nonlinear least square fitting procedure to a function,

$$\left( X(t) = \int_0^t E(t') R(t - t') dt' \right) \quad (2-5)$$

comprising of convolution of the instrument response function (IRF) ( $E(t)$ ) with a sum of exponentials,

$$\left( R(t) = A + \sum_{i=1}^N B_i \exp(-t/\tau_i) \right) \quad (2-6)$$

with pre-exponential factors ( $B_i$ ), characteristic lifetimes ( $\tau_i$ ) and a background ( $A$ ). Relative concentration in a multi-exponential decay is finally expressed as;

$$\alpha_n = \frac{B_n}{\sum_{i=1}^N B_i}. \quad (2-7)$$

The relative contribution of a particular decay component ( $f_n$ ) in the total fluorescence is defined as,

$$f_n = \frac{\tau_n B_n}{\sum_{i=1}^N B_i \tau_i} \times 100. \quad (2-8)$$

The quality of the curve fitting is evaluated by reduced chi-square (0.9-1.1) and residual data. The purpose of the fitting is to obtain the decays in an analytical form suitable for further data analysis.

To construct time resolved emission spectra (TRES) we follow the technique described in references [14, 15]. As described above, the emission intensity decays are analyzed in terms of the multi-exponential model,

$$I(\lambda, t) = \sum_{i=1}^N \alpha_i(\lambda) \exp(-t/\tau_i(\lambda)) \quad (2-9)$$

where  $\alpha_i(\lambda)$  are the pre-exponential factors, with  $\sum_i \alpha_i(\lambda) = 1.0$ . In this analysis we compute a new set of intensity decays, which are normalized so that the time-integrated intensity at each wavelength is equal to the steady-state intensity at that wavelength. Considering  $F(\lambda)$  to be the steady-state emission spectrum, we calculate a set of  $H(\lambda)$  values using,

$$H(\lambda) = \frac{F(\lambda)}{\int_0^{\infty} I(\lambda, t) dt} \quad (2-10)$$

which for multiexponential analysis becomes,

$$H(\lambda) = \frac{F(\lambda)}{\sum_i \alpha_i(\lambda)\tau_i(\lambda)} \quad (2-11)$$

Then, the appropriately normalized intensity decay functions are given by,

$$I(\lambda, t) = H(\lambda)I(\lambda, t) = \sum_{i=1}^N \alpha'_i(\lambda) \exp\left(-t/\tau_i(\lambda)\right) \quad (2-12)$$

where  $\alpha'_i(\lambda) = H(\lambda)\alpha_i(\lambda)$ . The values of  $I(\lambda, t)$  are used to calculate the intensity at any wavelength and time, and thus the TRES. The values of the emission maxima and spectral width are determined by nonlinear least-square fitting of the spectral shape of the TRES. The spectral shape is assumed to follow a lognormal line shape [14],

$$I(\bar{\nu}) = I_0 \exp\left\{-\left[\ln 2 \left(\frac{\ln(\alpha + 1)}{b}\right)^2\right]\right\} \quad (2-13)$$

with  $\alpha = \frac{2b(\bar{\nu} - \bar{\nu}_{\max})}{\Delta} - 1$  where  $I_0$  is amplitude,  $\bar{\nu}_{\max}$  is the wavenumber of the emission

maximum and spectral width is given by,  $\Gamma = \Delta \left[ \frac{\sinh(b)}{b} \right]$ . The terms  $b$  and  $\Delta$  are asymmetry and width parameters, respectively and equation (2-9) reduces to a Gaussian function for  $b = 0$ .

The time-dependent fluorescence Stokes shifts, as estimated from TRES are used to construct the normalized spectral shift correlation function or the solvent correlation function  $C(t)$  and is defined as,

$$C(t) = \frac{\bar{\nu}(t) - \bar{\nu}(\infty)}{\bar{\nu}(0) - \bar{\nu}(\infty)} \quad (2-14)$$

where,  $\bar{\nu}(0)$ ,  $\bar{\nu}(t)$  and  $\bar{\nu}(\infty)$  are the emission maxima (in  $\text{cm}^{-1}$ ) of the TRES at time zero,  $t$  and infinity, respectively. The  $\bar{\nu}(\infty)$  value is considered to be the emission frequency beyond which insignificant or no spectral shift is observed. The  $C(t)$  function represents the temporal response of the solvent relaxation process, as occurs around the probe following its photoexcitation and the associated change in the dipole moment.

In order to further investigate possible heterogeneity in the positional distribution of fluoroprobes at the interfaces of biomimicking self-assemblies we follow time resolved area normalized emission spectroscopy (TRANES), which is a well-established technique [16, 17] and is a modified version of TRES. TRANES were constructed by normalizing the area of each spectrum in TRES such that the area of the spectrum at time  $t$  is equal to the area of the spectrum at  $t = 0$ . A useful feature of this method is the presence of an isoemissive point in the spectra involving emission from two species, which are kinetically coupled either irreversibly or reversibly or not coupled at all.

**2.1.2. Fluorescence Anisotropy:** Anisotropy is defined as the extent of polarization of the emission from a fluorophore. Anisotropy measurements are commonly used in biochemical applications of fluorescence. It provides information about the size and shape of proteins or the rigidity of various molecular environments. Anisotropy measurements have also been used to measure protein-protein associations, fluidity of membranes and for immunoassays of numerous substances. These measurements are based on the principle of photoselective excitation of those fluorophore molecules whose absorption transition dipoles are parallel to the electric vector of polarized excitation light. In an isotropic solution, fluorophores are oriented randomly. However, upon selective excitation, partially oriented population of fluorophores with polarized fluorescence emission results. The relative angle between the absorption and emission transition dipole moments determines the maximum measured anisotropy ( $r_0$ ). The fluorescence anisotropy ( $r$ ) and polarization ( $P$ ) are defined by,

$$r = \frac{I_{\parallel} - I_{\perp}}{I_{\parallel} + 2I_{\perp}} \quad (2-15)$$

$$\text{and } P = \frac{I_{\parallel} - I_{\perp}}{I_{\parallel} + I_{\perp}} \quad (2-16)$$

where,  $I_{\parallel}$  and  $I_{\perp}$  are the fluorescence intensities of vertically and horizontally polarized emission when the fluorophore is excited with vertically polarized light. Polarization and anisotropy are interrelated as,

$$r = \frac{2P}{3 - P} \quad (2-17)$$

$$\text{and } P = \frac{3r}{2+r} \quad (2-18)$$

Although polarization and anisotropy provides the same information, anisotropy is preferred since the latter is normalized by total fluorescence intensity ( $I_T = I_{\parallel} + 2I_{\perp}$ ) and in case of multiple emissive species anisotropy is additive while polarization is not. Several phenomena, including rotational diffusion and energy transfer, can decrease the measured anisotropy to values lower than maximum theoretical values. Following a pulsed excitation the fluorescence anisotropy,  $r(t)$  of a sphere is given by,

$$r(t) = r_0 \exp(-t/\tau_{\text{rot}}) \quad (2-19)$$

where  $r_0$  is the anisotropy at time  $t = 0$  and  $\tau_{\text{rot}}$  is the rotational correlation time of the sphere.

**2.1.2.1. Theory:** For a radiating dipole the intensity of light emitted is proportional to the square of the projection of the electric field of the radiating dipole onto the transmission axis of the polarizer. The intensity of parallel and perpendicular projections are given by,

$$I_{\parallel}(\theta, \psi) = \cos^2 \theta \quad (2-20)$$

$$I_{\perp}(\theta, \psi) = \sin^2 \theta \sin^2 \psi \quad (2-21)$$

where  $\theta$  and  $\psi$  are the orientational angles of a single fluorophore relative to the z and y-axis, respectively (Figure 2.4(a)). In solution, fluorophores remain in random distribution and the anisotropy is calculated by excitation photoselection. Upon photoexcitation by polarized light, the molecules having absorption transition moments aligned parallel to the electric vector of the polarized light have the highest probability of absorption. For the excitation polarization along z-axis, all molecules having an angle  $\psi$  with respect to the y-axis will be excited. The population will be symmetrically distributed about the z-axis. For experimentally accessible molecules, the value of  $\psi$  will be in the range from 0 to  $2\pi$  with equal probability. Thus, the  $\psi$  dependency can be eliminated.

$$\langle \sin^2 \psi \rangle = \frac{\int_0^{2\pi} \sin^2 \psi d\psi}{\int_0^{2\pi} d\psi} = \frac{1}{2} \quad (2-22)$$

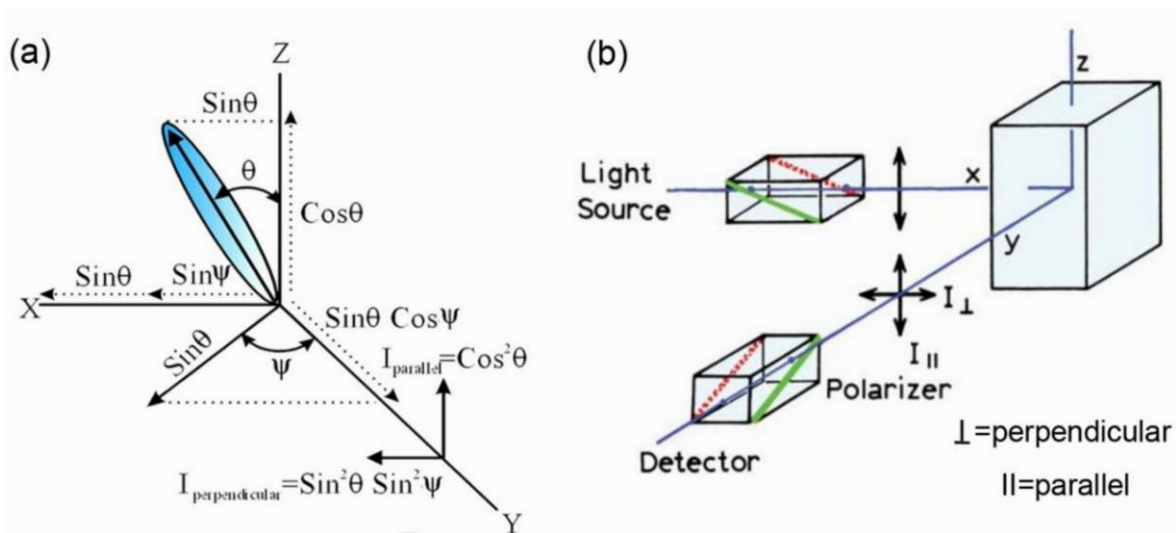


**Figure 2.4:** (a) Emission intensity of a single fluorophore (blue ellipsoid) in a coordinate system. (b) Schematic representation of the measurement of fluorescence anisotropy.

and

$$I_{\parallel}(\theta) = \cos^2 \theta \quad (2-23)$$

$$I_{\perp}(\theta) = \frac{1}{2} \sin^2 \theta \quad (2-24)$$

Consider a collection of molecules oriented relative to the z-axis with probability  $f(\theta)$ . Then, measured fluorescence intensities for this collection after photoexcitation are,

$$I_{\parallel} = \int_0^{\pi/2} f(\theta) \cos^2 \theta d\theta = k \langle \cos^2 \theta \rangle \quad (2-25)$$

$$I_{\perp} = \int_0^{\pi/2} f(\theta) \sin^2 \theta d\theta = \frac{k}{2} \langle \sin^2 \theta \rangle \quad (2-26)$$

where  $f(\theta)d\theta$  is the probability that a fluorophore is oriented between  $\theta$  and  $\theta+d\theta$  and is given by,

$$f(\theta)d\theta = \cos^2 \theta \sin \theta d\theta \quad (2-27)$$

$k$  is the instrumental constant. Thus, the anisotropy ( $r$ ) is defined as,

$$r = \frac{3 \langle \cos^2 \theta \rangle - 1}{2} \quad (2-28)$$

when  $\theta = 54.7^\circ$  i.e. when  $\cos^2 \theta = 1/3$ , the complete loss of anisotropy occurs. Thus, the fluorescence taken at  $\theta = 54.7^\circ$  with respect to the excitation polarization is expected to be

free from the effect of anisotropy and is known as magic angle emission. For collinear absorption and emission dipoles, the value of  $\langle \cos^2 \theta \rangle$  is given by the following equation,

$$\langle \cos^2 \theta \rangle = \frac{\int_0^{\pi/2} \cos^2 \theta f(\theta) d\theta}{\int_0^{\pi/2} f(\theta) d\theta} \quad (2-29)$$

Substituting equation (2-27) in equation (2-29) one can get the value of  $\langle \cos^2 \theta \rangle = 3/5$  and anisotropy value to be 0.4 (from equation (2-28)). This is the maximum value of anisotropy obtained when the absorption and emission dipoles are collinear and when no other depolarization process takes place. However, for most fluorophores, the value of anisotropy is less than 0.4 and it is dependent on the excitation wavelength. It is demonstrated that as the displacement of the absorption and emission dipole occurs by an angle  $\gamma$  relative to each other, it causes further loss of anisotropy (reduction by a factor 2/5) [15] from the value obtained from equation (2-28). Thus, the value of fundamental anisotropy,  $r_0$  is given by,

$$r_0 = \frac{2}{5} \left( \frac{3 \cos^2 \gamma - 1}{2} \right) \quad (2-30)$$

For any fluorophore randomly distributed in solution, with one-photon excitation, the value of  $r_0$  varies from -0.2 to 0.4 for  $\gamma$  values varying from  $90^\circ$  to  $0^\circ$ .

**2.1.2.2. Experimental Methods:** For time resolved anisotropy ( $r(t)$ ) measurements (Figure 2.4(b)), emission polarization is adjusted to be parallel and perpendicular to that of the excitation polarization. Spencer and Weber [18] have derived the relevant equations for the time dependence of  $I_{\parallel}(t)$  (equation (2-31)) and  $I_{\perp}(t)$  (equation (2-32)) for single rotational and fluorescence relaxation times,  $\tau_{rot}$  and  $\tau_f$ , respectively,

$$I_{\parallel}(t) = \exp(-t/\tau_f) (1 + 2r_0 \exp(-t/\tau_{rot})) \quad (2-31)$$

$$I_{\perp}(t) = \exp(-t/\tau_f) (1 - r_0 \exp(-t/\tau_{rot})) \quad (2-32)$$

The total fluorescence is given by,

$$F(t) = I_{\parallel}(t) + 2I_{\perp}(t) = 3 \exp(-t/\tau_f) = F_0 \exp(-t/\tau_f) \quad (2-33)$$

The time dependent anisotropy,  $r(t)$  is given by,

$$r(t) = \frac{I_{\parallel}(t) - I_{\perp}(t)}{I_{\parallel}(t) + 2I_{\perp}(t)} = r_0 \exp(-t/\tau_{\text{rot}}) \quad (2-34)$$

$F(t)$  depends upon  $\tau_f$  and  $r(t)$  only upon  $\tau_{\text{rot}}$  so that these two lifetimes can be separated. This separation is not possible in steady-state measurements. It should be noted that the degree of polarization ( $P$ ) is not independent of  $\tau_f$  and is therefore not as useful as  $r$ . For reliable measurement of  $r(t)$ , three limiting cases can be considered,

- (a) If  $\tau_f < \tau_{\text{rot}}$  the fluorescence decays before the anisotropy decays, and hence only  $r_0$  can be measured.
- (b) If  $\tau_{\text{rot}} < \tau_f$ , in contrast to steady-state measurements,  $\tau_{\text{rot}}$  can be measured in principle. The equations (2-31) and (2-32) show that the decay of the parallel and perpendicular components depends only upon  $\tau_{\text{rot}}$ . The experimental disadvantage of this case is that those photons emitted after the lapse of a few times  $\tau_{\text{rot}}$  can not contribute to the determination of  $\tau_{\text{rot}}$ , but can be avoided with a good signal-to-noise ratio.
- (c) If  $\tau_{\text{rot}} \approx \tau_f$ , then it becomes the ideal situation since almost all photons are counted within the time (equal to several rotational relaxation times) in which  $r(t)$  shows measurable changes.

For systems with multiple rotational correlation times,  $r(t)$  is given by,

$$r(t) = r_0 \sum_i \beta_i e^{-t/\tau_i} \quad (2-35)$$

where  $\sum_i \beta_i = 1$ . It should be noted that the instrument monitoring the fluorescence, particularly the spectral dispersion element, responds differently to different polarizations of light, thus emerging the need for a correction factor. For example, the use of diffraction gratings can yield intensities of emission, which depend strongly upon orientation with respect to the plane of the grating. It is necessary when using such instruments to correct for the anisotropy in response. This instrumental anisotropy is usually termed as G-factor (grating factor) and is defined as the ratio of the transmission efficiency for vertically polarized light to that for horizontally polarized light ( $G = I_{\parallel}/I_{\perp}$ ). Hence, values of fluorescence anisotropy,  $r(t)$  corrected for instrumental response, would be given by [19],

$$r(t) = \frac{I_{\parallel}(t) - GI_{\perp}(t)}{I_{\parallel}(t) + 2GI_{\perp}(t)} \quad (2-36)$$

The G-factor at a given wavelength can be determined by exciting the sample with horizontally polarized excitation beam and collecting the two polarized fluorescence decays, one parallel and other perpendicular to the horizontally polarized excitation beam. G-factor can also be determined following longtime tail matching technique [19]. If  $\phi < \tau_f$ , it can be seen that the curves for  $I_{\parallel}(t)$  and  $I_{\perp}(t)$  should become identical. If in any experiment they are not, it can usually be assumed that this is due to a non-unitary G-factor. Hence normalizing the two decay curves on the tail of the decay eliminates the G-factor in the anisotropy measurement.

**2.1.3. Arrhenius Theory of Activation Energy:** The dynamics of solvation at a macromolecular interface can be exploited to extract information on the energetics of the participating water molecules [9, 20-23]. Water present at the surface of biomolecules or biomimicking systems can broadly be distinguished as bound type (water hydrogen bonded to the interface) and bulk type water (Figure 2.5). In the water layer around the surface, the

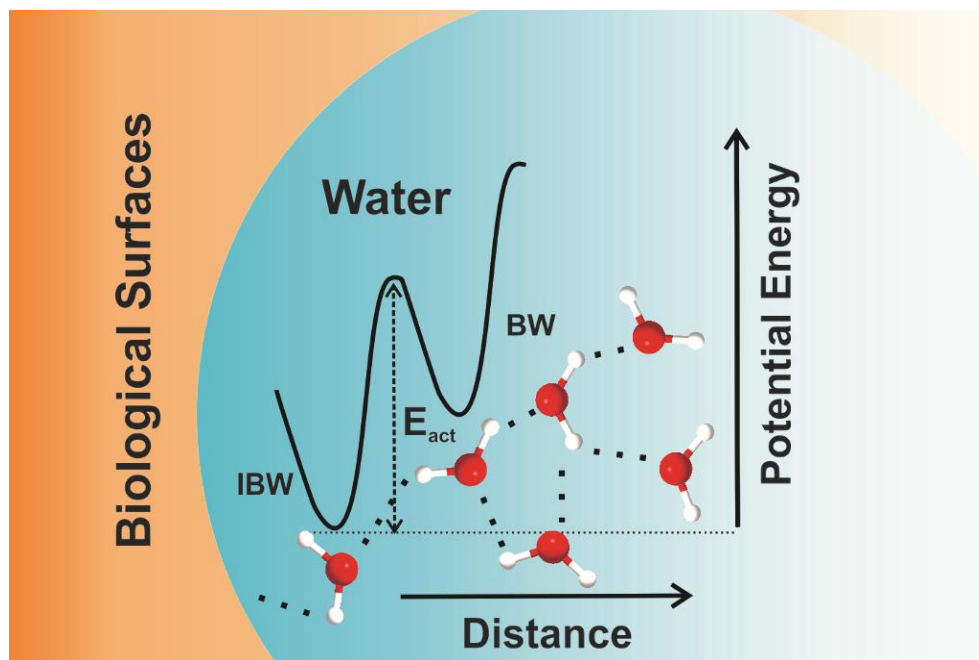
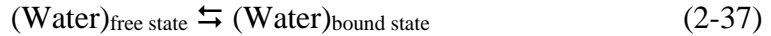


*Figure 2.5: Schematic representation of different types of water molecules present at various biomolecular interfaces and the corresponding activation energy barrier.*

interaction with water involves hydrogen bonding to the polar and charged groups of the surface. When strongly bonded to the biomacromolecules or biomimicking surfaces, the water molecules cannot contribute to solvation dynamics because they can neither rotate nor translate. However, hydrogen bonding is transient and there exists a dynamic equilibrium between the free and the bound water molecules. The potential of interaction can be represented by a double-well structure to symbolize the processes of bond breaking and bond forming. In general, the bonded water molecules become free by translational and rotational motions. The equilibrium between bound and free water can be written as [20, 24, 25],



and from the activated complex theory one can have,

$$k_{\text{bf}} = (k_{\text{B}}T/h)\exp(-\Delta G^0/RT) \quad (2-38)$$

where,  $k_{\text{bf}}$  is the rate constant of the bound to free transition. Now, if the transition process (2-37) follows a typical Arrhenius type of energy barrier crossing model, one can write,

$$\frac{1}{\tau_{\text{solv}}} \approx k_{\text{bf}} = A\exp(-E_{\text{act}}/RT) \quad (2-39)$$

where  $E_{\text{act}}$  is the activation energy for the transition process and  $A$  is the pre-exponential factor. A plot of  $\ln(1/\tau_{\text{solv}})$  against  $1/T$  produces a straight line and from the slope of the line  $E_{\text{act}}$  can be calculated. The temperature dependence of the solvation follows the Arrhenius equation and yields the activation energy needed for the conversion of bound and free forms [26].

**2.1.4. Förster Resonance Energy Transfer (FRET):** Förster resonance energy transfer (FRET) is an electrodynamic phenomenon involving the non-radiative transfer of the excited state energy from the donor dipole (D) to an acceptor dipole (A) in the ground state (Figure 2.6(a)). FRET has got wide applications in all fluorescence applications including medical diagnostics, DNA analysis and optical imaging. Since FRET can measure the size of a protein molecule or the thickness of a membrane, it is also known as “spectroscopic ruler” [27]. FRET is very often used to measure the distance between two sites on a macromolecule [28]. Basically, FRET is of two types: (a) Homo-molecular FRET and (b) Hetero-molecular

FRET. In the former case the same fluorophore acts both as energy donor and acceptor, while in the latter case two different molecules act as donor and acceptor.

Each donor-acceptor (D-A) pair participating in FRET is characterized by a distance known as Förster distance ( $R_0$ ) i.e., the D-A separation at which energy transfer is 50% efficient. The  $R_0$  value ranges from 20 to 60 Å. The rate of resonance energy transfer ( $k_T$ ) from donor to an acceptor is given by [15],

$$k_T = \frac{1}{\tau_D} \left( \frac{R_0}{r} \right)^6 \quad (2-40)$$

where  $\tau_D$  is the lifetime of the donor in the absence of acceptor and  $r$  is the donor to acceptor (D-A) distance. The rate of transfer of donor energy depends upon the extent of overlap of

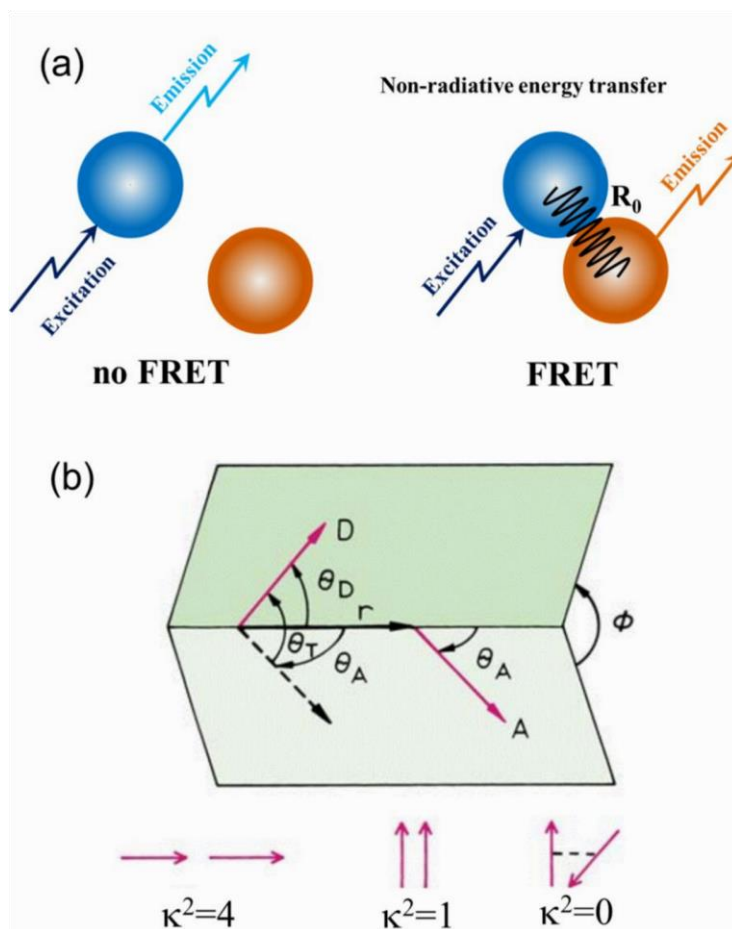


**Figure 2.6:** (a) Schematic illustration of the Förster resonance energy transfer (FRET) process. (b) Dependence of the orientation factor  $\kappa^2$  on the directions of the emission and absorption dipoles of the donor and acceptor, respectively.

the emission spectrum of the donor with the absorption spectrum of the acceptor ( $J(\lambda)$ ), the quantum yield of the donor ( $Q_D$ ), the relative orientation of the donor and acceptor transition dipoles ( $\kappa^2$ ) and the distance between the donor and acceptor molecules ( $r$ ) (Figure 2.6(b)). In order to estimate FRET efficiency of the donor and hence to determine distances between donor-acceptor pairs, the methodology described below is followed [15].  $R_0$  is given by,

$$R_0 = 0.211 [\kappa^2 n^{-4} Q_D J(\lambda)]^{1/6} \text{ (in \AA)} \quad (2-41)$$

where  $n$  is the refractive index of the medium,  $Q_D$  is the quantum yield of the donor and  $J(\lambda)$  is the overlap integral.  $\kappa^2$  is defined as,

$$\kappa^2 = (\cos\theta_T - 3\cos\theta_D \cos\theta_A)^2 = (\sin\theta_D \sin\theta_A \cos\phi - 2\cos\theta_D \cos\theta_A)^2 \quad (2-42)$$

where  $\theta_T$  is the angle between the emission transition dipole of the donor and the absorption transition dipole of the acceptor,  $\theta_D$  and  $\theta_A$  are the angles between these dipoles and the vector joining the donor and acceptor and  $\phi$  is angle between the planes of the donor and acceptor (Figure 2.6(b)).  $\kappa^2$  value can vary from 0 to 4. For collinear and parallel transition dipoles,  $\kappa^2 = 4$ ; for parallel dipoles,  $\kappa^2 = 1$ ; and for perpendicularly oriented dipoles,  $\kappa^2 = 0$ . For donor and acceptors that randomize by rotational diffusion prior to energy transfer, the magnitude of  $\kappa^2$  is assumed to be 2/3. However, in systems where there is a definite site of attachment of the donor and acceptor molecules, to get physically relevant results, the value of  $\kappa^2$  has to be estimated from the angle between the donor emission and acceptor absorption dipoles.  $J(\lambda)$ , the overlap integral, which expresses the degree of spectral overlap between the donor emission and the acceptor absorption, is given by,

$$J(\lambda) = \frac{\int_0^{\infty} F_D(\lambda) \varepsilon_A(\lambda) \lambda^4 d\lambda}{\int_0^{\infty} F_D(\lambda) d\lambda} \quad (2-43)$$

where  $F_D(\lambda)$  is the fluorescence intensity of the donor in the wavelength range of  $\lambda$  to  $\lambda+d\lambda$  and is dimensionless.  $\varepsilon_A(\lambda)$  is the extinction coefficient (in  $M^{-1}cm^{-1}$ ) of the acceptor at  $\lambda$ . If  $\lambda$  is in nm, then  $J(\lambda)$  is in units of  $M^{-1}cm^{-1}nm^4$ .

Once the value of  $R_0$  is known, the efficiency of energy transfer can be calculated. The efficiency of energy transfer ( $E$ ) is the fraction of photons absorbed by the donor which are transferred to the acceptor and is defined as,

$$E = \frac{k_T(r)}{\tau_D^{-1} + k_T(r)} \quad (2-44)$$

or

$$E = \frac{R_0^6}{r^6 + R_0^6} \quad (2-45)$$

The transfer efficiency is measured using the relative fluorescence intensity of the donor, in absence ( $F_D$ ) and presence ( $F_{DA}$ ) of the acceptor as,

$$E = 1 - \frac{F_{DA}}{F_D} \quad (2-46a)$$

For D-A systems decaying with multiexponential lifetimes,  $E$  is calculated from the amplitude weighted lifetimes  $\langle \tau \rangle = \sum_i \alpha_i \tau_i$  of the donor in absence ( $\tau_D$ ) and presence ( $\tau_{DA}$ ) of the acceptor as,

$$E = 1 - \frac{\tau_{DA}}{\tau_D} \quad (2-46b)$$

The D-A distances can be measured using equations (2-45), (2-46a) and (2-46b). The distances measured using equations (2-46a) and (2-46b) are revealed as  $R^S$  (steady-state measurement) and  $R^{TR}$  (time-resolved measurement), respectively. In one of recent studies from our group [29], we have shown that the energy transfer efficiency  $E$ , calculated from steady-state experiment (equation 2-46a) might be due to re-absorption of donor emission, but not due to dipole-dipole interaction (FRET).

**2.1.5. Excited State Proton Transfer (ESPT):** The transfer of a proton from one atom to another in the electronic excited state is commonly known as excited state proton transfer (ESPT) reaction and is of fundamentally important process that plays a crucial role in lots of reactions, especially chemical and biological processes. Such reactions occur because light absorption frequently changes the electron distribution within the fluorophore, which in turn increases the acidity/basicity in the first excited electronic state. Thus, deprotonation occurs more readily in the excited state. The best-known example of ESPT are phenols and naphthols. In neutral solution they lose the phenolic or naphtholic proton

in the excited state because the electrons on the phenolic/naphtholic hydroxyl groups are shifted into the aromatic ring, making the hydroxyl group more acidic. In a typical ESPT reaction from a photoacid (ROH) involves three basic steps: initial proton transfer ( $k_{PT}$ ), recombination of the geminate ion pair ( $k_{rec}$ ) and dissociation of the geminate pair into a solvent-separated ion pair ( $k_{diss}$ ) (Figure 2.7).

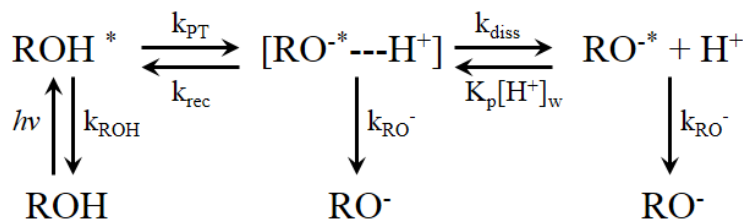
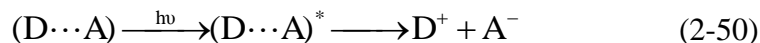


*Figure 2.7: Schematic representation of the photo-physical processes of an ESPT probe (ROH).*

**2.1.6. Photoinduced Electron Transfer (PET):** Electron transfer (ET) reactions are of fundamental importance to both chemistry and biology and can be interpreted by the classical ET theory developed by Marcus. In simple terms, PET can be ascribed as the movement of an electron, caused by the absorption of light, from an electron-rich species (a donor D) to an electron deficient species (an acceptor A) as shown in equation 2-47,



**2.1.6.1. Theory:** The first law of photochemistry tells us that a photoinduced process must be initiated by the absorption of light. In PET, the absorbing species can either be a donor, the acceptor, or a ground-state complex between the donor and acceptor, often referred to as a charge transfer complex. These possibilities are shown in equations 2-48–2-50.



**2.1.6.2. Experimental Methods:** In order to study PET, fluorescence decay transients of the donor molecule is taken in presence and absence of the acceptor molecules. The observed decay transients were fitted multi-exponentially using the nonlinear least square

fitting procedure to determine the ultrafast time scale of the reaction. The apparent rate constants,  $k_{nr}$ , for the non-radiative processes were determined by comparing the lifetimes of donor in the absence ( $\tau_0$ ) and in the presence ( $\tau$ ) of an acceptor, using equation 2-51.

$$k_{nr} = 1/\langle\tau\rangle - 1/\langle\tau_0\rangle \quad (2-51)$$

## 2.2. Systems:

**2.2.1. Organized Assemblies (Biomimetics):** Amphiphilic molecules, such as surfactants, aggregate to form macromolecular assemblies like micelles and reverse micelles. Since these assemblies closely resemble certain structural and dynamical properties of biomolecules, they are widely used as mimics of the actual biological systems. In the following section we will discuss about these systems.

**2.2.1.1. Reverse Micelle:** Reverse micelle (RM) or water-in-oil microemulsions (Figure 2.8) are nanopools of polar solvent protected by a monolayer of surfactant molecules at the periphery with polar headgroups pointing inward into the polar solvent and the hydrocarbon tails directed toward the nonpolar organic solvents [30, 31]. RMs with water nanopools resemble the water pockets found in various bioaggregates such as proteins, membranes and mitochondria. Thus, these systems are very often considered as templates for the synthesis of nanoparticles and as excellent biomimetic for exploration of biological membranes and biologically confined water molecules [32, 33]. Aqueous RMs are generally characterized by the degree of hydration ( $w_0$ ), which is the ratio of molar concentration of water to that of surfactant, where the radius of the water pool ( $r$  in Å) is empirically defined as,  $r = 2 \times w_0$  [34]. Shapes and sizes of the surfactant aggregates depend strongly on the type and concentration of the surfactant and on the nature of counter ion [35] and external solvent. In principle, reverse micelles can be formed in the presence and in the absence of solubilized water. However, it has generally been proposed that if the medium is completely water-free, there is not a well-defined CMC (critical micelle concentration) and the aggregates formed are very small and polydisperse, indicating minimum cooperativity in the surfactant association. This has been particularly established for surfactant sodium bis(2-ethylhexyl) sulfosuccinate (AOT) in several organic solvents [36]. RMs with  $w_0$  values less than 20 are stable and monodisperse over a

wide range of temperatures. The AOT-alkane-water system is interesting as the solution is homogeneous and optically transparent over a wide range of temperature, pressure and pH. The AOT RM can compartmentalize a large amount of water in its central core, and the nanoscale aggregation process is fairly well-characterized with respect to size and shape at various water contents. The CMC of AOT in hydrocarbon solvent is about 0.1 mM [37]. In liquid alkanes, AOT RMs ( $w_0 = 0$ ) are completely associated and each micelle contains 23

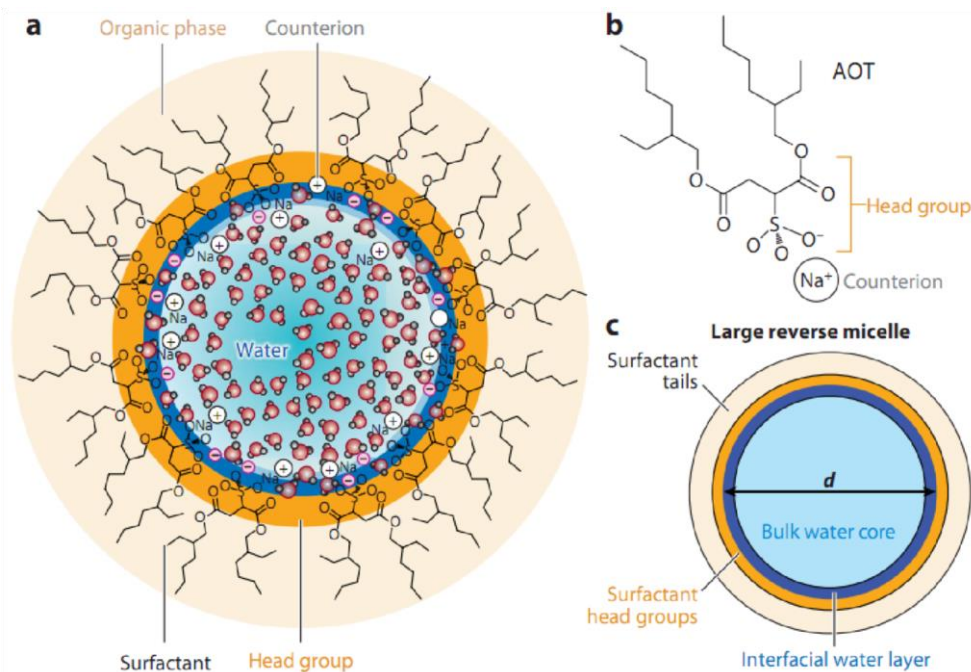


**Figure 2.8:** (a) Schematic depiction of a potential structure of a reverse micelle. Water molecules reside in the interior, sometimes interacting with headgroups and counterions. Surfactant tails reside in contact with the continuous, nonpolar, organic supporting phase. (b) Chemical structure of AOT (sodium bis(2-ethylhexyl) sulfosuccinate). (c) Schematic of a large reverse micelle showing important features of the structure.

monomers. The structures of these RMs are slightly asymmetric and are of round cylindrical nature. Spherical RMs are generally formed by surfactants with high values of the packing parameter,  $\theta > 3$ . AOT RMs can dissolve large amounts of water, being able to reach  $w_0$  values as large as 40-60, depending on the surrounding nonpolar organic medium and temperature [38]. At low  $w_0$  values, the systems are usually referred to as reverse micelle, whereas the term water-in-oil microemulsion is frequently used for higher  $w_0$  values. Fluorescence spectroscopy has been extensively used to study the AOT RM system. Fluorescent probes have been used to determine the viscosity, binding site, rigidity

and proximity within the water pool. These studies have shown that water inside the RM is generally of two types: i) interfacial (bound) and ii) core (free) water. One of the studies [39] has shown the existence of third type of water (trapped) molecules present between the polar headgroups of the individual surfactant molecules. Thus, the interior of RMs is extremely heterogeneous. Dielectric relaxation studies [40] indicate the presence of 7 ns component for bound water in RM, very similar to those of water molecules in the close vicinity of biological macromolecules (biological water). In contrast to AOT which does not require any cosurfactant to form reverse micelles, cationic surfactants do not form RMs in the absence of cosurfactants [41]. Several nonionic or neutral surfactants (Brij 30) have been reported to form RMs in pure and mixed hydrocarbon solvents [42]. Reverse micelles also have been extensively employed as media to synthesize different metal and semiconductor nanoparticles.

**2.2.1.2. Micelle:** Micelle are spherical or nearly spherical aggregates of amphiphilic surfactant molecules formed in aqueous solution above a concentration known as critical micellar concentration (CMC). Micelles are formed above a critical temperature called “Kraft point” which is different for different surfactants. Micellar aggregates have diameter varying within 10 nm and the aggregation number, i.e., the number of surfactant molecules per micelle, ranges from 20 to 200. Israelachvili et al. [43] have proposed that surfactant molecular packing considerations are determinant in the formation of large surfactant aggregates. In particular, it is considered that the surfactant packing parameter  $\theta$ , defined by,  $\theta = v/\sigma l$ , where  $v$  is the surfactant molecular volume;  $\sigma$ , the area per polar head; and  $l$ , the length of hydrophobic part; gives a good idea of the shape of aggregates which will form spontaneously. It is considered that normal or direct rod-like micelles are formed when  $2 < \theta < 3$  [44]. Micelles can be neutral (Triton X-100) or ionic (sodium dodecyl sulfate, SDS (anionic) and cetyltrimethylammonium bromide, CTAB (cationic)). The structure of a typical micelle is schematically shown in Figure 2.9. The core of a micelle is essentially “dry” and consists of the hydrocarbon chains with the polar and charged head groups projecting toward the bulk water. The Stern layer, surrounding the core, comprises of the ionic or polar head groups, bound counter ions and water molecules. Between the

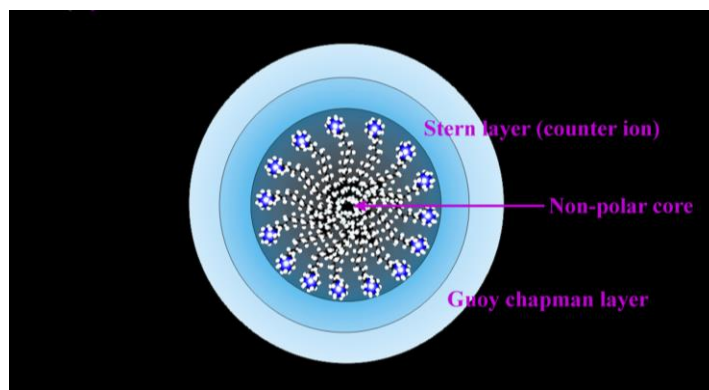


**Figure 2.9:** (a) Schematic representation of the structure of a micelle.

Stern layer and the bulk water there is a diffused Guoy-Chapman (GC) layer (Figure 2.9), which contains the free counter ions and water molecules. In non-ionic polyoxyethylated surfactants e.g. Triton X-100 (TX-100), the hydrocarbon core is surrounded by a palisade layer, which consists of the polyoxyethylene groups hydrogen-bonded to water molecules. Small angle X-ray and neutron scattering have provided detailed information on the structure of the CTAB micelles [45]. According to these studies, CMC and aggregation number of CTAB micelle are 0.8 and 52 mM, respectively and the thickness of the Stern layer is 6-9 Å. The overall radius of CTAB micelle is about 50 Å. For TX-100 micelle, the CMC, thickness of the palisade layer and overall radius of the hydrophobic core are reported to be 0.1 mM, 51 Å and 25-27 Å, respectively and that of SDS micelles are 8.6 mM, 33 Å and 5 Å, respectively [46].

**2.2.2. Proteins:** Two types of model proteins; Subtilisin *Carlsberg* (SC) and Riboflavin Binding Protein (RBP) have been used in our studies.

**2.2.2.1. Subtilisin *Carlsberg* (SC):** Subtilisin *Carlsberg* (SC) [EC: 3.4.21.62] extracted from *Bacillus licheniformis* having molecular weight of 27,600 Da [47] is another member of serine protease. It is also known as *Subtilisin A*, *Subtilopeptidase A* and *Alcalase Novo* and was discovered by Linderstrom-Lang and Ottensen [48] while they were studying the conversion of ovalbumin to plakalbumin. It contains a single polypeptide chain of 274 amino acid residues with two  $\text{Ca}^{2+}$  ion binding sites [49-51]. SC has 34 %  $\alpha$ -helix content [52]. It was observed that 119 water molecules are bound to SC in aqueous solution [53].

The amino acid sequence contains a single tryptophan (Trp113) and thirteen tyrosine (Tyr) [47] with no cysteine residues. In this enzyme, Tyr fluorescence overwhelms the fluorescence of Trp which is not the case in other proteins due to energy transfer from Tyr to Trp residue. The *catalytic triad* of SC comprises of Asp32, His64 and Ser221 residues [54] and it catalyzes the hydrolysis of peptides and esters by the same acyl-enzyme mechanism as for chymotrypsin. It is important to note that SC differs from the pancreatic enzymes by having a shallow binding groove on the surface, rather than the deep binding

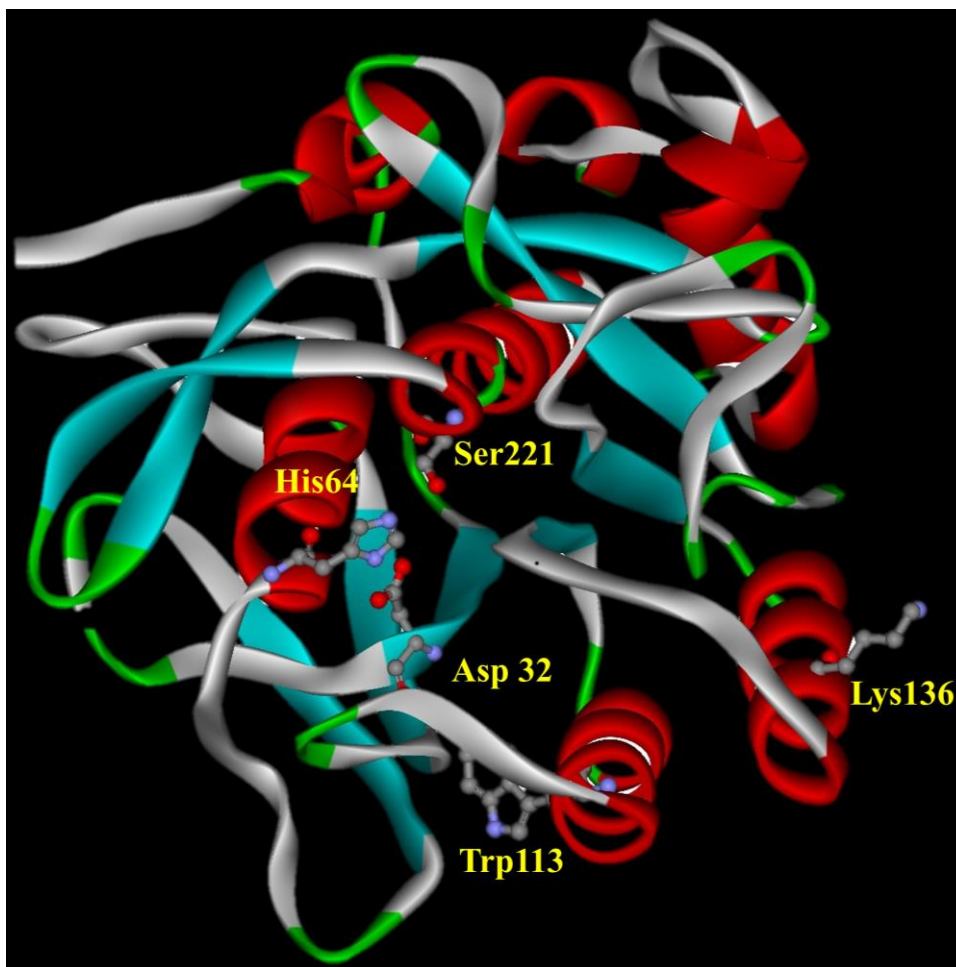


**Figure 2.10:** X-Ray crystallographic structure (PDB code: 1SCD) of Subtilisin Carlsberg depicting the catalytic triads.

pocket of the pancreatic enzymes, to which it is related by convergent evolution [55]. Subtilisins are of considerable interest not only scientifically but also industrially, for they are used in such diverse applications as meat tenderizers, laundry detergents, and

proteolytic medicines [56, 57]. Furthermore, their catalytic efficiency and specificity in organic media would enhance practical uses related to synthetic applications [58-61]. Subtilisins are covalently inactivated by standard serine protease inhibitors such as PMSF and DFP, and also by peptidyl-halomethanes [62, 63] and peptidyl-boronic acids [64].

**2.2.2.2. Riboflavin Binding Protein (RBP):** RBP is a globular monomeric protein extracted from chicken egg white having molecular weight of 29,200 Da [65]. The



*Figure 2.11: X-Ray crystallographic structure of Riboflavin Binding Protein (RBP) depicting the riboflavin binding domain.*

molecule is a three-dimensional ellipsoid of dimensions  $50 \times 40 \times 35 \text{ \AA}$  and comprises a single polypeptide chain of 219 amino acids, nine disulfide bridges, six  $\alpha$ -helices, and four series of discontinuous areas of  $\beta$  structure [66]. The primary function of RBP is to deliver

riboflavin (Rf) to the embryo in mammals. The ligand-binding domain of RBP is a hydrophobic cleft, 20 Å wide and 15 Å deep. The binding of Rf occurs in the cleft with the isoalloxazine ring stacked between the parallel planes of tryptophan 156 (Trp156) and tyrosine 75 (Tyr75) (Figure 2.11). The isoalloxazine ring of flavins is amphipathic: the xylene portion is hydrophobic, and the pyrimidine moiety is hydrophilic. The X-ray structure reveals that the major interactions of the isoalloxazine ring with the protein are hydrophobic, and the xylene moiety is buried most deeply in the protein. There are also four tryptophan residues (Trp-54, Trp-106, Trp-120, and Trp-124) in the vicinity of the binding site. The complexation of Rf with RBP leads to quenching of both the Rf and Trp fluorescence. The quenching of Rf upon binding with RBP is a consequence of ultrafast ET to the flavin chromophore (Rf) in the excited electronic state from nearby Trp or Tyr residues present in RBP whereas, quenching of Trp emission of RBP in presence of Rf is due to the combination of dynamic and static quenching [66-68].

**2.2.3. Molecular Probes:** In this section we will discuss about the different probe molecules that have been used in the course of study.

**2.2.3.1. N-CBZ-Gly-Gly-Leu-p-Nitroanilide (CBZ-GGL-pNA):** N-CBZ-Gly-Gly-Leu-p-Nitroanilide (CBZ-GGL-pNA) is an aromatic tripeptide substrate for serine protease (Figure 2.12A). Its concentration is determined using  $\epsilon = 14 \text{ mM}^{-1}\text{cm}^{-1}$  at 315 nm. The rate of catalytic activity is determined by monitoring absorbance of cleaved product (p-Nitroanilide) having  $\epsilon = 8.8 \text{ mM}^{-1}\text{cm}^{-1}$  at 410 nm [69].

**2.2.3.2. Coumarin 500 (C500):** The solvation probe C500 (Figure 2.12B) is sparingly soluble in water and shows reasonably good solubility in isooctane. In bulk water the absorption peak (400 nm) is significantly red shifted compared to that in isooctane (360 nm). The emission peak of C500 in bulk water (500 nm) also shows a 90 nm red shift compared to that in isooctane (excitation at 350 nm). The significantly large solvochromic effect in the absorption and emission spectra of C500 makes the dye an attractive solvation probe for microenvironments. The photophysics of the probe have also been studied in detail [70].

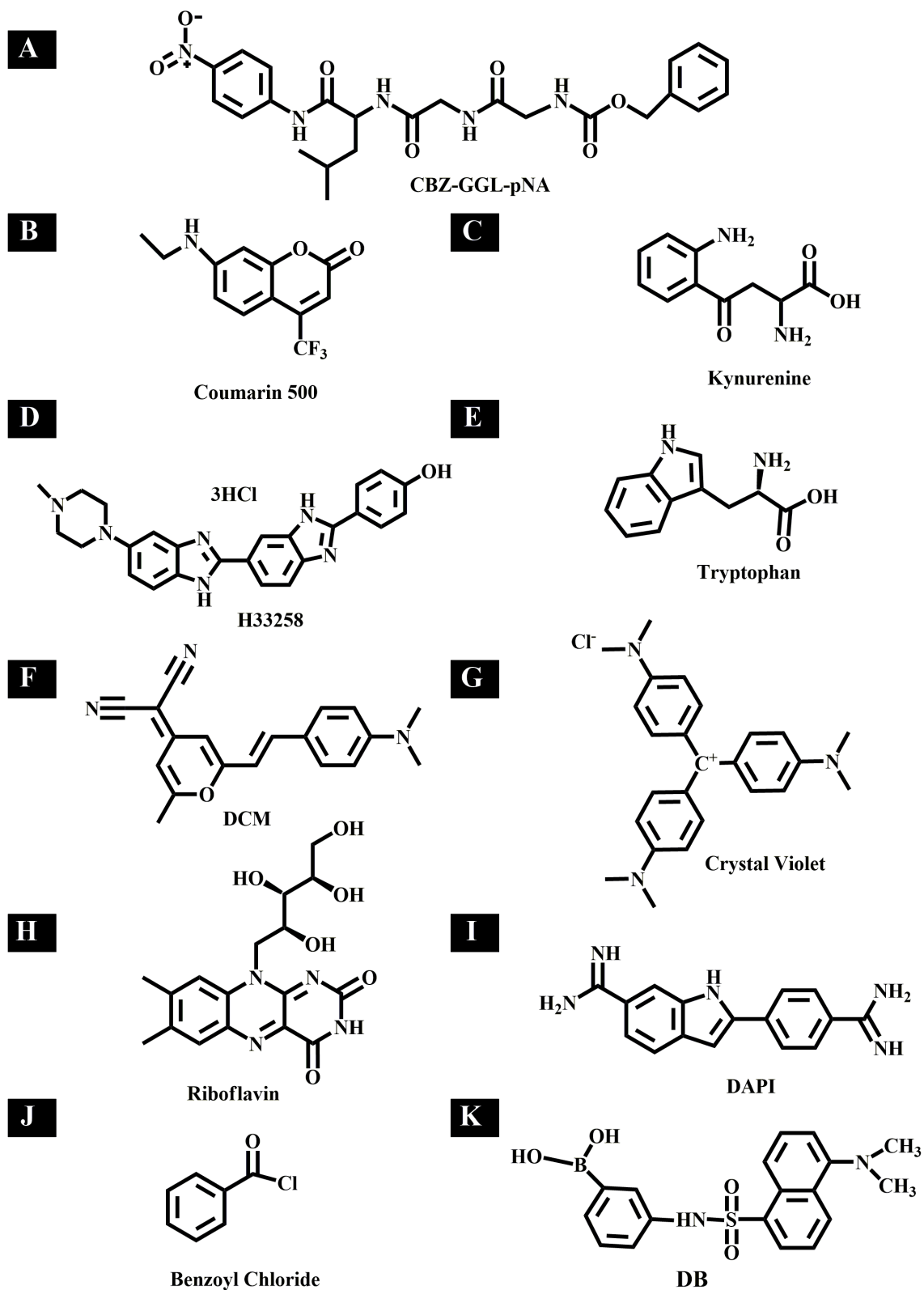


Figure 2.12: Molecular Structure of A) CBZ-GGL-pNA; B) Coumarin 500; C) Kynurenine; D) Hoechst 33258; E) Tryptophan; F) DCM; G) Crystal Violet; H) Riboflavin; I) DAPI; J) Benzoyl Chloride; K) 3-(Dansylamino)phenylboronic acid (DB).

**2.2.3.3. Kynurenine (KN):** It is one of the Trp metabolites (Figure 2.12C) and omnipresent in the lens of human eyes in order to protect retina from possible UV (300-400 nm) radiation damage [71]. KN is a central compound of the Trp metabolism pathway since it can change to the neuroprotective agent kynurenic acid or to the neurotoxic agent quinolinic acid. It is a weak photosensitizer and redirect the absorbed light energy into benign channels. They are characterized by a low fluorescence quantum yield and short lifetime values [71].

**2.2.3.4. 2'-(4-hydroxyphenyl)-5-[5-(4-methylpiperazine-1-yl)-benzimidazo-2-yl]-benzimidazole, Hoechst 33258:** The commercially available probe H33258 (Figure 2.12D) is widely used as fluorescent cytological stain of DNA. Since it has affinity for the double stranded DNA, H33258 can affect transcription/translation, and block topomerase/helicase activities. The dye is also used as a potential antihelminthic drug. X-ray crystallographic and NMR studies of the dye bound to a dodecamer DNA shows that the dye is bound to A-T rich sequence of the DNA minor groove. The binding constant of the dye to double stranded DNA at low [dye]:[DNA] ratio is found to be  $5 \times 10^5 \text{ M}^{-1}$ . The solvchromic properties of the dye [72] can be used to report the hydration dynamics [73] as well as the dynamics of restricted systems [74].

**2.2.3.5. Tryptophan [(2S)-2-Amino-3-(1H-Indol-3-yl) Propanoic acid] (Trp):** Trp (Figure 2.12E) is one of the 22 standard amino acids and an essential amino acid in the human diet. Only the L-stereoisomer of Trp is found in enzymes and proteins. However, the D-stereoisomer is occasionally found in naturally produced peptides. Tryptophan has large bulky aromatic side chain and is significantly more polar than other aromatic amino acids, because of the nitrogen of the Trp indole ring. Trp absorbs light at 280 nm and the molar extinction coefficient value is  $5,579 \text{ M}^{-1} \text{ cm}^{-1}$  at 278 nm. The fluorescence emission peak of Trp dissolved in water is  $\sim 350 \text{ nm}$  and the quantum yield is 0.14 [75].

**2.2.3.6. 4-(dicyanomethylene)-2-methyl-6-(p-dimethylaminostyryl)-4H-pyran (DCM):** The laser dye DCM (Figure 2.12F), is completely insoluble in water, and has selective binding affinity to the micellar surface [76]. The dye is completely hydrophobic (nonpolar) in the ground state. However, UV excitation increases dipole moment of the

probe making it polar and hence increases its hydrophilicity in the excited state. Thus the excited DCM diffuses from the micellar surface (relatively nonpolar) towards polar bulk water phase revealing a fluorescence emission signature (temporal line width) of the excursion through multiple environments in the excited state [77].

**2.2.3.7. Crystal Violet (CV):** CV has a positively charged ammonium ion and three aromatic rings (Figure 2.12G), used as a staining material. It can bind to the negatively charged phosphate backbone of DNA, negatively charged amino acids of proteins. It is highly soluble in water and other polar solvents. Its concentration is determined using extinction coefficient,  $112,000 \text{ M}^{-1}\text{cm}^{-1}$  at 509 nm [78].

**2.2.3.8. Riboflavin (Rf):** Rf (Figure 2.12H) is well known as vitamin B<sub>2</sub>. It is the central component of the cofactors FAD and FMN, and is therefore required by all Flavoproteins. As such, vitamin B<sub>2</sub> is required for a wide variety of cellular processes. It plays a key role in energy metabolism, and for the metabolism of fats, carbohydrates and proteins. Milk, cheese, leafy green vegetables, liver, kidneys, legumes, tomatoes, yeast, mushrooms, and almonds are good sources of vitamin B<sub>2</sub>, but exposure to light destroys Rf. Rf is very important for the preservation of food in right light condition [79]. The photochemical reactions of Rf are well understood [80-83]. It has already been demonstrated that the intramolecular electron transfer process is responsible for the photoreduction of the chromophore [84, 85]. It has been proposed that two photoproducts, lumichrome and lumiflavin are generated via an intermediate compound deuteroflavin during the photodeterioration of the Rf chromophore in presence of oxygen [85]. The role of proton transfer from the ribityl chain to the side nitrogen moiety for the generation of the photoproduct is also identified. In a recent study, it has been established that Rf is a potential photosensitizer and the activated triplet state in the molecule is concluded to be responsible for the photosensitization [83, 86]. It is to be noted that the photoproducts of Rf are also very hazardous for the biological activity as they degrade important amino acids including the Trp and Tyr [87].

**2.2.3.9. 4',6-Diamidino-2-phenylindole (DAPI):** The dye DAPI (Figure 2.12I) is another commercially available fluorescent cytological stain for DNA. Studies on the DAPI-DNA complexes show that the probe exhibits a wide variety of interactions of different strength and specificity with DNA [88]. The dye exhibits intramolecular proton transfer as an important mode of excited state relaxation at physiological pH [89], which takes place from the amidino to the indole moiety. Suppression of this excited state pathway leads to enhancement of fluorescence quantum yield and hence the fluorescence intensity in hydrophobic restricted environments.

**2.2.3.10. Benzoyl Chloride (BzCl):** BzCl is an organochlorine hydrophobic compound (Figure 2.12J). It is a colourless fuming liquid with an irritating odour and has poor solubility in water. It shows an absorption maximum around 282 nm in isooctane. In microemulsion, it gets compartmentalized into the organic phase and the interphase [61]. The solvolysis of benzoyl chlorides is a well-known process in water (rate constant =  $1.1 \text{ s}^{-1}$ ) and in different solvents [62]; in such a way that acyl group transfer can occur by means of three mechanisms: dissociative, associative and concerted displacement. These mechanisms are well-defined, with a clear borderline between them. The mechanism of a given reaction depends on the nature of the substituent and the solvent in which the reaction takes place [90].

**2.2.3.11. 3-(Dansylamino)phenylboronic acid (DB):** DB (Figure 2.12K) is a potent competitive inhibitors of serine proteases [91]. It is sparingly soluble in water and other polar solvents. In methanol the absorbance and emission maxima is around 337 and 517 nm. However, when bound to protein the emission maxima shift to 490 nm. Therefore can be used to report the hydration dynamics around the protein surface as well as in the restricted environments [92].

## References

- [1] S.K. Pal, A.H. Zewail, Dynamics of water in biological recognition, *Chem. Rev.* 104 (2004) 2099.
- [2] J.A. Rupley, G. Careri, Protein hydration and function, Academic Press, London, 1991.
- [3] J.A. Kornblatt, M.J. Kornblatt, Water as it applies to the function of enzymes, *Int. Rev. Cytol.* 215 (2002) 49.
- [4] Y. Pocker, Water in enzyme reaction: Biophysical aspects of hydration-dehydration processes, *Cell. Mol. Life Sci.* 57 (2000) 1008.
- [5] B. Bagchi, R. Biswas, Polar and nonpolar solvation dynamics, ion diffusion and vibrational relaxation: Role of biphasic solvent response in chemical dynamics, *Adv. Chem. Phys.* 109 (1999) 207.
- [6] B. Bagchi, Dynamics of solvation and charge transfer reactions in dipolar liquids, *Ann. Rev. Phys. Chem.* 40 (1989) 115.
- [7] G.R. Fleming, M. Cho, Chromophore-solvent dynamics, *Ann. Rev. Phys. Chem.* 47 (1996) 109.
- [8] R. Jimenez, G.R. Fleming, P.V. Kumar, M. Maroncelli, Femtosecond solvation dynamics of water, *Nature* 369 (1994) 471.
- [9] S.K. Pal, J. Peon, B. Bagchi, A.H. Zewail, Biological water: Femtosecond dynamics of macromolecular hydration, *J. Phys. Chem. B* 106 (2002) 12376.
- [10] L. Onsager, Comments on "effects of phase density on the ionization process and electron localization in fluids" by J. Jortner and A. Gathon, *Can. J. Chem.* 55 (1977) 1819.
- [11] R.M. Stratt, M. Maroncelli, Nonreactive dynamics in Solution: The emerging molecular view of solvation dynamics and vibrational relaxation, *J. Phys. Chem.* 100 (1996) 12981.
- [12] C.P. Hsu, X. Song, R.A. Marcus, Time-dependent Stokes shift and its calculation from solvent dielectric dispersion data, *J. Phys. Chem. B* 101 (1997) 2546.
- [13] J.T. Hynes, Outer-sphere electron transfer reactions and frequency-dependent friction, *J. Phys. Chem.* 90 (1986) 3701.

- [14] M.L. Horng, J.A. Gardecki, A. Papazyan, M. Maroncelli, Subpicosecond measurements of polar solvation dynamics: Coumarin 153 revisited, *J. Phys. Chem.* 99 (1995) 17311.
- [15] J.R. Lakowicz, Principles of fluorescence spectroscopy, Kluwer Academic/Plenum, New York, 1999.
- [16] R. Sarkar, S.K. Pal, Ligand-DNA interaction in a nanocage of reverse micelle, *Biopolymers* 83 (2006) 675.
- [17] A.S.R. Koti, M.M.G. Krishna, N. Periasamy, Time-resolved area-normalized emission spectroscopy (TRANES): A novel method for confirming emission from two excited states, *J. Phys. Chem. A* 105 (2001) 1767.
- [18] R.D. Spencer, G. Weber, Measurements of subnanosecond fluorescence lifetimes with a cross-correlation phase fluorometer, *Ann. N. Y. Acad. Sci* 158 (1969) 361.
- [19] D.V. O'Conner, D. Philips, Time-correlated single photon counting, Academic Press, London, 1984.
- [20] B. Bagchi, Water dynamics in the hydration layer around proteins and micelles, *Chem. Rev.* 105 (2005) 3197.
- [21] S. Pal, S. Balasubramanian, B. Bagchi, Identity, energy, and environment of interfacial water molecules in a micellar solution, *J. Phys. Chem. B* 107 (2003) 5194.
- [22] S. Balasubramanian, S. Pal, B. Bagchi, Hydrogen-bond dynamics near a micellar surface: Origin of the universal slow relaxation at complex aqueous interfaces, *Phys. Rev. Lett.* 89 (2002) 115505.
- [23] S.K. Pal, J. Peon, A.H. Zewail, Biological water at the protein surface: Dynamical solvation probed directly with femtosecond resolution, *Proc. Natl. Acad. Sci. USA* 99 (2002) 1763.
- [24] P. Grigolini, M. Maestro, A two-state stochastic model for the dynamics of constrained water in reversed micelles, *Chem. Phys. Lett.* 127 (1986) 248.
- [25] N. Nandi, B. Bagchi, Dielectric relaxation of biological water, *J. Phys. Chem. B* 101 (1997) 10954.
- [26] R.K. Mitra, S.S. Sinha, S.K. Pal, Temperature dependent hydration at micellar surface: Activation energy barrier crossing model revisited, *J. Phys. Chem. B* 111 (2007) 7577.

- [27] L. Stryer, Fluorescence energy transfer as a spectroscopic ruler, *Ann. Rev. Biochem.* 47 (1978) 819.
- [28] P.K. Verma, S.K. Pal, Ultrafast resonance energy transfer in bio-molecular systems, *Eur. Phys. J. D* 60 (2010) 137.
- [29] P. Majumder, R. Sarkar, A.K. Shaw, A. Chakraborty, S.K. Pal, Ultrafast dynamics in a nanocage of enzymes: Solvation and fluorescence resonance energy transfer in reverse micelles, *J. Colloid Interface Sci.* 290 (2005) 462.
- [30] T.K. De, A. Maitra, Solution behaviour of aerosol OT in non-polar solvents, *Adv. Colloid Interface Sci.* 59 (1995) 95.
- [31] P.L. Luisi, M. Giomini, M.P. Pileni, B.H. Robinson, Reverse micelles as hosts for proteins and small molecules, *Biochim. Biophys. Acta Rev. Biomembr.* 947 (1988) 209.
- [32] K. Bhattacharyya, Solvation dynamics and proton transfer in supramolecular assemblies, *Acc. Chem. Res.* 36 (2003) 95.
- [33] B. Cohen, D. Huppert, K.M. Solntsev, Y. Tsfadia, E. Nachliel, M. Gutman, Excited state proton transfer in reverse micelles, *J. Am. Chem. Soc.* 124 (2002) 7539.
- [34] M.P. Pileni, Water in oil colloidal droplets used as microreactors, *Adv. Colloid Interface Sci.* 46 (1993) 139.
- [35] F. Caboi, G. Capuzzi, P. Baglioni, M. Monduzzi, Microstructure of Ca-AOT/water/decane w/o microemulsions, *J. Phys. Chem. B* 101 (1997) 10205.
- [36] M. Zulauf, H.F. Eicke, Inverted micelles and microemulsions in the ternary system water/aerosol-OT/isooctane as studied by photon correlation spectroscopy, *J. Phys. Chem.* 83 (1979) 480.
- [37] Y.C. Jean, H.J. Ache, Determination of critical micelle concentrations in micellar and reversed micellar systems by positron annihilation techniques, *J. Am. Chem. Soc.* 100 (1978) 984.
- [38] C. Petit, P. Lixon, M.P. Pileni, Structural study of divalent metal bis(2-ethylhexyl) sulfosuccinate aggregates, *Langmuir* 7 (1991) 2620.
- [39] T.K. Jain, M. Varshney, A. Maitra, Structural studies of aerosol OT reverse micellar aggregates by FT-IR spectroscopy, *J. Phys. Chem.* 93 (1989) 7409.
- [40] M.A. Middleton, R.S. Schechter, K.P. Johnston, Dielectric properties of anionic and nonionic surfactant microemulsions, *Langmuir* 6 (1990) 920.

- [41] J. Lang, N. Lalem, R. Zana, Quaternary water in oil microemulsions. 1. Effect of alcohol chain length and concentration on droplet size and exchange of material between droplets, *J. Phys. Chem.* 95 (1991) 9533.
- [42] S. Rakshit, N. Goswami, S.K. Pal, Slow solvent relaxation dynamics of nanometer sized reverse micellar systems through tryptophan metabolite, kynurenine, *Photochem. Photobiol.* 88 (2012) 38.
- [43] J.N. Israelachvili, D.J. Mitchell, B.W. Ninham, Theory of self-assembly of hydrocarbon amphiphiles into micelles and bilayers, *J. Chem. Soc. Faraday Trans.* 72 (1976) 1525.
- [44] D.J. Mitchell, B.W. Ninham, Micelles, vesicles and microemulsions, *J. Chem. Soc. Faraday Trans.* 77 (1981) 601.
- [45] S.S. Berr, E. Caponetti, J.S. Johnson, R.R.M. Jones, L.J. Magid, Small-angle neutron scattering from hexadecyltrimethylammonium bromide micelles in aqueous solutions, *J. Phys. Chem.* 90 (1986) 5766.
- [46] N.J. Turro, X.G. Lei, K.P. Ananthapadmanabhan, M. Aronson, Spectroscopic probe analysis of protein-surfactant interactions: The BSA/SDS system, *Langmuir* 11 (1995) 2525.
- [47] R.J. DeLange, E.L. Smith, Subtilisin carlsberg I. Amino acid composition; isolation and composition of peptides from the tryptic hydrolysate, *J. Biol. Chem.* 243 (1968) 2134.
- [48] K. Linderstrom-Lang, M. Ottensen, A new protein from ovalbumin, *Nature* 159 (1947) 807.
- [49] W. Bode, E. Papamokos, D. Musil, The high-resolution X-ray crystal structure of the complex formed between subtilisin carlsberg and eglin c, an elastase inhibitor from the leech *hirudo medicinalis*, *Eur. J. Biochem.* 166 (1987) 673.
- [50] C.A. McPhalen, M.N.G. James, Structural comparison of two serine proteinase-protein inhibitor complexes: Eglin-C-subtilisin carlsberg and CI-2-subtilisin Novo, *Biochemistry* 27 (1988) 6582.
- [51] D.J. Neidhart, G.A. Petsko, The refined crystal structure of subtilisin carlsberg at 2.5 Å resolution, *Protein Eng.* 2 (1988) 271.

- [52] J.L. Schmitke, L.J. Stern, A.M. Klivanov, The crystal structure of subtilisin carlsberg in anhydrous dioxane and its comparison with those in water and acetonitrile, *Proc. Natl. Acad. Sci. USA* 94 (1997) 4250.
- [53] P.A. Fitzpatrick, A.C. Steinmetz, D. Ringe, A.M. Klivanov, Enzyme crystal structure in a neat organic solvent, *Proc. Natl. Acad. Sci. USA* 90 (1993) 8653.
- [54] P. Castner, J.A. Wells, Dissecting the catalytic triad of serine protease, *Nature* 332 (1988) 564.
- [55] A. Fersht, Enzyme structure and mechanism in protein science: A guide to enzyme catalysis and protein folding, W. H. Freeman and Company, New York, 1999.
- [56] N. Genov, B. Filippi, D. Dolashka, K.S. Wilson, C. Betzel, Stability of subtilisins and related proteinases (subtilases), *Int. J. Peptide Protein Res.* 45 (1995) 391.
- [57] P.A. Fitzpatrick, D. Ringe, A.M. Klivanov, X-Ray crystal structure of cross-linked subtilisin carlsberg in water vs acetonitrile, *Biochem. Biophys. Res. Commun.* 198 (1994) 675.
- [58] J. Broos, A.J.W.G. Visser, J.F.J. Engbersen, W. Verboom, A. van Hoek, D.N. Reinhoudt, Flexibility of enzymes suspended in organic solvents probed by time-resolved fluorescence anisotropy. Evidence that enzyme activity and enantioselectivity are directly related to enzyme flexibility, *J. Am. Chem. Soc.* 117 (1995) 12657.
- [59] S. Chatterjee, A.J. Russell, Kinetic analysis of the mechanism for subtilisin in essentially anhydrous organic solvents, *Enzyme Micro. Technol.* 15 (1993) 1022.
- [60] A.K. Chaudhary, S.V. Kamat, E.J. Beckman, D. Nurok, R.M. Kleyle, P. Hajdu, A.J. Russell, Control of subtilisin substrate specificity by solvent engineering in organic solvents and supercritical fluorofom, *J. Am. Chem. Soc.* 118 (1996) 12891.
- [61] T. Kijima, S. Yamamoto, H. Kise, Fluorescence spectroscopic study of subtilisins as relevant to their catalytic activity in aqueous-organic media, *Bull. Chem. Soc. Jpn.* 67 (1994) 2819.
- [62] K. Morihara, T. Oka, Subtilisin BPN': Inactivation by chloromethyl ketone derivatives of peptide substrates, *Arch. Biochem. Biophys.* 138 (1970) 526.
- [63] T.L. Poulos, R.A. Alden, S.T. Freer, J.J. Birktoft, J. Kraut, Polypeptide halomethyl ketones bind to serine proteases as analogs of the tetrahedral intermediate. X-ray

crystallographic comparison of lysine- and phenylalanine-polypeptide chloromethyl ketone-inhibited subtilisin, *J. Biol. Chem.* 251 (1976) 1097.

[64] D.A. Matthews, R.A. Alden, J.J. Birktoft, S.T. Freer, J. Kraut, X-ray crystallographic study of boronic acid adducts with subtilisin BPN' (Novo). A model for the catalytic transition state, *J. Biol. Chem.* 250 (1975) 7120.

[65] Y. Hamazume, T. Mega, T. Ikenaka, Characterization of hen egg white- and yolk-riboflavin binding proteins and amino acid sequence of egg white-riboflavin binding protein, *J. Biochem.* 95 (1984) 1633.

[66] D.P. Zhong, A.H. Zewail, Femtosecond dynamics of flavoproteins: Charge separation and recombination in riboflavine (vitamin B-2)-binding protein and in glucose oxidase enzyme, *Proc. Natl. Acad. Sci. USA* 98 (2001) 11867.

[67] S. Rakshit, R. Saha, P.K. Verma, R.K. Mitra, S.K. Pal, Ultrafast electron transfer in riboflavin binding protein in macromolecular crowding of nano-sized micelle, *Biochimie* 94 (2012) 2673.

[68] R. Saha, S. Rakshit, P.K. Verma, R.K. Mitra, S.K. Pal, Protein-cofactor binding and ultrafast electron transfer in riboflavin binding protein under the spatial confinement of nanoscopic reverse micelles, *J. Mol. Recognit.* 26 (2013) 59.

[69] J.K.A. Kamal, T. Xia, S.K. Pal, L. Zhao, A.H. Zewail, Enzyme functionality and solvation of subtilisin carlsberg: From hours to femtoseconds, *Chem. Phys. Lett.* 387 (2004) 209.

[70] S. Nad, H. Pal, Photophysical properties of coumarin-500 (C500): Unusual behavior in nonpolar solvents, *J. Phys. Chem. A* 107 (2003) 501.

[71] P.S. Sherin, J. Grilj, Y.P. Tsentalovich, E. Vauthey, Ultrafast excited-state dynamics of kynurenine, a UV filter of the human eye, *J. Phys. Chem. B* 113 (2009) 4953.

[72] R. Jin, K.J. Breslauer, Characterization of the minor groove environment in a drug-DNA complex: Bisbenzimidazole bound to the poly[d(AT)].poly[d(AT)]duplex, *Proc. Natl. Acad. Sci. USA* 85 (1988) 8939.

[73] S.K. Pal, L. Zhao, A.H. Zewail, Water at DNA surfaces: Ultrafast dynamics in minor groove recognition, *Proc. Natl. Acad. Sci. USA* 100 (2003) 8113.

[74] D. Banerjee, S.K. Pal, Ultrafast charge transfer and solvation of DNA minor groove binder: Hoechst 33258 in restricted environments, *Chem. Phys. Lett.* 432 (2006) 257.

- [75] P.G. Wu, L. Brand, Resonance energy transfer: Methods and applications, *Anal. Biochem.* 218 (1994) 1.
- [76] S.K. Pal, D. Sukul, D. Mandal, S. Sen, K. Bhattacharyya, Solvation dynamics of DCM in micelles, *Chem. Phys. Lett.* 327 (2000) 91.
- [77] R. Sarkar, A.K. Shaw, M. Ghosh, S.K. Pal, Ultrafast photoinduced deligation and ligation dynamics: DCM in micelle and micelle-enzyme complex, *J. Photochem. Photobiol. B* 83 (2006) 213.
- [78] H. Langhals, Color chemistry: Synthesis, properties and applications of organic dyes and pigments, *Angew. Chem. Int. Ed.* 43 (2004) 5291.
- [79] O.W. Parks, C. Allen, Photodegradation of riboflavin to lumichrome in milk exposed to sunlight, *J. Dairy Sci.* 60 (1977) 1038.
- [80] G. Oster, N. Wotherspoon, Photoreduction of methylene blue by ethylenediaminetetraacetic acid, *J. Am. Chem. Soc.* 79 (1957) 4836.
- [81] W.J. Nickerson, G. Strauss, The photochemical cleavage of water by riboflavin, *J. Am. Chem. Soc.* 82 (1960) 5007.
- [82] N. Wotherspoon, G. Oster, Light induced spectral shift of the thiazine dyes in the bound state, *J. Am. Chem. Soc.* 79 (1957) 3992.
- [83] M. Halwer, The photochemistry of riboflavin and related compounds, *J. Am. Chem. Soc.* 73 (1951) 4870.
- [84] W.M. Moore, J.T. Spence, F.A. Raymond, S.D. Colson, Photochemistry of riboflavin. I. The hydrogen transfer process in the anaerobic photobleaching of flavins, *J. Am. Chem. Soc.* 85 (1963) 3367.
- [85] B. Holmström, G. Oster, Riboflavin as an electron donor in photochemical reactions, *J. Am. Chem. Soc.* 83 (1961) 1867.
- [86] G.B. Sancar, Enzymatic photoreactivation: 50 years and counting, *Mutat. Res.* 451 (2000) 25.
- [87] E. Silva, Biological implications of aerobically obtained riboflavin-sensitized photoproducts of tryptophan, *J. Photochem. Photobiol. B* 14 (1992) 142.
- [88] W.D. Wilson, F.A. Tanious, H.J. Barton, R.L. Jones, K. Fox, R.L. Wydra, L. Strekowski, DNA sequence dependent binding modes of 4',6-diamidino-2-phenylindole (DAPI), *Biochemistry* 29 (1990) 8452.

- [89] M.L. Barcellona, E. Gratton, A molecular approach to 4',6-diamidine-2-phenylindole (DAPI) photophysical behaviour at different pH values, *Biophys. Chem.* 40 (1991) 223.
- [90] B.D. Song, W.P. Jencks, Mechanism of solvolysis of substituted benzoyl halides, *J. Am. Chem. Soc.* 111 (1989) 8470.
- [91] R. Smoum, A. Rubinstein, V.M. Dembitsky, M. Srebnik, Boron containing compounds as protease inhibitors, *Chem. Rev.* 112 (2012) 4156.
- [92] S. Rakshit, R. Saha, S.K. Pal, Modulation of environmental dynamics at the active site and activity of an enzyme under nanoscopic confinement: Subtilisin carlsberg in anionic AOT reverse micelle, *J. Phys. Chem. B* (2013) doi.org/10.1021/jp4061494.

# Chapter 3

## Instrumentation and Sample Preparation

In this chapter the details of instrumental setup and sample preparation techniques used in our studies have been described.

### 3.1. Instrumental Setups:

**3.1.1. Steady-State UV-Vis Absorption and Emission Measurement:** Steady-state UV-Vis absorption and emission spectra of the probe molecules were measured with Shimadzu UV-2450 spectrophotometer and Jobin Yvon Fluoromax-3 fluorimeter, respectively. Schematic ray diagrams of these two instruments are shown in Figures 3.1 and 3.2.

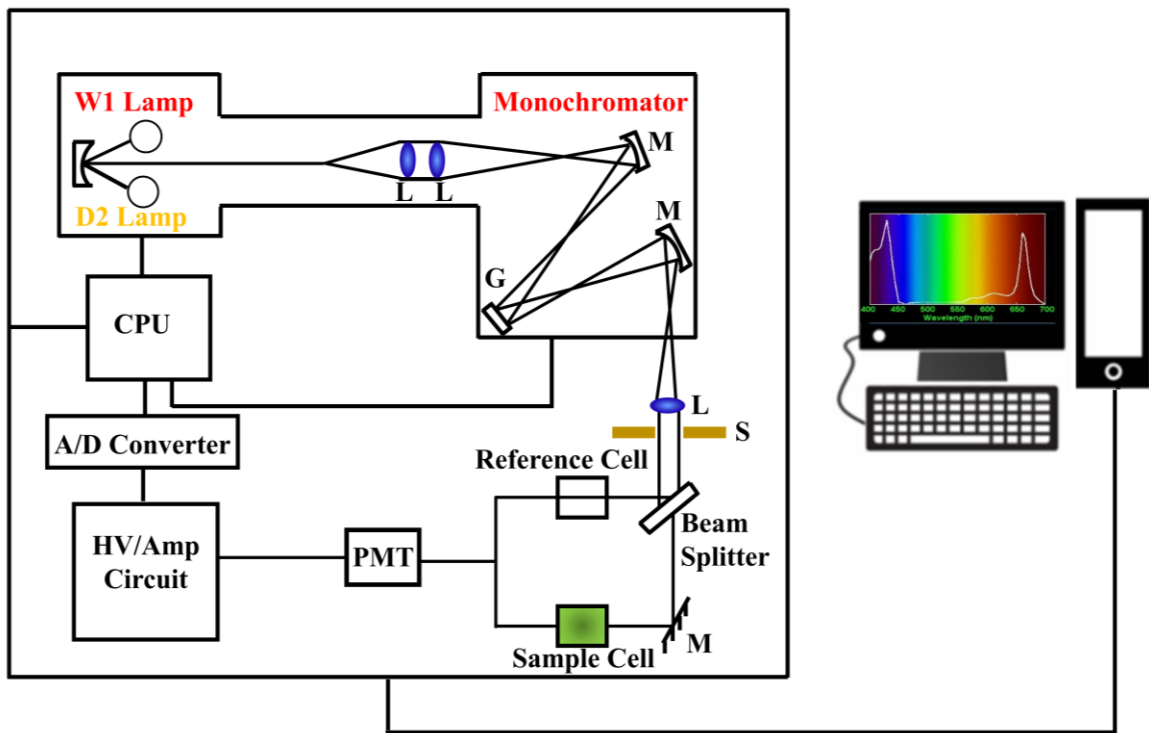


*Figure 3.1: Schematic ray diagram of an absorption spectrophotometer. Tungsten halogen (W1) and Deuterium lamps (D2) are used as light sources in the visible and UV regions, respectively. M, G, L, S, PMT designate mirror, grating, lens, shutter and photomultiplier tube, respectively. CPU, A/D converter and HV/Amp indicate central processing unit, analog to digital converter and High-voltage/Amplifier circuit, respectively.*

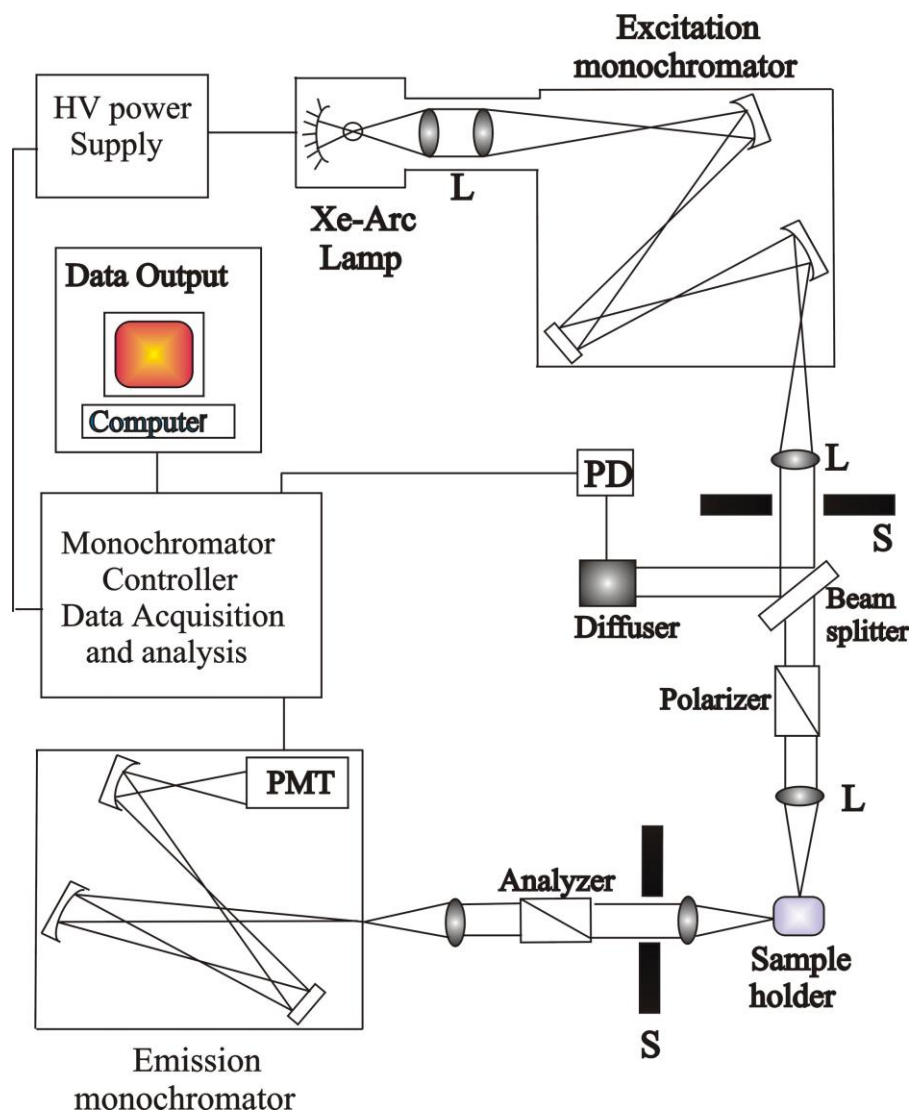


*Figure 3.2: Schematic ray diagram of an emission spectrofluorimeter. M, G, L, S, PMT and PD represent mirror, grating, lens, shutter, photomultiplier tube and reference photodiode, respectively.*

**3.1.2. Circular Dichroism (CD) Measurement:** CD is a form of spectroscopy based on the differential absorption of left and right-handed circularly polarized light. It can be used to determine the structure of macromolecules (including the secondary structure of proteins and the handedness of DNA). The CD measurements were done in a JASCO spectropolarimeter with a temperature controller attachment (Peltier) (Figure 3.3). The CD spectra were acquired using a quartz cell of 1 cm path length. For proteins, the typical concentration used for CD measurements were within 10  $\mu\text{M}$ . The secondary structural data of the CD spectra were analyzed using CDNN and K2D deconvolution program.

The working principle of CD measurement is as follows: when a plane polarized light passes through an optically active substance, not only do the left (L) and right (R) circularly polarized light rays travel at different speeds,  $c_L \neq c_R$ , but these two rays are absorbed to different extents, i.e.,  $A_L \neq A_R$ . The difference in the absorbance of the left and right circularly polarized light, i.e.,  $\Delta A = A_L - A_R$ , is defined as circular dichroism [1]. CD spectroscopy follows Beer-Lambert law. If  $I_0$  is the intensity of light incident on the cell, and  $I$ , that of emergent light, then absorbance is given by,

$$A = \log_{10} \left( \frac{I_0}{I} \right) = \epsilon c l \quad (3-1)$$

where,  $A$  is proportional to concentration ( $c$ ) of optically active substance and optical path length ( $l$ ). If ' $c$ ' is in  $\text{moles L}^{-1}$  and ' $l$ ' is in  $\text{cm}$ , then  $\epsilon$  is called the molar absorptivity or molar extinction coefficient. In an optically active medium, two absorbances,  $A_L$  and  $A_R$  are considered, where  $A_L = \log_{10} (I_0/I_L)$  and  $A_R = \log_{10} (I_0/I_R)$ . At the time of incidence on the sample, intensity of left and right circularly polarized light are same, i.e.  $I_0 = I_L = I_R$ . Any micrograph passes periodically changing light through the medium, oscillating between left and right circular polarization, and the difference in absorbances are recorded directly [2].

$$\Delta A = A_L - A_R = \log_{10} \left( \frac{I_0}{I_L} \right) - \log_{10} \left( \frac{I_0}{I_R} \right) = \log_{10} \left( \frac{I_R}{I_L} \right) \quad (3-2)$$

or 
$$\Delta A = (\Delta \epsilon) c l \quad (3-3)$$

As seen from equation 3.2,  $I_0$  does not appear in this final equation, so there is no need for a reference beam. The instruments are, therefore, of single beam type. Most of the CD spectropolarimeters, although they measure differential absorption, produce a CD spectrum in units of ellipticity ( $\theta$ ) expressed in millidegrees versus  $\lambda$ , rather than  $\Delta A$  versus  $\lambda$ . The relation between ellipticity and CD is given by,

$$\theta = \frac{2.303 \times 180 \times (A_L - A_R)}{4\pi} \text{ degrees} \quad (3-4)$$

To compare the results from different samples, optical activity is computed on a molar or residue basis. Molar ellipticity,  $[\theta]$  is defined as,

$$[\theta] = \frac{\theta}{c l} \quad (3-5)$$

where, ' $\theta$ ' is in degrees, ' $c$ ' is in  $\text{molesL}^{-1}$  and ' $l$ ' is in cm. The unit of molar ellipticity is  $\text{deg M}^{-1} \text{cm}^{-1}$ .

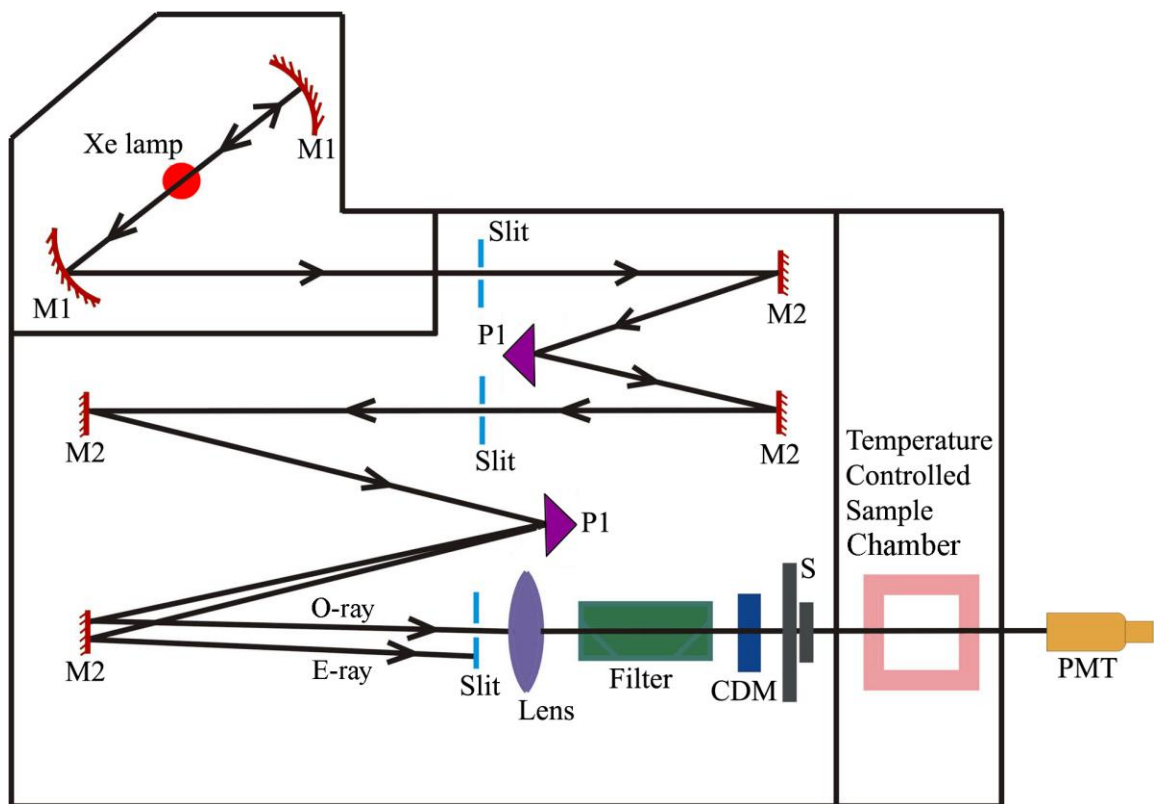


*Figure 3.3: Schematic ray diagram of a Circular Dichroism (CD) spectropolarimeter. M1, M2, P1, S, PMT, CDM, O-ray and E-ray represent concave mirror, plain mirror, reflecting prism, shutter, photomultiplier tube, CD-modulator, ordinary ray and extraordinary ray, respectively.*

**3.1.3. Time-Related Single Photon Counting (TCSPC) Technique:** All the picosecond-resolved fluorescence transients were recorded using TCSPC technique. The schematic block diagram of a TCSPC system is shown in Figure 3.4. TCSPC setup from Edinburgh instruments, U.K., was used during fluorescence decay acquisitions. The instrument response functions (IRFs) of the laser sources at different excitation wavelengths varied between 60 ps to 80 ps. The fluorescence from the sample was detected by a photomultiplier after dispersion through a grating monochromator [3]. For all transients, the polarizer in the emission side was adjusted to be at  $54.7^\circ$  (magic angle) with respect to the polarization axis of excitation beam. For 290-300 nm laser excitation, we have used a femtosecond-coupled TCSPC setup in which the sample was excited by the

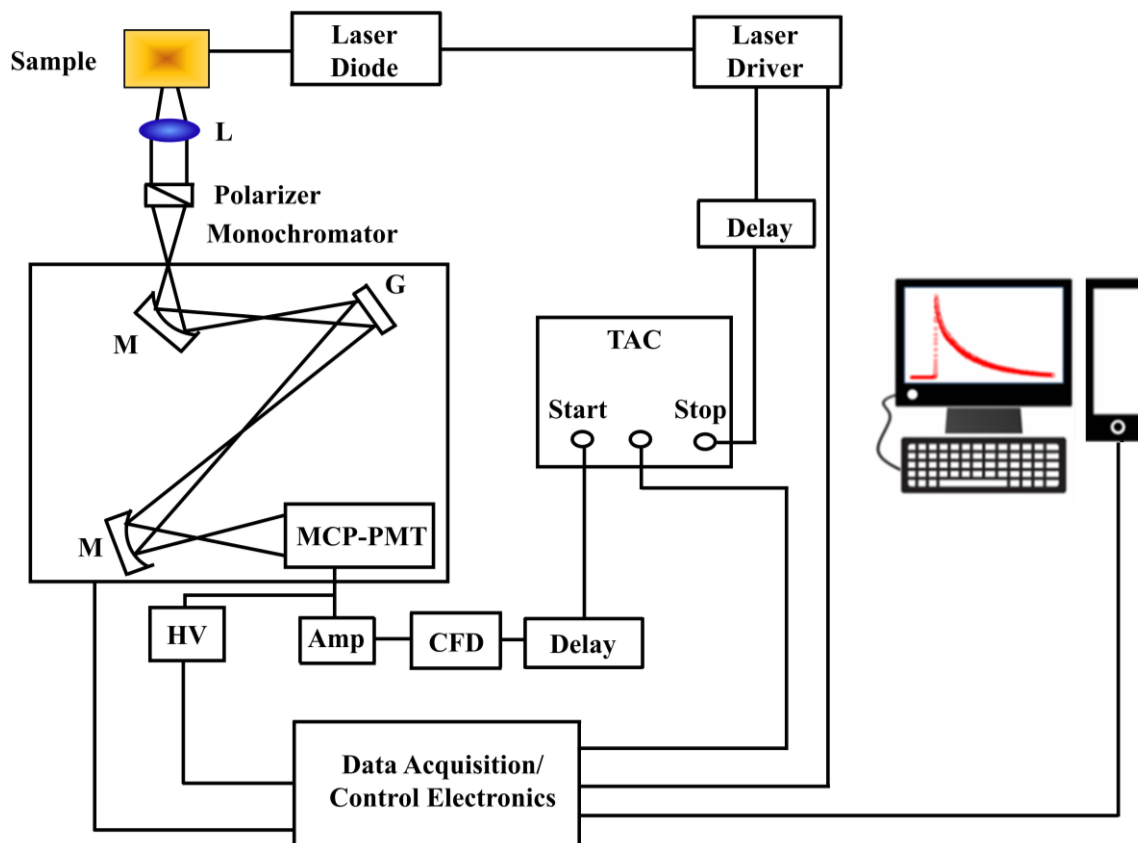


*Figure 3.4: Schematic ray diagram of a time correlated single photon counting (TCSPC) spectrophotometer. A signal from microchannel plate photomultiplier tube (MCP-PMT) is amplified (Amp) and connected to start channel of time to amplitude converter (TAC) via constant fraction discriminator (CFD) and delay. The stop channel of the TAC is connected to the laser driver via a delay line. L, M, G and HV represent lens, mirror, grating and high voltage source, respectively.*

third harmonic laser beam (290-300 nm) of the 870-900 nm (0.5 nJ per pulse) using a modelocked Ti-sapphire laser with an 80 MHz repetition rate (Tsunami, Spectra-Physics), pumped by a 10 W Millennia (Spectra-Physics) followed by a pulse-peaker (rate 8 MHz) and a third harmonic generator (model 3980, Spectra-Physics). The third harmonic beam was used for excitation of the sample inside the TCSPC instrument (IRF = 70 ps) and the second harmonic beam was collected for the start pulse.

**3.1.4. Femtosecond-Resolved Fluorescence Upconversion Technique:** The femtosecond-resolved fluorescence spectroscopy was carried out using a femtosecond upconversion setup (FOG 100, CDP, Figure 3.5) in which the sample was excited at 385 nm, using the second harmonic of a mode-locked Ti-sapphire laser with 80 MHz repetition rate (Tsunami, Spectra Physics), pumped by 10 W Millennia (Spectra Physics). The

fundamental beam was passed through a periscopic arrangement (P) (Figure 3.5) before getting frequency doubled in a nonlinear crystal, NC1 (1 mm BBO,  $\theta = 25^\circ$ ,  $\phi = 90^\circ$ ). This beam was then sent into a rotating circular cell of 1 mm thickness containing the sample via a dichroic mirror (DM), a polarizer and a mirror (M6). The resulting fluorescence emission was collected, refocused with a pair of lenses (L4 and L5) and mixed with the fundamental beam (770 nm) coming through a delay line to yield an upconverted photon signal in a nonlinear crystal, NC2 (0.5 mm BBO ( $\beta$ -barium borate),  $\theta = 10^\circ$ ,  $\phi = 90^\circ$ ). The upconverted light was dispersed in a double monochromator and detected using photon counting electronics. A cross-correlation function obtained using the Raman scattering from water displayed a full width at half maximum (FWHM) of 165 fs. The femtosecond fluorescence decays were fitted using a Gaussian shape for the exciting pulse.

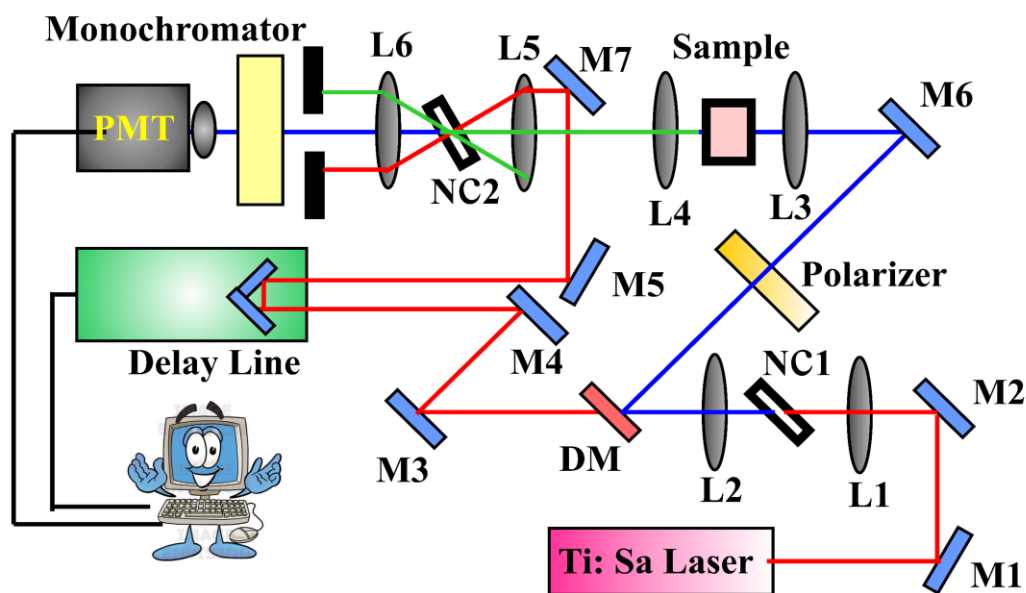


*Figure 3.5: Schematic diagram of a femtosecond fluorescence upconversion experimental setup. A BBO crystal (NC1) is used for second harmonic generation, which provides a pump beam in the UV region. Another BBO crystal (NC2) generates the upconversion signal of pump and probe beams. L and M indicate lenses and mirrors, respectively. M1, M2, M3, M4, M5, and M7 are IR mirrors whereas M6 is a UV mirror. DM is dichroic mirror, and P is periscope.*

**3.1.5. Differential Scanning Calorimetry (DSC):** DSC is a thermodynamical technique in which the difference in the amount of heat required to increase the temperature of a sample and reference is measured as a function of temperature. DSC is commonly used for

the study of biochemical reactions, such as, single molecular transition of a molecule from one conformation to another [4]. Thermal transition temperatures ( $T$ ; melting points) of the samples are also determined in solution, solid, or mixed phases such as suspensions [5]. In a basic DSC experiment, energy is introduced simultaneously into a sample cell (which contains a solution with the molecule of interest) and a reference cell (containing only the solvent). Temperatures of both cells are raised identically over time. The difference in the input energy required to match the temperature of the sample to that of the reference would be the amount of excess heat absorbed or released by the molecule in the sample (during an endothermic or exothermic process, respectively). The schematic of the DSC setup is shown in Figure 3.6.

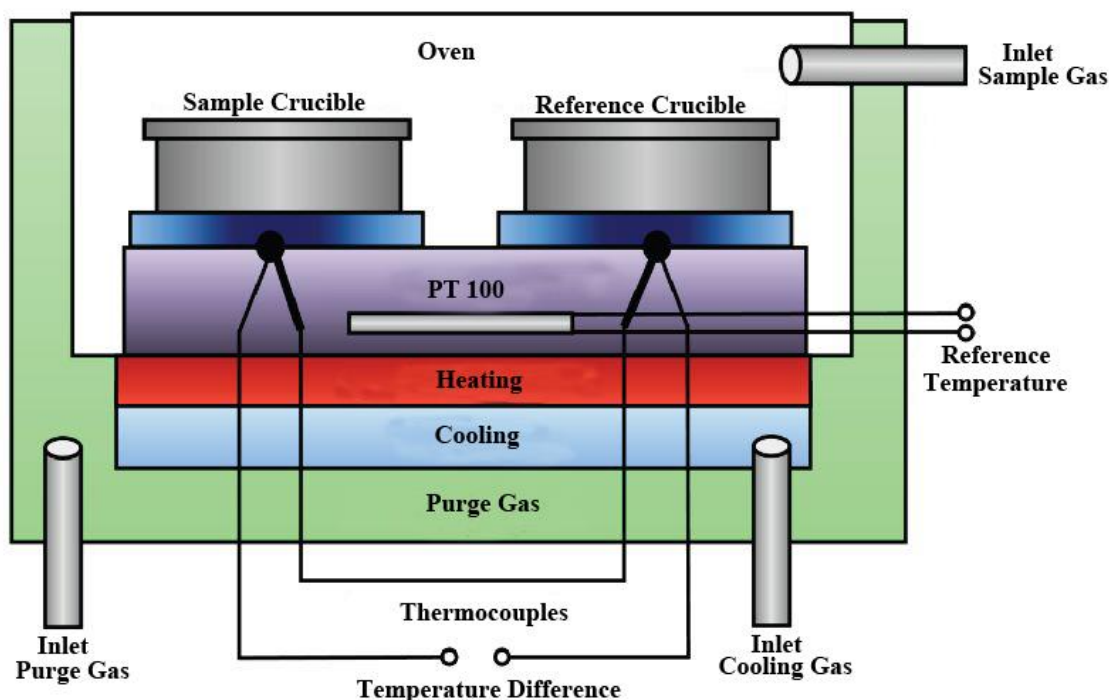


*Figure 3.6: The schematic representation of DSC setup.*

**3.1.6. Dynamic Light Scattering (DLS) Measurement:** DLS, also known as photon correlation spectroscopy (PCS) or quasi-elastic light scattering (QELS) is one of the most popular techniques used to determine the hydrodynamic size of the particle. DLS measurements were performed on a Nano S Malvern instrument, (U.K.) employing a 4 mW He-Ne laser ( $\lambda = 632.8$  nm) and equipped with a thermostatted sample chamber. The

instrument allows DLS measurements in which all the scattered photons are collected at  $173^\circ$  scattering angle (Figure 3.7). The instrument measures the time dependent fluctuation in intensity of light scattered from the particles in solution at a fixed scattering angle [6]. The ray diagram of the DLS setup is shown in Figure 3.7.

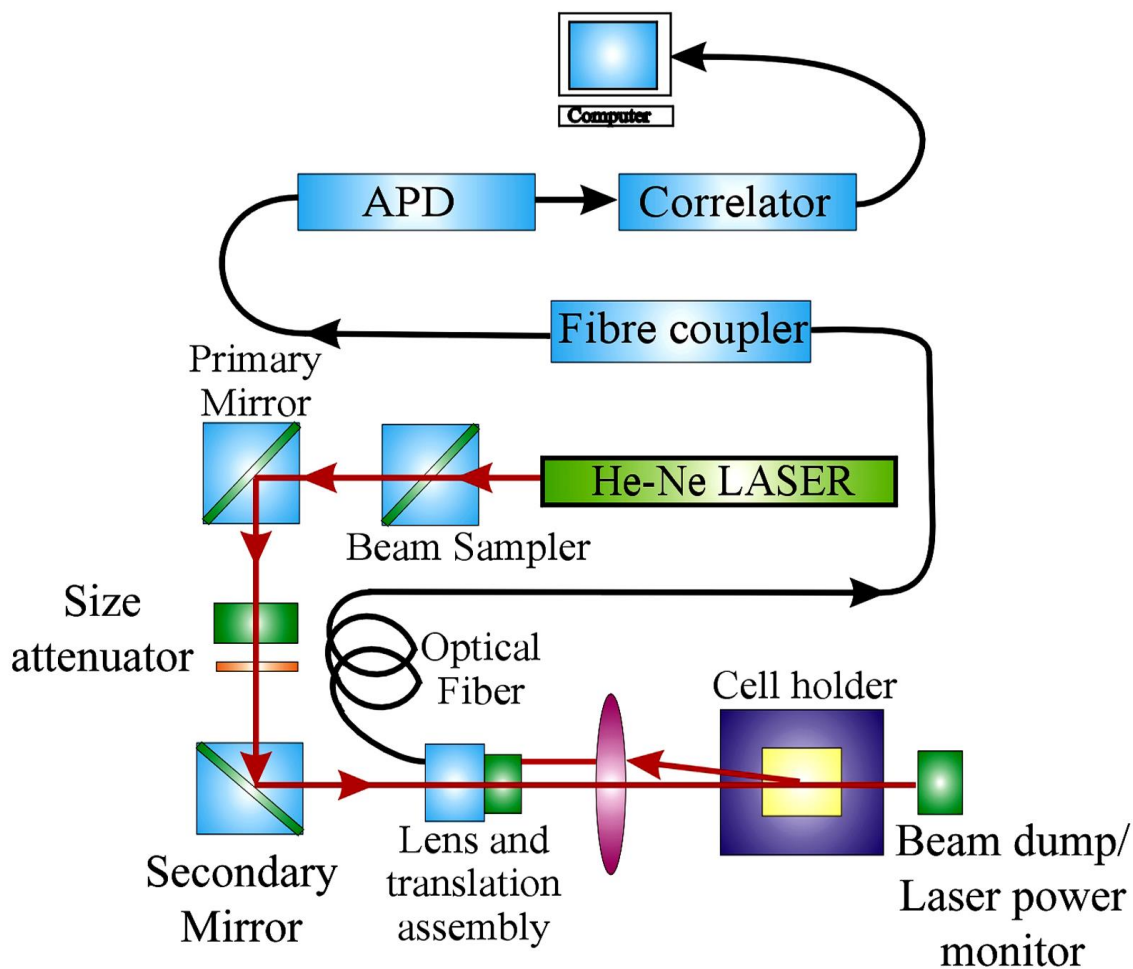


**Figure 3.7: Schematic ray diagram of dynamic light scattering (DLS) instrument. The avalanche photo diode (APD) is connected to preamplifier/amplifier assembly and finally to correlator. It has to be noted that lens and translational assembly, laser power monitor, size attenuator, laser are controlled by the computer.**

It has been seen that particles in dispersion are in a constant, random Brownian motion and this causes the intensity of scattered light to fluctuate as a function of time.

The correlator used in a DLS instrument constructs the intensity autocorrelation function  $G(\tau)$  of the scattered intensity,

$$G(\tau) = \langle I(t)I(t + \tau) \rangle \quad (3-6)$$

where  $\tau$  is the time difference (the sample time) of the correlator. For a large number of monodisperse particles in Brownian motion, the correlation function (given the symbol  $G$ ) is an exponential decaying function of the correlator time delay  $\tau$ ,

$$G(\tau) = A[1 + B\exp(-2\Gamma\tau)] \quad (3-7)$$

where  $A$  is the baseline of the correlation function,  $B$  is the intercept of the correlation function.  $\Gamma$  is the first cumulant and is related to the translational diffusion coefficient as,  $\Gamma = Dq^2$ , where  $q$  is the scattering vector and its magnitude is defined as,

$$q = \left( \frac{4\pi n}{\lambda_0} \right) \sin\left(\frac{\theta}{2}\right) \quad (3-8)$$

where  $n$  is the refractive index of dispersant,  $\lambda_0$  is the wavelength of the laser and  $\theta$ , the scattering angle. For polydisperse samples, the equation can be written as,

$$G(\tau) = A \left[ 1 + B |g^{(1)}(\tau)|^2 \right] \quad (3-9)$$

where the correlation function  $g^{(1)}(\tau)$  is no longer a single-exponential decay and can be written as the Laplace transform of a continuous distribution  $G(\Gamma)$  of decay times,

$$g^{(1)}(\tau) = \int_0^{\infty} G(\Gamma) \exp(-\Gamma\tau) d\Gamma \quad (3-10)$$

The scattering intensity data in DLS were processed using the instrumental software to obtain the hydrodynamic diameter ( $d_H$ ) and the size distribution of the scatterer in each sample. In a typical size distribution graph from the DLS measurement, X-axis shows a distribution of size classes in nm, while the Y-axis shows the relative intensity of the scattered light. The diffusion coefficient ( $D$ ) can be calculated using  $d_H$  of the particle by using the Stoke-Einstein relation,

$$D = \frac{k_B T}{3\pi\eta d_H} \quad (3-11)$$

where  $k_B$ ,  $T$ ,  $d_H$ ,  $\eta$  are Boltzmann constant, temperature in Kelvin, hydrodynamic diameter and viscosity, respectively.

**3.1.7. Fourier Transform Infrared (FTIR) Measurement:** FTIR spectroscopy is a technique that can provide very useful information about functional groups in a sample. An infrared spectrum represents the fingerprint of a sample with absorption peaks which correspond to the frequencies of vibrations between the bonds of the atoms making up the material. Because each different material is a unique combination of atoms, no two compounds produce the exact same infrared spectrum. Therefore, infrared spectroscopy can result in a positive identification (qualitative analysis) of all different kinds of material. In addition, the size of the peaks in the spectrum is a direct indication of the amount of material present. The two-beam Michelson interferometer is the heart of FTIR

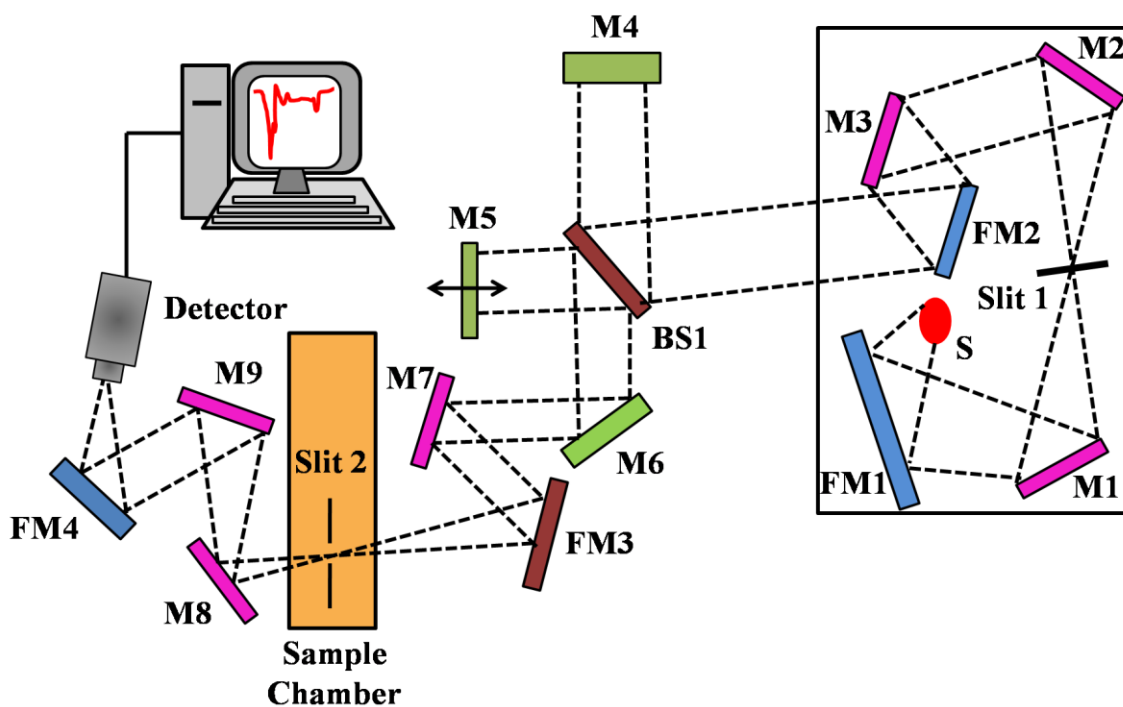


*Figure 3.8: Schematic of Fourier Transform Infrared (FTIR) spectrometer. It is basically a Michelson interferometer in which one of the two fully-reflecting mirrors is movable, allowing a variable delay (in the travel-time of the light) to be included in one of the beams. M, FM and BS1 represent the mirror, focussing mirror and beam splitter, respectively. M5 is a moving mirror.*

spectrometer. It consists of a fixed mirror (M4), a moving mirror (M5) and a beam-splitter (BS1), as illustrated in Figure 3.8. The beam-splitter is a laminate material that reflects and transmits light equally. The collimated IR beam from the source is partially transmitted to the moving mirror and partially reflected to the fixed mirror by the beam-splitter. The two

IR beams are then reflected back to the beam-splitter by the mirrors. The detector then sees the transmitted beam from the fixed mirror and reflected beam from the moving mirror, simultaneously. The two combined beams interfere constructively or destructively depending on the wavelength of the light (or frequency in wavenumbers) and the optical path difference introduced by the moving mirror. The resulting signal is called an interferogram which has the unique property that every data point (a function of the moving mirror position) which makes up the signal has information about every infrared frequency which comes from the source. Because the analyst requires a frequency spectrum (a plot of the intensity at each individual frequency) in order to make identification, the measured interferogram signal cannot be interpreted directly. A means of “decoding” the individual frequencies is required. This can be accomplished *via* a well-known mathematical technique called the Fourier transformation. This transformation is performed by the computer which then presents the user with the desired spectral information for analysis. FTIR measurements were performed on a JASCO FTIR-6300 spectrometer (transmission mode). Each spectrum consists of 100 scans (1500–4000  $\text{cm}^{-1}$ ) acquired at 0.5  $\text{cm}^{-1}$  resolution.

**3.1.8. Laser Raman Spectroscopy:** Raman spectroscopy is a useful technique for the identification of a wide range of substances solids, liquids, and gases. It is a straightforward, non-destructive technique requiring no sample preparation. Raman spectroscopy involves illuminating a sample with monochromatic light and using a spectrometer to examine light scattered by the sample.

At the molecular level photons can interact with matter by absorption or scattering processes. Scattering may occur either elastically, or inelastically. The elastic process is termed Rayleigh scattering, whilst the inelastic process is termed Raman scattering. The electric field component of the scattering photon perturbs the electron cloud of the molecule and may be regarded as exciting the system to a ‘virtual’ state. Raman scattering occurs when the system exchanges energy with the photon, and the system subsequently decays to vibrational energy levels above or below that of the initial state. The frequency shift corresponding to the energy difference between the incident and scattered photon is termed the Raman shift. Depending on whether the system has lost or gained vibrational

energy, the Raman shift occurs either as an up or down-shift of the scattered photon frequency relative to that of the incident photon. The down-shifted and up-shifted components are called, respectively, the Stokes and anti-Stokes lines. A plot of detected number of photons versus Raman shift from the incident laser energy gives a Raman spectrum. Different materials have different vibrational modes, and therefore characteristic Raman spectra. This makes Raman spectroscopy a useful technique for material identification. There is one important distinction to make between the Raman spectra of gases and liquids, and those taken from solids– in particular, crystals. For gases and liquids it is meaningful to speak of the vibrational energy levels of the individual molecules which make up the material. Crystals do not behave as if composed of molecules with specific vibrational energy levels, instead the crystal lattice undergoes vibration. These macroscopic vibrational modes are called phonons.

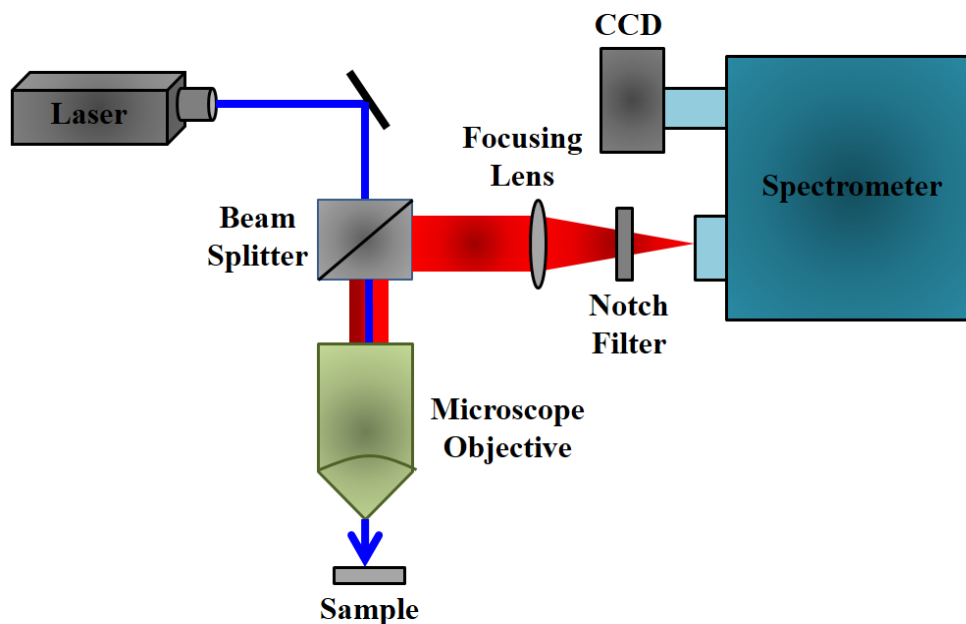


*Figure 3.9: Schematic diagram of a Raman spectrometer is shown.*

In our Raman spectrometers (LabRAM HR, Jobin Yvon), lasers are used as a photon source due to their highly monochromatic nature, and high beam fluxes (Figure 3.9). This is necessary as the Raman effect is weak, typically the Stokes lines are  $\sim 10^5$  times weaker than the Rayleigh scattered component. In the visible spectral range, Raman spectrometers use notch filters to cut out the signal from a very narrow range centred on the frequency corresponding to the laser radiation. Most Raman spectrometers for material

characterization use a microscope to focus the laser beam to a small spot ( $<1\text{--}100\ \mu\text{m}$  diameter). Light from the sample passes back through the microscope optics into the spectrometer. Raman shifted radiation is detected with a charge-coupled device (CCD) detector, and a computer is used for data acquisition and curve fitting. These factors have helped Raman spectroscopy to become a very sensitive and accurate technique. In our experiments, Raman scattering measurements were performed in a back scattering geometry using a micro-Raman setup consisting of a spectrometer (model LabRAM HR, JobinYvon) and a Peltier-cooled CCD detector. An air cooled argon ion laser with a wavelength of 488 nm was used as the excitation light source. Raman spectra of all samples have been recorded at room temperature in the frequency range of  $50\text{--}4000\ \text{cm}^{-1}$ .

**3.1.9. Density and Sound Velocity Measurement:** The density and sound velocity measurements were done in DSA 5000 from Anton Paar. The instrument measures density and sound velocity with accuracies of  $10^{-6}\ \text{g cm}^{-3}$  and  $10\ \text{cm s}^{-1}$  respectively. The density and velocity are measured according to the following measuring principle. A U-shaped glass tube of known volume and mass is filled with the liquid sample and excited electronically by a Piezo element (Figure 3.10). The U-tube is kept oscillating continuously at the characteristic frequency  $f$ . Optical pick-ups record the oscillation

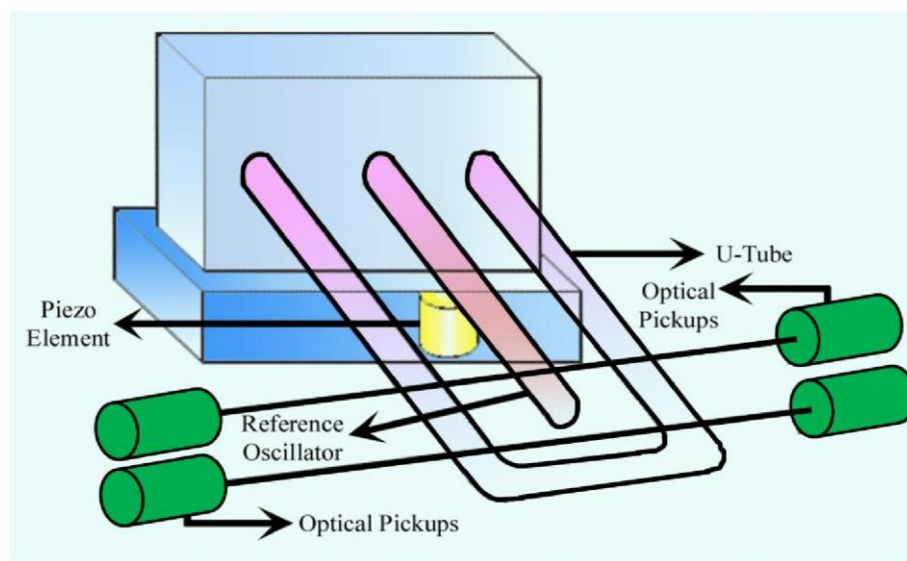


*Figure 3.10: Schematic representation of the density and sound velocity measurement setup.*

period  $P$  as  $P = 1/f$ . This frequency is inversely proportional to the density,  $\rho$  of the filled-in sample. The reference oscillator speeds up the measurements when aiming at various measuring temperatures. The density is calculated as,

$$\rho = A \times P^2 - B \quad (3-12)$$

where  $A$  and  $B$  are parameters. Once the instrument has been adjusted with air and water, the density of the sample can be determined. Hence related parameters can be calculated from the density.

**3.1.10. Viscosity Measurement:** The viscosity of the mixtures were measured by an automated micro viscometer (AVMn) from Anton Paar (Austria). The viscosity of the sample are measured by Höppler falling ball principle. The basic concept is to measure the elapsed time required for the ball to fall under gravity through a sample-filled tube inclined

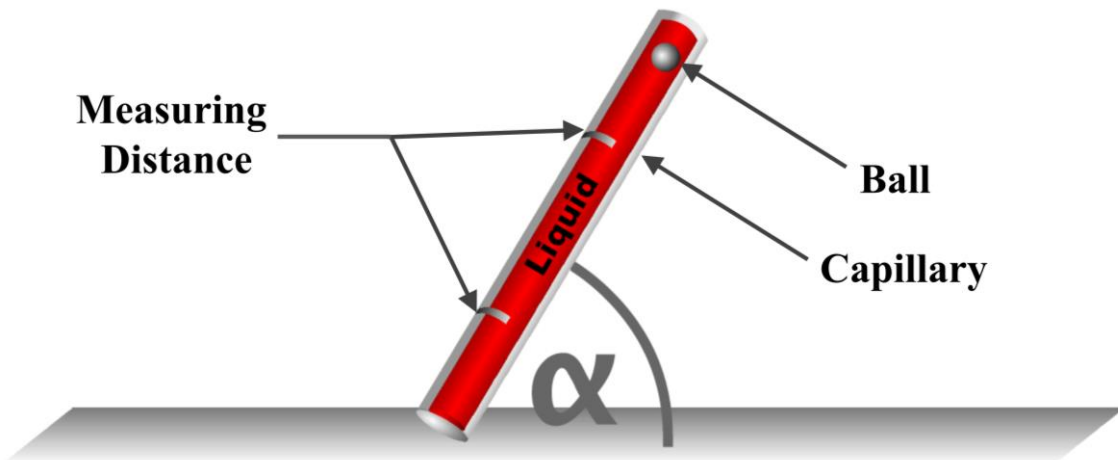


*Figure 3.11: Schematic representation of the automated micro viscometer.*

at an angle. The tube is mounted on a pivot bearing which quickly allows rotation of the tube by 180 degrees, thereby allowing a repeat test to run immediately. Several measurements are taken and the average time is converted into a final viscosity value in centipoise (cP).

The dynamic viscosity in Höppler falling ball method is calculated by the following equation:

$$\eta = t(\rho_1 - \rho_2)K * F \quad (3-13)$$

where:  $\eta$  is the dynamic viscosity [mPa.s];  $t$  travelling time of the ball [s];  $\rho_1$  density of the ball [g cm<sup>-3</sup>];  $\rho_2$  density of the sample [g cm<sup>-3</sup>];  $K$  ball constant [mPa·cm<sup>3</sup> g<sup>-1</sup>];  $F$  working angle constant.

**3.1.11. Refractive Indices Measurement:** Refractive indices of the solutions were measured by using a Rudolph J357 automatic refractometer. The instrument measures the refractive indices using sodium D-line of wavelength 589.3 nm with accuracies  $\pm 0.00004$ . The measurement of the refractive index of the sample is based on the determination of the critical angle of total reflection. A light source, usually a long-life LED, is focused onto a prism surface via a lens system. Due to the focusing of light to a spot at the prism surface, a wide range of different angles is covered. As the measured sample is in direct contact

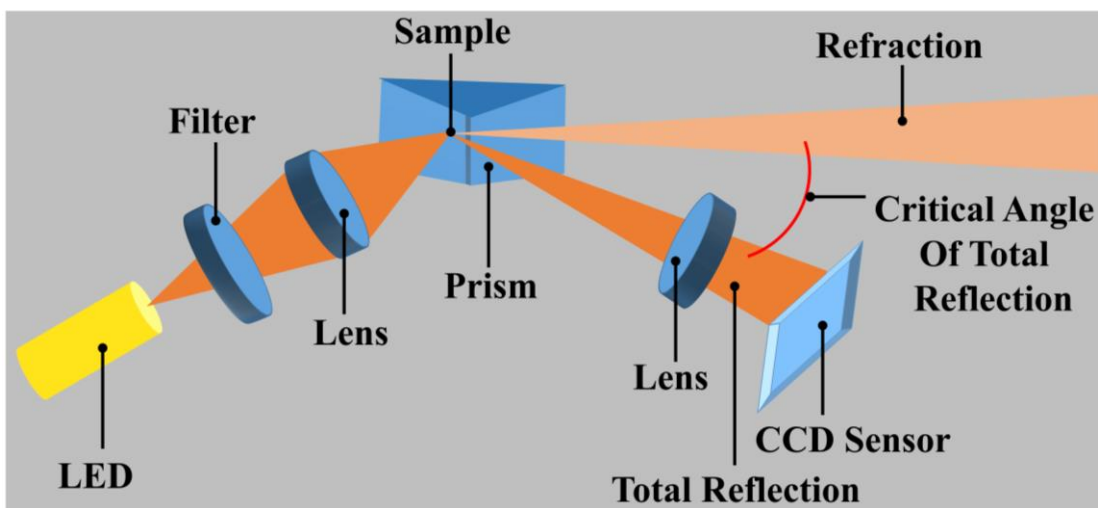


*Figure 3.12: Schematic representation of the refractometer.*

with the measuring prism. Depending on its refractive index, the incoming light below the critical angle of total reflection is partly transmitted into the sample, whereas for higher angles of incidence the light is totally reflected. This dependence of the reflected light intensity from the incident angle is measured with a high-resolution sensor array. From the video signal taken with the CCD sensor the refractive index of the sample can be calculated.

**3.2. Sample Preparation:** In this section the different sample preparation methods have been discussed.

**3.2.1. Chemicals Used:** The chemicals, spectroscopic probes, and proteins were procured from the following sources. All the aqueous solutions were prepared using double distilled water. The chemicals phosphate buffer (disodium hydrogen phosphate, monosodium hydrogen phosphate), methyl *tert*-butyl ether (MTBE), isooctane (i-Oc), 4',6-diamidino-2-phenylindole (DAPI), benzo[ $\alpha$ ]pyrene, kynurenine (KN), hoechst 33258 (H33258), crystal violet (CV), 1-naphthol, L-tryptophan (L-Trp), riboflavin (Rf), N-CBZ-Gly-Gly-Leu p-nitroanilide (CBZ-GGL-pNA) and 3-(dansylamino)phenylboronic acid (DB) were obtained from Sigma/Aldrich. Sodium bis(2ethylhexyl) sulfosuccinate (AOT), tetraethylene glycol monododecyl ether (Brij-30), and sodium dodecyl sulfate (SDS) were obtained from Fluka. The fluorescent probes 4-(dicyanomethylene)-2-methyl-6-(p-dimethylamino-styryl)-4H-pyran (DCM), coumarin 500 (C500) were purchased from Exciton. Anthracene and naphthalene were obtained from Loba Chemie. Benzoyl chloride (BzCl) was purchased from Merck. 1, 4-dioxane (DX) was purchased from Spectrachim. The proteins riboflavin binding protein (RBP; Apo form) and subtilisin *carlsberg* (SC) were obtained from Sigma Aldrich. All the chemicals and the proteins were of highest purity available and used without further purification.

**3.2.2. Preparation of Micellar Solution:** The micellar solutions were prepared by dissolving surfactant salts in buffer of required pH. Micellar solutions of the probe were prepared by adding known concentrated aqueous probe solution to micellar solution of desired concentration with simultaneous stirring of the mixture for an hour [7].

**3.2.3. Preparation of Reverse Micellar Solution:** Reverse micellar solutions of specific degree of hydration ( $w_0 = [\text{H}_2\text{O}]/[\text{Surfactant}]$ ) were prepared by addition of calculated volume of aqueous solution of the probe in known volume of 100 mM AOT/200 mM Brij 30 solution in isooctane [8, 9]. In order to ensure that each reverse micelle contains not more than one probe molecule, the overall probe concentration was kept less than that of micellar concentration.

**3.2.4. Preparation of DB-SC Complex:** The binding of DB to SC was achieved by adding DB to the protein solution with overnight incubation at 4 °C, with constant stirring. The enzyme concentration was maintained higher than that of the probe DB in order to avoid free DB in solution [8].

**3.2.5. Measurement of Enzymatic Activity of Subtilisin *Carlsberg* (SC):** For the measurement of the enzymatic activity of SC, CBZ-GGL-pNA was used as the substrate. For the kinetics experiment, the concentration of SC was maintained at 1 μM, whereas that of substrate was maintained at 850 μM [8]. The rate of formation of product was followed by measuring the absorbance of product at 410 nm. We have measured the activity in specific activity unit, which is defined as the number of enzyme units per ml divided by the concentration of protein in mg ml<sup>-1</sup>. Specific activity values are therefore quoted as units/mg and for native SC it is 7-15 units mg<sup>-1</sup>.

**3.2.6. Cytotoxicity Assay Protocol:** The MTBE induced cytotoxicity in yeast cells was assessed using the MTT based cell viability assay. Briefly, 5 ml of the cells was transferred to six different test tubes at a density of 12.5×10<sup>6</sup> cells ml<sup>-1</sup>. The cells were then treated with various concentrations of MTBE (0.0, 7.4, 14.8, 29.6, 37.0, 44.4 mg ml<sup>-1</sup> of MTBE) and incubated at 25 °C for 3 h, with shaking. The 200 μl of each of the cell suspensions was mixed with 20 μl of MTT based cell viability assay kit (CCK-8) and incubated at 25 °C for 3 h, with shaking. The absorbance of the supernatants was measured at 450 nm and from the CCK-8 standard curve the number of viable cells per ml at various known amounts of MTBE treated cell suspensions were estimated. The impact of MTBE cytotoxicity was also assessed by studying the time dependent MTT assay for the cells treated with MTBE with respect to a control experiment. Briefly, in 3 ml of the yeast cell culture (in mid log phase of growth) MTBE was added at its highest solubility (44.4 mg ml<sup>-1</sup>). The cells were next incubated at 25 °C with shaking in the presence of 300 μl of CCK-8. At various time intervals a specific amount of the culture was recovered and the absorbance of the supernatants was measured at 450 nm. A similar experiment was also performed for the control set [10].

**3.2.7. Computational Methods for Water-MTBE Interactions:** All theoretical calculations were carried out using the Gaussian 03 program [11]. The geometries of

different MTBE-water complexes were optimized, and the frequency calculations were followed by using both DFT level with B3LYP functional and Møller-Plesset correlation energy correction truncated at second-order (MP2) in conjunction with 6-31g basis set i.e., MP2/6-31g at the ground state. However, the results obtained from MP2/6-31G are more consistent with the experimental finding, so the theoretical calculations at the MP2/6-31G level are only reported. We represented MTBE in water by the model system, MTBE/(water)<sub>n</sub> (where, n = 1, 2, 3) and water in MTBE system by Water/(MTBE)<sub>n</sub> (where, n = 1, 2, 3). Each of these species is the minimum energy structure as all the normal modes of vibrations are positive. Binding energy ( $\Delta E$ ) of MTBE-water complexes was determined from calculation at the MP2 level. Calculated energy values included both zero point correction ( $\Delta ZPE$ ) and basis set superposition error (BSSE) in the counterpoise method, for more accurate results. Energy of the prototype hydrogen bond was also calculated from the water dimer at the same level. Thermo-chemical parameters like enthalpy of formation ( $\Delta H$ ) and Gibbs free energy change ( $\Delta G$ ) in forming molecular clusters from monomers were estimated using the following equations [12],

$$\Delta H = H_{\text{Product}} - H_{\text{Reactant}} = H_{\text{MTBE-(H}_2\text{O)}_n} - (H_{\text{MTBE}} + nH_{\text{H}_2\text{O}}) \quad (3-14)$$

and

$$\Delta G = G_{\text{Product}} - G_{\text{Reactant}} = G_{\text{MTBE-(H}_2\text{O)}_n} - (G_{\text{MTBE}} + nG_{\text{H}_2\text{O}}) \quad (3-15)$$

**3.2.8. Quantum Yield (Q<sub>D</sub>) Calculation:** Q<sub>D</sub> of the dye kynurenine (KN) in reverse micelle (RM) was calculated according to the following equation,

$$Q = Q_R \left( \frac{I}{I_R} \right) \left( \frac{OD_R}{OD} \right) \left( \frac{n^2}{n_R^2} \right) \quad (3-16)$$

where Q and Q<sub>R</sub> are the quantum yield of KN in the RM of different w<sub>0</sub> values and reference (protein bound KN). I and I<sub>R</sub> are the integrated fluorescence intensities of KN in the RM of different w<sub>0</sub> values and reference respectively. OD and OD<sub>R</sub> are the optical densities of KN in the RM of different w<sub>0</sub> values and reference at the excitation wavelength 375 nm, and n and n<sub>R</sub> are the refractive indices of KN in the RM of different w<sub>0</sub> values and reference solutions respectively. The absolute quantum yield of protein bound KN [13] was taken to be 4.8 × 10<sup>-3</sup>. Refractive indices of the solutions were measured by using Rudolph J357 automatic refractometer.

## References

- [1] A. Rodger, B. Nordén, Circular dichroism and linear dichroism, Oxford University Press, 1997.
- [2] N. Berova, K. Nakanishi, Circular dichroism: Principles and applications, Wiley-VCH, 2000.
- [3] D.V. O'Conner, D. Philips, Time-correlated single photon counting, Academic Press, London, 1984.
- [4] K.E.V. Holde, W.C. Johnson, P.S. Ho, Principles of physical biochemistry, Pearson Prentice Hall, New Jersey, 2006.
- [5] A. Cooper, M.A. Nutley, A. Walood, Protein-ligand interactions: Hydrodynamics and calorimetry, Oxford University Press, Oxford, 2000.
- [6] R. Pecora, Dynamic light scattering: Applications of photon correlation spectroscopy, Springer, 1985.
- [7] S. Rakshit, R. Saha, P.K. Verma, R.K. Mitra, S.K. Pal, Ultrafast electron transfer in riboflavin binding protein in macromolecular crowding of nano-sized micelle, *Biochimie* 94 (2012) 2673.
- [8] S. Rakshit, R. Saha, S.K. Pal, Modulation of environmental dynamics at the active site and activity of an enzyme under nanoscopic confinement: Subtilisin carlsberg in anionic AOT reverse micelle, *J. Phys. Chem. B* (2013) doi.org/10.1021/jp4061494.
- [9] S. Rakshit, N. Goswami, S.K. Pal, Slow solvent relaxation dynamics of nanometer sized reverse micellar systems through tryptophan metabolite, kynurenine, *Photochem. Photobiol.* 88 (2012) 38.
- [10] S. Rakshit, R. Saha, A. Singha, Z.S.A. Seddigi, S.K. Pal, Molecular interaction, co-solubilization of organic pollutants and ecotoxicity of a potential carcinogenic fuel additive MTBE in water, *J. Mol. Liq.* 180 (2013) 235.
- [11] M.J. Frisch, G.W. Trucks, H.B. Schlegel, G.E. Scuseria, M.A. Robb, J.R. Cheeseman, J.A. Montgomery, Jr., T. Vreven, K.N. Kudin, J.C. Burant, J.M. Millam, S.S. Iyengar, J. Tomasi, V. Barone, B. Mennucci, M. Cossi, G. Scalmani, N. Rega, G.A. Petersson, H. Nakatsuji, M. Hada, M. Ehara, K. Toyota, R. Fukuda, J. Hasegawa, M. Ishida, T. Nakajima, Y. Honda, O. Kitao, H. Nakai, M. Klene, X. Li, J.E. Knox, H.P. Hratchian, J.B. Cross, C. Adamo, J. Jaramillo, R. Gomperts, R.E. Stratmann, O. Yazyev,

A.J. Austin, R. Cammi, C. Pomelli, J.W. Ochterski, P.Y. Ayala, K. Morokuma, G.A. Voth, P. Salvador, J.J. Dannenberg, V.G. Zakrzewski, S. Dapprich, A.D. Daniels, M.C. Strain, O. Farkas, D.K. Malick, A.D. Rabuck, K. Raghavachari, J.B. Foresman, J.V. Ortiz, Q. Cui, A.G. Baboul, S. Clifford, J. Cioslowski, B.B. Stefanov, G. Liu, A. Liashenko, P. Piskorz, I. Komaromi, R.L. Martin, D.J. Fox, T. Keith, M.A. Al-Laham, C.Y. Peng, A. Nanayakkara, M. Challacombe, P.M.W. Gill, B. Johnson, W. Chen, M.W. Wong, C. Gonzalez, J.A. Pople, Gaussian 03, Revision C.02, *Gaussian, Inc., Wallingford CT* (2004).

[12] M.E. Dunn, E.K. Pokon, G.C. Shields, Thermodynamics of forming water clusters at various temperatures and pressures by Gaussian-2, Gaussian-3, complete basis set-QB3, and complete basis set-APNO model chemistries; implications for atmospheric chemistry, *J. Am. Chem. Soc.* 126 (2004) 2647.

[13] N. Goswami, A. Makhal, S.K. Pal, Toward an alternative intrinsic probe for spectroscopic characterization of a protein, *J. Phys. Chem. B* 114 (2010) 15236.

# Chapter 4

## Structural and Dynamical Studies on the Solubilisation of Hydrophobic molecules in Bulk Water

### 4.1. Introduction:

The specific interaction of water molecules with hydrophobic solvents is very important from both basic science and technological application point of view. A detailed scientific understanding becomes more crucial when the hydrophobic solvent is a potential threat of environment (water in particular) and health. For example, methyl *tert*-butyl ether (MTBE) is a hydrophobic solvent; as a widely used fuel additive it is much more soluble in water (4% wt/wt) than most of the other components of gasoline. The potential risk of ground water pollution through leakage of underground storage tank of fuel containing MTBE and unacceptable health hazards including carcinogenesis led Environmental Protection Agency (EPA) to issue an advisory on MTBE in the year 2002. Here we would like to highlight that significant solubility of organic MTBE in water is also a potential threat of indirect water pollution through the enhanced co-solubilization of other sparingly soluble environmental pollutants, which has been relatively less attended in the literature. Earlier studies show that [1] the apparent water solubility of some water-insoluble organic solutes (e.g., 1,1-bis(*p*-chlorophenyl)-2,2,2-trichloroethane (DDT), 1,2,3-trichlorobenzene (TCB)) can be significantly enhanced by low concentrations of dissolved organic matter (DOM) like humic and fulvic acids. Investigation on enhanced contamination of other water pollutants in the presence of MTBE in water is one of the motives of the present study. By using picosecond-resolved fluorescence spectroscopy, we have also explored the localization of one of the organic matters, 4-(dicyanomethylene)-2-methyl-6-(*p*-dimethylaminostyryl)-4H-pyran (DCM) and accordingly rationalized the molecular basis for the enhanced solubilization.

Due to the chemical properties like high aqueous solubility [2], low Henry's law constant [3, 4], small molecular size and low volatility, MTBE is not readily amenable to

treatment by conventional techniques such as air stripping and activated carbon adsorption or chemical oxidation. A significant technological advancement for the removal of the volatile MTBE from water including photo-catalytic techniques using various nanoparticles as catalysts has been reported earlier [5-7]. However, a full-proof technique for the complete removal of MTBE from water is most desirable and yet to be developed. It has to be noted that a detailed understanding of the bulk physico-chemical properties as well as the molecular interaction of the MTBE molecules with water is important for the design of efficient removal procedure. In a recent thermodynamic study [8] on the interaction of MTBE with water, it was interestingly concluded that solubilization of MTBE in the hydrogen bond network of water is exothermic while that of the water molecules in the hydrophobic environments is endothermic. Using Fourier transformed infrared spectroscopy (FTIR) and ab initio calculation, another study has shown that C-O and C-C stretching vibrational frequencies of MTBE are heavily affected on interaction with water molecules in the diluted aqueous solution and concluded to be due to hydrogen bonding interaction of MTBE with host water molecules [9]. In spite of all those efforts, a detailed and systematic study on the water–MTBE mixture starting from bulk physico-chemical properties to molecular interaction of organic solutes in the mixture is sparse in the literature and thus is one of the motives of the present work. An ecological consequence of the MTBE contamination on the mortality of model microbial organism yeast in the aqueous environments has also been addressed.

## **4.2. Results and Discussion:**

### **4.2.1. Molecular Interaction, Co-solubilisation of Organic Pollutants and Ecotoxicity of a Potential Carcinogenic Fuel Additive MTBE in Water [10]:**

The experimental values of the densities ( $\rho$ ), viscosities ( $\eta$ ), refractive indices ( $n_D$ ) and sound velocity data at 20 °C for the binary mixtures of water–MTBE at various concentrations are listed in Table 4.1 and are shown in Figure 4.1. From the figure, it is clear that as the MTBE content increases, the density of binary mixture decreases as the density of MTBE is lower than water whereas, refractive indices of the mixture increases

as

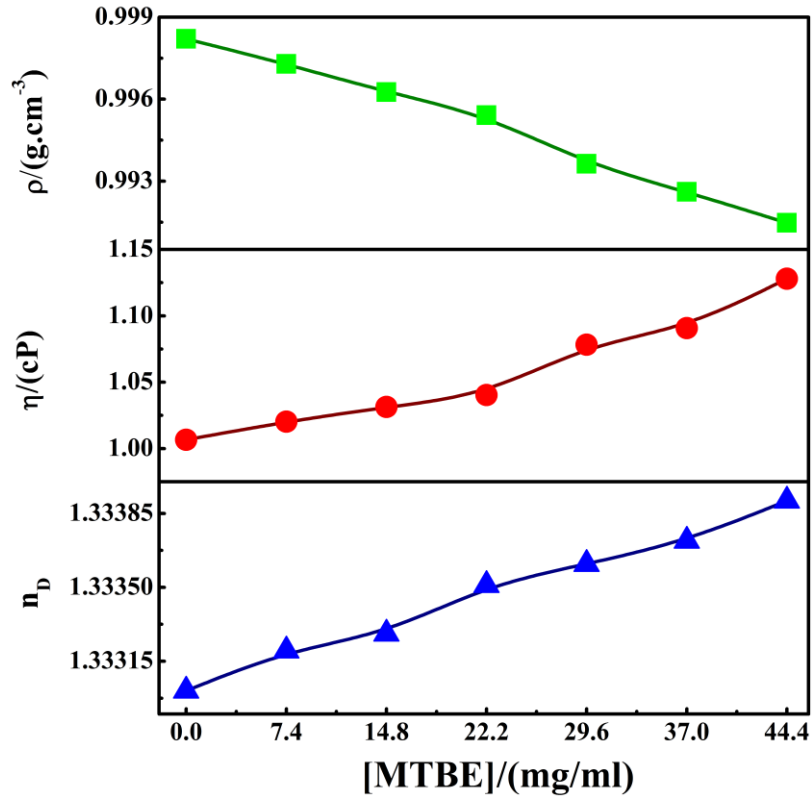


**Figure 4.1: Density (square), viscosity (circle) and refractive index (triangle) of pure water and water–MTBE mixtures at different concentrations.**

the refractive index of MTBE is higher than water. However, the viscosity of the binary mixtures increases with an increase in the concentration of MTBE, although the viscosity of MTBE (0.4086 mPa·S) is lower than water (1.0066 mPa·S). The observation can be rationalized in terms of the contraction of overall volume of the mixed solvents due to the formation of ordered hydrogen bonded structures between MTBE and water molecules. The excess molar volume ( $V_E$ ), viscosity deviations ( $\delta\eta$ ), refractive index deviations ( $\delta n_D$ ), adiabatic compressibility ( $\beta_S$ ) and deviation in adiabatic compressibility ( $\delta\beta_S$ ) can be calculated from the experimental results according to the following equations [11-13], respectively,

$$V^E = \left( x_1 M_1 + x_2 M_2 / \rho_{\text{Mix}} \right) - \left( x_1 M_1 / \rho_1 \right) - \left( x_2 M_2 / \rho_2 \right) \quad (4-1)$$

$$\delta\eta = \eta_{\text{Mix}} - (x_1 \eta_1 + x_2 \eta_2) \quad (4-2)$$

$$\delta n_D = n_{D_{\text{Mix}}} - (x_1 n_{D1} + x_2 n_{D2}) \quad (4-3)$$

$$\beta_s = \frac{1}{\rho u^2} \quad (4-4)$$

$$\Delta\beta_s = \beta_{\text{Mix}} - (x_1\beta_{s1} + x_2\beta_{s2}) \quad (4-5)$$

where  $x_1$  and  $x_2$  are the mole fractions;  $M_1$  and  $M_2$  are molar masses;  $\rho_1$  and  $\rho_2$  are the densities;  $\eta_1$  and  $\eta_2$  are the viscosities;  $n_{D1}$  and  $n_{D2}$  are the refractive indices of pure water and MTBE, and  $\beta_{s1}$  and  $\beta_{s2}$  are the adiabatic compressibility, respectively. The subscript “Mix” represents properties of the mixture. Table 4.1 shows that  $V_E$  values are negative

**Table 4.1: Densities ( $\rho$ ), excess molar volumes ( $V_E$ ), viscosities ( $\eta$ ), viscosity deviations ( $\delta\eta$ ), refractive index deviations ( $\delta n_D$ ), speed of sound ( $u$ ), adiabatic compressibility ( $\beta_s$ ) and deviation in adiabatic compressibility ( $\delta\beta_s$ ) for the mixture of water–MTBE at 20 °C.**

[MTBE] (mg/ml)	$\rho$ (g.cm <sup>-3</sup> )	$V^E$ (cm <sup>3</sup> .mol <sup>-1</sup> )	$\eta$ (cP)	$\Delta\eta$ (cP)	$n_D$	$\delta n_D$	$u$ (m.s <sup>-1</sup> )	$10^{11}\beta_s$ (N <sup>-1</sup> .m <sup>2</sup> )	$\delta\beta_s$ (N <sup>-1</sup> .m <sup>2</sup> )
0.0	0.998204	0.000	1.0066	0.000	1.33301	0.0000	1482.50	45.58	0.000
7.4	0.997289	-0.030	1.0203	0.015	1.33320	7.49e-5	1487.39	45.32	-0.367
14.8	0.996260	-0.057	1.0313	0.027	1.33328	1.00e-4	1493.00	45.03	-0.770
22.2	0.995413	-0.088	1.0403	0.036	1.33351	2.75e-4	1497.68	44.79	-1.123
29.6	0.993632	-0.100	1.0782	0.075	1.33361	3.20e-4	1507.69	44.27	-1.746
37.0	0.992608	-0.126	1.0991	0.089	1.33372	3.76e-4	1513.71	43.97	-2.160
44.4	0.991473	-0.150	1.1280	0.127	1.33391	5.12e-4	1519.79	43.67	-2.570

over the entire range of composition indicating a significant volume contraction on mixing of MTBE with water. On the other hand the positive values of the viscosity deviations suggest that the interaction forces occurring through hydrogen bonding plays an important role in this regard [14]. It is also observed from Table 4.1 that the adiabatic compressibility ( $\beta_s$ ) of the solution shifts to a lower value and the negative magnitude of the deviation in adiabatic compressibility ( $\delta\beta_s$ ) increases with an increase in volume fraction of MTBE solute, which suggests that hydrogen bonding interaction is taking place. A similar conclusion was also drawn for the aqueous binary mixtures of glycol ethers by Dhondge et al. [15]. We have also studied density ( $\rho$ ), viscosity ( $\eta$ ), and refractive index ( $n_D$ ) of water saturated with MTBE (44.4 mg ml<sup>-1</sup>) from 10 °C to 50 °C as shown in Figure 4.2a and Table 4.2. From the experimental observation, it is also evident that the effect of temperature on viscosity is more pronounced than that on density and refractive index due

to the specific hydrogen bonding interactions of MTBE with water molecules. It should be noted that due to a low boiling point of MTBE (55.2 °C) we could not measure the refractive index value of pure MTBE above 40 °C.

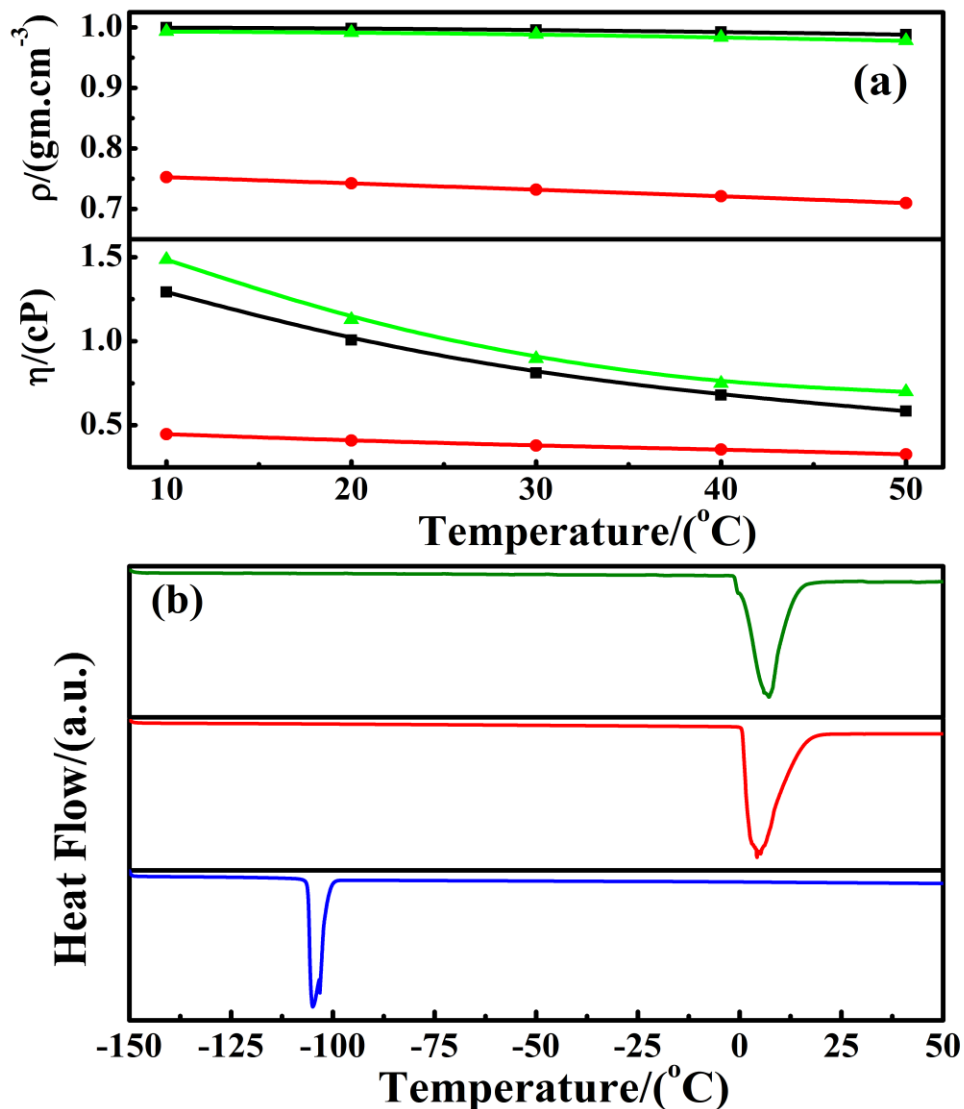


**Figure 4.2:** (a) Temperature dependent density and viscosity of pure water (square), MTBE (circle) and water at highest concentration of MTBE (44.4 mg ml<sup>-1</sup>) (triangle). (b) DSC thermogram of water (middle panel), MTBE (lower panel) and saturated solution of MTBE in water (44.4 mg ml<sup>-1</sup>) (upper panel) using empty vessel as reference.

The DSC thermograms obtained for water and water–MTBE mixture (44.4 mg ml<sup>-1</sup>) and pure MTBE are shown in Figure 4.2b. Upon heating, pure water shows an endotherm at 0 °C which is ascribed to the melting of the ice and is consistent with the

**Table 4.2: Temperature dependent densities ( $\rho$ ), viscosities ( $\eta$ ), refractive indices ( $n_D$ ) and speed of sound ( $u$ ) for water–MTBE mixture at a concentration of 44.4 mg ml<sup>-1</sup>.**

Sample	Temperature (°C)	$\rho$ (g.cm <sup>-3</sup> )	$\eta$ (cP)	$n_D$	$u$ (m.s <sup>-1</sup> )
<b>Water-MTBE</b>	10	0.993245	1.4849	1.33436	1492.99
	20	0.991473	1.1280	1.33391	1519.79
	30	0.988426	0.8952	1.33205	1537.44
	40	0.983398	0.7482	1.33102	1545.22
	50	0.978066	0.6991	1.32958	1550.82

reported thermogram in the literature [16]. At MTBE concentration of 44.4 mg ml<sup>-1</sup>, water–MTBE mixture shows a single endotherm at -0.66 °C (Figure 4.2b) indicating the formation of extended H-bonding structure among the solvent molecules and the formation of eutectic melt in the solution mixture. In order to infer on the possible formation of any microstructure in the eutectic melt, a prior knowledge of the heat of fusion ( $\Delta_f H$ ) in the water–MTBE mixture is very important. The values of enthalpy of fusion determined by the DSC and entropy of fusion for the pure components and for the binary system calculated by the following relation are reported in Table 4.3.

$$\Delta_f S = \frac{\Delta_f H}{T} \quad (4-6)$$

where  $\Delta_f H$  is the heat of fusion and T is the melting temperature of the compound on absolute scale. The values of the  $\Delta_f S$  (Table 4.3) are found to be positive suggesting that there is an increase in randomness of the system during melting as expected.

**Table 4.3: Heat of fusion ( $\Delta_f H$ ) and entropy of fusion data ( $\Delta_f S$ ) of pure water, MTBE and saturated solution of MTBE in water.**

Sample	$\Delta_f H$ /(kJ mol <sup>-1</sup> )		$\Delta_f S$ /(J mol <sup>-1</sup> K <sup>-1</sup> )	
	This work	Literature	This work	Literature
<b>Water</b>	6.11	6.01	22.04	22.00
<b>MTBE</b>	7.57	7.60 [17]	45.32	46.18 [17]
<b>Water-MTBE</b>	4.76	-	17.48	-

If the binary system is assumed to be a mechanical mixture of two components involving no enthalpy of mixing or any type of association in the melt, the heat of fusion could be given by the mixture law [18],

$$(\Delta_f H)_{cal} = x_1 \Delta_f H_1^0 + x_2 \Delta_f H_2^0 \quad (4-7)$$

where,  $x_i$  and  $\Delta_f H_i$  are the mole fraction and enthalpy of fusion of the components indicated by the subscripts, respectively. From the calculated values of enthalpy of fusion (Table 4.3), it can be inferred that they are not simple mechanical mixture of the components. Therefore, the enthalpy of mixing ( $\Delta_{\text{mix}}H$ ), which is the difference between the experimental,  $(\Delta_f H)_{\text{exp}}$  and the calculated values of enthalpy of fusion,  $(\Delta_f H)_{\text{cal}}$  is given by the equation,

$$\Delta_{\text{mix}}H = (\Delta_f H)_{\text{exp}} - (\Delta_f H)_{\text{cal}} \quad (4-8)$$

The thermo-chemical studies suggest that the structure of the binary eutectic melt depends on the sign and magnitude of heat of mixing ( $\Delta_{\text{mix}}H$ ) [18]. Accordingly, three types of structure are suggested: quasieutectic for which  $\Delta_{\text{mix}}H > 0$ ; clustering of molecules in which  $\Delta_{\text{mix}}H < 0$ , and molecular solutions, for which  $\Delta_{\text{mix}}H = 0$ . We have found the value of enthalpy of mixing ( $\Delta_{\text{mix}}H$ ) =  $-1.2 \text{ kJ mol}^{-1}$  for the water–MTBE system suggesting the clustering of molecules in the melt of the binary system.

The direct experimental evidence of the formation of MTBE cluster in water is also revealed in the dynamic light scattering (DLS) experiment as shown in Figure 4.3. Figure 4.3a depicts the DLS measurement of water–MTBE mixture. The average hydrodynamics diameter ( $d_H$ ) of the binary mixture at room temperature is about 700 nm (Figure 4.3a), which does not change appreciably (within 5% error range) when the MTBE concentration changes in the mixture. Such a high value of  $d_H$  thus could be argued due to the formation of aggregate structures in the system and corroborates well with the negative value of the  $\Delta_{\text{mix}}H$ . Similar aggregate structures of water molecules in a hydrophobic solvent (dioxane) were reported recently [19, 20]. Figure 4.3b shows the persistence of the droplets up to 70 °C, which is much higher than the boiling point of pure MTBE (55.2 °C). The reduced diameter of the aggregates at higher temperature is very much similar with our previous studies on dioxane–water mixture [20, 21] and could be due to the shading of water molecules from the hydration layer, as has also been observed for micelles [22], vesicles [23] at higher temperature. It is important here to note that the solubility of MTBE decreases with an increase in temperature [2]. Therefore there is a possibility to form a super saturated solution at higher temperatures, which could be in non-equilibrium turbid

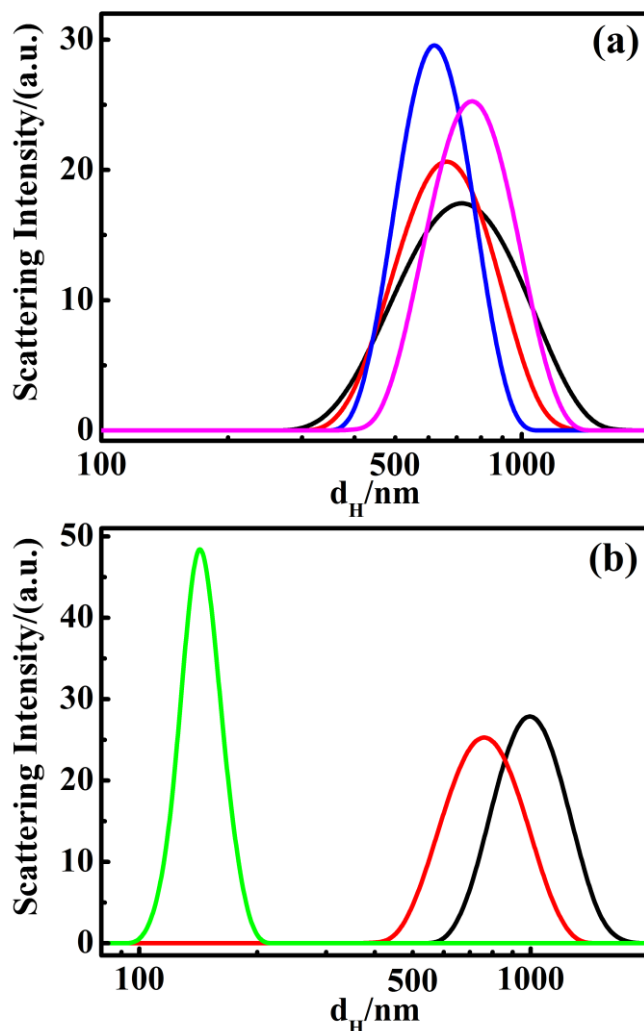


**Figure 4.3:** (a) DLS spectra of water–MTBE mixture at different concentrations of MTBE (black line,  $7.4 \text{ mg ml}^{-1}$ ; red line,  $14.8 \text{ mg ml}^{-1}$ ; blue line,  $29.6 \text{ mg ml}^{-1}$ ; magenta line,  $44.4 \text{ mg ml}^{-1}$ ). (b) Temperature dependent DLS spectra of water–MTBE mixture at highest concentration of MTBE ( $44.4 \text{ mg ml}^{-1}$ ). Black line,  $5 \text{ }^{\circ}\text{C}$ ; red line,  $20 \text{ }^{\circ}\text{C}$  and green line,  $70 \text{ }^{\circ}\text{C}$ .

states. However we could not find any such kind of non-equilibrium turbid states. This may be due to the either phase separation of excess MTBE or due to the vaporization of excess MTBE. The single intense peak at  $70 \text{ }^{\circ}\text{C}$  in our DLS experiment also confirms the absence of any such kind of non-equilibrium turbid states. The formation of micelle-like aggregate [22] of MTBE in the aqueous solution has never been reported in the literature and is a very important consideration for the design of removal strategy of MTBE from the drinking water.

In order to have a better understanding on the interaction mechanism between water and MTBE molecules in the molecular level, we have performed FTIR and Raman measurements. Figure 4.4 shows the FTIR absorption spectra of pure MTBE (Figure 4.4b) and water saturated with MTBE (Figure 4.4a). For pure MTBE the characteristic bands are located at 1021, 1084, 1202, 1232, 1263 and 1365  $\text{cm}^{-1}$ . The peaks at 1084 and 1202  $\text{cm}^{-1}$  are assigned to C-O stretching between the oxygen atom and the carbon atom on the methyl group and the tertiary carbon, respectively [9]. The observed vibrational mode at

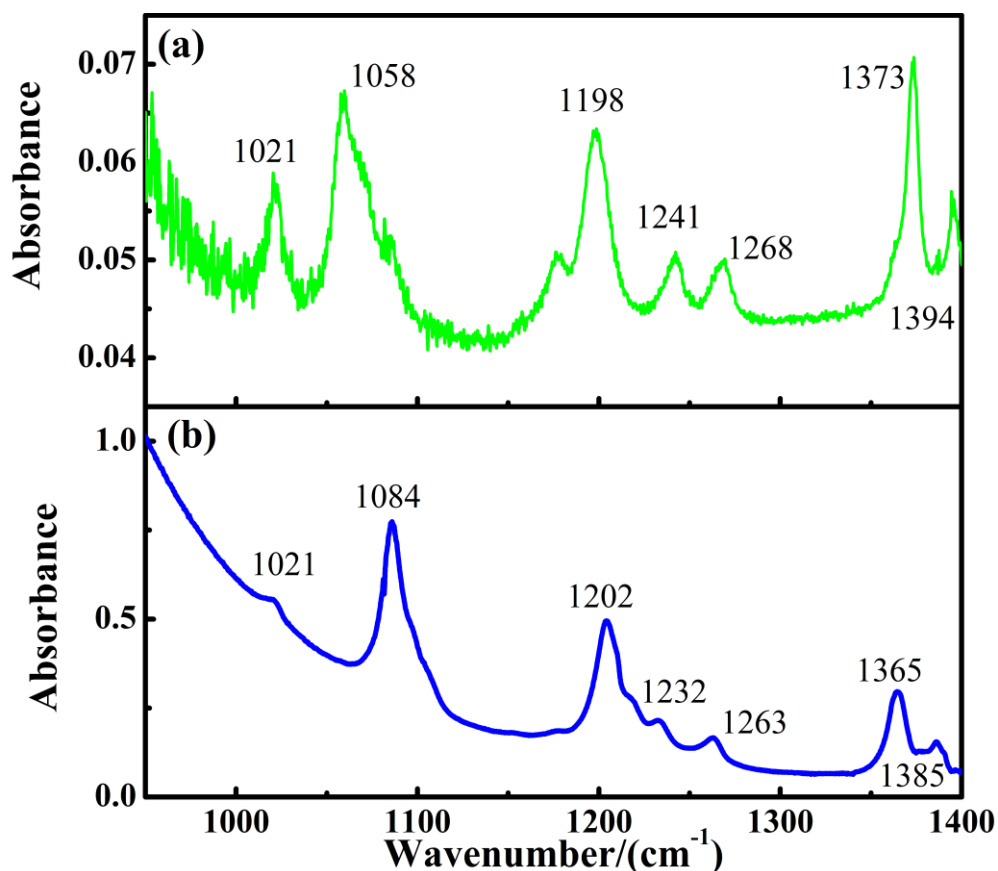
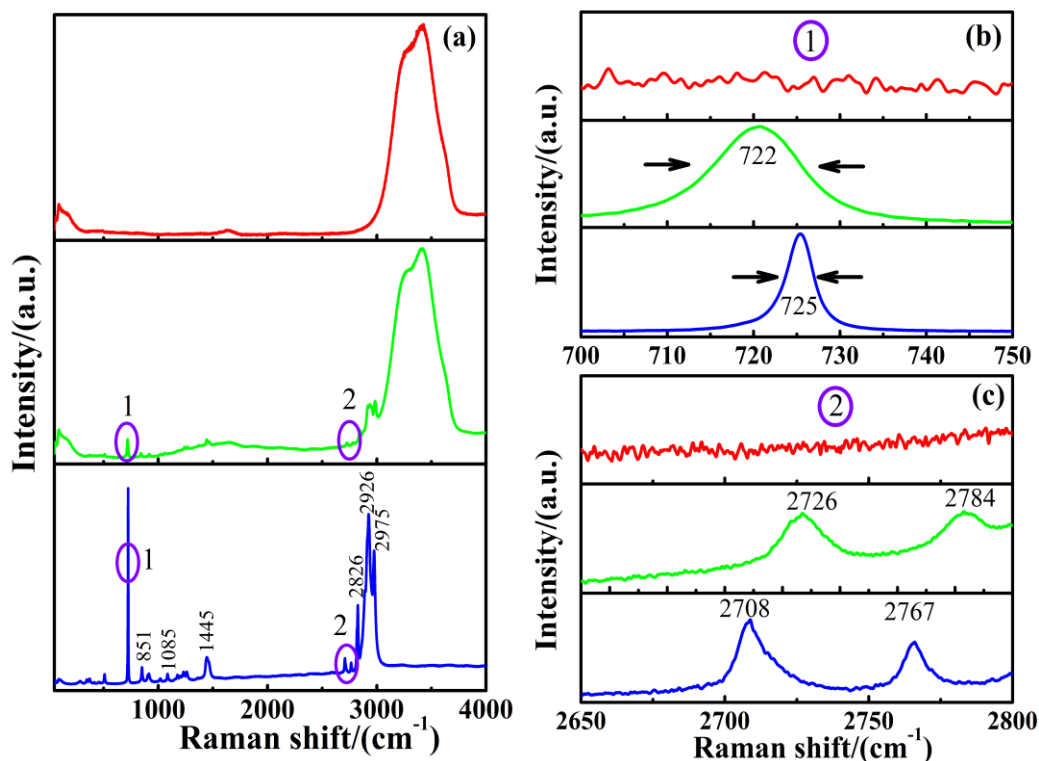


**Figure 4.4:** FTIR spectra of (a) MTBE in water (concentration of MTBE is 44  $\text{mg ml}^{-1}$ ) and (b) pure MTBE. The contribution of water has been subtracted from the FTIR spectra of the solution.

1232  $\text{cm}^{-1}$  is due to C-C asymmetric stretching between tertiary carbon and methyl carbons opposite to the oxygen atom, because they are strongly coupled and essentially inseparable in nature whereas the peak at 1263  $\text{cm}^{-1}$  is assigned to the asymmetric stretching between tertiary carbon and the remaining methyl carbon. The peak at 1021

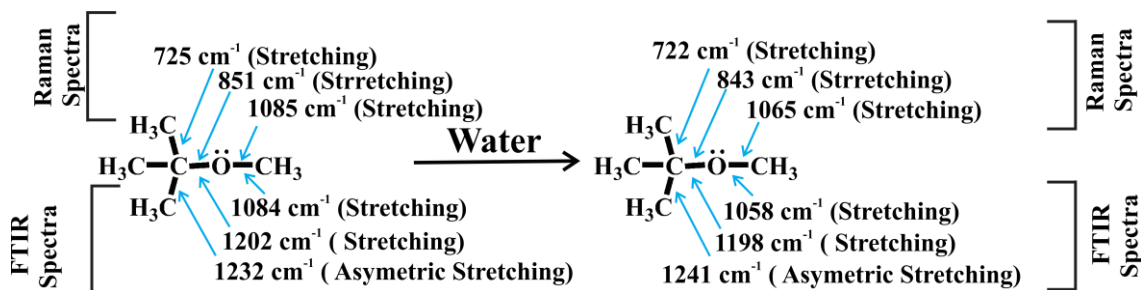
$\text{cm}^{-1}$  is assigned to the  $\text{CH}_3$  rocking vibration and 1365 and 1385  $\text{cm}^{-1}$  peaks are due to splitting of the symmetric umbrella deformation. When water molecules are added to MTBE molecules, the hydrogen atom of the water molecules interacts with the oxygen atom of the MTBE molecule through hydrogen bonding. This hydrogen bond tends to weaken the C-O bond of the MTBE molecule, causing an increase in the C-O bond length. The increase of C-O bond length in turn causes a stronger interaction between C-C atoms in  $-\text{CCH}_3$  group, which leads to the decrease in the C-C bond length compared to that of the bare MTBE molecule. Therefore, a shift in the vibrational frequencies of MTBE molecules due to the presence of water molecule is expected. Figure 4.4a shows the FTIR spectra of MTBE in water. In the presence of water, the peaks of MTBE at 1084 and 1202  $\text{cm}^{-1}$  are shifted to lower frequency (red shift) by 26 and 4  $\text{cm}^{-1}$  respectively due to the weakening of the C-O bond, and the peaks at 1232 and 1263  $\text{cm}^{-1}$  are shifted to a higher frequency (blue shift) by 9 and 5  $\text{cm}^{-1}$  due to the strengthening of the C-C bond compared to bare MTBE spectrum. The umbrella bending of  $-\text{CH}_3$  is also blue shifted by 9  $\text{cm}^{-1}$  whereas the peak due to the rocking vibration of  $\text{CH}_3$  at 1021  $\text{cm}^{-1}$  is not changed in the presence of water, suggesting that hydrogen bond has little effect on the vibrations that are not associated with the backbone of MTBE molecule.

Figure 4.5 shows the Raman spectra of pure MTBE and water–MTBE complex in the frequency range of 50–4000  $\text{cm}^{-1}$ . In pure MTBE the observed vibrational mode at 725  $\text{cm}^{-1}$  is due to the C-C symmetric stretching of tertiary carbon in the *tert*-butyl group [24]. The C-C asymmetric stretching modes of same carbon are observed at 1232 and 1262  $\text{cm}^{-1}$ . The peaks at 851 and 1085  $\text{cm}^{-1}$  are due to C-O stretching of tertiary carbon and the carbon on methyl group, respectively. The modes that are at 1445 and 1018  $\text{cm}^{-1}$  are due to the methyl CH deformation and  $\text{CH}_3$  rocking vibration, respectively. The symmetric and asymmetric C-H stretching modes are observed at 2826, 2915, 2926 and 2975  $\text{cm}^{-1}$ . Two Raman active overtones of the  $\text{CH}_3$  “umbrella” deformation splitting are also observed at 2767 and 2708  $\text{cm}^{-1}$ . In water–MTBE mixture, similar to our FTIR result, the Raman mode due to C-C asymmetric stretching of tertiary carbon at 1232 and 1262  $\text{cm}^{-1}$  are shifted to a higher frequency and modes at 851 and 1085  $\text{cm}^{-1}$ , due to C-O asymmetric stretching of tertiary carbon and the carbon on methyl group are red shifted to 845 and



**Figure 4.5:** (a) Raman spectra of water (upper panel), MTBE (lower panel) and water–MTBE mixture ( $44.4 \text{ mg ml}^{-1}$ ) (middle panel). (b) and (c) are similar spectra of (a) at smaller frequency scale ( $\text{cm}^{-1}$ ) indicated as 1 and 2 respectively.

$1065 \text{ cm}^{-1}$ . Apart from this result, we have found some addition behavior from Raman spectrum. The C-C symmetric stretching of tertiary carbon on methyl group at  $725 \text{ cm}^{-1}$  is red shifted of about  $3 \text{ cm}^{-1}$  and the overtones of the  $\text{CH}_3$  “umbrella” deformation are blue shifted of about  $18 \text{ cm}^{-1}$  respectively as shown in Figure 4.5b and c. Therefore, the Raman



**Scheme 4.1:** Schematic representation showing IR and Raman active bands in pure MTBE and in water–MTBE mixture.

measurements provide a fingerprint of hydrogen bond between hydrogen atom of water molecule and the oxygen atom of the MTBE molecule. Overall FTIR and Raman spectroscopic observations are schematically shown in Scheme 4.1.

The DLS studies followed by the FTIR and Raman spectroscopic data suggest that the micelle-like MTBE micro-droplets in the aqueous solution are in strong interaction (through hydrogen bonding) with the water molecules. Micelles are well known to solubilize organic matters [25] in the core. Given the fact that MTBE forms a similar structure in water–MTBE mixture, one should expect enhanced solubility of other organic molecules in the mixture. To check the enhanced water solubility of relatively insoluble organic pollutants by dissolved organic matter (DOM), we have investigated the co-solubilization of some model organic matters (pollutants) like anthracene [26, 27], naphthalene [28], benzo[ $\alpha$ ]pyrene [29], and DCM [30] by absorption spectroscopic

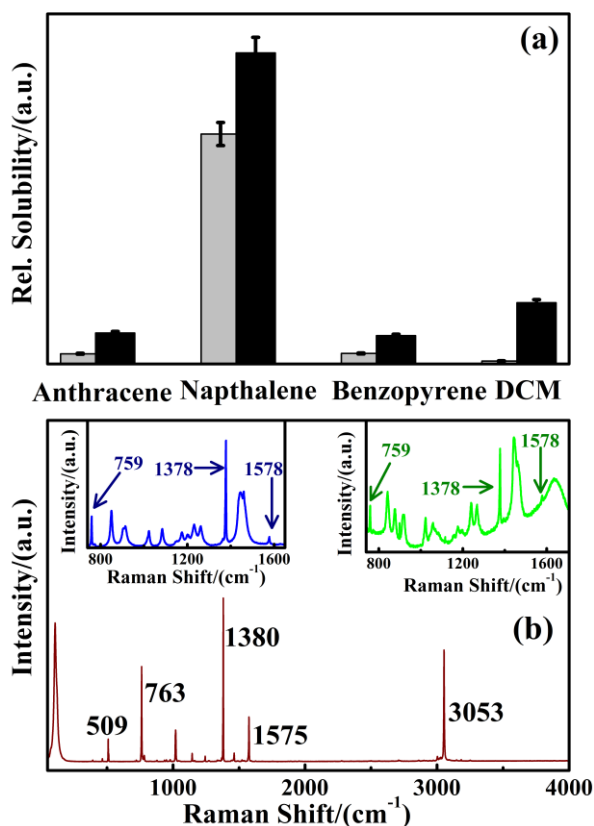


**Figure 4.6:** (a) Relative solubility of model hydrophobic organic pollutant in water (gray box) and water–MTBE mixture ( $44.4 \text{ mg ml}^{-1}$ ) (black box) with standard error of  $\sim 5\%$ . (b) Raman spectrum of solid naphthalene. Inset shows the Raman spectra of naphthalene in pure MTBE (left) and water MTBE mixture ( $44.4 \text{ mg ml}^{-1}$ ) (right).

measurements. It has to be noted here that anthracene, naphthalene and benzo[ $\alpha$ ]pyrene are the organic pollutants, which are the product of incomplete combustion of the fuel. Figure 4.6a (top) shows the relative water solubilities of the pollutant in water and saturated solution of MTBE in water ( $44.4 \text{ mg ml}^{-1}$ ). A comparison of the results from Figure 4.6a indicates that MTBE effectively enhances the water solubility of the organic pollutants in the presence of MTBE. The enhancement of solubility of the hydrophobic solute in the presence of MTBE is also confirmed by Raman spectroscopy of one of the organic matters that is naphthalene in water–MTBE mixture. Figure 4.6b shows the Raman spectrum of solid naphthalene. The intense bands observed at  $509$ ,  $763$ ,  $1380$ ,  $1575$  and  $3053 \text{ cm}^{-1}$  are attributed to  $-\text{C-C-C}-$  bending; radial breathing mode; C-C stretching and ring deformation; and in phase C=C stretching and out of phase C-H stretching, respectively [31]. When naphthalene is dissolved in MTBE, these intense peaks are shifted to of about  $2\text{--}4 \text{ cm}^{-1}$  (left inset of Figure 4.6b) showing the interaction of naphthalene with MTBE. However, in water–MTBE mixtures the peaks are not shifted which reveal the presence of naphthalene in the MTBE core. The study thus explores another fatal consequence of MTBE contamination in water, which enhances the solubilization of other hydrophobic organic pollutants in water making contaminated water more polluted.

From the above investigation, it is clear that organic pollutants essentially co-solubilize in the micelle-like hydrophobic core of the MTBE in the aqueous solution. Picosecond-resolved studies on an model organic matter 4-(dicyanomethylene)-2-methyl-6-(*p*-dimethylaminostyryl)-4H-pyran (DCM), which is reported to be mutagenic in nature [30] and well known water-insoluble spectroscopic probe [32-34] is expected to unravel the localization of DCM in the MTBE-water mixture. The emission spectra of DCM in pure MTBE, a relatively polar solvent (methanol) and in the binary mixture are shown in Figure 4.7a and b respectively. In the cluster of the binary mixture solution (Figure 4.7b), there are two possible locations of the probe (DCM), e.g., inner hydrophobic core of MTBE cluster or its surface. However, in the hydrophobic core the emission maximum is expected to be similar to that of pure MTBE which is not the case here, rather similar to that on the micellar surface [35]. Another observation is the vivid lengthening of excited state lifetime of DCM in the binary mixture compared to that in pure MTBE. The lifetime

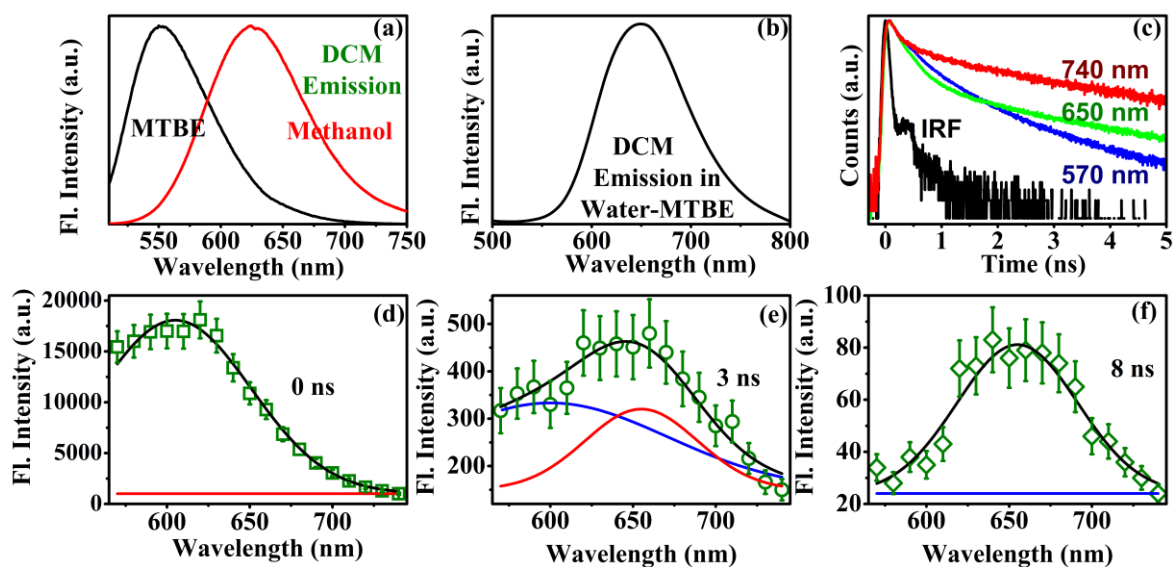


**Figure 4.7:** (a) The steady state emission spectra of DCM in MTBE (black line) and in methanol (red line). (b) Emission spectrum of DCM in water–MTBE mixture ( $44.4 \text{ mg ml}^{-1}$ ). (c) Fluorescence decay transients of DCM in water–MTBE mixture at different emission wavelengths. Black line, instrument response function (IRF); red line, 740 nm; green line 650 nm and blue line, 570 nm. Time gated fluorescence spectra of DCM in water–MTBE mixture at different time intervals 0 ns, (d); 3 ns (e) and 8 ns (f) with standard error of  $\sim 10\%$ . Blue and red lines are the de-convolution spectra showing the presence of DCM in multiple environments.

of DCM in MTBE is found to be less than 100 ps, which is close to the IRF of our instrument and evidently much shorter than that in the binary mixture (Figure 4.7c). The three characteristic fluorescence transients detected at different wavelengths of the DCM emission spectrum in the mixture are shown in Figure 4.7c. We have measured the fluorescence lifetime of DCM in the mixture at different wavelengths across the entire emission spectrum and tabulated in Table 4.4. Figure 4.7d–f shows the time-gated fluorescence emission spectrum of DCM in binary mixture. At around  $t = 0 \text{ ns}$ , DCM shows that emission maximum is around 605 nm and a faster decay profile reveals a distribution of the probe molecules in a non-polar environment. As the time goes, the excited DCM molecules in the non-polar environment come to ground state with their faster lifetime and survive in the relatively polar region (surface of MTBE cluster). In particular, the emission spectrum at 3 ns can be de-convoluted into two distinct spectra peaking at 605 nm (less-polar) and 655 nm (polar). Eventually, at 8 ns the emission spectrum essentially shows one peak at 655 nm (polar). The picosecond studies thus

**Table 4.4: The fluorescence lifetimes ( $\tau_i$ ) and the relative weight percentage of the time component ( $a_i$ ) of DCM in saturated solution of MTBE in water with a standard error of ~5%.**

Wavelength (nm)	$a_1$	$\tau_1$ (ns)	$a_2$	$\tau_2$ (ns)	$a_3$	$\tau_3$ (ns)
560	57	0.159	35	0.447	8	1.193
570	57	0.154	33	0.383	10	1.135
580	48	0.135	42	0.307	10	1.109
590	46	0.124	46	0.288	8	1.174
600	30	0.08	62	0.242	8	1.162
610	35	0.0292	59	0.246	6	1.275
620	36	0.094	59	0.239	5	1.437
630	32	0.074	63	0.223	5	1.551
640	31	0.085	64	0.223	5	1.721
650	28	0.07	66	0.214	6	1.809
660	29	0.08	65	0.216	6	1.931
670	30	0.06	63	0.207	7	1.983
680	29	0.066	63	0.207	8	2.046
690	30	0.061	61	0.206	9	2.157
700	25	0.069	66	0.206	9	2.143
710	36	0.086	52	0.218	12	2.209
720	39	0.095	46	0.23	15	2.188
730	67	0.133	18	0.332	15	2.36
740	73	0.133	12	0.644	15	2.806

confirm the localization of the DCM molecules in the heterogeneous environments of micelle like MTBE cluster in water. Our observation also reveals that majority of the DCM population in the ground state (in the absence of light to the spectrum at  $t = 0$ ) prefer to stay in the non-polar core of the MTBE cluster, which is well described in our recent study [36].

Finally, we study the eco-toxicity of the MTBE-contaminated water on the mortality of a model microorganism (yeast) in light of the mode of action. Microorganisms respond to potentially hazardous organics at various biochemical and physiological levels and their growth rate is diminished to a degree depending on the concentration of the toxic compound(s). However, few studies on MTBE-induced ecotoxicity in vitro can be consulted. Previous ecotoxic effects of MTBE in the model organism *Pseudomonas putida* KT2440 showed that MTBE-concentration of 25.8 mg ml<sup>-1</sup> (293 mM) is sufficient to kill 50% of the cells within 10 min [37]. In the present study the result of the cytotoxicity assay

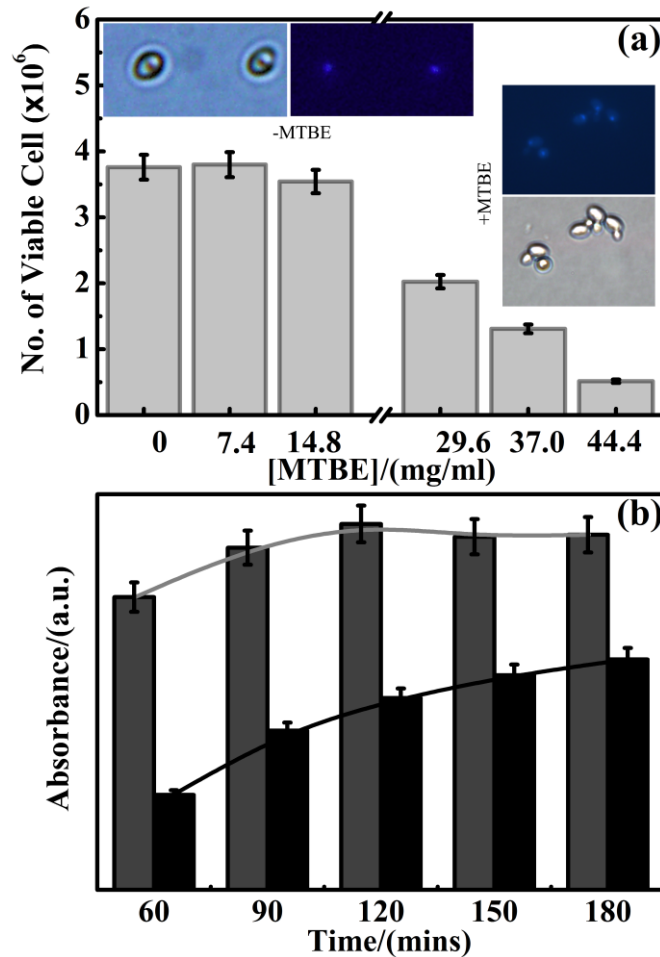


**Figure 4.8:** (a) Effect of MTBE on yeast cell viability at different MTBE concentrations. Inset shows both bright-field and fluorescence micrographic images of DAPI stained yeast cell nucleus upon treatment with MTBE along with the control sets. (b) Time dependent MTT based cytotoxicity assay for the yeast cells in absence (gray box) and presence of MTBE (black box). The standard error of the experiment is about of 5%.

is presented in Figure 4.8a. Incubation of yeast cells for 3 h with MTBE at a higher dose level ( $>29.6 \text{ mg ml}^{-1}$ ) shows a decrease in cell viability compared to control. The results of this study clearly indicate that MTBE metabolism has a relationship with the MTBE concentration and at higher dose levels ( $29.6$  to  $44.4 \text{ mg ml}^{-1}$ ) MTBE has direct toxic effects on yeast cells. The metabolic toxicity of MTBE to yeast cell is also evident in the time dependent MTT assay (Figure 4.8b), where the MTBE treated yeast cells show reduced production of formazan compared to the control set. In order to find out whether MTBE cytotoxicity has any influence on yeast cell nucleus we stain the MTBE ( $44.4 \text{ mg ml}^{-1}$ ) treated yeast cell nucleus with DAPI. However, no observable damage of the cell

nucleus is noticeable compared to the control experiment (Figure 4.8). Although the concentrations used for this experiment is much higher than the concentrations measured in contaminated sites, our studies clearly reveal that metabolic disturbance of yeast by MTBE is a mode of action in the environment.

### **4.3. Conclusion:**

In the present study, we have investigated the interactions between methyl *tert*-butyl ether (MTBE) and water. The thermodynamic quantity like enthalpy of mixing ( $\Delta_{\text{mix}}H$ ) indicates the non-ideal mixing of MTBE with water. The negative value of the excess molar volumes and positive value of viscosity and refractive index deviations support interaction occurring through hydrogen bonding, which is also confirmed from FTIR and Raman spectra. The water solubility study of model hydrophobic organic pollutants in the presence of MTBE shows the enhanced magnitude of water pollution. Finally, the MTBE induced aquatic ecotoxicity shows that metabolic disturbance of yeast by MTBE is a mode of action in the environment and not the morphology change.

## References

- [1] C.T. Chiou, R.L. Malcolm, T.I. Brinton, D.E. Kile, Water solubility enhancement of some organic pollutants and pesticides by dissolved humic and fulvic acids, *Environ. Sci. Technol.* 20 (1986) 502.
- [2] R.M. Stephenson, Mutual solubilities: Water-ketones, water-ethers, and water-gasoline-alcohols, *J. Chem. Eng. Data* 37 (1992) 80.
- [3] B.G. Bierwagen, A.A. Keller, Measurement of Henry's law constant for methyl tert-butyl ether using solid-phase microextraction, *Environ. Toxicol. Chem.* 20 (2001) 1625.
- [4] A. Fischer, M. Müller, J. Klasmeier, Determination of Henry's law constant for methyl tert-butyl ether (MTBE) at groundwater temperatures, *Chemosphere* 54 (2004) 689.
- [5] R.D. Barreto, K.A. Gray, K. Anders, Photocatalytic degradation of methyl-tert-butyl ether in TiO<sub>2</sub> slurries: A proposed reaction scheme, *Water Res.* 29 (1995) 1243.
- [6] M.M. Chan, R. Lynch, Photocatalytic degradation of aqueous methyl-tert-butyl-ether (MTBE) in a supported-catalyst reactor, *Environ. Chem. Lett.* 1 (2003) 157.
- [7] A.K. Boulamanti, C.J. Philippopoulos, Photocatalytic degradation of methyl tert-butyl ether in the gas-phase: A kinetic study, *J. Hazard. Mat.* 160 (2008) 83.
- [8] T.B. Nielsen, S. Hvidt, S.R. Keiding, C. Petersen, P. Westh, K. Keiding, Thermodynamic investigations of methyl tert-butyl ether and water mixtures, *Phys. Chem. Chem. Phys.* 13 (2011) 1182.
- [9] Z. Li, S. Singh, FTIR and Ab Initio investigations of the MTBE–water complex, *J. Phys. Chem. A* 112 (2008) 8593.
- [10] S. Rakshit, R. Saha, A. Singha, Z.S.A. Seddigi, S.K. Pal, Molecular interaction, co-solubilization of organic pollutants and ecotoxicity of a potential carcinogenic fuel additive MTBE in water, *J. Mol. Liq.* 180 (2013) 235.
- [11] L. Morávková, Z. Wagner, J. Linek, Volumetric behaviour of binary liquid systems composed of toluene, isooctane, and methyl tert-butyl ether at temperatures from (298.15 to 328.15) K, *J. Chem. Thermodyn.* 41 (2009) 591.
- [12] L. Morávková, Z. Wagner, Z. Sedláková, J. Linek, Volumetric behaviour of the ternary liquid system composed of methyl tert-butyl ether, toluene, and isooctane at

temperatures from (298.15 to 328.15) K: Experimental data and correlation, *J. Chem. Thermodyn.* 42 (2010) 920.

[13] S. Paul, A.K. Panda, Physicochemical investigations on the aqueous solution of an ionic liquid, 1-butyl-3-methylimidazolium methanesulfonate, [bmim][MS], in a concentrated and dilute regime, *Colloids Surf., A* 404 (2012) 1.

[14] G.M. Xu, X.X. Li, Y.J. Hu, Y.W. Wang, G.C. Fan, M. Zhang, Density and viscosity of the binary mixture of triethylene glycol monoethyl ether + water from (293.15 to 333.15) K at atmospheric pressure, *J. Chem. Eng. Data* 55 (2009) 2345.

[15] S.S. Dhondge, C.P. Pandhurnekar, D.V. Parwate, Density, speed of sound, and refractive index of aqueous binary mixtures of some glycol ethers at T = 298.15 K, *J. Chem. Eng. Data* 55 (2010) 3962.

[16] P. Boonme, K. Krauel, A. Graf, T. Rades, V.B. Junyaprasert, Characterization of microemulsion structures in the pseudoternary phase diagram of isopropyl palmitate/water/Brij 97 : 1-butanol, *AAPS Pharmscitech* 7 (2006).

[17] E.S. Domalski, E.D. Hearing, Heat capacities and entropies of organic compounds in the condensed phase, vol 3, *J. Phys. Chem. Ref. Data* 25 (1996) 1.

[18] U.S. Rai, R.N. Rai, Physical chemistry of organic eutectic and monotectic: Hexamethylbenzene–succinonitrile system, *Chem. Mater.* 11 (1999) 3031.

[19] C. Yang, W. Li, C. Wu, Laser light-scattering study of solution dynamics of water/cycloether mixtures, *J. Phys. Chem. B* 108 (2004) 11866.

[20] S. Rakshit, R. Saha, P.K. Verma, S.K. Pal, Role of solvation dynamics in excited state proton transfer of 1-naphthol in nanoscopic water clusters formed in a hydrophobic solvent, *Photochem. Photobiol.* 88 (2012) 851.

[21] R.K. Mitra, P.K. Verma, S.K. Pal, Exploration of the dynamical evolution and the associated energetics of water nanoclusters formed in a hydrophobic solvent, *J. Phys. Chem. B* 113 (2009) 4744.

[22] R.K. Mitra, S.S. Sinha, S.K. Pal, Temperature dependent hydration at micellar surface: Activation energy barrier crossing model revisited, *J. Phys. Chem. B* 111 (2007) 7577.

- [23] R. Saha, P.K. Verma, R.K. Mitra, S.K. Pal, Structural and dynamical characterization of unilamellar AOT vesicles in aqueous solutions and their efficacy as potential drug delivery vehicle, *Colloids Surf., B* 88 (2011) 345.
- [24] J.B. Cooper, K.L. Wise, W.T. Welch, R.R. Bledsoe, M.B. Sumner, Determination of weight percent oxygen in commercial gasoline: A comparison between FT-Raman, FT-IR, and dispersive near-IR spectroscopies, *Appl. Spectrosc.* 50 (1996) 917.
- [25] D.E. Kile, C.T. Chiou, Water solubility enhancements of DDT and trichlorobenzene by some surfactants below and above the critical micelle concentration, *Environ. Sci. Technol.* 23 (1989) 832.
- [26] J.T. Oris, J.P. Giesy Jr, The photoenhanced toxicity of anthracene to juvenile sunfish (*Lepomis* spp.), *Aquat. Toxicol.* 6 (1985) 133.
- [27] J.T. Oris, J.P. Giesy, P.M. Allred, D.F. Grant, P.F. Landrum, Photoinduced toxicity of anthracene in aquatic organisms: An environmental perspective, Elsevier, 1984.
- [28] T. Valaes, S.A. Doxiadis, P. Fessas, Acute hemolysis due to naphthalene inhalation, *J. Pediatr.* 63 (1963) 904.
- [29] M.F. Denissenko, A. Pao, M.S. Tang, G.P. Pfeifer, Preferential formation of benzo[a]pyrene adducts at lung cancer mutational hotspots in P53, *Science* 274 (1996) 430.
- [30] B.J.Y. Wuebbles, J.S. Felton, Evaluation of laser dye mutagenicity using the ames/salmonella microsome test, *Environ. Mutag.* 7 (1985) 511.
- [31] A. Srivastava, V.B. Singh, Theoretical and experimental studies of vibrational spectra of naphthalene and its cation, *Indian J. Pure Appl. Phys.* 45 (2007) 714.
- [32] H. Zhang, A.M. Jonkman, P. van der Meulen, M. Glasbeek, Femtosecond studies of charge separation in phot-excited DCM in liquid solution, *Chem. Phys. Lett.* 224 (1994) 551.
- [33] P. van der Meulen, H. Zhang, A.M. Jonkman, M. Glasbeek, Subpicosecond solvation relaxation of 4-(dicyanomethylene)-2-methyl-6-(p-(dimethylamino)styryl)-4H-pyran in polar liquids, *J. Phys. Chem.* 100 (1996) 5367.
- [34] S.K. Pal, D. Sukul, D. Mandal, S. Sen, K. Bhattacharyya, Solvation dynamics of DCM in micelles, *Chem. Phys. Lett.* 327 (2000) 91.

- [35] R. Sarkar, A.K. Shaw, M. Ghosh, S.K. Pal, Ultrafast photoinduced deligation and ligation dynamics: DCM in micelle and micelle-enzyme complex, *J. Photochem. Photobiol. B* 83 (2006) 213.
- [36] S.K. Pal, A.H. Zewail, Dynamics of water in biological recognition, *Chem. Rev.* 104 (2004) 2099.
- [37] M. Krayl, D. Benndorf, N. Loffhagen, W. Babel, Use of proteomics and physiological characteristics to elucidate ecotoxic effects of methyl tert-butyl ether in *Pseudomonas putida* KT2440, *Proteomics* 3 (2003) 1544.

# Chapter 5

## Studies on Structure, Dynamics and Energetics of Water in Hydrophobic Environments

### 5.1. Introduction:

Segregation of nonpolar molecules from water is commonly known as the hydrophobic effect [1] and is the key to many biological processes [2-4], including protein folding, formation of various self-assemblies (like lipid bilayers), molecular recognition, etc. However, the hydrophobic interaction imposed by a biomolecule on water is quite complex, and so forth to the presence of variety of polar and nonpolar side chains [5]. The range of possible interactions is too vast even for experimental studies that simple organic model systems are usually chosen as an alternative. To this end, great efforts have been directed toward understanding the interactions of water with organic molecules. Especially the organic molecule that contains a hydrophobic backbone along with the hydrophilic group is a good prototype for studying the chemical heterogeneity, without the additional effect of topological disorder, typical of protein surfaces. Notably, in all these systems, the hydrophobic interaction seems to cause clustering of water molecules [6] or hydrophobic unit [7, 8] in respective solvents. Therefore, such systems provide a rare opportunity for studying the effect of hydrophobic interaction on water molecules, which also mimics the isolated buried water present in biological systems such as the protein interior [9-11]. Hence, there are numerous experimental and theoretical studies regarding the organic–water molecular complexes. Infrared spectroscopic studies have been conducted to elucidate the perturbation of hydrogen bonding network of water molecules in presence of nonpolar organic solvents [12-16]. Various studies have been undertaken on the dynamics of such isolated water molecules to see how the translational and rotational dynamics of water molecules changes, by changing the global structural rearrangement of the hydrogen bond network [17-22]. In spite of all these experimental and theoretical works, the effect of hydrophobic interaction on water structures is not clear enough as the

solvents so far used are less hydrophobic, for example, methanol, acetonitrile, dimethyl formamide (DMF), and so forth.

For better understanding, an organic solvent having hydrophobicity similar to the protein interior should be chosen. Methyl *tert*-butyl ether (MTBE) is an example of such a solvent having a bulky hydrophobic *tert*-butyl group, along with a less polar C–O bond. The choice of MTBE also lies in the fact that the molecule is the most common gasoline oxygenate and has become a widespread contaminant in surface water and groundwater [23-29] due to its high water solubility (44 g L<sup>-1</sup> at 20 °C). The presence of MTBE in drinking water and groundwater resources causes different physical hazards. Moreover, there is also evidence that MTBE is a possible human carcinogen [30]. Thus, it is very important to investigate the water–MTBE molecular complexes in considerable detail. Recently, Nielsen et al. [31] studied the interactions between water and MTBE from a thermodynamic point of view. Li and Singh [32] have investigated the interaction of water–MTBE complexes using Fourier transform infrared (FTIR) spectroscopy and ab initio calculations. All these studies suggest that complexation of MTBE with water occurs through hydrogen bonding, and essentially focus on the effect of hydrogen bonding on the MTBE moiety. In spite of all these efforts, our understanding about the changes in the hydrogen bonding network of water moieties under the hydrophobic interaction of MTBE is still limited and requires more detailed investigations. In the present study, we explore the structural and dynamical characterization of water molecules in both water/MTBE and MTBE/water binary systems. We have used dynamic light scattering (DLS) techniques to determine the size of the clusters being formed in respective solvents. The changes in O–H stretching frequency of water, induced by MTBE have been examined using FTIR measurements. Femtosecond resolved fluorescence upconversion technique has been explored to understand the ultrafast internal motions of water molecules. The diffusive translational motion of the water molecules has been revealed using picosecond-resolved time correlated single photon counting (TCSPC) method. Temperature dependent solvation dynamics of water have been studied to understand the energetics of the hydrogen bond network in the clusters. Attempt has also been made to correlate the experimental findings with theoretical estimations. Using detailed ab initio calculations at the MP2 level, we predict the possible lowest energy structures, and corresponding energies and

thermodynamic parameters of different MTBE–water molecular complexes. Finally, to correlate the dynamics of water with its reactivity, we have measured solvolysis kinetics of benzoyl chloride (BzCl) in a typical water/MTBE system, at various temperature values.

## 5.2. Results and Discussion:

### 5.2.1. Effect of Hydrophobic Interaction on Structure, Dynamics and Reactivity of Water [33]:

**5.2.1.1. MTBE in Water (MTBE/Water):** It is known that organic molecules tend to form clusters when solubilized in water [34]. To reveal the microscopic behavior of MTBE/water binary system, DLS experiments have been carried out. Figure 5.1a shows

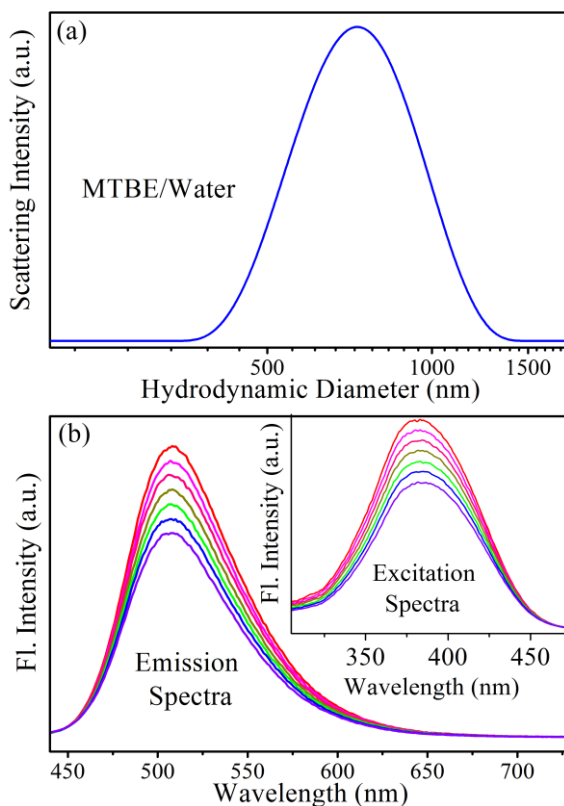


**Figure 5.1:** (a) DLS spectrum of MTBE/water mixture at MTBE concentration of 60  $\mu\text{L/mL}$  (v/v). (b) Normalized emission spectra ( $\lambda_{\text{ex}} = 375 \text{ nm}$ ) of C500 in MTBE/water system with different MTBE concentrations (0, 10, 20, 30, 40, 50, 60  $\mu\text{L/mL}$ ). Corresponding normalized excitation spectra ( $\lambda_{\text{em}} = 510 \text{ nm}$ ) is shown in the inset. (Both the excitation and emission spectra of C500 in different MTBE concentrations are conveniently normalized to show the insignificant change in the respective peak positions.)

the DLS signals of the MTBE/water system (60  $\mu\text{L}/\text{mL}$ , v/v), at room temperature with the cluster size being 800 nm. It can be emphasized here that the distribution profile is unimodal in both intensity ( $\propto d^6$ ) distribution as well as in volume ( $\propto d^3$ ) distribution profile (d being the diameter of the clusters) with relatively low ( $\sim 0.3$ ) polydispersity index (PDI), suggesting the existence of aggregates of uniform sizes. The high value of hydrodynamic diameter ( $d_H$ ) could be argued due to the formation of micelle-like aggregate structures in water [8], and offers a unique opportunity to investigate the effect of hydrophobic interactions on the dynamic behavior of water, quite significant with respect to the *in vivo* cellular environment. The formation of the micelle-like clusters of MTBE in water is also supported by thermochemical studies of the binary eutectic melt of the system using DSC measurement [35]. The negative enthalpy of mixing ( $\Delta_{\text{mix}}H = -1.2 \text{ kJ mol}^{-1}$ ) for the MTBE/water system suggests the clustering of MTBE molecules in the eutectic melt of the binary system [35].

To probe the dynamics of the water molecules in the microenvironment of the clusters, coumarin 500 (C500) is used as a solvation probe. C500 is sparingly soluble in water and shows a large solvatochromic effect (solvation) in polar and nonpolar medium [22, 36]. Figure 5.1b depicts the steady-state excitation (inset) and emission spectra of C500 in different concentrations of MTBE. It is important to note that, in pure MTBE, the emission peak of C500 is at ca. 450 nm (Figure 5.5), and it is red-shifted to 515 nm in bulk water. The observed red shift in the peak position of C500 to ca. 508 nm in the MTBE/water system compared to that in bulk MTBE suggests that C500 resides at the highly restricted polar environment of MTBE–water interface projecting more toward bulk water. Consequently, the observed insignificant change in the excitation and emission peak positions of C500 (Figure 5.1b) with varying MTBE concentrations suggests the essential location of the probe at the water–MTBE interface in all the studied concentrations of MTBE.

The probe C500 has previously been used to report the solvation dynamics of water in various restricted environments [7, 22, 36, 37]. In the present study, we investigate the dynamics of water molecules in the micelle-like clusters of MTBE/water binary mixture

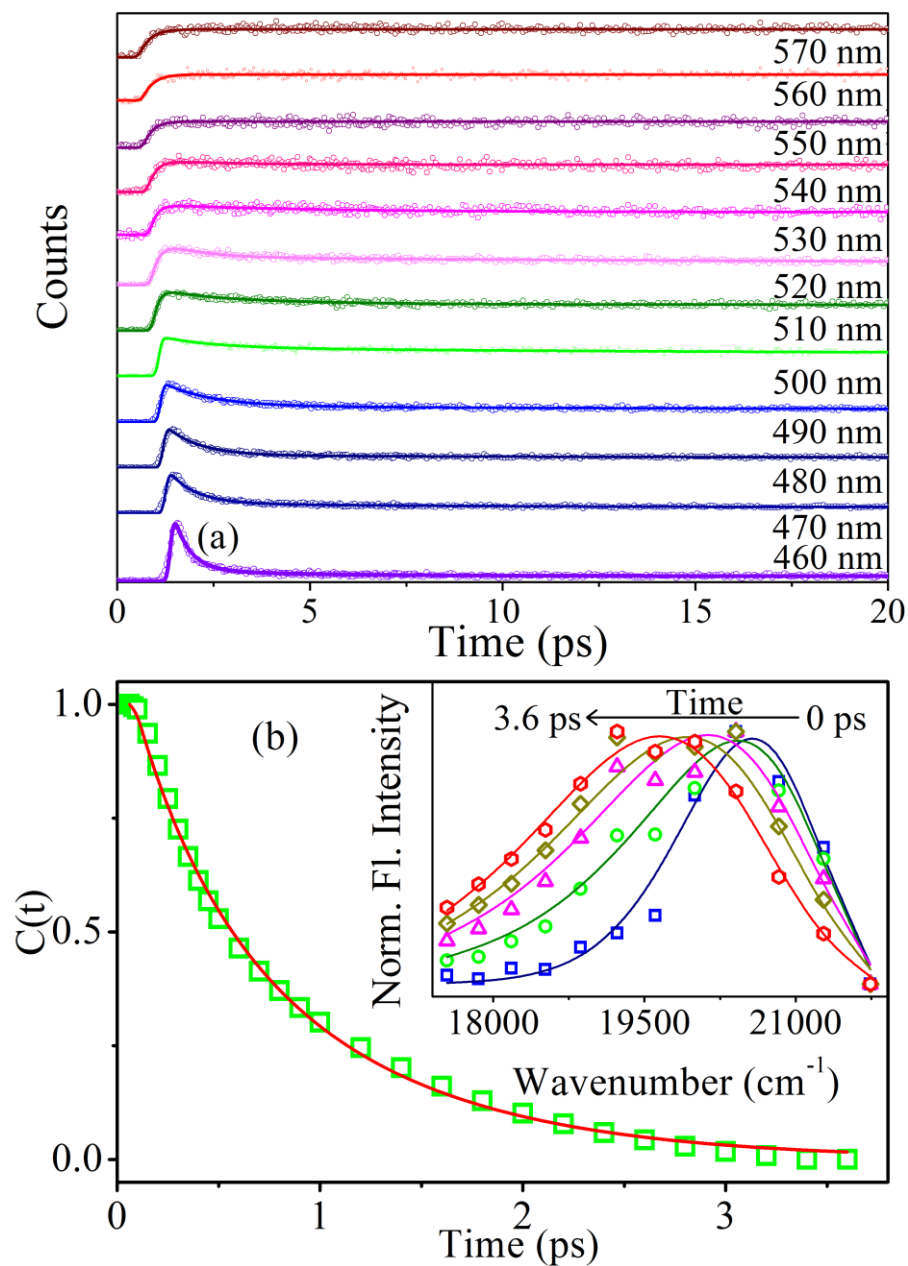


**Figure 5.2:** (a) Femtosecond-resolved fluorescence transients ( $\lambda_{ex} = 385 \text{ nm}$ ) of C500 at different detection wavelengths in MTBE/water mixture with MTBE concentration  $60 \mu\text{L/mL}$ . (b) Solvation correlation function,  $C(t)$ , of C500 in MTBE/water mixture with MTBE concentration of  $60 \mu\text{L/mL}$ . Corresponding TRES in MTBE/ water mixture are shown in the inset.

using C500 as a solvation probe. Figure 5.2a depicts the femtosecond-resolved fluorescence decay transients of C500 in a MTBE/water mixture ( $60 \mu\text{L/mL}$ , v/v). At the blue end of the spectrum (460 nm), the signal decays with time constants of 410 fs (84%), 3 ps (9%), and 3700 ps (7%), and at the red end (570 nm) the transient rises in 280 fs (49%) with subsequent decay in 3700 ps (51%). The initial femtosecond decay at the blue

side and the rise at the red side dominantly result from solvation stabilization processes [37-40], which is associated with the spectral shift of  $926 \text{ cm}^{-1}$  in the 3.6 ps window (Figure 5.2b, inset). Following TRES, we construct the solvent correlation function,  $C(t)$ , to obtain the solvation time,  $\langle \tau_s \rangle (= \sum_i a_i \tau_i)$ , as shown in Figure 5.2b. The temporal decay of  $C(t)$  (Table 5.1) shows biexponential decay with time constants ( $\tau_i$ ) of 322 and 920 fs. Femtosecond-resolved studies by Maroncelli et al. [41] and Barbara et al. [42] reveal that the solvation response of bulk water is bimodal revealing a fast inertial response indicating librational motion and a slower diffusional motion. In a recent study from our group, we have explored the nature of solvation dynamics of bulk water (C500 as fluorescent probe) with time constants 330 and 710 fs [37]. Thus, femtosecond-resolved fluorescence upconversion study of C500 in the MTBE/water system suggests the dynamic behavior of water to be quite similar to that of the bulk water.

**Table 5.1: Femtosecond-resolved solvent correlation function time scales for C500 in MTBE/water ([MTBE] = 60  $\mu\text{l/ml}$ ) water/MTBE ([water] = 5  $\mu\text{l/ml}$ ) mixtures.**

System	$a_1$	$\tau_1$ (ps)	$a_2$	$\tau_2$ (ps)	$\langle \tau_s \rangle$ (ps)
MTBE/Water	0.28	0.32	0.72	0.92	0.75
Water/MTBE	0.74	0.20	0.26	4.03	1.20

To quantify the energetics associated to the interaction process, we calculate the free energy change ( $\Delta G^\ddagger$ ) using the Eyring equation [43],

$$k = \frac{1}{\langle \tau_s \rangle} = \left( \frac{k_B T}{h} \right) \exp\left( \frac{-\Delta G^\ddagger}{RT} \right) \quad (5-1)$$

where  $k_B$  the Boltzmann constant,  $h$  Plank's constant, and  $k$  the rate constant at temperature  $T$ . From our previous results of femtosecond dynamics of bulk water [37], we calculate the Gibbs free energy of solvation to be  $\sim 750 \text{ cal mol}^{-1}$ . However, inclusion of MTBE molecules into water increases the free energy change of the system to  $\sim 900 \text{ cal mol}^{-1}$ , and is due to the possible perturbation of hydrogen-bonding network of water molecules by the MTBE induced interactions.

To further investigate the genesis of the interaction, ab initio calculations have been performed for MTBE-water complexes. We consider simple model systems, where with one MTBE molecule,  $n$  number of water molecules, can interact such that  $\text{MTBE} + n\text{H}_2\text{O}$

→ MTBE/(water)<sub>n</sub>, where n = 1, 2, 3, and so forth. Based on our computation results, it is found that addition of third water molecule does not affect the number of hydrogen bonds in the MTBE-(H<sub>2</sub>O)<sub>2</sub> complex; that is, a third water molecule does not impose any effective contribution to the hydrogen bonding network between MTBE and water. Accordingly, we focus on the hydrogen bonding interaction within MTBE/(water)<sub>n</sub> complexes with n = 1, 2.

**Table 5.2: Calculated energy parameters of MTBE-water complexes at MP2/6-31g level.**

<i>Systems</i>	$\Delta E_{bsse+zpc}$ (kcal mole <sup>-1</sup> )	$\Delta G$ (cal mole <sup>-1</sup> )	$\Delta H$ (kcal mole <sup>-1</sup> )
<i>MTBE/(Water)<sub>1</sub></i>	3.0	439	-8.00
<i>MTBE/(Water)<sub>2</sub></i>	6.5	753	-17.00
<i>Water/(MTBE)<sub>2</sub></i>	5.0	2700	-12.55

We first choose water dimer, the benchmark system for hydrogen bonding study, and calculate the energy parameters associated with hydrogen bonding at the MP2/6-31g level. We find the binding energy ( $\Delta E$ ) and enthalpy ( $\Delta H$ ) of dimerization to be  $\sim 4$  and  $\sim -6$  kcal mol<sup>-1</sup>, respectively, which are similar to the previously estimated experimental/theoretical values [44-46]. The close agreement of the experimental and calculated results for the water dimer leads us to estimate the energy parameters for MTBE-water complexes at the same level. Distinct energy parameters for different MTBE-water complexes are shown in Table 5.2. When one water molecule is added to MTBE, one of the hydrogen atoms within the water molecule interacts with oxygen atom of MTBE, by forming a hydrogen bond (O2...H20) with a bond length of 1.84 Å (Figure 5.3). Computed  $\Delta E$  for MTBE/(water)<sub>1</sub> complex is  $\sim 3$  kcal mol<sup>-1</sup>, which is quite close to hydrogen bond energy of water. When two water molecules are added to MTBE molecule, MTBE/(H<sub>2</sub>O)<sub>2</sub> is formed. As shown in Figure 5.3, there is a possibility of formation of three hydrogen bonds in this complex. Both the water molecules form a hydrogen bond with the oxygen atom of MTBE, with bond lengths of (O2...H20) 1.64 Å and (O2...H24) 2.17 Å, respectively, and internal hydrogen bond between two water molecules (O19...H23) with bond length of 1.67 Å. Calculated  $\Delta E$  is  $\sim 6.5$  kcal mol<sup>-1</sup>. Calculation of thermochemical parameters shows that complexation between MTBE-water is an exothermic process with the estimated change in enthalpy ( $\Delta H$ ) of  $-8$  kcal mol<sup>-1</sup> (for MTBE-(H<sub>2</sub>O)<sub>1</sub>, a single H-

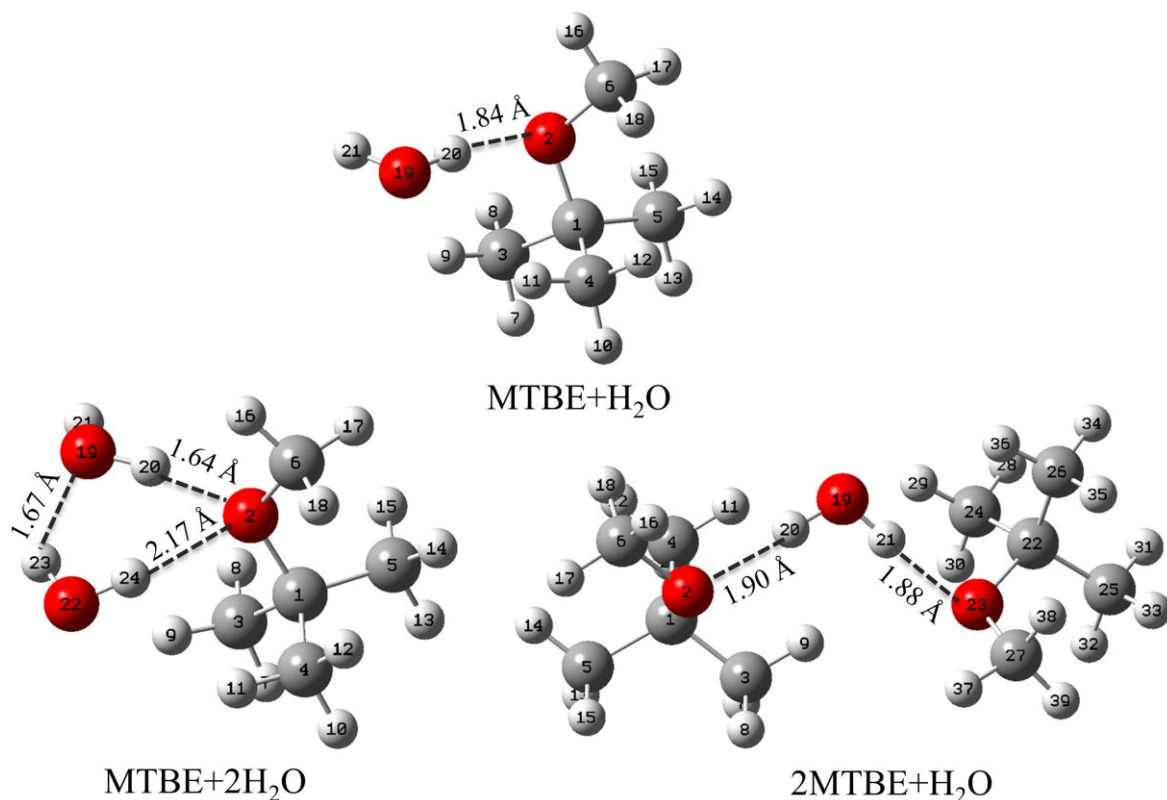


**Figure 5.3:** Optimized structures of different MTBE–water complexes at the MP2/6-31g level. The red ball indicates the oxygen atom, dark gray ball indicates the carbon atom, and white ball indicates the hydrogen atom. Dotted lines indicate hydrogen bonding between two atoms.

bonded system) and  $-17 \text{ kcal mol}^{-1}$  (for MTBE–(H<sub>2</sub>O)<sub>2</sub>, three H-bonded system). Thus, enthalpy analysis essentially predicts the energy release due to formation of MTBE–(H<sub>2</sub>O)<sub>1</sub> complex is quite close to the enthalpy of formation for intermolecular water–water hydrogen bond in the water dimer. The enthalpy is also found to increase with the increase in the number of hydrogen bonds, revealing the complexation process to be thermodynamically more favorable. The calculated free energy change ( $\Delta G$ ) associated with the complexation process of MTBE/(water)<sub>n = 1, 2</sub> is found to be ca. 439 and 753 cal mol<sup>-1</sup>, respectively, which is in the same order of magnitude as our experimental findings of the free energy change associated with the solvation process. Accordingly, theoretical studies clearly indicate that hydrogen bonding interaction between MTBE and water plays the crucial role, and as such the calculated  $\Delta G$  of complexation is largely contributed by the solvation process.

**5.2.1.2. Water in MTBE (Water/MTBE):** Figure 5.4a depicts the DLS spectrum of the water/MTBE system (5  $\mu\text{L}/\text{mL}$ , v/v), showing the appearance of a DLS peak at around 7 nm. The DLS peak is monodispersed and suggests the formation of water clusters in the MTBE continuum. It was found that water forms very small clusters of 2–10 water molecules in the hydrophobic environment of organic solvents, and the molecular origin of this interaction is water–organic hydrogen bonding [6, 8]. To study the water–MTBE hydrogen bonding interaction, we perform FTIR measurements of the water clusters, as shown in Figure 5.4b. In the frequency region of 3000–4000  $\text{cm}^{-1}$ , the spectrum has three

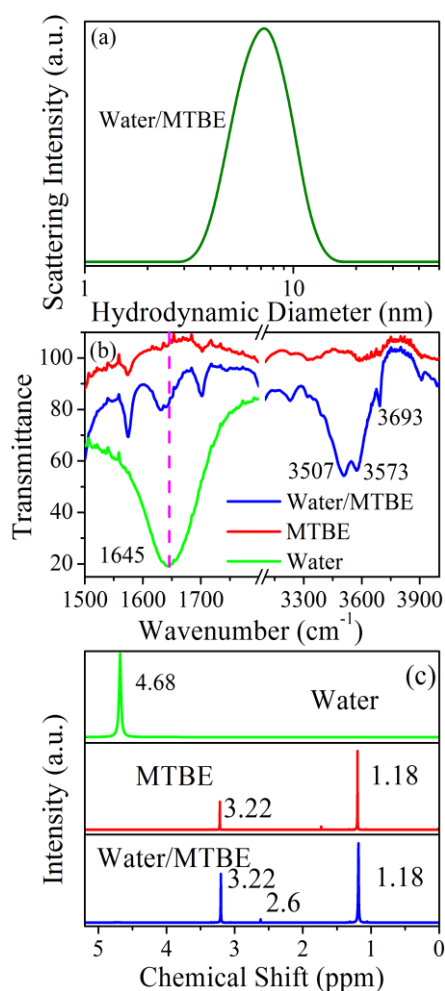


**Figure 5.4:** (a) DLS signals of water/MTBE system ( $[\text{water}] = 5 \mu\text{L}/\text{mL}$ ) at 293 K. (b) FTIR spectra of pure water, pure MTBE, and water/MTBE mixture with water concentration of 5  $\mu\text{L}/\text{mL}$ . (c)  $^1\text{H}$  NMR spectra of water, MTBE, and water/MTBE mixture with water concentration of 5  $\mu\text{L}/\text{mL}$ . Inset shows the zoomed view of the newly generated peak at 2.62 ppm due to hydrogen bond formation of water with MTBE.

absorption peaks at around 3693, 3573, and 3507  $\text{cm}^{-1}$ . The band at 3693  $\text{cm}^{-1}$  is due to the O–H stretching mode of isolated water molecules. The intense peaks at 3573 and 3507  $\text{cm}^{-1}$  are due to the O–H stretching mode of hydrogen bonded water molecules, forming “one-bonded” complex of  $\text{H–O–H}::\text{OMe}(\text{tBu})$  (where (tBu)MeO stands for MTBE) and “two-bonded” complex of  $(\text{tBu})\text{MeO}::\text{H–O–H}::\text{OMe}(\text{tBu})$ , respectively. Similar results have been found for O–H stretching of water dissolved into the solution of other ethers, including di-n-butyl ether (BE) and di-n-octyl ether (OE) [13]. Notably, in the FTIR spectrum, the O–H bending of water at 1645  $\text{cm}^{-1}$  is found to be red-shifted by about 12  $\text{cm}^{-1}$  in MTBE and is possibly due to hydrogen bond formation with MTBE [47]. Formation of hydrogen bond with MTBE is also reflected in  $^1\text{H}$  NMR spectra. The upper and middle panels of Figure 5.4c show the proton NMR signal of water and MTBE, respectively. The  $^1\text{H}$  NMR signal for water found is at 4.68 ppm, whereas for MTBE it is found at 3.22 (for  $-\text{OCH}_3$ ) and 1.18 (for  $-\text{CCH}_3$ ) ppm [48], respectively. However, for the water/MTBE system, the  $^1\text{H}$  NMR spectra (lower panel of Figure 5.4c) shows an extra peak (instead of 4.68, 3.22, and 1.18 ppm) at around 2.62 ppm because of the increased electron density around the water proton as intermolecular hydrogen bond formed with the oxygen of MTBE and hence the chemical shift decreases [49].

The observed changes in the O–H vibration band of water in presence of MTBE can also lead to dynamical properties different from the bulk properties as observed previously for water in dioxane [21, 22]. We have studied the dynamical properties of water clusters using C500 as fluorophore. Figure 5.5a and b shows the absorption and emission spectra of C500 in various water/MTBE mixtures, respectively. Both absorption and fluorescence bands shift further to the red side with increasing concentration of water. It can be argued that with increasing water content the probe experiences more polar environment, which produces the observed red shift [36]. The above observation can further be validated from the difference of the absorption spectrum of C500 in water/MTBE mixture from that in MTBE. The difference absorption spectrum exhibits a negative absorption at 365 nm and a distinct positive peak at 410 nm (Figure 5.5b, inset). The negative absorption peak clearly indicates that, upon addition of water, the population of C500 in the bulk MTBE decreases. On the other hand, the emergence of the positive

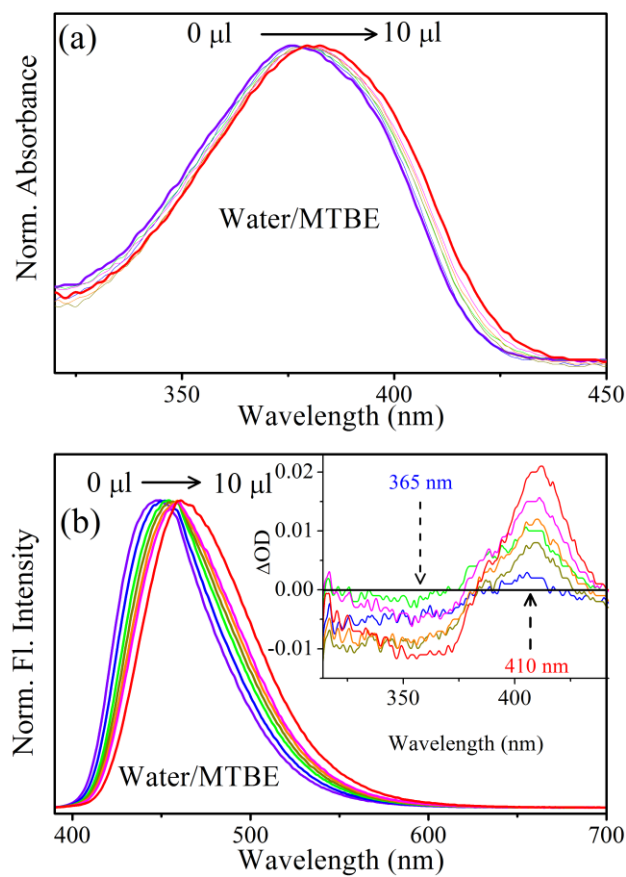


**Figure 5.5:** Absorption (a) and emission (b) spectra of C500 ( $\lambda_{ex} = 375$  nm) in the water/MTBE system with different water concentrations. Difference absorption spectra of C500 in the water/MTBE system with respect to C500 in MTBE in different water concentrations are presented in the inset of (b).

absorption peak at 410 nm is due to the C500 molecules migrating to a higher polar region of the water–MTBE interface. In order to investigate the dynamics of water molecules, we have performed femtosecond-resolved fluorescence spectroscopic technique for the binary mixture containing 5  $\mu\text{L}/\text{mL}$  of MTBE in water. Figure 5.6a shows the femtosecond decay transients of C500 for a series of detected fluorescence wavelengths. It is clear from the figure that the fluorescence transients are strongly wavelength dependent showing a faster decay in the blue end and eventual rise in the red end of the emission spectrum, which is indicative of solvation of the probe in the binary mixture [37-39]. Using the decay transients at different wavelengths, we construct the TRES (Figure 5.6b; inset), wherein a significant dynamic fluorescence Stokes shift of  $700\text{ cm}^{-1}$  in 15 ps is observed. Figure 5.6b depicts the solvent correlation function,  $C(t)$ , of the system. As shown in the figure,  $C(t)$

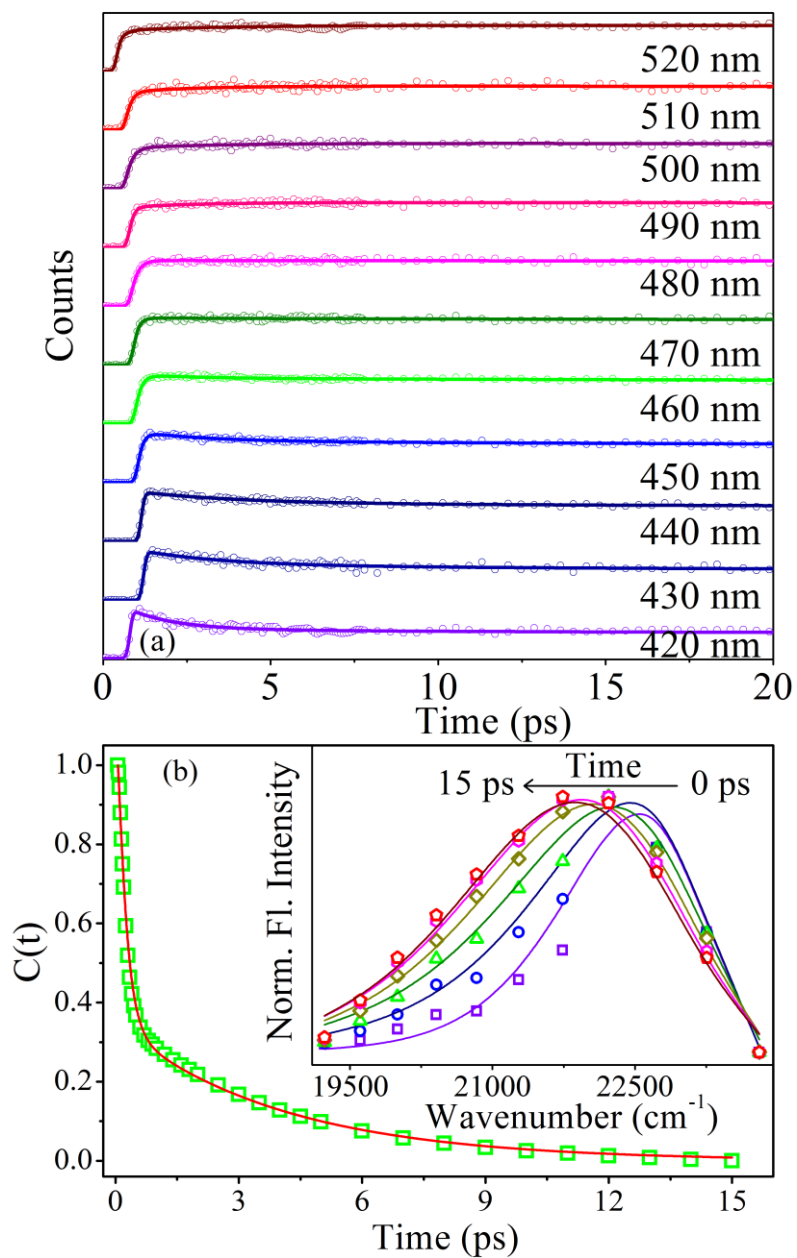


**Figure 5.6:** (a) Femtosecond-resolved decay transients ( $\lambda_{ex} = 385$  nm) of C500 at different wavelengths in water/MTBE system ( $[water] = 5 \mu\text{L/mL}$ ) at 293 K. (b) Solvent correlation function,  $C(t)$ , of C500 in water/MTBE system ( $[water] = 5 \mu\text{L/mL}$ ). The corresponding TRES is shown in the inset.

can be fitted biexponentially with time components of 0.20 ps (74%) and 4.03 ps (26%) (Table 5.1), which are quite similar to those obtained for a water–dioxane mixture [22]. The origin of the observed slower component is due to the cooperative relaxation of the hydrogen bond network of water, whereas the faster subpicosecond time scale arises due to the relaxation of water molecules that are not part of the tetrahedral hydrogen bond

network of the water clusters, that is, the isolated water molecules, or the water molecules forming weak hydrogen bonds with the ether oxygen of MTBE, that is, “one-bonded” or “two-bonded” complex of water molecules mentioned earlier. Using the Eyring equation, we calculate the  $\Delta G^\ddagger$  of the system to be  $1200 \text{ cal mol}^{-1}$ , which is quite consistent with the theoretically calculated value as discussed below.

The thermochemical calculations on the model system  $\text{H}_2\text{O}/(\text{MTBE})_n$  (where  $n = 1, 2, 3$ ) are similarly performed, assuming that, in the water/MTBE system, a water molecule is surrounded by  $n$  number of MTBE molecules. In our calculation, the  $n$  value is limited up to 2, because higher  $n$  ( $>2$ ) does not affect the H-bonding network in the  $\text{H}_2\text{O}/(\text{MTBE})_2$  complex. The corresponding energy optimized molecular structure of the  $\text{H}_2\text{O}/(\text{MTBE})_2$  complex can be seen in Figure 5.3, showing two MTBE molecules forming hydrogen bonds with one water molecule with bond lengths ( $\text{O}23 \cdots \text{H}21$ )  $1.88 \text{ \AA}$  and ( $\text{O}2 \cdots \text{H}20$ )  $1.90 \text{ \AA}$ , respectively. The  $\Delta E$  for water/(MTBE) system is found to be  $3 \text{ kcal mol}^{-1}$ , whereas for the water/(MTBE)<sub>2</sub> system the value is  $5 \text{ kcal mol}^{-1}$ . The corresponding  $\Delta H$  for complexation in water/(MTBE) and water/(MTBE)<sub>2</sub> is found to be exothermic in nature with calculated values of ca.  $-8$  and  $-12.55 \text{ kcal mol}^{-1}$ , respectively (Table 5.2). The calculated  $\Delta G$  value for the water/(MTBE)<sub>2</sub> system is found to be ca.  $2700 \text{ cal mol}^{-1}$ , which is quite consistent with the experimentally estimated value for  $\Delta G$  of solvation.

Water clusters in nonpolar solvent have been reported to exhibit slow solvation dynamics at the picosecond time scale [7, 22, 50]. This slow solvation has been concluded to be due to the translational diffusion of water in the solvation shell displacing the nonpolar solvent molecules in the cluster. To get insight on the slow dynamics of the water/MTBE system, we perform picosecond-resolved fluorescence spectroscopy using TCSPC setup. Figure 5.7a depicts the fluorescence decay transients of C500 in the water/MTBE system ( $5 \text{ }\mu\text{L/mL}$ ) at various wavelengths across the emission spectrum. The decay transient at  $400 \text{ nm}$  (blue end) is fitted triexponentially with time constants of  $50$ ,  $1120$ , and  $3870 \text{ ps}$ . For the extreme red wavelength ( $550 \text{ nm}$ ), a distinct rise component of  $510 \text{ ps}$  is produced along with the decay components of  $4770 \text{ ps}$ . The difference in transients in the red and blue ends clearly point to the presence of solvation in the system

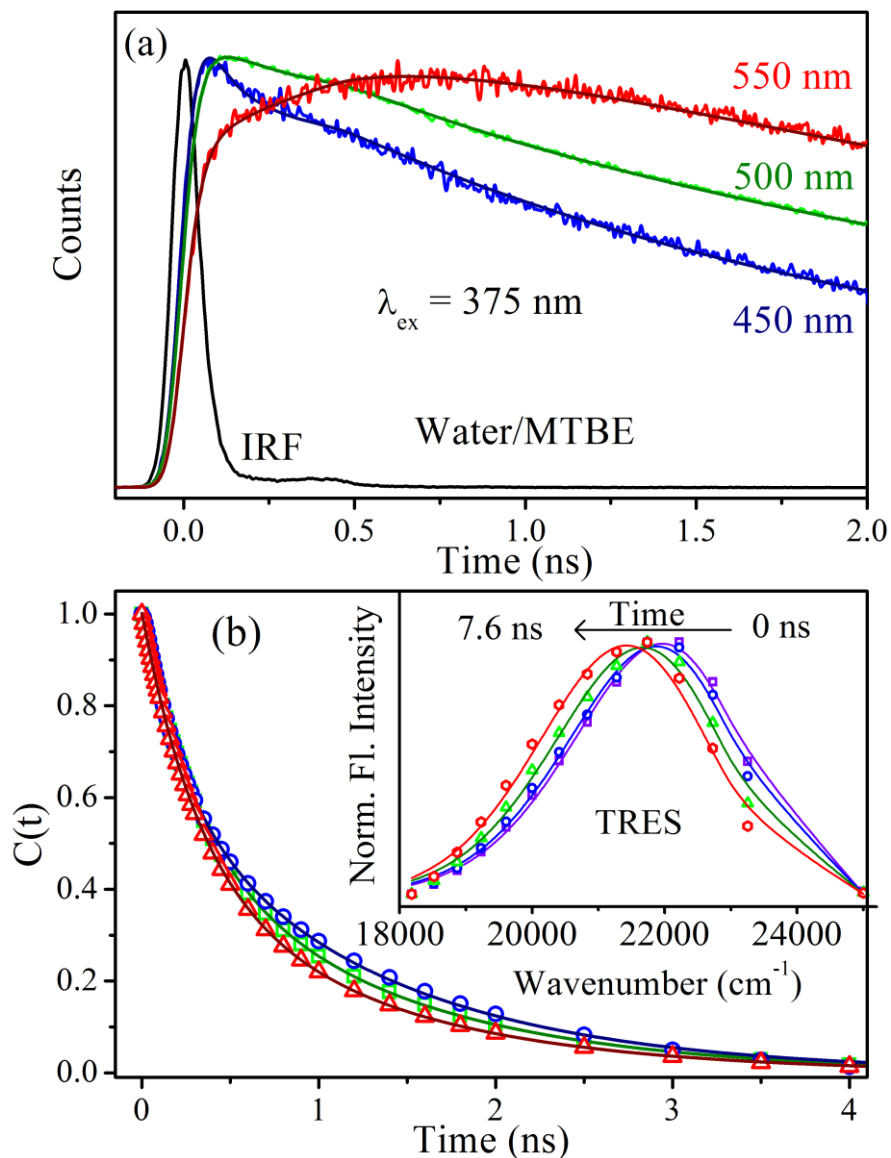


**Figure 5.7:** (a) Fluorescence decay transients ( $\lambda_{ex} = 375 \text{ nm}$ ) of C500 in water/MTBE system ( $[\text{water}] = 5 \mu\text{L/mL}$ ), at 293 K. (b) Solvation correlation function,  $C(t)$ , of C500 in water/MTBE system with different water concentration: 2.5 (blue circle), 5.0 (green square), and 10  $\mu\text{L/mL}$  (red triangle) at 293 K. TRES for C500 in water/MTBE system ( $[\text{water}] = 5 \mu\text{L/mL}$ ) at 293 K is shown in the inset.

[7, 22, 38]. The inset of Figure 5.7b depicts the constructed TRES, and the corresponding  $C(t)$  can be fitted biexponentially with time constants of 0.30 ns (46%) and 1.22 ns (54%) (Figure 5.7b and Table 5.3). With an increase in the water concentration, the dynamics become faster (Figure 5.7b and Table 5.3). The decrease in  $\langle\tau_s\rangle$  with increasing water content is associated with the increase of bulk type of water molecules consistent with these in reverse micelles with higher hydration numbers [36, 38, 51].

**Table 5.3: Solvent correlation data for C500 in water/MTBE mixture at various water concentrations.<sup>a</sup>**

Water ( $\mu\text{l/ml}$ )	Fluorescence peak (nm)	$a_1$	$\tau_1$ (ns)	$a_2$	$\tau_2$ (ns)	$\langle \tau_s \rangle$ (ns)
2.5	454	0.62	1.23	0.38	0.22	0.85
5.0	459	0.54	1.22	0.46	0.30	0.79
10	463	0.46	1.18	0.54	0.32	0.71

<sup>a</sup> $\tau_i$  represents the solvation correlation time constants,  $a_i$  represents its relative contribution, and  $\langle \tau_s \rangle$  is the average solvation time constant.

To understand the nature of hydrogen bond formation and the possible equilibrium between the two types of water present in the cluster, we measure solvation dynamics of water, containing 5  $\mu\text{L/mL}$  MTBE, at different temperatures (in the temperature window of 278–318 K). From the temperature dependent emission peaks of C500 (Table 5.4), it is evident that the fluorescence maximum of C500 exhibits a small blue shift (around 3 nm). The observed blue shift indicates a less polar environment experienced by the probe at elevated temperatures due to the breakdown of hydrogen bond network followed by formation of small water clusters, similar to those reported previously [7, 22]. Figure 5.8a, b shows the fluorescence decay transients of C500 at 278 and 318 K, respectively. The figure depicts considerable difference between the decay patterns at particular wavelengths, clearly indicating temperature dependency on solvation behavior. We construct the TRES at different temperatures, and the corresponding  $C(t)$  values are given in Table 5.4. It is observed that solvation dynamics gets faster with increasing temperature and probe molecules get solvated with faster moving water molecules at the

**Table 5.4: Solvent correlation data for C500 in water/MTBE mixture ( $[\text{water}] = 5 \mu\text{l/mL}$ ) at different temperatures and activation energy value.<sup>a</sup>**

Temperature (K)	Fluorescence peak (nm)	$a_1$	$\tau_1$ (ns)	$a_2$	$\tau_2$ (ns)	$\langle \tau_s \rangle$ (ns)	$E_{act}$ (kcal mol <sup>-1</sup> )
278	459	0.28	0.27	0.72	1.28	0.99	2.2
283	459	0.33	0.29	0.67	1.26	0.94	
288	459	0.39	0.30	0.61	1.26	0.89	
293	459	0.46	0.30	0.54	1.22	0.79	
298	459	0.57	0.33	0.43	1.48	0.83	
303	458	0.53	0.25	0.47	1.20	0.70	
308	457	0.58	0.26	0.42	1.22	0.66	
313	456	0.60	0.23	0.40	1.28	0.65	
318	456	0.65	0.22	0.35	1.36	0.61	

<sup>a</sup> $\tau_i$  represents the solvation correlation time constants,  $a_i$  represents its relative contribution, and  $\langle \tau_s \rangle$  is the average solvation time constant.

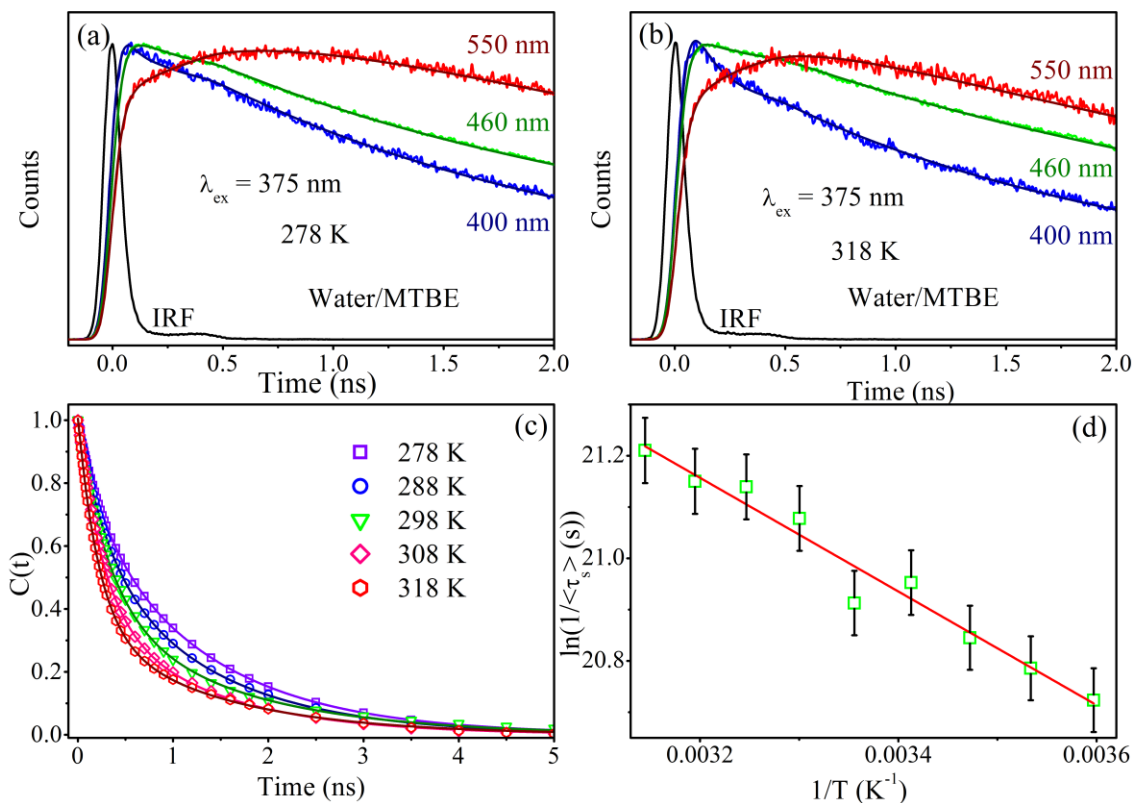


**Figure 5.8:** (a, b) Fluorescence decay transients ( $\lambda_{ex} = 375$  nm) of C500 in water/MTBE system (5  $\mu\text{L}/\text{mL}$ ), at 278 and 318 K. (c) Solvation correlation function,  $C(t)$ , of C500 in water/MTBE ([water] = 5  $\mu\text{L}/\text{mL}$ ) system, at different temperatures. (d) Plot of  $\ln(1/\langle\tau_s\rangle)$  against  $1/T$  for water/MTBE system ([water] = 5  $\mu\text{L}/\text{mL}$ ), with linear fit.

higher temperatures. This observation indicates that at the elevated temperature the hydrogen bond network present in the bulk like cluster breaks down and isolated small clusters consisting of weakly hydrogen bonded water molecules start growing, producing the faster solvation dynamics. The temperature-dependent solvation of water is associated with the dynamic exchange between free type (weakly hydrogen-bonded or partially bonded to the ether oxygen of MTBE) and bound type (strongly hydrogen bonded) water. The energetics of the exchange depends upon the strength and the number of hydrogen bonds between the water molecules at the interface and related to solvation time constant according to Arrhenius type of activation energy barrier crossing model by the following equation [7, 22, 36]:

$$k_{bf} \approx \frac{1}{\langle\tau_s\rangle} = A \exp\left(\frac{-E_{act}}{RT}\right) \quad (5-2)$$

where  $\langle \tau_s \rangle$  represents the average solvation time constant ( $\langle \tau_s \rangle = \sum_i a_i \tau_i$ ),  $k_{bf}$  is the rate constant for bound-to-free water conversion,  $A$  is the pre-exponential factor, and  $E_{act}$  is the corresponding activation energy for the transition process. A plot of  $\ln(1/\langle \tau_s \rangle)$  versus  $1/T$  produces a good linear fit (Figure 5.8d), and the corresponding activation energy value is  $2.2 \text{ kcal mol}^{-1}$ . The observed  $E_{act}$  value is smaller than the bulk hydrogen bond energy [46, 52] of  $5 \text{ kcal mol}^{-1}$  and, therefore, must be associated with some other bonding pattern. As already mentioned, C500 resides mainly at the cluster interface, and hence, the observed  $E_{act}$  corresponds to the transition occurring at the interface. Notably, the ether (like dioxane)–water hydrogen bond energy is reported to be ca.  $2.3 \text{ kcal mol}^{-1}$  [53]. In the present study, the estimated hydrogen bond energy of the MTBE–water complex is  $\sim 3.0 \text{ kcal mol}^{-1}$  for each hydrogen bond. Thus, the observed  $E_{act}$  is essentially the manifestation of the MTBE–water hydrogen bond energy.

From the above discussion, it is evident that temperature can change the water dynamics significantly in the MTBE continuum. Therefore, it is important to know whether this change in water dynamics can alter the reaction property of the confined water molecules. In order to address this issue, we have studied the kinetics of a standard solvolysis reaction of benzoyl chloride (BzCl) with varying temperature. The reaction is a well-studied one in the restricted medium and is reported to follow simple first order kinetics [54-56]. The decay kinetics of BzCl hydrolysis in the mixed system ( $5 \mu\text{L/mL}$ ) at different temperatures is shown in Figure 5.9a. The corresponding observed rate constants ( $R_k^{obs}$ ) of the reactions are given in Table 5.5. The rate constant is found to be much slower than that in pure water ( $R_k = 1.1 \text{ s}^{-1}$ ) [57], indicating the reaction occurs at the interface of the clusters. It has already been confirmed that free type interfacial water molecules act as nucleophile in the solvolysis reaction [51]. The observed acceleration of  $R_k^{obs}$  with temperature (Table 5.5) is thus due to the increased fraction of the interfacial free water molecules at elevated temperatures (Table 5.4), as has been observed in the present solvation dynamics study. In order to determine the dependency of the rate of the reaction on temperature, we apply the Arrhenius model and plot  $\ln(R_k^{obs})$  against  $1/T$  (Figure 5.9b).

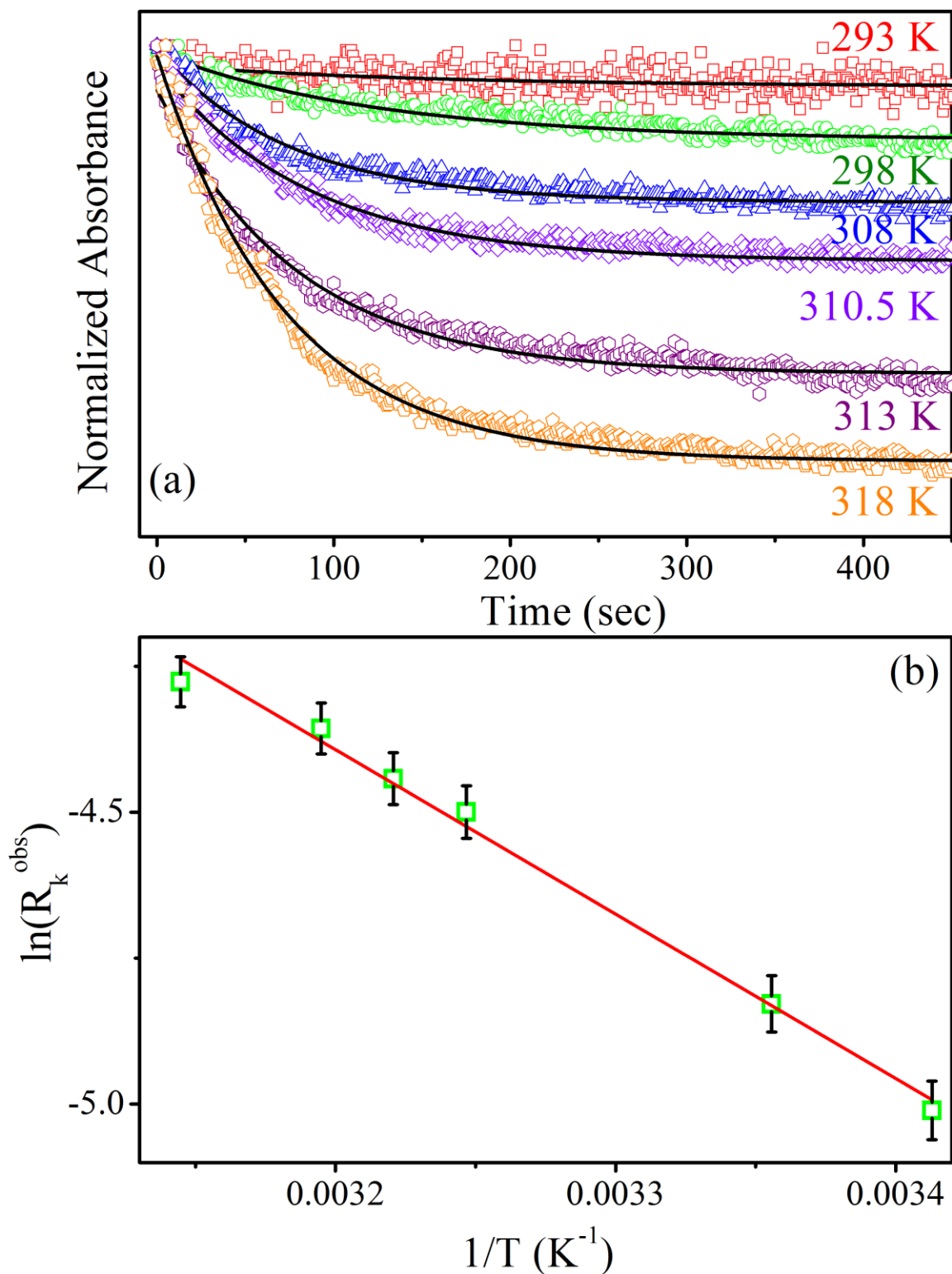


Figure 5.9: (a) Decay kinetics of solvolysis of benzoyl chloride monitored at 288 nm for water/MTBE system ( $[water] = 5 \mu L/mL$ ) at different temperatures. (b) Arrhenius plot ( $\ln(R_k^{obs})$  vs  $1/T$ ) for solvolysis of benzoyl chloride.

**Table 5.5: Rate constants (observed,  $R_k^{obs}$ ) for solvolysis of benzoyl chloride in water/MTBE mixture ( $[water] = 5 \mu\text{l}/\text{mL}$ ) at different temperatures and activation energy value.**

Temperature (K)	$R_k^{obs}(s^{-1})$	$E_{act}(\text{kcal mol}^{-1})$
293.0	0.007	5.6
298.0	0.008	
308.0	0.011	
310.5	0.012	
313.0	0.013	
318.0	0.014	

Reasonably good linear fit with the  $E_{act}^{(rcn)}$  value of  $5.6 \text{ kcal mol}^{-1}$  is obtained. Note that the activation energy values obtained from the kinetic measurements ( $E_{act}^{(rcn)}$ ) are higher than those obtained from the solvation measurements ( $E_{act}^{(solv)}$ ). This is because solvolysis in confined systems could be assumed to take place through two steps [51]. In the initial step, free water molecules are formed at the interface, which corresponds to the  $E_{act}^{(solv)}$  values. In the following step, these free type water molecules act as a nucleophile to bring about the solvolysis process. This difference in  $E_{act}^{(rcn)}$  values confirms our earlier observation that at the cluster interface there exists heterogeneous hydrogen bonding between the ether oxygen of MTBE and water along with water–water hydrogen bond, and breaking–remaking of such bonds contributes to the slow solvation in concentrated water–MTBE mixture.

### 5.3. Conclusion:

In summary, the present study investigates the effect of hydrophobic interaction on the structure, dynamics, and reactivity of water in the presence of a hydrophobic molecule MTBE. DLS measurements confirm the formation of nanometer sized molecular clusters in both the MTBE and water continuum. Vibrational shift in FTIR studies confirm the MTBE–water complexation to occur through hydrogen bonding. The dynamics of solvation of the clusters is successfully probed by the solvatochromic dye C500. Both steady-state absorption and emission spectra show the dye to reside in the solvation shell of the MTBE–water interface. Femto- and picosecond-resolved fluorescence studies successfully probes the modification of water solvation dynamics due to hydrophobic interaction, in both the MTBE and water continuum. Theoretical calculations predict the possible hydrogen bonding interaction in MTBE–water complexes. Calculated Gibbs free energy changes for different complexes are consistent with experimental results. Solvation

dynamics becomes faster with increasing temperature due to the breakage of tetrahedral hydrogen bond network in the water clusters. The activation energy for the process has been calculated to be  $2.2 \text{ kcal mol}^{-1}$ , which is similar to the hydrogen bond energy of a typical ether–water bond. Temperature dependent dynamics of water solvation has been well manifested in the altered reaction property of confined water molecules with temperature. Solvolysis of BzCl shows increased reaction kinetics with temperature and is attributed to the formation and availability of free water molecules at the interface. These results might be helpful for the understanding of the hydrophobic interaction imposed by a biomolecule on water. The detailed understanding about the physicochemical properties of the MTBE–water system would also be useful for the designing of efficient removal strategy of MTBE from drinking water.

## References

- [1] D. Chandler, Interfaces and the driving force of hydrophobic assembly, *Nature* 437 (2005) 640.
- [2] C. Tanford, The hydrophobic effect and the organization of living matter, *Science* 200 (1978) 1012.
- [3] C. Tanford, Hydrophobic free energy, micelle formation and the association of proteins with amphiphiles, *J. Mol. Biol.* 67 (1972) 59.
- [4] W. Kauzmann, Some factors in the interpretation of protein denaturation, *Adv. Protein Chem.* 14 (1959) 1.
- [5] F. Pizzitutti, M. Marchi, F. Sterpone, P.J. Rossky, How protein surfaces induce anomalous dynamics of hydration water, *J. Phys. Chem. B* 111 (2007) 7584.
- [6] S. Vaitheeswaran, H. Yin, J.C. Rasaiah, G. Hummer, Water clusters in nonpolar cavities, *Proc. Natl. Acad. Sci. USA* 101 (2004) 17002.
- [7] S. Rakshit, R. Saha, P.K. Verma, S.K. Pal, Role of solvation dynamics in excited state proton transfer of 1-naphthol in nanoscopic water clusters formed in a hydrophobic solvent, *Photochem. Photobiol.* 88 (2012) 851.
- [8] C. Yang, W. Li, C. Wu, Laser light-scattering study of solution dynamics of water/cycloether mixtures, *J. Phys. Chem. B* 108 (2004) 11866.
- [9] K. Takano, Y. Yamagata, K. Yutani, Buried water molecules contribute to the conformational stability of a protein, *Protein Eng.* 16 (2003) 5.
- [10] J. Ernst, R. Clubb, H. Zhou, A. Gronenborn, G. Clore, Demonstration of positionally disordered water within a protein hydrophobic cavity by NMR, *Science* 267 (1995) 1813.
- [11] A.A. Rashin, M. Iofin, B. Honig, Internal cavities and buried waters in globular proteins, *Biochemistry* 25 (1986) 3619.
- [12] Z.S. Nickolov, K. Ohno, H. Matsuura, FTIR-ATR studies of the hydration of 15-crown-5 and 18-crown-6 in aqueous solutions, *J. Phys. Chem. A* 103 (1999) 7544.
- [13] R. Iwamoto, T. Matsuda, T. Sasaki, H. Kusanagi, Basic interactions of water with organic compounds, *J. Phys. Chem. B* 107 (2003) 7976.
- [14] M. Besnard, Y. Danten, T. Tassaing, Dynamics of solitary water in benzene and hexafluorobenzene: An infrared and Raman study, *J. Chem. Phys.* 113 (2000) 3741.

- [15] E. Zoidis, J. Yarwood, T. Tassaing, Y. Danten, M. Besnard, Vibrational spectroscopic studies on the state of aggregation of water in carbon tetrachloride, in dioxane and in the mixed solvents, *J. Mol. Liq.* 64 (1995) 197.
- [16] S. Suzuki, P.G. Green, R.E. Bumgarner, S. Dasgupta, W.A. Goddard, G.A. Blake, Benzene forms hydrogen bonds with water, *Science* 257 (1992) 942.
- [17] A.E. Bragg, G.U. Kanu, B.J. Schwartz, Nanometer-scale phase separation and preferential solvation in THF–water mixtures: Ultrafast electron hydration and recombination dynamics following CTTS excitation of  $\Gamma^-$ , *J. Phys. Chem. Lett.* 2 (2011) 2797.
- [18] J.A. Gardecki, M. Maroncelli, Solvation and rotational dynamics in acetonitrile/propylene carbonate mixtures: A binary system for use in dynamical solvent effect studies, *Chem. Phys. Lett.* 301 (1999) 571.
- [19] K. Tominaga, G.C. Walker, Femtosecond experiments on solvation dynamics of an anionic probe molecule in methanol, *J. Photochem. Photobiol. A* 87 (1995) 127.
- [20] B.M. Luther, J.R. Kimmel, N.E. Levinger, Dynamics of polar solvation in acetonitrile-benzene binary mixtures: Role of dipolar and quadrupolar contributions to solvation, *J. Chem. Phys.* 116 (2002) 3370.
- [21] T. Molotsky, D. Huppert, Solvation statics and dynamics of coumarin 153 in dioxane-water solvent mixtures, *J. Phys. Chem. A* 107 (2003) 8449.
- [22] R.K. Mitra, P.K. Verma, S.K. Pal, Exploration of the dynamical evolution and the associated energetics of water nanoclusters formed in a hydrophobic solvent, *J. Phys. Chem. B* 113 (2009) 4744.
- [23] J.F. Pankow, N.R. Thomson, R.L. Johnson, A.L. Baehr, J.S. Zogorski, The urban atmosphere as a non-point source for the transport of MTBE and other volatile organic compounds (VOCs) to shallow groundwater, *Environ. Sci. Technol.* 31 (1997) 2821.
- [24] J.E. Reuter, B.C. Allen, R.C. Richards, J.F. Pankow, C.R. Goldman, R.L. Scholl, J.S. Seyfried, Concentrations, sources, and fate of the gasoline oxygenate methyl tert-butyl ether (MTBE) in a multiple-use lake, *Environ. Sci. Technol.* 32 (1998) 3666.
- [25] C. Achten, A. Kolb, W. Püttmann, P. Seel, R. Gühr, Methyl tert-butyl ether (MTBE) in river and wastewater in Germany, *Environ. Sci. Technol.* 36 (2002) 3652.

- [26] P.J. Squillace, J.S. Zogorski, W.G. Wilber, C.V. Price, Preliminary assessment of the occurrence and possible sources of MTBE in groundwater in the United States, 1993–1994, *Environ. Sci. Technol.* 30 (1996) 1721.
- [27] P.J. Squillace, M.J. Moran, W.W. Lapham, C.V. Price, R.M. Clawges, J.S. Zogorski, Volatile organic compounds in untreated ambient groundwater of the United States, 1985–1995, *Environ. Sci. Technol.* 33 (1999) 4176.
- [28] A.L. Baehr, P.E. Stackelberg, R.J. Baker, Evaluation of the atmosphere as a source of volatile organic compounds in shallow groundwater, *Water Resour. Res.* 35 (1999) 127.
- [29] J. Klinger, C. Stieler, F. Sacher, H.J. Brauch, MTBE (methyl tertiary-butyl ether) in groundwaters: Monitoring results from Germany, *J. Environ. Monitor.* 4 (2002) 276.
- [30] F. Belpoggi, M. Soffritti, C. Maltoni, Methyl-tertiary-butyl ether (MTBE)–A gasoline additive–Causes testicular and lympho haematopoietic cancers in rats, *Toxicol. Ind. Health* 11 (1995) 119.
- [31] T.B. Nielsen, S. Hvidt, S.R. Keiding, C. Petersen, P. Westh, K. Keiding, Thermodynamic investigations of methyl tert-butyl ether and water mixtures, *Phys. Chem. Chem. Phys.* 13 (2011) 1182.
- [32] Z. Li, S. Singh, FTIR and Ab Initio investigations of the MTBE–water complex, *J. Phys. Chem. A* 112 (2008) 8593.
- [33] S. Rakshit, R. Saha, A. Chakraborty, S.K. Pal, Effect of hydrophobic interaction on structure, dynamics, and reactivity of water, *Langmuir* 29 (2013) 1808.
- [34] T. Takamuku, A. Yamaguchi, M. Tabata, N. Nishi, K. Yoshida, H. Wakita, T. Yamaguchi, Structure and dynamics of 1,4-dioxane-water binary solutions studied by X-ray diffraction, mass spectrometry, and NMR relaxation, *J. Mol. Liq.* 83 (1999) 163.
- [35] S. Rakshit, R. Saha, A. Singha, Z.S.A. Seddigi, S.K. Pal, Molecular interaction, co-solubilization of organic pollutants and ecotoxicity of a potential carcinogenic fuel additive MTBE in water, *J. Mol. Liq.* 180 (2013) 235.
- [36] P.K. Verma, R. Saha, R.K. Mitra, S.K. Pal, Slow water dynamics at the surface of macromolecular assemblies of different morphologies, *Soft Matter* 6 (2010) 5971.
- [37] D. Banerjee, P.K. Verma, S.K. Pal, Temperature-dependent femtosecond-resolved hydration dynamics of water in aqueous guanidinium hydrochloride solution, *Photochem. Photobiol. Sci.* 8 (2009) 1441.

- [38] S. Rakshit, N. Goswami, S.K. Pal, Slow solvent relaxation dynamics of nanometer sized reverse micellar systems through tryptophan metabolite, kynurenine, *Photochem. Photobiol.* 88 (2012) 38.
- [39] M.L. Horng, J.A. Gardecki, A. Papazyan, M. Maroncelli, Subpicosecond measurements of polar solvation dynamics: Coumarin 153 revisited, *J. Phys. Chem.* 99 (1995) 17311.
- [40] R. Saha, S. Rakshit, R.K. Mitra, S.K. Pal, Microstructure, morphology, and ultrafast dynamics of a novel edible microemulsion, *Langmuir* 28 (2012) 8309.
- [41] R. Jimenez, G.R. Fleming, P.V. Kumar, M. Maroncelli, Femtosecond solvation dynamics of water, *Nature* 369 (1994) 471.
- [42] W. Jarzeba, G.C. Walker, A.E. Johnson, M.A. Kahlow, P.F. Barbara, Femtosecond microscopic solvation dynamics of aqueous solutions, *J. Phys. Chem.* 92 (1988) 7039.
- [43] N. Nandi, B. Bagchi, Dielectric relaxation of biological water, *J. Phys. Chem. B* 101 (1997) 10954.
- [44] S.J. Suresh, V.M. Naik, Hydrogen bond thermodynamic properties of water from dielectric constant data, *J. Chem. Phys.* 113 (2000) 9727.
- [45] K.A.T. Silverstein, A.D.J. Haymet, K.A. Dill, The strength of hydrogen bonds in liquid water and around nonpolar solutes, *J. Am. Chem. Soc.* 122 (2000) 8037.
- [46] M.W. Feyereisen, D. Feller, D.A. Dixon, Hydrogen bond energy of the water dimer, *J. Phys. Chem.* 100 (1996) 2993.
- [47] K.A. Sharp, B. Madan, E. Manas, J.M. Vanderkooi, Water structure changes induced by hydrophobic and polar solutes revealed by simulations and infrared spectroscopy, *J. Chem. Phys.* 114 (2001) 1791.
- [48] H.E. Gottlieb, V. Kotlyar, A. Nudelman, NMR chemical shifts of common laboratory solvents as trace impurities, *J. Org. Chem.* 62 (1997) 7512.
- [49] R.J. Abraham, M. Mobli, An NMR, IR and theoretical investigation of <sup>1</sup>H Chemical Shifts and hydrogen bonding in phenols, *Magn. Reson. Chem.* 45 (2007) 865.
- [50] K. Sahu, S.K. Mondal, D. Roy, R. Karmakar, K. Bhattacharyya, Slow solvation dynamics of 4-AP and DCM in binary mixtures, *J. Photochem. Photobiol. A* 172 (2005) 180.

- [51] P.K. Verma, A. Makhal, R.K. Mitra, S.K. Pal, Role of solvation dynamics in the kinetics of solvolysis reactions in microreactors, *Phys. Chem. Chem. Phys.* 11 (2009) 8467.
- [52] P.L. Moore Plummer, Applicability of semi-empirical methods to the study of small water clusters: Cubic structures for (H<sub>2</sub>O)<sub>n</sub> (n = 8, 12, 16), *J. Mol. Struct. Theochem* 417 (1997) 35.
- [53] V.Y. Buz'ko, I.V. Sukhno, V.T. Panyushkin, D.N. Ramazanov, Theoretical investigation of 1,4-dioxane complexes with water in the chair conformation by semiempiric MNDO/PM3 method, *J. Struct. Chem.* 46 (2005) 596.
- [54] L. Garcia-Rio, J.R. Leis, J.A. Moreira, Reactivity in water/oil microemulsions. Influence of sodium bis(2-ethylhexyl) sulfosuccinate/isooctane/water microemulsions on the solvolysis mechanism of substituted benzoyl chlorides, *J. Am. Chem. Soc.* 122 (2000) 10325.
- [55] L. Garcia-Rio, J.R. Leis, E. Iglesias, Influence of water structure on solvolysis in water-in-oil microemulsions, *J. Phys. Chem.* 99 (1995) 12318.
- [56] E. Fernández, L. García-Río, A. Godoy, J.R. Leis, Reactivity in w/o microemulsions. Activation parameters for solvolysis in AOT/isooctane/water systems, *New J. Chem.* 27 (2003) 1207
- [57] C. Cabaleiro-Lago, L. Garcia-Rio, P. Herves, J. Perez-Juste, Reactivity of benzoyl chlorides in nonionic microemulsions: Potential application as indicators of system properties, *J. Phys. Chem. B.* 109 (2005) 22614.

## Chapter 6

# Studies on the Role of Dynamics of Isolated Water Molecules in Proton Transfer Reaction in Biologically Important Hydrophobic/Confined Environments

### 6.1. Introduction:

Hydrogen bonding interaction and associated intramolecular processes like proton transfer in biomolecules following photoexcitation is of fundamental importance in modern chemistry and has received significant attention in recent time [1, 2]. In the past years, the hydrogen bonding effects on the structures and dynamics of many important molecular systems have been well investigated [3-11]. For example, Zhao and Han have extensively studied hydrogen bonding in the ground and excited states of organic and biological chromophores as well as its influence to their structures and dynamics in solution by use of combined experimental and theoretical methods. They have demonstrated that intermolecular hydrogen bonds formed between carbonyl chromophores and polar protic solvents can be significantly strengthened in electronically excited states of carbonyl chromophores [11], whereas it gets weakened for thiocarbonyl chromophores [4]. Furthermore, they have also reported that radiationless deactivation processes, such as internal conversion (IC), intersystem crossing (ISC), photoinduced electron transfer (PET), excited state intramolecular proton transfer (ESIPT) and excited state double proton transfer (ESDPT) etc. are strongly influenced by excited state intermolecular hydrogen bonding interactions [5-7]. Their study demonstrates that molecular photochemistry (like intramolecular charge transfer [ICT]) in solution can be tuned by hydrogen bonding interactions in electronically excited states [7]. Very recently, studies involving site-specific solvation (SSS) of the photoexcited protochlorophyllide a (Pchl<sub>a</sub>) in methanol using the time-dependent density functional theory method, have theoretically confirmed that intermolecular coordination and hydrogen bonds between Pchl<sub>a</sub> and methanol

molecules can be strengthened in the electronically excited state of Pchl<sub>a</sub> [3]. Moreover, the SSS of the photoexcited Pchl<sub>a</sub> in methanol can be induced by the intermolecular coordination and hydrogen-bond strengthening upon photoexcitation.

Proton transfer is a fundamentally important process that plays a crucial role in many chemical and biological processes. To study the hydrogen bonding interactions and their consequences in the proton transfer, various organic photoacids are found to be ideal model systems, where a significant reduction of pK<sub>a</sub> of the organic molecules upon photoexcitation allows measurement of proton transfer process conveniently. Although, over the past few decades, various photoacids have been extensively studied in different solvents as well as in nanoscopic confined environments [12-15]. However, studies focusing on the solvent dynamics around photoacids are sparse in the present literature. This is due to the presence of two competing relaxation processes (intermolecular proton transfer and solvation stabilization) in the excited state, which is quite complicated to interpret separately. Also, the dynamics and energetics of water in the immediate vicinity of an ion [16] or organized assemblies [17, 18] is very much different from those of pure water. Therefore, this chapter summarizes the attempt to explore the influence of water dynamics of nanometer sized small water clusters in non-aqueous solvent in proton transfer process of 1-naphthol (NpOH) and kynurenine (KN).

## **6.2. Results and Discussion:**

### **6.2.1. Role of Solvation Dynamics in Excited State Proton Transfer of 1-Naphthol in Nanoscopic Water Clusters Formed in a Hydrophobic Solvent [19]:**

The absorption and emission spectra of NpOH in pure water, dioxane (DX) and water–DX mixtures are shown in Figure 6.1. Dynamic light scattering (DLS) studies confirm the formation of water nanocluster (1–400 nm) in the water–DX mixtures. The absorption spectra are insensitive to the relative concentrations of water and DX solvent mixture. This suggests that ground state property of NpOH hardly depends on the polarity of the host solvent. However, the emission spectra (Figure 6.1b) show two distinct emission bands whose intensities are sensitive to water concentrations. In a pure DX solvent, there is a

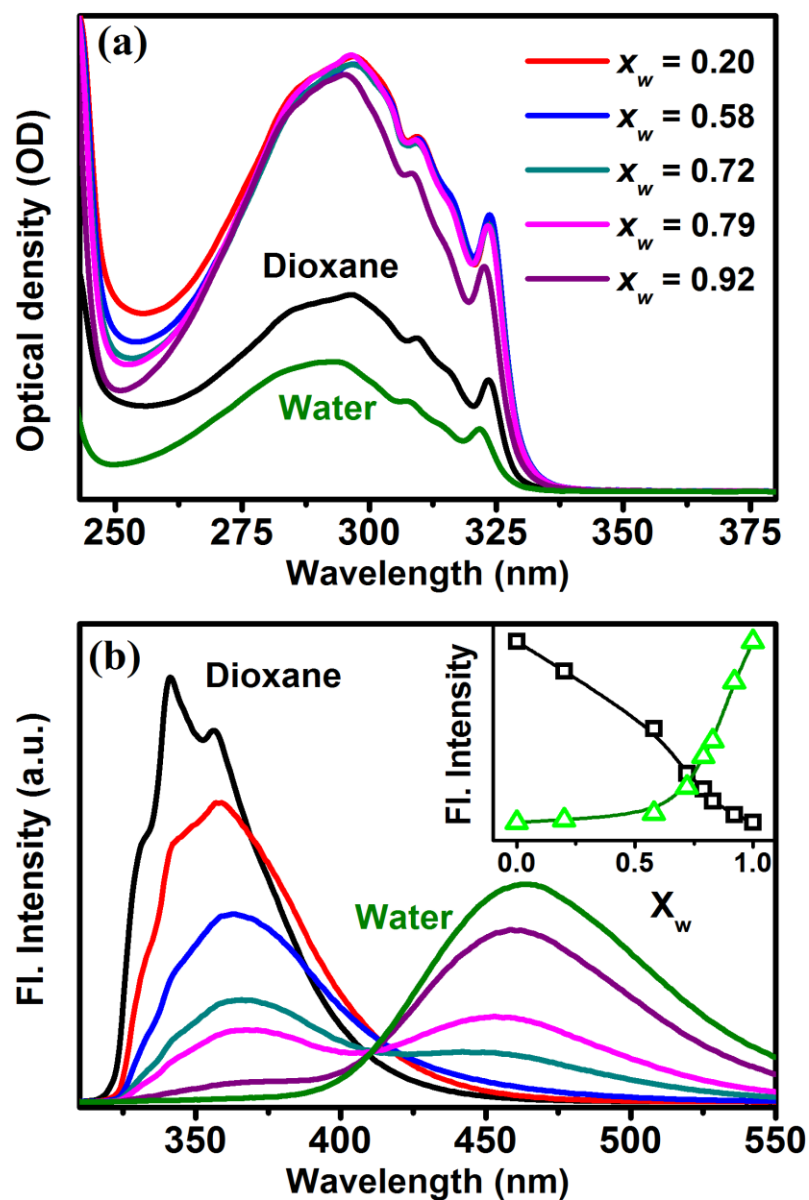
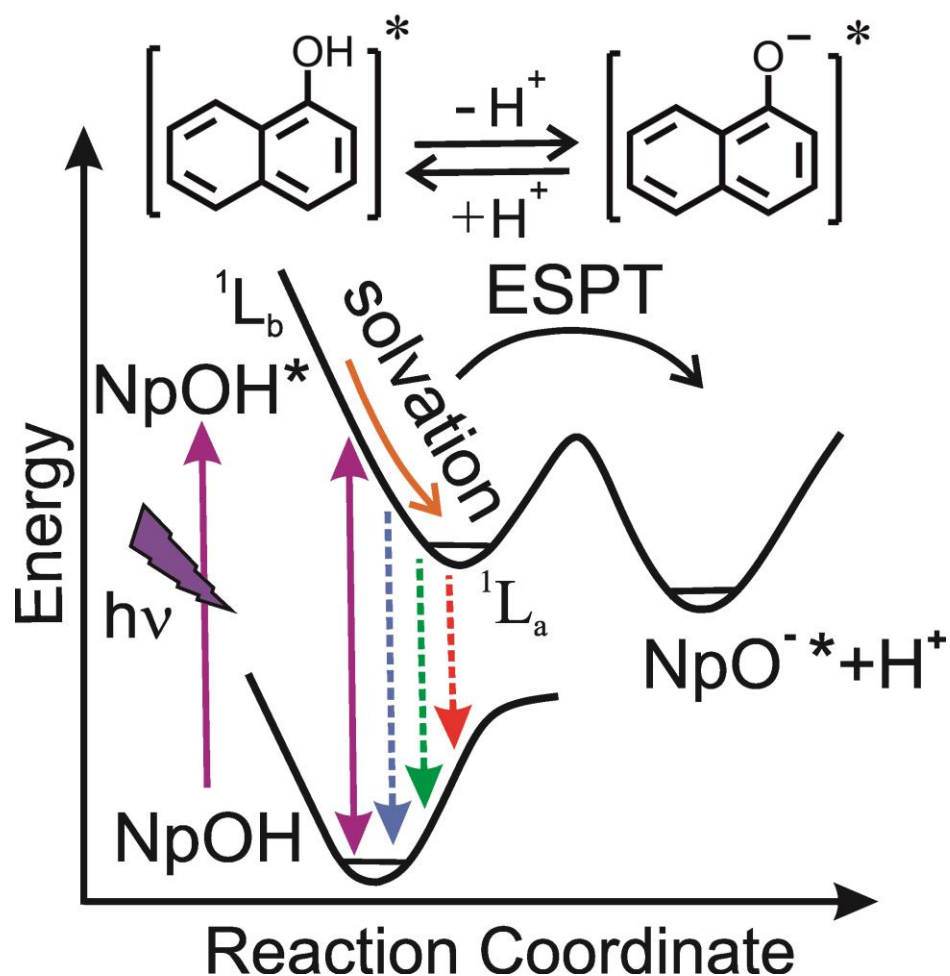


**Figure 6.1:** (a) Absorption and (b) emission spectra of 1-naphthol in water–DX mixture with different mole fraction ( $x_w$ ) of water. Inset: plot of variation of the normalized-fluorescence intensity of the protonated naphthol (NpOH) and deprotonated (NpO<sup>-</sup>) formed at different mole fractions of water in water–DX mixture.

single emission band centered at 360 nm. On addition of water, the intensity of this band decreases, and a new band grows at 460 nm. The short wavelength emission has been attributed to protonated NpOH, whereas the long wavelength emission to deprotonated 1-naphtholate anion (NpO<sup>-</sup>), characteristic of the excited state proton transfer (ESPT) between NpOH and water as solvent [20]. The relative fluorescence intensity of the protonated and deprotonated form with increasing mole fractions of water is shown in the

inset of Figure 6.1b. As the water content increases, the ESPT process is more and more facilitated. This progressive increase in ESPT is related to polarity of the solvent mixture, which mainly refers to the hydrogen bonding ability of the solvent. One may note that the ESPT process is believed to follow a three-state two-step model [21] as shown in Scheme 6.1. Optical excitation of NpOH leads to  $^1L_b$  state. Depending upon the hydrogen bonding ability and dielectric constant, the relatively nonpolar first excited state relaxes to the second polar acidic excited state  $^1L_a$  that has the oxygen-to-ring charge transfer character, which is required for ESPT. This is followed by removal of the proton in coordination with relaxation of the solvent around the new ion pair. Thus, properties of the solvent and relaxation dynamics determine whether only the first or both steps take place.



*Scheme 6.1: Schematic illustration of the excited state solvation of 1-naphthol in coordination with proton transfer process. Optical excitation of NpOH leads to  $^1L_b$  state, which attains the second polar acidic excited state  $^1L_a$  after solvation and finally removal of the proton to the surrounding water molecules.*

In pure nonpolar DX, the only emitting species is first relatively nonpolar excited state and as such there is no ESPT. However, in the case of water–DX mixture, after the first step, the lowest excited state interacts with the solvent water molecule, leading to the ESPT reaction. It should also be noted that there is no sign of ESPT reaction up to  $x_w = 0.58$  (Figure 6.1b). This might be due to NpOH, that does not get enough water molecules in their immediate environment. Previously, it was shown that clusters composed of a minimum of approximately 30 or more water molecules are required around the probe NpOH so that proton affinity of the cluster is sufficient to promote ESPT [21]. The observed decrease in the fluorescence intensity at ca 330 nm (characteristic of neutral NpOH) and consecutive growth at ca 450 nm (characteristic of NpO<sup>-</sup>) are the consequences of the progressive increase in water cluster size (Figure 6.1b). It has to be noted that at 0.79 mole fraction of water ( $x_w$ ), the intensity of the protonated and deprotonated forms are comparable (Figure 6.1b). Hence, the time-resolved measurements are carried out at this particular concentration ( $x_w = 0.79$ ). The choice of this concentration also lies in the fact that at  $x_w = 0.79$ , the water clusters have different geometry than that in the bulk water due to the breakage of the hydrogen bond network. Pure water clusters begin to appear at the critical point  $x_w \geq 0.83$  [22]. This is also reflected in the faster relaxation rate with increase in the water content in water–DX, which increases the number of hydrogen bonds per oxygen atom [23]. Our DLS experiment confirms a cluster size of ~350 nm in the  $x_w$  of 0.79.

We have measured fluorescence decays at a number of wavelengths across the emission spectrum of NpOH in water–DX mixture of  $x_w = 0.79$  and the fitting parameters are tabulated in Table 6.1. Figure 6.2a shows the decay transients at three representative wavelengths (330, 440 and 490 nm). It is observed that the fluorescence decays are wavelength dependent, and there is evidence of a rise in the intensity as a function of time at the longest wavelengths (490 nm). It is known that this type of rise in intensity is characteristic of an excited state process in which the emitting species is not directly excited but rather forms, from a previously excited state [24]. We have used the fluorescence transients to construct TRES (time-resolved emission spectra) as shown in Figure 6.2b. In TRES, the temporal profiles are well fitted by the sum of two lognormal

**Table 6.1: The fluorescence lifetimes for 1-naphthol and Coumarin 500 in water–dioxane mixture with  $x_w = 0.79$  with a standard error of ca 10%.**

	Wavelength (nm)	$a_1$ (%)	$\tau_1$ (ps)	$a_2$ (%)	$\tau_2$ (ps)	$a_3$ (%)	$\tau_3$ (ps)
<b>1-Naphthol</b>	330	10	220	82	1000	8	2350
	340	3	260	86	970	11	2140
	350	-	-	95	1010	5	2750
	360	-	-	95	1010	5	2640
	370	-12	20	105	980	7	2760
	380	-12	70	108	1020	4	2860
	390	-18	90	113	1020	5	3400
	400	-16	50	111	1060	5	5840
	410	-12	70	102	1070	10	6710
	420	-25	80	102	1150	23	7450
	430	-35	100	90	1300	45	7580
	440	-45	160	72	1560	73	7780
	450	-69	220	61	1930	108	8020
	460	-93	270	67	3110	126	8320
	470	-120	360	77	3530	143	8550
	480	-154	380	100	4130	154	8830
	490	-179	430	167	5080	112	10260
<b>C500</b>	450	70	60	5	560	25	4980
	460	55	70	5	1050	040	5010
	470	43	80	5	1380	52	5000
	480	28	100	8	2410	64	5070
	490	18	100	10	2630	72	5060
	500	11	100	15	2960	74	5120
	510	3	110	32	3640	65	5310
	520	1	100	27	3600	73	5200
	530	-3	420	9	2110	94	4950
	540	-10	700	11	1180	99	4880
	550	-14	540	13	1000	101	4880
	560	-7	240	12	3040	95	4980
	570	-8	200	56	4120	52	5480
	580	-11	170	52	4140	59	5370
590	-19	70	83	4420	39	5270	
600	-36	80	11	3800	125	4875	

functions revealing two excited state processes. At time  $t = 0$  ns, only one peak centered at  $27\,140\text{ cm}^{-1}$  is observed revealing the signature of neutral NpOH. As time progresses, the peak intensity decreases (Figure 6.2b) and shows time-dependent Stokes shift (TDSS), which is indicative of dynamic solvation. A new band near  $22\,332\text{ cm}^{-1}$  appears, which is a characteristic of ESPT. The intensity of this new band keeps growing, which can be readily used to measure the kinetics of the NpO<sup>-</sup> ion formation. Thus, the rate of proton transfer (formation of NpO<sup>-</sup>) is estimated by plotting the time-dependent intensity at  $22\,332\text{ cm}^{-1}$  as shown in the inset of Figure 6.2b, which reveals a time constant of 220 ps (Table 6.2).

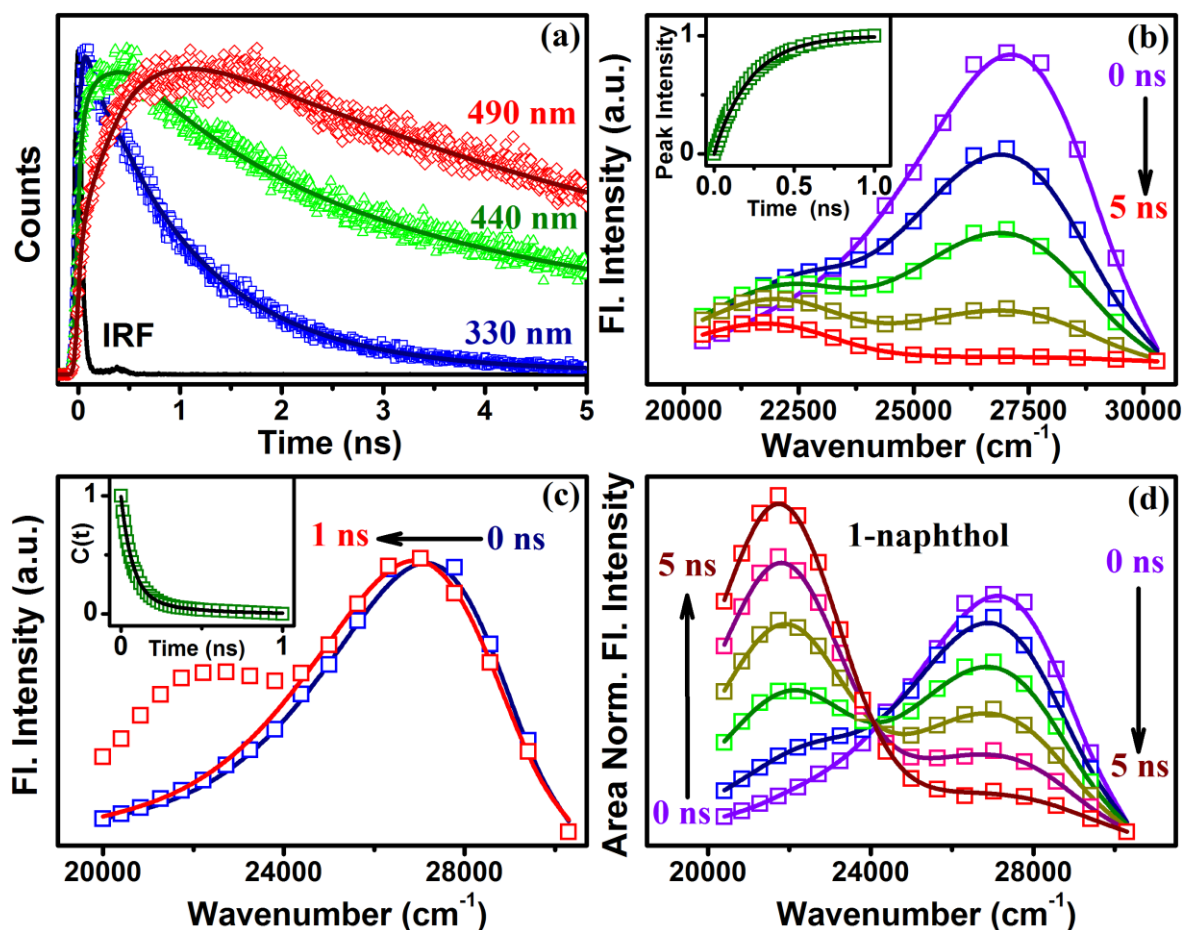


**Figure 6.2:** (a) Picosecond-resolved decay transients of 1-naphthol at 330, 440 and 490 nm in water-DX mixture with  $x_w = 0.79$  at room temperature (excitation at 300 nm). (b) Time-resolved emission spectra (TRES) of 1-naphthol for  $x_w = 0.79$  in water-DX mixture. The peak fluorescence intensity at 450 nm of naphtholate anion (NpO<sup>-</sup>) is shown in the inset. (c) Normalized time-resolved emission spectra of 1-naphthol in water-DX mixture with  $x_w = 0.79$ . The corresponding solvent correlation function,  $C(t)$ , has been shown in the inset. (d) TRANES of 1-naphthol for  $x_w = 0.79$ .

From the TRES it is also evident that emission from locally excited state (LE) is dominant in the wavelength region of 30 303–23 809  $\text{cm}^{-1}$ . On the other hand, the emission from the NpO<sup>-</sup> is prevailing in the region of 21 739  $\text{cm}^{-1}$ . It is evident from Table 6.1 that the longer time component (ca 2.3 ns) of the fluorescence transients gradually increases with the increase in the detection wavelength (from 2.4 ns at 330 nm to 8.0 ns at 450 nm) of LE emission. The observation is consistent with the fact that NpOH molecules, which are stabilized by the solvation, are expected to encounter higher solvation energy barrier for the ESPT process as shown in Scheme 6.1. Our observation is consistent with the results reported in the earlier femtosecond-resolved studies on a twisted intramolecular

charge transfer (ICT) probe (2-(*p*-toluidino)naphthalene-6-sulfonate; TNS), where two competing processes, namely solvation and twisting dynamics, were found to be major deactivation channels in the excited state of the probe molecule [25].

**Table 6.2: Proton transfer and solvent correlation time constants for 1-naphthol and Coumarin 500 in water–dioxane mixture with  $x_w = 0.79$  with a standard error of ca 10%.**

<i>Probe</i>	<i>Temperature (K)</i>	$\tau_1$ (ps) (%)	$\tau_2$ (ps) (%)	$\langle \tau \rangle$ (ps)	$\tau_T$ (ps)
<i>1-Naphthol</i>	278	76 (90)	1000 (10)	168	380
	293	70 (85)	340 (15)	110	220
	313	65 (100)	-	65	230
<i>C500</i>	278	99 (87)	55 (13)	160	-
	293	67 (55)	15 (45)	105	-
	313	72 (69)	13 (31)	89	-

To show the TDSS of LE NpOH more clearly, we have normalized the fluorescence intensity at 27 140  $\text{cm}^{-1}$  and fitted with a lognormal function as shown in Figure 6.2c. The observed Stokes shift is roughly 255  $\text{cm}^{-1}$  over a time window of 1 ns. From the dynamic Stokes shift, we have constructed the solvent correlation function ( $C(t)$ ) to obtain the solvation time constants (inset of Figure 6.2c). The constructed  $C(t)$ , can be fitted biexponentially with time constants of 70 (85%) and 340 ps (15%) (Table 6.2). It should be noted that both the observed time constants are much slower than the subpicosecond solvation time constant of bulk water [26]. These slow components might have their genesis in the translational diffusion of water into the solvation shell displacing the nonpolar solvent molecule in the cluster [27-29]. Such slow solvation dynamics in relatively concentrated solutions of polar fluid in hydrophobic solvents has previously been reported [27, 30]. The average solvation time constant ( $a_1\tau_1 + a_2\tau_2 = \langle \tau_s \rangle = 110$  ps) in our case is in good agreement with that reported by Mitra et al. [23] with Coumarin 500 for a similar system with  $x_w = 0.826$ . A significant retardation in the proton transfer rate and the dynamics of solvation in our experimental condition ( $x_w = 0.79$ ) can be rationalized as follows.

In pure water, NpOH undergoes ESPT in ca 35 ps, causing a 35 ps fall time of the protonated species and a ca 35 ps rise time for the deprotonated product, 1-naphtholate anion [20]. At  $x_w = 0.79$ , we have also observed a fall (at 330 nm for the protonated form)

and rise (at 450 nm for the deprotonated form) time of ca 220 ps (Table 6.1). Thus, the ESPT in water–DX mixture is slowed down approximately seven times compared with that in pure water. The reduction in ESPT has two probable causes. First, local concentration of water molecules near the photoacid, NpOH in water–DX mixture should be sufficient to promote proton transfer. In fact, a cluster composed of minimum of 30–50 water molecules is required to promote ESPT [31]. Second, the solvation reorganization in water–DX mixture (ca 110 ps) is much slower compared with that in bulk water (ca 1 ps). For water–DX mixture, water clusters are present with considerably different geometry than that in the pure water due to breakage of the hydrogen bond network. Previously, Knochenmuss and Smith suggested that the ESPT rate is controlled by the rate at which the water relaxes around the NpOH fluorophore, via interaction with two electronic excited states [32]. Thus, time-resolved analysis as discussed above clearly indicates that the dynamical rearrangement (solvation of average time of 110 ps) is an essential requirement prior to the ESPT (average time of 220 ps). An isoemissive point at  $24\,086\text{ cm}^{-1}$  in the TRANES as shown in Figure 6.2d indicates the presence of two distinct species [33] namely neutral NpOH and the  $\text{NpO}^-$  anion revealing characteristic peaks at  $27\,140$  and  $22\,332\text{ cm}^{-1}$ . It is evident from Figure 6.2d that at time  $t = 0$ , there is only one emission band centered at  $27\,140\text{ cm}^{-1}$  and the emission is from the LE NpOH. As time progresses, the band at  $22\,332\text{ cm}^{-1}$  is clearly seen to grow at the expense of the one at  $27\,140\text{ cm}^{-1}$ .

To check the reliability of the solvation time constants as revealed by NpOH, we have studied the excited state dynamics of Coumarin 500 (C500), a well-known solvation probe in the same composition of water–DX mixture. To construct the TRES, the decay transients of C500 have been monitored at 16 different wavelengths from 450 to 600 nm with 10 nm interval. Figure 6.3a represents the emission decays at two extreme wavelengths (450 and 600 nm). On the blue edge of the spectrum (450 nm), the fluorescence transient undergoes decay, whereas on the red edge (600 nm) it rises, which is the clear indication of relaxation dynamics of C500. The inset of Figure 6.3b denotes the constructed TRES of the system. The constructed TRES shows a spectral shift of  $395\text{ cm}^{-1}$  and the corresponding solvent response function (Figure 6.3b) is well fitted biexponentially with time constants of 67 ps (55%) and 150 ps (45%; Table 6.2). It is to be

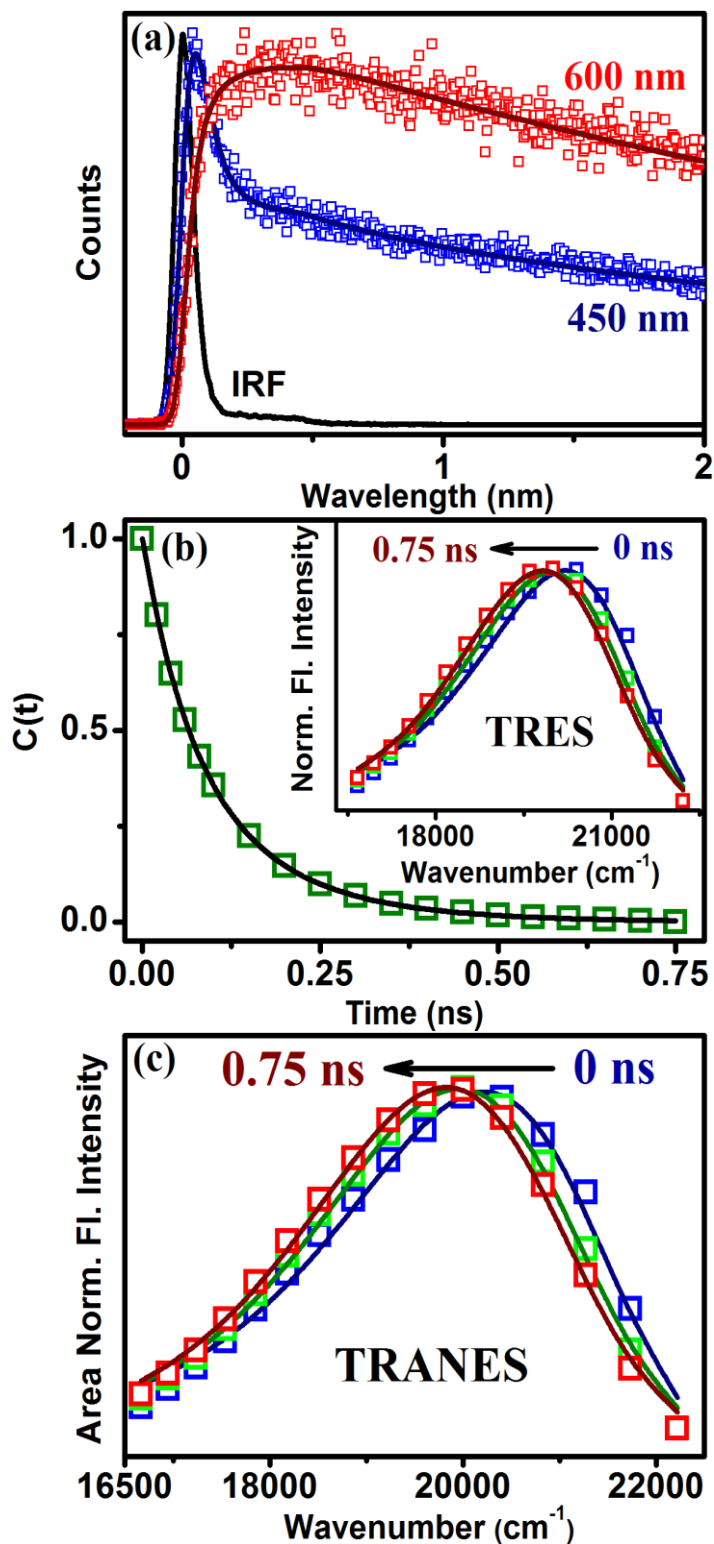
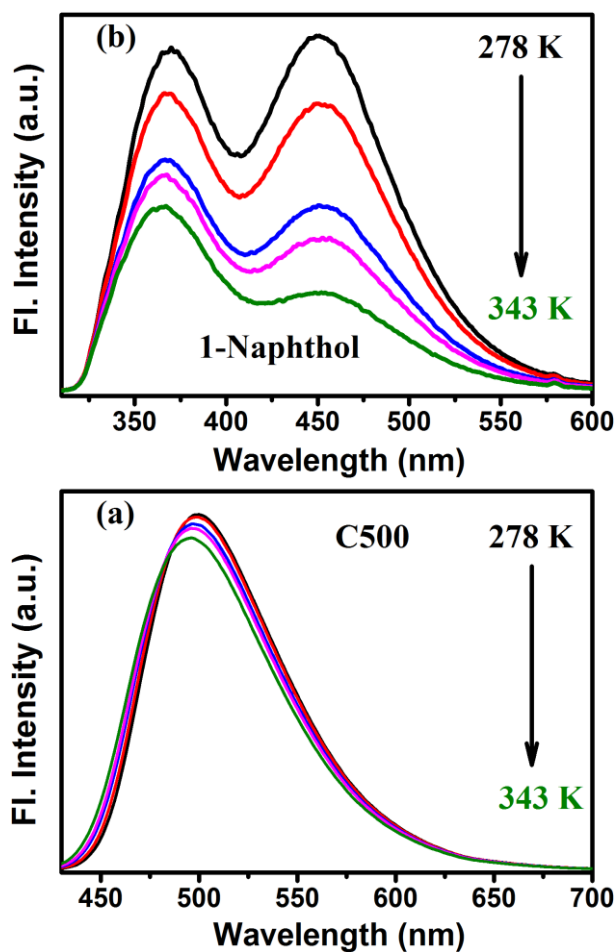


Figure 6.3: (a) Picosecond-resolved decay transients of C500 at 450 and 600 nm detection wavelength in water-DX mixture with  $x_w = 0.79$  ( $\lambda_{ex} = 409$  nm). (b) Solvent correlation function,  $C(t)$ , of C500 in water-DX mixture with  $x_w = 0.79$ . The corresponding TRES has been shown in the inset. (c) TRANES of C500 in water-DX mixture with  $x_w = 0.79$ .

noted that TRANES analysis of C500 (Figure 6.3c) is devoid of any isoemissive point indicating the fact that there is a single emitting species in the excited state and the continuous time evolution is due to the solvation dynamics only. The average solvation time constant of 105 ps is in good agreement with that obtained using NpOH (Table 6.2).

The solvent reorganization around NpOH certainly involves breaking of hydrogen bonds as molecules translate and rotate, and this will require activation. It is therefore constructive to perform a temperature dependent study of the system. Figure 6.4 shows the emission spectra of NpOH and C500 with  $x_w = 0.79$  at five different temperatures. From Figure 6.4a it is evident that emission intensity of NpOH decreases significantly with increasing temperature. In fact, the extent of decrease of fluorescence intensity for the



*Figure 6.4: Emission spectra of 1-naphthol (a) and C500 (b) in water–DX mixture of  $x_w = 0.79$  at different temperatures.*

anionic form (450 nm) is higher than that for the neutral species (360 nm). A small blueshift (around 4-5 nm) of the peak at 360 nm is also evident. However, no such change in the absorbance spectra is found for NpOH with increasing temperature. The steady-state emission spectra of the system using C500 (Figure 6.4b) shows a marginal (3–4 nm) blueshift as the temperature is increased from 278 to 343 K. The observed blueshift indicates a less polar environment experienced by the probe at elevated temperatures. To gain more insight, we performed time-resolved measurement of  $x_w = 0.79$  at five different temperatures. The constructed TRES are shown in the Figure 6.5a, b at 278

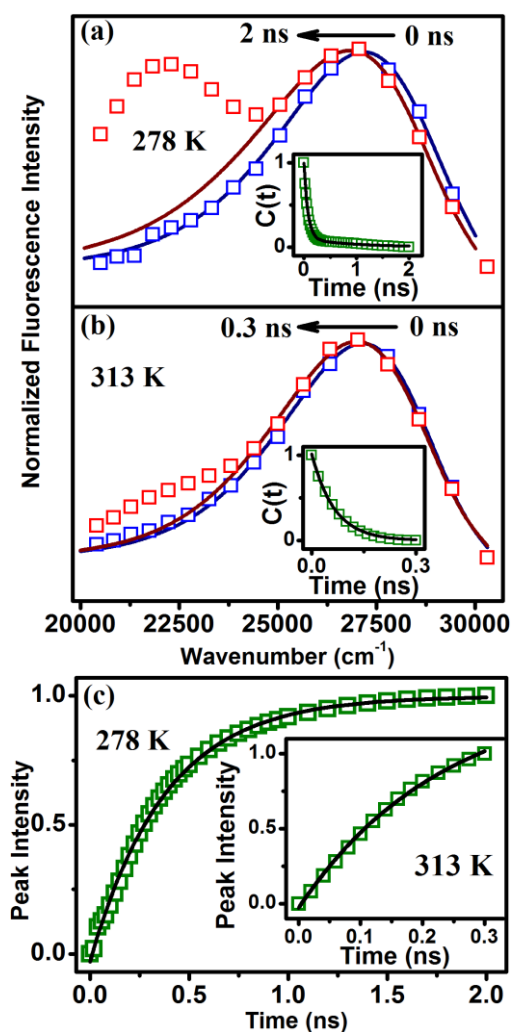


**Figure 6.5:** Normalized time-resolved emission spectra of 1-naphthol in water–DX mixture with  $x_w = 0.79$  at 278 K (a) and 313 K (b). The corresponding solvent correlation function,  $C(t)$ , has been shown in the inset. (c) The increase in peak intensity of the deprotonated form (NpO<sup>-</sup>) at two different temperatures (278 and 313 K), respectively.

and 313 K, respectively. TDSS of the protonated species is used to construct solvent correlation function and the values are listed in Table 6.2. The overall decrease of the average solvation time on increasing temperature reveals that an increase in temperature accelerates the solvation process. It has to be noted that due to our limited instrumental resolution we could not resolve the water dynamics at higher temperature ( $>313$  K) in the present system. The temperature-induced acceleration of solvation dynamics is possibly due to breakdown of the hydrogen bond network followed by the formation of smaller clusters with increasing temperature [23]. In fact, it has been suggested that DX

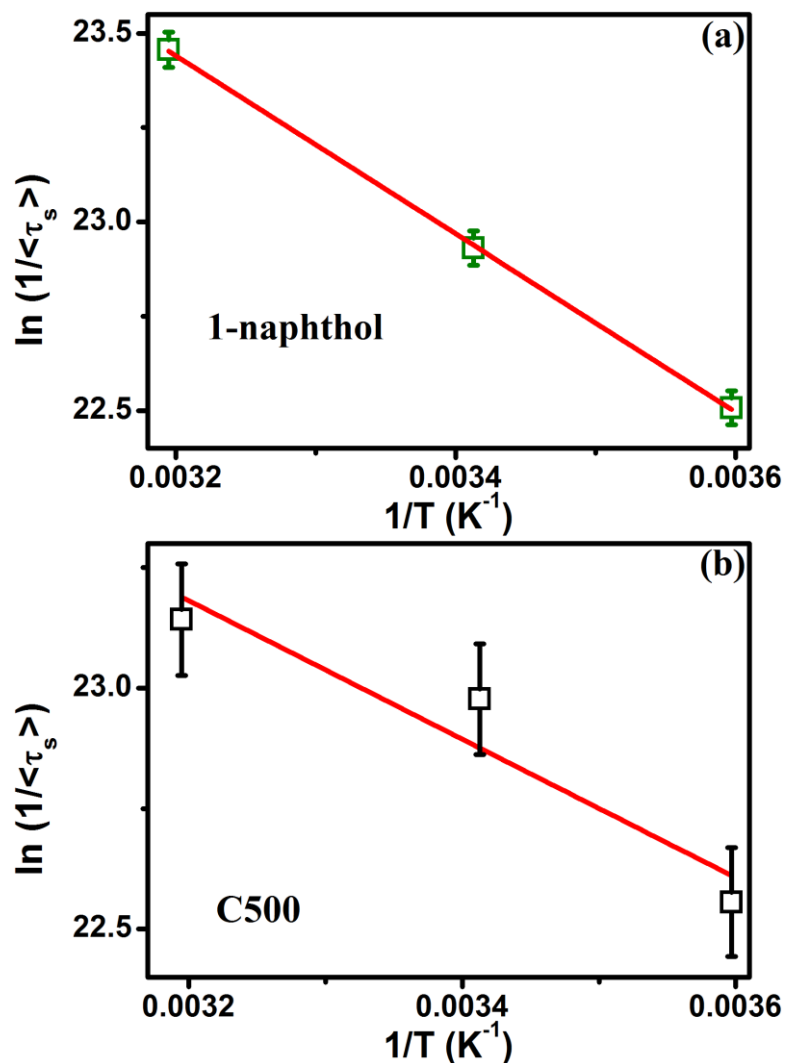


*Figure 6.6: Arrhenius plot for water–DX mixture in  $x_w = 0.79$  with two different dyes (1-naphthol and C500). The solid lines are the best linear fit. The error bars are of 0.2% and 0.5%, respectively.*

specifically binds five or six water molecules into more strongly bound hydrogen-bonded structures than in liquid water itself [34, 35]. There exists a dynamic equilibrium between the bound type (strongly hydrogen bonded to ether oxygen of DX) and free type (not directly hydrogen bonded to DX). The energetic of the exchange depends upon the strength and the number of hydrogen bonds among the water molecules at the interface (i.e., water–DX interface). The bound to free type transition of water molecules with temperature is assumed to be governed by an Arrhenius type of activation energy barrier crossing model [36, 37]. We fit an Arrhenius plot using the  $\langle \tau_s \rangle$  values listed in Table 6.2 (Figure 6.6a). Plots of  $\ln(1/\langle \tau_s \rangle)$  vs  $1/T$  produce good linear fit with corresponding activation energy ( $E_{\text{act}}$ ) values of  $4.60 \pm 0.2$  kcal mol<sup>-1</sup>. We also perform similar measurement (Figure 6.6b) using C500 in identical system, which purely senses solvent relaxation (Table 6.2) and  $E_{\text{act}}$  is found to be  $2.85 \pm 0.4$  kcal mol<sup>-1</sup>. Solvent reorganization results from solvent relaxation around the solute molecule (fluorophore) following a change in the excited state dipole moment. The difference in the activation energies is probably due to the difference in specific hydrogen bonding interactions of the probe fluorophores in the water clusters [23, 30].

Having understood the temperature-induced acceleration of solvation dynamics, we now focus on the proton transfer rate. The peak intensity of the deprotonated form provides the value of proton transfer time constant. The proton transfer time constant becomes faster on raising the temperature from 278 to 293 K and then does not change appreciably (Table 6.2). This is in contrast to the solvation dynamics where a progressive decrease in average solvation time constant is observed with increasing temperature. This discrepancy can be understood as follows. As discussed earlier, ESPT is mainly controlled by two factors namely local concentration of water molecules near the photoacid and solvent reorganization. We have discussed that at elevated temperatures, the hydrogen bond network of clusters break down and isolated small clusters consisting of different geometry of hydrogen bonded water start growing. This lowers the polarity of the system due to breakage of hydrogen bonded network, which is also evident from the steady-state emission spectra of the probe as discussed earlier (Figure 6.4a,b). Both the lowering in the polarity and local concentration of water favor the emission from the relatively nonpolar

first excited state  $^1L_b$  and disfavor second polar acidic excited state  $^1L_a$  that has the oxygen-to-ring charge transfer character, which is required for ESPT.

### 6.2.2. Slow Solvent Relaxation Dynamics of Nanometer Sized Reverse Micellar Systems Through Tryptophan Metabolite, Kynurenine [38]:

Figure 6.7a depicts the results obtained from DLS measurement of Brij 30 reverse micelle (RM) in isooctane (i-Oc) at different  $w_0$  values. It can be observed that Brij 30 RM

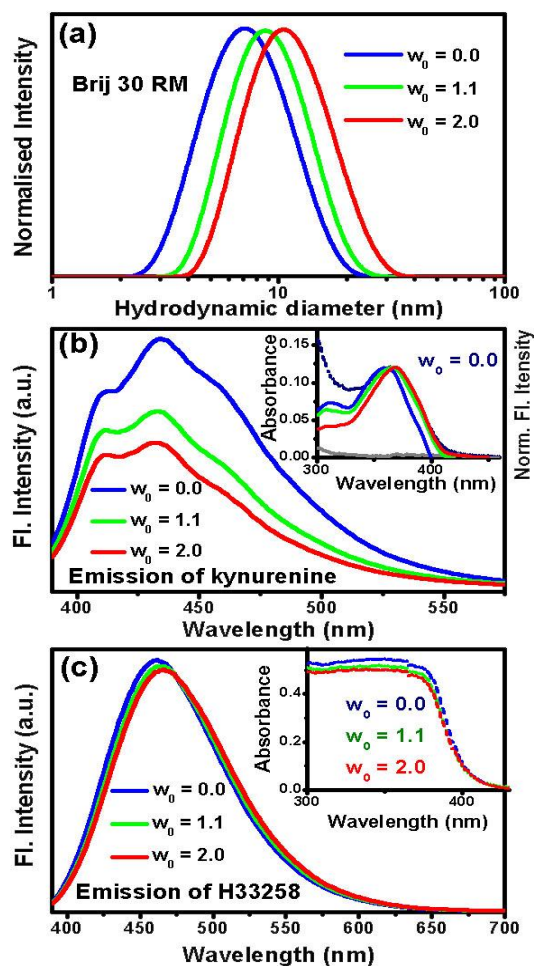


*Figure 6.7: (a) Hydrodynamic diameter of Brij-30 / isooctane / water reverse micellar systems with  $w_0 = 0.0, 1.1$  and  $2.0$ . (b) Emission spectra ( $\lambda_{ex} = 375$  nm) of KN in reverse micelles of different  $w_0$  values. Inset. Isooctane subtracted absorption spectra of the empty RM (solid gray line) and KN at  $w_0 = 0$  (dash line). Normalized excitation spectra of KN (solid line) with  $w_0 = 0$  monitored at 410 nm, 430 nm and 460 nm are also presented in the inset. (c) Emission ( $\lambda_{ex} = 375$  nm) and absorption (inset) spectra of H33258 in the nano-cavity of reverse micelle at different  $w_0$  values.*

produces spherical and monodispersed droplets with a hydrodynamic diameter of 7.8 nm for  $w_0 = 0$ . As  $w_0$  increases, the hydrodynamic diameter of the RM increases due to the increase of water pool size. Inset of Figure 6.7b shows the absorbance of kynurenine (KN) in the RM at  $w_0 = 0$  (dash line) and the empty RM (gray line). The broadening of the absorption spectrum of KN could be due to the existence of KN at different locations, as empty RM are not supposed to absorb at this wavelength region. Emission spectra of KN in the RM with different  $w_0$  values are shown in Figure 6.7b. A small redshift in the absorption spectrum and a significant blueshift in the emission spectrum compared to KN in water [39] due to the stabilization of excited state energy on varying the nature of the solvent, reveal the binding of KN with the RM. KN exhibits the emission spectrum with three shoulders at around 410, 435 and 460 nm respectively, which may be due to different locations of the probe in the RM system [39]. The emission peak at 460 nm corresponds to KN in the polar region of associated water molecules (pool) in the RM [40]; 435 nm stands for the probe near the polar head groups of Brij 30 and the small water pool which is similar to protein bound KN [41], whereas 410 nm corresponds to KN in the interface between Brij 30 and i-Oc due to maximum destabilization of S1 state [39]. We have also checked that the empty RM has no emission at this wavelength region which excludes the possibility of any contribution from empty RM. We have also recorded excitation spectra (inset of Figure 6.7b) at different selected wavelengths over the whole emission spectrum of KN in the RM. The overall similarity of the excitation spectra except for the shift of maxima (ca 3 nm) due to the heterogeneity in the location of KN and their consistency with the corresponding absorption spectra (inset of Figure 6.7b) clearly rules out the possibility of fluorescence signal from impurities in the sample.

The decay transients of KN bound to the RM have been studied at 14 different wavelengths, starting from 400 to 530 nm throughout the emission spectra for different  $w_0$  values. Figure 6.8a represents the fluorescence decay transients of KN in Brij 30 RM of  $w_0 = 0$  at two different wavelengths 400 and 530 nm. On the blue edge of the spectrum (400 nm) the signal is seen to decay, whereas on the red edge (530 nm) it rises, which is the clear indication of the excited state relaxation dynamics of KN. Similar results are found for the other  $w_0$  values. From this family of transients, we have constructed the TRES

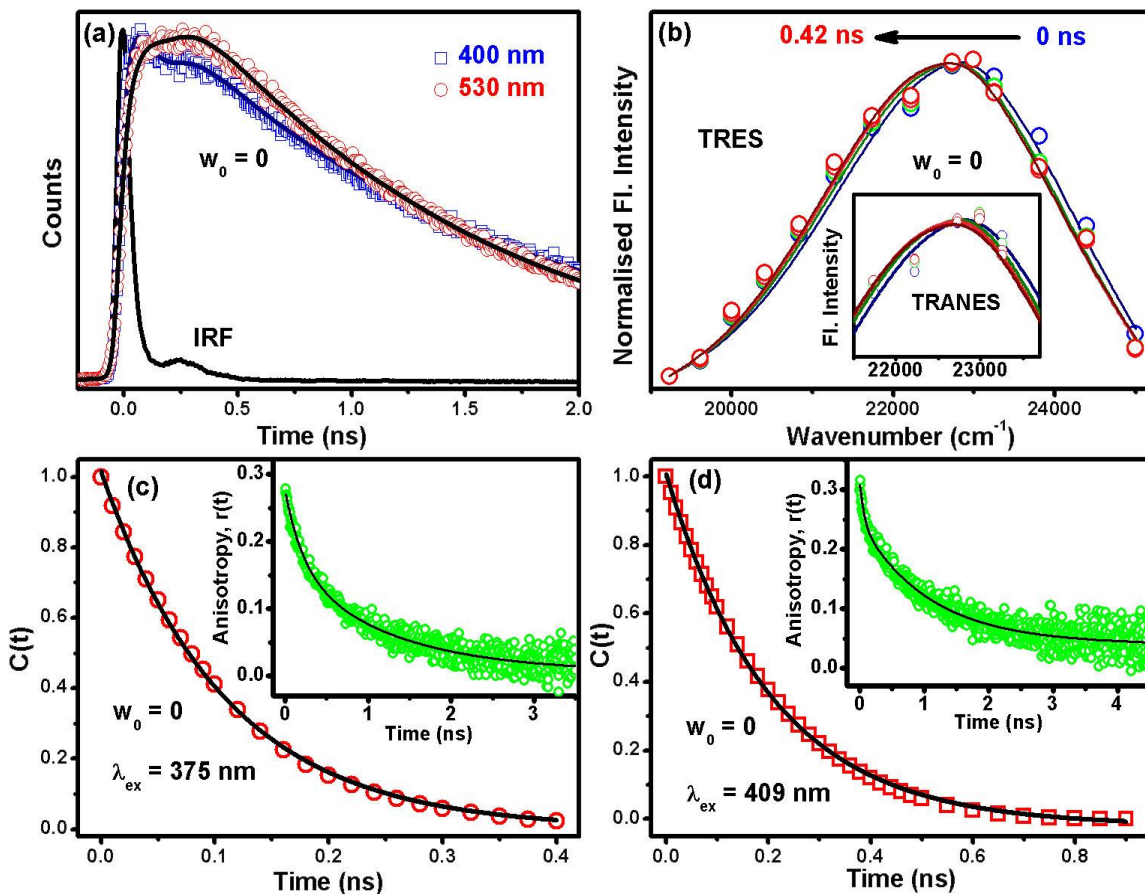


**Figure 6.8:** (a) Fluorescence transients, (b) TRES and TRANES (inset) of KN in Brij 30 RM at  $w_0 = 0$ . (c) and (d) Solvent relaxation dynamics and fluorescence anisotropy decay (inset) of KN in Brij 30 RM at  $w_0 = 0$  at 375 and 409 nm excitation, respectively.

at different  $w_0$  values. The observed dynamical Stokes shift is relatively small ( $160 \text{ cm}^{-1}$ ) for  $w_0 = 0$  and eventually completed within 420 ps (shown in Figure 6.8b). To explore the environmental dynamics of KN at different  $w_0$  values, the temporal decay of solvent correlation function,  $C(t)$  has been constructed. Figure 6.8c reveals the  $C(t)$  decay of KN at  $w_0 = 0$ , which shows an apparent mono-exponential decay with time constant of 105 ps. With an increase of  $w_0$  values,  $C(t)$  becomes faster (see Table 6.3). It could also be noted that an ultrafast component of the solvent response, which is due to the relaxation of bulk-like water (of the order of a few picoseconds) is not resolvable in our experimental setup. In order to calculate the missing spectral shift in the solvent relaxation process, we have applied the method suggested by Fee et al. [42]. The real time-zero in the emission maximum ( $\nu(t = 0)$ ) can be estimated from the steady-state absorption and fluorescence maxima by the following equation:

$$v(t=0) = v_p(\text{abs}) - [v_{np}(\text{abs}) - v_{np}(\text{fl})] \quad (6-1)$$

where the subscripts ‘‘p’’ and ‘‘np’’ refers to the spectra in polar and nonpolar environments respectively. In the present study, we have used protein bound KN spectra as a nonpolar environment with absorption and emission maxima at 360 and 435 nm respectively and water is used as the polar solvent where KN shows an absorption peak at 360 nm. The percentage of missing spectral shift is  $((v_{\text{cal}}(0) - v(0)) / (v_{\text{cal}}(0) - v(\infty))) \times 100$ . The observed time zero frequency and the time infinity frequency for KN in RM of  $w_0 = 0$  are  $22\,778\text{ cm}^{-1}$  and  $22\,618\text{ cm}^{-1}$ , respectively. The missing spectral shift corresponding to the unobservable solvent relaxation component for the present time resolution and the percentage of missing spectral shift are also listed in Table 6.3. On addition of water to the RM the missing spectral shift gradually increases. This result seems to be logical because the formation of bulk type water molecules in the pool increases upon addition of water above  $w_0 = 0$ , leading to faster environmental dynamics beyond the resolution of our experimental setup.

**Table 6.3: Solvent relaxation time constant and rotational time constants of kynurenine (KN) in the reverse micellar system at various  $w_0$  values with a standard error of ca 10%.**

$w_0$	Solvation time constant $\tau$ (ps)	$\Delta\nu$ ( $\text{cm}^{-1}$ )	Missing Spectral Shift	Rotational time constants		
				$\tau_1$ (ps)	$\tau_2$ (ns)	$\tau_3$ (ns)
<b>0.0</b>	105	160	57%	210 (39%)	1.2 (57%)	30 (4%)
<b>1.1</b>	54	70	63%	100 (36%)	1.0 (58%)	55 (6%)
<b>2.0</b>	49	66	71%	160 (36%)	1.2 (61%)	100 (4%)

In order to investigate the existence of multiple emitting species in various environments with different excited state lifetime values leading to time-dependent spectral shift, we have employed the TRANES technique. For  $w_0 = 0$  the TRANES are shown in the inset of Figure 6.8b. An isoemissive point at  $22\,730\text{ cm}^{-1}$  for  $w_0 = 0$  is clearly evident, revealing the possible coexistence of at least two species in the microenvironments of the RM. The observation is consistent with the fact that the probe KN may interact with water molecules in the excited state [39] by different strength revealing distinct spectroscopic signature of emission maximum. In other words KN at the micellar interface is less likely to form hydrogen bond with water molecules [41] (emission peak ca  $23\,000\text{ cm}^{-1}$ ) compared to that in the water pool of the RM [39] (emission peak ca  $22\,000\text{ cm}^{-1}$ ),

revealing the signature of multiple species in the excited state. The temporal decay of fluorescence anisotropy ( $r(t)$ ) of the KN–RM complex at  $w_0 = 0$  is shown in the inset of Figure 6.8c. It has to be noted that the time constants associated with the decay of  $r(t)$  are consistent with the geometric restriction of the probe in the restricted environments. The decay transients have been fitted triexponentially, and the results are shown in Table 6.3. It can be observed that the time constants are of the order of hundreds of picoseconds and a few nanoseconds, which are in the same order of magnitudes for wobbling motion and lateral diffusion respectively, similar to previous result for a coumarin dye in the Brij 30 RM systems [40]. In the present analysis we have fixed the longer time constant indicative of the overall rotation of the RM and estimated from the following well-known Debye–Stokes–Einstein equation:

$$\tau = \frac{\eta V}{k_b T} \quad (6-2)$$

where  $\eta$  is the microviscosity experienced by the probe and  $V$  is molecular volume of the RM. A minor change in the locations of the probe in the RM with various hydrations ( $w_0$ ) is clearly evident from the anisotropy data (Table 6.3). It has to be noted that in the case of the broadening of KN absorption band, the fluorescence lifetime of KN may depend on the excitation wavelength, due to relative contributions from KN at different locations in the RM. The decay time constant of the solvent correlation function ( $C(t)$ ) in Figure 6.8d from a series of detected fluorescence transients with excitation wavelength of 409 nm is found to be comparable with that of the 375 nm excitation (Figure 6.8c). Similarly, the anisotropy decay at 409 nm excitation wavelength (inset of Figure 6.8d) is also consistent with that at 375 nm excitation (inset of Figure 6.8c).

In order to investigate the nature of relaxation dynamics as revealed by the probe KN; intermolecular hydrogen bonding in the excited state causes faster deactivation through IC or solvent stabilization (solvation), we have also studied the excited state dynamics of H33258, a well-known solvation probe in the similar restricted environments for comparison. H33258 is a positively charged dye at neutral pH with absorption and emission maxima at 345 and 500 nm, respectively [43], which binds to the surface of the Brij 30 RM revealing emission maximum at 460 nm in the RM of  $w_0 = 0$  at room temperature (shown in Figure 6.7c). It is seen from Figure 6.7c that the peak corresponding

to maximum emission shows a progressive redshift with increasing water pool size depicting more polar environments at higher  $w_0$  values. The absorption spectra (inset in Figure 6.7c) remain unaltered in the entire  $w_0$  values, indicating insignificant perturbation in the ground state stabilization of the probe H32258 in the RM.

To construct TRES, the fluorescence transients are taken at 10 equidistant wavelengths from 400 to 550 nm throughout the emission band over time windows up to 20 ns for different  $w_0$  values. The transients show faster decay in the blue end and rise in the red end (Figure 6.9a) indicative of solvent relaxation dynamics [44]. The constructed TRES shows a spectral shift of  $1800\text{ cm}^{-1}$ . To ascertain whether the associated spectral shift is due to the environmental relaxation or is associated with excited heterogeneity due to the presence of multiple species, TRANES are constructed in a similar manner as described above. Figure 6.9d shows the constructed TRANES of RM-H33258 complex at

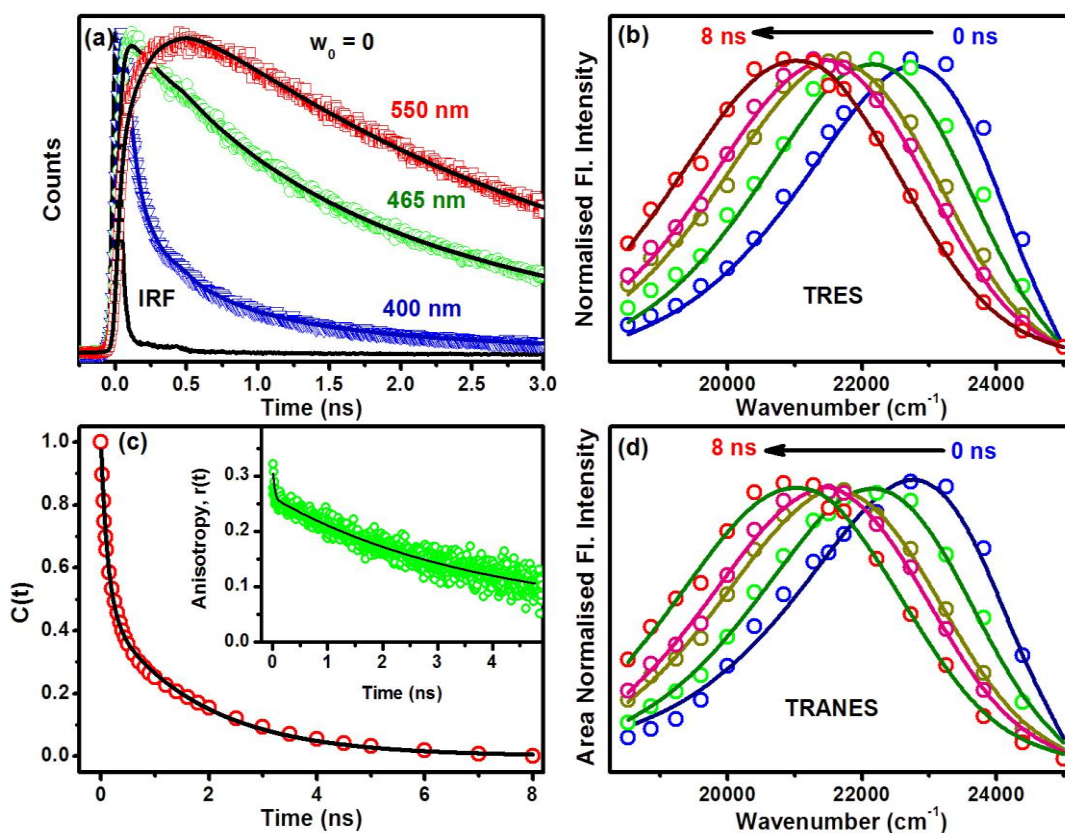


**Figure 6.9:** (a) Fluorescence transients, (b) TRES, (c) solvation correlation function and temporal decay of fluorescence (inset), (d) TRANES spectra of H33258 in Brij 30 RM at  $w_0 = 0$ .

$w_0 = 0$ . The absence of isoemissive point in the TRANES is indicative of a single conformer in the relaxation process, and the measured dynamics indeed reflects environmental stabilization (solvation). The solvation correlation function (Figure 6.9c) shows biexponential decay with time constants of 0.1 ns (53%) and 1.8 ns (47%), respectively, consistent with the previous studies [45]. These solvent relaxation time constants are much slower than H33258 in free aqueous solution (195 fs and 1.2 ps) as reported by Pal et al. [46]. Faster and slower components might be attributed to those water molecules near the polar head group of Brij 30 and in the central region of the water pool respectively. The temporal nature of  $r(t)$ s at different  $w_0$  values (Table 6.4) are similar, which confirms the residence of the probe at the micellar surface. Thus, it could be concluded that the environmental dynamics as reported by H33258 are far off from that of the dynamics as probed by KN with faster IC.

**Table 6.4: Solvation correlation time constants and rotational time constants of H33258 in the reverse micellar system at various  $w_0$  values with a standard error of ca 10%.**

$w_0$	Solvation time constants			$\Delta\nu$ ( $\text{cm}^{-1}$ )	Missing Spectral Shift	Rotational time constants		
	$\tau_1$ (ns)	$\tau_2$ (ns)	$\tau_{av}$ (ns)			$\tau_1$ (ps)	$\tau_2$ (ns)	$\tau_3$ (ns)
<b>0.0</b>	0.1 (53%)	1.8 (47%)	0.9	1800	7%	200 (16%)	3.5 (65%)	30 (19%)
<b>1.1</b>	0.1 (56%)	1.9 (44%)	0.8	1693	11%	100 (19%)	3.5 (74%)	55 (7%)
<b>2.0</b>	0.1 (64%)	1.4 (36%)	0.5	1627	17%	90 (8%)	3.0 (88%)	100 (4%)

In order to establish the binding position of KN into the micellar environment, we have used FRET associated with the nonradiative transfer of excited state energy from the donor fluorophore KN to the surface bound organic dyes, crystal violet (CV) [47] and coumarin 500 (C500) [40], respectively. Figure 6.10a shows the considerable spectral overlap of the probe KN emission with the absorption spectrum of CV, suggesting the possibility of FRET. The significant quenching in the steady-state emission and picosecond-resolved fluorescence transient (at 450 nm) as a consequence of the D–A dipolar interaction is clearly evident from Figure 6.10b. For the estimation of the FRET efficiency, we have considered the faster time constants of the D–A pair, which was absent in the donor emission in absence of the acceptor molecules. We have

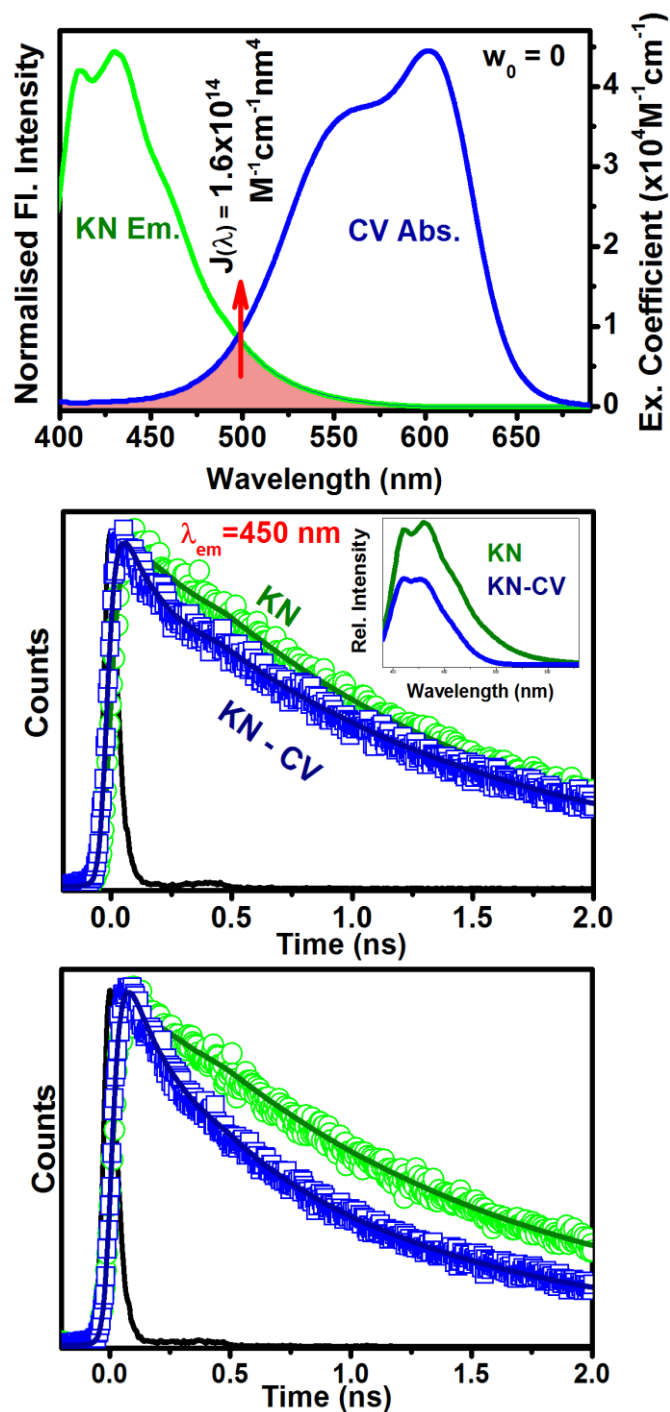


*Figure 6.10: (a) Steady-state absorption spectrum of CV in the form of extinction coefficient and the normalized emission spectrum of KN in Brij 30 RM at  $w_0 = 0$ . An overlapping zone between emission of KN and absorption of acceptor CV is indicated as a pink-shaded zone. (b) Picosecond-resolved fluorescence transients of KN in the absence and in the presence of acceptor CV (excitation at 375 nm) collected at 450 nm. Inset of panel (b) shows the steady-state emission spectrum of KN in Brij 30 RM at  $w_0 = 0$  in the presence and absence of CV. (c) Picosecond-resolved fluorescence transients of KN in the absence and in the presence of acceptor C500 (excitation at 375 nm) collected at 410 nm.*

**Table 6.5: Time-resolved fluorescence decay (excitation at 375 nm and collected at 450 nm) and FRET data of KN in RM at different  $w_0$  values in the absence and presence of CV. Values in parentheses represent the relative weight percentage of the time component with a standard error of ca 10%.**

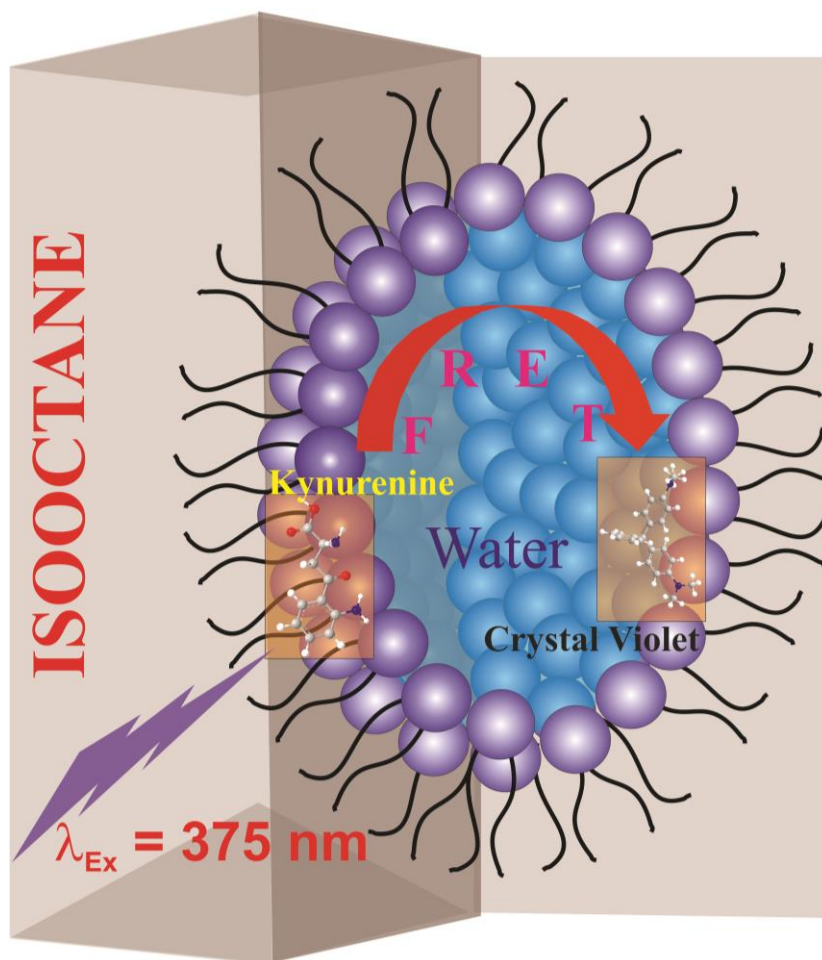
$w_0$	System	$\tau_1$ (ps)	$\tau_2$ (ps)	$\tau_3$ (ps)	$\langle\tau_D\rangle$ (ps)	$Q_D$	$J(\lambda)$ ( $M^{-1} cm^{-1} nm^4$ )	$E$	$R_0$ (nm)	$R$ (nm)
0	KN		1230 (94%)	6120 (6%)	1530	$78.64 \times 10^{-3}$				
	KN-CV	90 (29%)	1220 (65%)	5900 (6%)			$1.6 \times 10^{14}$	94%	2.4	1.5
1.1	KN		1165 (91%)	5150 (9%)	1520	$30.78 \times 10^{-3}$				
	KN-CV	715 (45%)	1130 (49%)	5460 (6%)			$1.8 \times 10^{14}$	95%	2.1	1.3
2	KN		1150 (91%)	4860 (9%)	1485	$16.10 \times 10^{-3}$				
	KN-CV	630 (49%)	1120 (45%)	5100 (6%)			$1.9 \times 10^{14}$	96%	1.9	1.1

**Table 6.6: Time-resolved fluorescence decay (excitation at 375 nm and collected at 410 nm) and FRET data of KN in RM at different  $w_0$  values in the absence and presence of C500. Values in parentheses represent the relative weight percentage of the time component with a standard error of ca 10%.**

$w_0$	System	$\tau_1$ (ps)	$\tau_2$ (ps)	$\tau_3$ (ps)	$\tau_4$ (ps)	$\langle\tau_D\rangle$ (ps)	$J(\lambda)$ ( $M^{-1} cm^{-1} nm^4$ )	$E$	$R_0$ (nm)	$R$ (nm)
0	KN			1220 (88%)	5050 (12%)	1680				
	KN-C500	140 (28%)	540 (26%)	1230 (41%)	4460 (5%)		$1.5 \times 10^{14}$	89%	2.4	1.6
1.1	KN			1230 (88%)	5210 (12%)	1690				
	KN-C500	110 (25%)	520 (28%)	1300 (43%)	5020 (4%)		$1.6 \times 10^{14}$	90%	2.1	1.5
2	KN			1255 (88%)	5600 (12%)	1760				
	KN-C500	100 (19%)	470 (28%)	1290 (49%)	5100 (4%)		$1.5 \times 10^{14}$	91%	1.8	1.2

estimated the FRET efficiency to be 94% (for 29% donor population) and the characteristic Förster distance,  $R_0$  of 2.4 nm. From FRET dynamics, the estimated effective distance ( $R$ ) between the donor (KN) and the acceptor (CV) is found to be 1.5 nm. As evident in Table 6.5, the change in D–A distance with the increase of  $w_0$  clearly indicates the redistribution of the probe molecules with the degree of hydration of the RM. It has to be noted that we have done a similar study by using another well-known fluorophore, C500 and the result is

similar with the KN-CV FRET experiment (tabulated in Table 6.6). The relative location of the donor (KN) with respect to the acceptor (CV) in the Brij 30 RM is shown in Scheme 6.2.



*Scheme 6.2: Schematic representation of the FRET in Brij 30 RM.*

### 6.3. Conclusion:

In conclusion, the present study explores the role of solvent relaxation on ESPT of NpOH in water–DX mixture quantitatively. Time-resolved studies distinctly differentiate the dynamics of two time dependent excited state processes, the solvent relaxation and the deprotonation. The extent of proton transfer of NpOH is found to be retarded in water–DX mixture compared with that in bulk water. This retardation is attributed to the local concentration of water molecules near the photoacid and solvent reorganization. Solvent dynamics become faster with increasing temperature due to breakage of cooperative

hydrogen bond network present in the large clusters to smaller clusters. Increased solvent relaxation at higher temperature makes deprotonation faster. ESPT of a photoacid is an optimization between the local concentration of water and solvent relaxation. At elevated temperature local concentration of water reduces due to breakdown of hydrogen bonded network and ESPT does not change appreciably, although solvation becomes faster.

In addition, we have also reported the relaxation dynamics of KN in a nonionic Brij 30 RM system and compared the results with a well-known solvation probe H33258 in the restricted environments. While DLS studies confirm the structural integrity of the RM, picosecond-resolved fluorescence anisotropy and the FRET of the probe KN confirm the location of KN in the interface of the RM. Our detail spectroscopic studies clearly indicate that the intermolecular (solute–solvent) hydrogen bonding dynamics of the probe KN leading to the IC of the probe in the restricted environments is much faster compared to the relaxation of the solvent molecules around it (solvation). These results suggest that the interfering excited state hydrogen bonding dynamics of the probe hinders the interrogation of slower environmental relaxation in the Brij 30 RM using KN.

## References

- [1] A. Lukacs, A. Haigney, R. Brust, R.K. Zhao, A.L. Stelling, I.P. Clark, M. Towrie, G.M. Greetham, S.R. Meech, P.J. Tonge, Photoexcitation of the blue light using FAD photoreceptor AppA results in ultrafast changes to the protein matrix, *J. Am. Chem. Soc.* 133 (2011) 16893.
- [2] W.T. Chuang, C.C. Hsieh, C.H. Lai, C.H. Lai, C.W. Shih, K.Y. Chen, W.Y. Hung, Y.H. Hsu, P.T. Chou, Excited-state intramolecular proton transfer molecules bearing o-hydroxy analogues of green fluorescent protein chromophore, *J. Org. Chem.* 76 (2011) 8189.
- [3] G.J. Zhao, K.L. Han, Site-specific solvation of the photoexcited protochlorophyllide a in methanol: Formation of the hydrogen-bonded intermediate state induced by hydrogen-bond strengthening, *Biophys. J.* 94 (2008) 38.
- [4] G.J. Zhao, K.L. Han, Effects of hydrogen bonding on tuning photochemistry: concerted hydrogen-bond strengthening and weakening, *ChemPhysChem* 9 (2008) 1842.
- [5] G.J. Zhao, K.L. Han, Hydrogen bonding in the electronic excited state, *Acc. Chem. Res.* 45 (2011) 404.
- [6] G.J. Zhao, J.Y. Liu, L.C. Zhou, K.L. Han, Site-selective photoinduced electron transfer from alcoholic solvents to the chromophore facilitated by hydrogen bonding: A new fluorescence quenching mechanism, *J. Phys. Chem. B* 111 (2007) 8940.
- [7] G.J. Zhao, B.H. Northrop, K.L. Han, P.J. Stang, The effect of intermolecular hydrogen bonding on the fluorescence of a bimetallic platinum complex, *J. Phys. Chem. A* 114 (2010) 9007.
- [8] L.G. Arnaut, S.J. Formosinho, Excited-state proton transfer reactions I. Fundamentals and intermolecular reactions, *J. Photochem. Photobiol. A* 75 (1993) 1.
- [9] S.J. Formosinho, L.G. Arnaut, Excited-state proton transfer reactions II. Intramolecular reactions, *J. Photochem. Photobiol. A* 75 (1993) 21.
- [10] K.B. Schowen, H.H. Limbach, G.S. Denisov, R.L. Schowen, Hydrogen bonds and proton transfer in general-catalytic transition-state stabilization in enzyme catalysis, *Biochim. Biophys. Acta, Bioenerg.* 1458 (2000) 43.

- [11] G.J. Zhao, K.L. Han, Early time hydrogen-bonding dynamics of photoexcited coumarin 102 in hydrogen-donating solvents: Theoretical study, *J. Phys. Chem. A* 111 (2007) 2469.
- [12] M. Itoh, T. Adachi, K. Tokumura, Time-resolved fluorescence and absorption spectra and two-step laser excitation fluorescence of the excited-state proton transfer in the methanol solution of 7-hydroxyquinoline, *J. Am. Chem. Soc.* 106 (1984) 850.
- [13] M. Itoh, K. Tokumura, Y. Tanimoto, Y. Okada, H. Takeuchi, K. Obi, I. Tanaka, Time-resolved and steady-state fluorescence studies of the excited-state proton transfer in 3-hydroxyflavone and 3-hydroxychromone, *J. Am. Chem. Soc.* 104 (1982) 4146.
- [14] B. Cohen, D. Huppert, K.M. Solntsev, Y. Tsfadia, E. Nachliel, M. Gutman, Excited State Proton Transfer in Reverse Micelles, *J. Am. Chem. Soc.* 124 (2002) 7539.
- [15] N. Agmon, Elementary steps in excited-state proton transfer, *J. Phys. Chem. A* 109 (2004) 13.
- [16] D. Banerjee, P.K. Verma, S.K. Pal, Temperature-dependent femtosecond-resolved hydration dynamics of water in aqueous guanidinium hydrochloride solution, *Photochem. Photobiol. Sci.* 8 (2009) 1441.
- [17] K. Bhattacharyya, Solvation dynamics and proton transfer in supramolecular assemblies, *Acc. Chem. Res.* 36 (2003) 95.
- [18] K. Bhattacharyya, B. Bagchi, Slow dynamics of constrained water in complex geometries, *J. Phys. Chem. A* 104 (2000) 10603.
- [19] S. Rakshit, R. Saha, P.K. Verma, S.K. Pal, Role of solvation dynamics in excited state proton transfer of 1-naphthol in nanoscopic water clusters formed in a hydrophobic solvent, *Photochem. Photobiol.* 88 (2012) 851.
- [20] J. Lee, G.W. Robinson, S.P. Webb, L.A. Phillips, J.H. Clark, Hydration dynamics of protons from photon initiated acids, *J. Am. Chem. Soc.* 108 (1986) 6538.
- [21] R. Knochenmuss, S. Leutwyler, Proton transfer from 1-naphthol to water: Small clusters to the bulk, *J. Chem. Phys.* 91 (1989) 1268.
- [22] S. Mashimo, N. Miura, T. Umehara, S. Yagihara, K. Higasi, The structure of water and methanol in p-dioxane as determined by microwave dielectric spectroscopy, *J. Chem. Phys.* 96 (1992) 6358.

- [23] R.K. Mitra, P.K. Verma, S.K. Pal, Exploration of the dynamical evolution and the associated energetics of water nanoclusters formed in a hydrophobic solvent, *J. Phys. Chem. B* 113 (2009) 4744.
- [24] J.R. Lakowicz, Principles of fluorescence spectroscopy, Kluwer Academic/Plenum, New York, 1999.
- [25] D. Zhong, S.K. Pal, A.H. Zewail, Femtosecond studies of protein-DNA binding and dynamics: Histone I, *ChemPhysChem* 2 (2001) 219.
- [26] R. Jimenez, G.R. Fleming, P.V. Kumar, M. Maroncelli, Femtosecond solvation dynamics of water, *Nature* 369 (1994) 471.
- [27] T. Molotsky, D. Huppert, Solvation statics and dynamics of coumarin 153 in dioxane-water solvent mixtures, *J. Phys. Chem. A* 107 (2003) 8449.
- [28] F. Cichos, A. Willert, U. Rempel, C. von Borczyskowski, Solvation dynamics in mixtures of polar and nonpolar solvents, *J. Phys. Chem. A* 101 (1997) 8179.
- [29] A. Chandra, B. Bagchi, Molecular theory of solvation and solvation dynamics in a binary dipolar liquid, *J. Chem. Phys.* 94 (1991) 8367.
- [30] S. Mukherjee, K. Sahu, D. Roy, S.K. Mondal, K. Bhattacharyya, Solvation dynamics of 4-aminophthalimide in dioxane–water mixture, *Chem. Phys. Lett.* 384 (2004) 128.
- [31] S.K. Kim, J.J. Breen, D.M. Willberg, L.W. Peng, A. Heikal, J.A. Syage, A.H. Zewail, Solvation ultrafast dynamics of reactions. 8. Acid-base reactions in finite-sized clusters of naphthol in ammonia, water, and piperidine, *J. Phys. Chem.* 99 (1995) 7421.
- [32] R.D. Knochenmuss, D.E. Smith, Time and internal energy dependent fluorescence spectra of naphthol-water clusters, *J. Chem. Phys.* 101 (1994) 7327.
- [33] A.S.R. Koti, M.M.G. Krishna, N. Periasamy, Time-resolved area-normalized emission spectroscopy (TRANES): A novel method for confirming emission from two excited states, *J. Phys. Chem. A* 105 (2001) 1767.
- [34] A.R. Tourky, H.A. Rizk, Y.M. Girgis, The dielectric properties of water in dioxane, *J. Phys. Chem.* 65 (1961) 40.
- [35] J.R. Goates, R.J. Sullivan, Thermodynamic properties of the system water-p-dioxane, *J. Phys. Chem.* 62 (1958) 188.

- [36] N. Nandi, B. Bagchi, Dielectric relaxation of biological water, *J. Phys. Chem. B* 101 (1997) 10954.
- [37] P.K. Verma, A. Makhal, R.K. Mitra, S.K. Pal, Role of solvation dynamics in the kinetics of solvolysis reactions in microreactors, *Phys. Chem. Chem. Phys.* 11 (2009) 8467.
- [38] S. Rakshit, N. Goswami, S.K. Pal, Slow solvent relaxation dynamics of nanometer sized reverse micellar systems through tryptophan metabolite, kynurenine, *Photochem. Photobiol.* 88 (2012) 38.
- [39] P.S. Sherin, J. Grilj, Y.P. Tsentalovich, E. Vauthey, Ultrafast excited-state dynamics of kynurenine, a UV filter of the human eye, *J. Phys. Chem. B* 113 (2009) 4953.
- [40] R.K. Mitra, S.S. Sinha, P.K. Verma, S.K. Pal, Modulation of dynamics and reactivity of water in reverse micelles of mixed surfactants, *J. Phys. Chem. B* 112 (2008) 12946.
- [41] J.E. Churchich, L-kynurenine: A fluorescent probe of serum albumins *Biochim. Biophys. Acta* 285 (1972) 91.
- [42] R.S. Fee, M. Maroncelli, Estimating the time-zero spectrum in time-resolved emission measurements of solvation dynamics, *Chem. Phys.* 183 (1994) 235.
- [43] K.K. Kalnisha, D.V. Pestova, Y.K. Roshchina, Absorption and fluorescence spectra of the probe Hoechst 33258, *J. Photochem. Photobiol. A* 83 (1994) 39.
- [44] S.K. Pal, A.H. Zewail, Dynamics of water in biological recognition, *Chem. Rev.* 104 (2004) 2099–2123.
- [45] D. Banerjee, S.K. Pal, Ultrafast charge transfer and solvation of DNA minor groove binder: Hoechst 33258 in restricted environments, *Chem. Phys. Lett.* 432 (2006) 257.
- [46] S.K. Pal, L. Zhao, A.H. Zewail, Water at DNA surfaces: Ultrafast dynamics in minor groove recognition, *Proc. Natl. Acad. Sci. USA* 100 (2003) 8113.
- [47] J. Santhanalakshmi, S. Balaji, Binding studies of crystal violet on proteins, *Colloids Surf., A* 186 (2001) 173.

# Chapter 7

## Exploration of Structure and Function of a Protein in Macromolecular Crowding

### 7.1. Introduction:

The detailed knowledge of the biophysical and biochemical reaction has traditionally been acquired through experiments conducted in buffer solutions containing low concentrations of biomolecules together with low molecular weight substrates, and cofactors as required, assuming the representation of the *in vivo* scenario. In contrast, the real biological environment differs from that idealized solvent bath in different aspects. Such as the intracellular environment is highly crowded because of the presence of large amounts of soluble and insoluble biomolecules, including proteins, nucleic acids, ribosomes, lipids and carbohydrates, etc [1-4]. This means that a significant fraction of the intracellular space is not available to other macromolecular species, as a result of this, macromolecular thermodynamic activities increase by several orders of magnitude. Therefore, biochemical reaction in a living cell may be quite different from those under idealized conditions [5]. In this sense, it is highly demanding to understand the effects of the crowding agents, termed “macromolecular crowding” [6, 7], on biophysical and biochemical reaction. Although the effect of macromolecular crowding, in particular on proteins *in vitro* with regard to folding and denaturation, has been well studied [8-13] less is known about the biochemical reactions. One such biochemical reaction is electron transfer (ET), which plays an important role in many processes in chemistry, physics and biology and has diverse technological applications. In biological systems, ET reactions are ubiquitous [14, 15] especially in enzymes with redox reactions. Flavoproteins with flavin chromophores are examples of such enzymes and are involved in various catalytic processes [15, 16]. The understanding of ET reactions of flavins in proteins and their redox reactions is critical to their functionality. In this report, we have studied ET dynamics of riboflavin (Rf; vitamin B2) in Rf binding protein (RBP), a globular monomeric protein and is responsible for the storage and active transport of riboflavin cofactor into developing embryo [17, 18], also

important for their functions as photoreceptors, in the presence of crowding environment of nanoscopic sodium dodecyl sulfate (SDS) micelles.

Although ET between Rf and RBP in dilute homogeneous aqueous solution has been studied quite thoroughly [19-22], much less is known about ET between Rf and RBP under crowded environments. Remarkably, crowded environment often alters the structure and functionality of many proteins. Biological function of a protein is possible only when it is folded into a specific three dimensional conformation. An understanding of the mechanisms of ET involving in crowded environments provides an important bridge between commonly employed dilute solutions *in vitro* studies and studies of the effects of a crowded environment, as found *in vivo*. The anionic surfactant SDS is often used to mimic cellular membrane and macromolecular crowding agent [23] and is used here as model crowding agent. Importance of using SDS as model crowding agent lies on the following facts. At a concentration below the critical micellar concentration (CMC; 3.3 mM in buffer), SDS essentially remains in monomeric form and expected to mimic molecular crowding. Above CMC, the SDS molecules form well-defined spherical micelles (4.4 nm diameter) comparable to the size of RBP (4.7 nm), and mimic the macromolecular crowding environments. It has also to be noted that, SDS is well known to act as a potential denaturants in their monomeric form [24], thus the use of the SDS surfactant as potential crowding agent is expected to mimic the cellular complex environment complicated by both chemical denaturant and molecular/macromolecular crowding agent.

In the present study, we have explored picosecond-resolved dynamics of both RBP and Rf in the RBP-Rf complex under various degrees of molecular/macromolecular crowding. While selective excitation (300 nm) and detection at 350 nm explores the dynamics of the ET from the tryptophan in the proximity of the cofactor Rf, the excitation of the complex at 445 nm (detection at 520 nm) clearly reveals the dynamics of ET of the cofactor Rf in the crowded environment. We have also monitored the effect of structural perturbation (both secondary and tertiary) of RBP on the observed ET dynamics using near- and far-UV circular dichorism (CD), dynamic light scattering (DLS) and UV-Vis spectroscopy of the bound cofactor Rf.

## 7.2. Results and Discussion:

### 7.2.1. Ultrafast Electron Transfer in Riboflavin Binding Protein in Macromolecular Crowding of Nano-Sized Micelle [25]:

Figure 7.1a and b shows the steady-state (insets) and picosecond resolved fluorescence decay transients of tryptophan ( $\lambda_{\text{ex}} = 300$  nm, fluorescence decay monitored at 350 nm) and Rf ( $\lambda_{\text{ex}} = 445$  nm, fluorescence decay monitored at 520 nm), respectively, of RBP-Rf complex in the presence of increasing amount of crowding agent SDS. Earlier studies have concluded that RBP quenches the fluorescence of Rf which is a consequence of ultrafast ET to the flavin chromophore (Rf) in the excited electronic state from nearby tryptophan or tyrosine residues present in RBP. It has also been shown that complexation of Rf with RBP quenches both the fluorescence of Rf and Trp of the protein [20, 21]. It is observed that addition of SDS to RBP-Rf complex leads to a recovery of Trp emission as well as that of Rf (insets of Figure 7.1a and b). It is interesting to note that Rf absorbs mostly  $\sim 450$  nm, however, it shows distinct absorbance in the 300 nm region. When RBP-Rf complex in buffer is excited at 300 nm, no emission peak in the 520 nm region is observed. However, as SDS is gradually added in the complex, a distinct peak at  $\sim 520$  nm appears and its intensity increases with the addition of SDS (inset of Figure 7.1a) and at high SDS concentrations the emission spectra resembles that of free Rf. The increase of Rf emission intensity with gradual addition of SDS is due to the expulsion of Rf from the ligand binding site of RBP, thereby hindering the ET process. Figure 7.1c shows the relative fluorescence intensities of Trp of RBP-Rf complex at 350 nm and Rf of RBP-Rf complex at 520 nm at different SDS concentrations. Figure 7.1c (inset) depicts the relative fluorescence intensity of Trp in RBP itself as a function of SDS concentrations. It is observed that fluorescence intensity increases with the addition of SDS, whereas that of Rf changes only marginally at all studied SDS concentrations.

Now to get a better insight into the ET dynamics and extent of interaction of protein with crowding agent and the observed changes in fluorescence intensity, picosecond-resolved fluorescence measurements of these systems are performed. Figure 7.1a shows fluorescence decay transients of Trp in RBP-Rf complex at 350 nm in

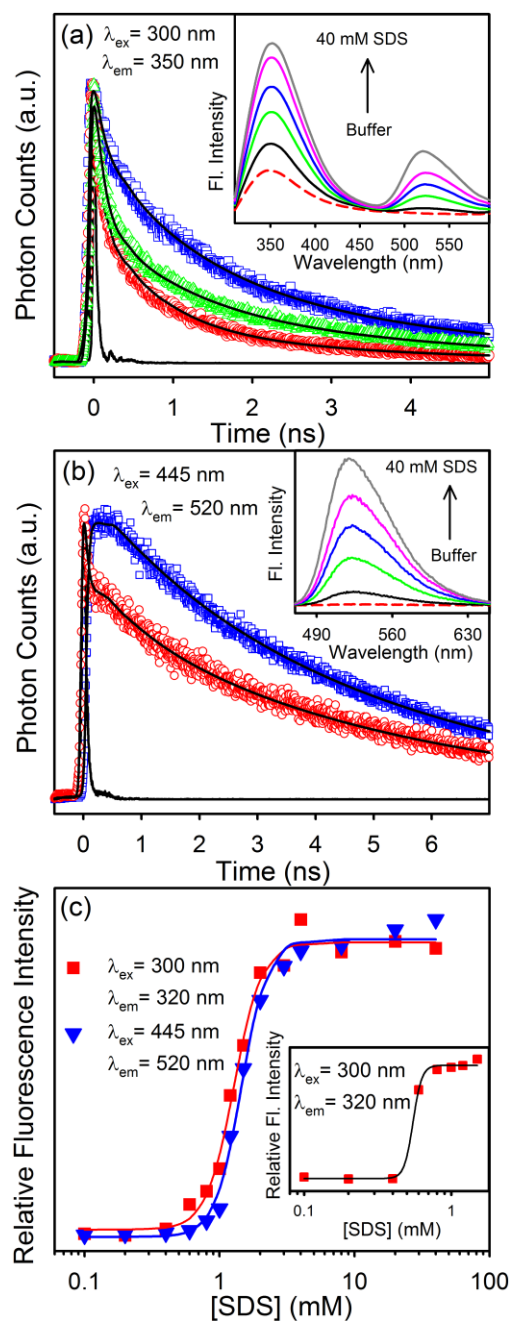


**Figure 7.1:** (a) Fluorescence decay transients of tryptophan of RBP-Rf complex ( $\lambda_{ex} = 300$  nm, decay monitored at 350 nm) in buffer (red; circle), 1 mM SDS (green, triangle) and 40 mM SDS (blue; square). The total emission spectrum of the RBP-Rf complex at different SDS concentration is shown in the inset ( $\lambda_{ex} = 300$  nm). (b) Fluorescence decay transient of Rf in RBP-Rf complex ( $\lambda_{ex} = 445$  nm; decay monitored at 520 nm) in 0.2 mM SDS (red; circle) and 40 mM SDS (blue; square). The total emission spectrum of the RBP-Rf complex at different SDS concentration is shown in the inset ( $\lambda_{ex} = 445$  nm). (c) Relative fluorescence intensity of trp ( $\lambda_{em} = 350$  nm) and Rf ( $\lambda_{em} = 520$  nm) of RBP-Rf complex at different SDS concentrations (square;  $\lambda_{ex} = 300$  nm, emission monitored at 350 nm and triangle;  $\lambda_{ex} = 445$  nm, emission monitored at 520 nm). Inset shows the relative fluorescence intensity of RBP ( $\lambda_{ex} = 300$  nm, emission monitored at 350 nm) at different concentration of SDS.

buffer (circle), 1 mM SDS (triangle) and 40 mM SDS (square) excited at 300 nm. Fluorescence decay of Trp residue of RBP in buffer is fitted triexponentially having time components of 0.14, 0.87, and 2.88 ns with average lifetime ( $\langle\tau\rangle$ ) of 0.82 ns (Table 7.1). On subsequent addition of the SDS,  $\langle\tau\rangle$  increases up to 2.0 mM SDS concentration (below CMC) beyond which it does not change appreciably (Table 7.1). This indicates that SDS

**Table 7.1: Average lifetimes ( $\langle\tau\rangle$ ) of RBP, and RBP-Rf complex in buffer and different concentrations of SDS.**

<i>[SDS] (mM)</i>	<i>Average Lifetime, <math>\langle\tau\rangle</math> (ns)</i>		
	<i>(<math>\lambda_{ex}=300</math> nm; <math>\lambda_{em}=350</math> nm)</i>		<i>(<math>\lambda_{ex}=445</math> nm; <math>\lambda_{em}=520</math> nm)</i>
	<i>RBP</i>	<i>RBP-Rf</i>	<i>RBP-Rf</i>
<b>0.0</b>	0.82	0.43	0.64
<b>0.2</b>	0.80	0.58	1.38
<b>0.4</b>	0.93	0.62	2.01
<b>0.6</b>	1.22	0.70	3.97
<b>0.8</b>	1.76	0.85	4.49
<b>1.0</b>	1.84	0.91	4.69
<b>1.5</b>	1.93	1.28	4.68
<b>2.0</b>	1.95	1.48	4.66
<b>3.0</b>	1.94	1.64	4.66
<b>4.0</b>	1.79	1.74	4.67
<b>8.0</b>	1.80	1.83	4.66
<b>20.0</b>	1.75	1.86	4.68
<b>40.0</b>	1.77	1.79	4.68

monomer significantly alters the ET dynamics as a molecular crowding agent. It is important to note here that Trp in aqueous solution has a distinct average lifetime of 2.8 ns whereas a single Trp protein HSA (human serum albumin) has an average lifetime of 5.8 ns [26]. The lifetime of tryptophan in proteins varies from a few hundred picoseconds to 9 ns [26]. It is widely believed that the large variation in its lifetime stems from the proximity of quenching groups like glutamic acid, aspartic acid, serine, threonine, methionine, arginine etc in the vicinity of the Trp [26]. A quenched average lifetime of 0.82 ns for Trp in RBP indicates the presence of nearby quenching amino acid residues such as glutamic acid, serine and arginine, which is also evident from the high resolution X-ray crystallographic studies of RBP [27]. Addition of a molecular crowding agent like SDS releases the fluorescence quenching and as a result lifetime of Trp increases (Figure 7.1 and Table 7.1). Previously, it has been observed that binding of SDS near Trp of BSA as well as HSA leads to the Trp fluorescence quenching and consequently decrease in

lifetime of Trp [28]. It was proposed that the quenching is static in case of HSA whereas both static and dynamic in case of BSA [28]. However, the present study reveals an opposite trend, i.e., quenching is released, which rules out a direct interaction between the crowding agent and Trp. In case of RBP-Rf complex increase in  $\langle\tau\rangle$  (Table 7.1) and fluorescence intensity of Trp (inset of Figure 7.1a) are due to the removal of neighbouring quencher amino acid residues and Rf form the ligand binding domain of RBP. At low SDS concentrations  $\langle\tau\rangle$  of Trp residue in RBP-Rf complex is smaller compared to that in RBP. However, beyond 4 mM SDS where RBP loses its vitamin binding capacity completely (discussed later),  $\langle\tau\rangle$  remains practically unchanged for both RBP and RBP-Rf complex.

It has been concluded that in ET process the fluctuation of the donor-acceptor distance also results in a change of the fluorescence lifetime [29]. Time-resolved fluorescence measurements provide with an estimation of the ET rate constant of  $1.35\times 10^9$  s<sup>-1</sup> for RBP-Rf complex in buffer. Upon addition of SDS, ET rate constant decreases and at 0.8 mM SDS it is found to be  $9.5\times 10^6$  s<sup>-1</sup>. Beyond this SDS concentration ET eventually stops. A low ET rate constant ( $10^6$  s<sup>-1</sup>) implies a distance of  $\sim 20$  Å between the isoalloxazine ring (Rf) and Trp-156 (RBP) which is much larger compared to the native distance of  $\sim 3.7$  Å in the absence of SDS [27, 29]. This indicates that the observed decrease in vitamin binding capacity as well as inefficient ET process in presence of SDS is due to perturbation of protein structure as induced by the crowding agent. To understand this in more detail, we monitor the structure of RBP using circular dichroism (CD) technique. Figure 7.2a shows the far-UV CD spectra of RBP-Rf complex in absence and presence of SDS in 200-260 nm wavelength windows. As observed from Figure 7.2 and Table 7.2, addition of SDS molecules increases the helicity of the protein at the expense of a decrease in the percentage of random coil. Similar trend in the far-UV CD spectrum of RBP is also observed when SDS is added to RBP (inset of Figure 7.2a). It should be noted here that the change in the helical content is most significant at a concentration below CMC (2.0 mM) (Table 7.2) beyond which the effect is minimal. It appears that low concentration of SDS (below CMC) acts as molecular crowder which functionally strengthen the protein's secondary structure. Such low SDS concentrations are incapable of forming an aggregate of the RBP polypeptide (see DLS measurement). Thus the protein

structure must be stabilized by a specific function, probably a “crosslinking function” of the bound SDS as suggested by Markus et al. [30].

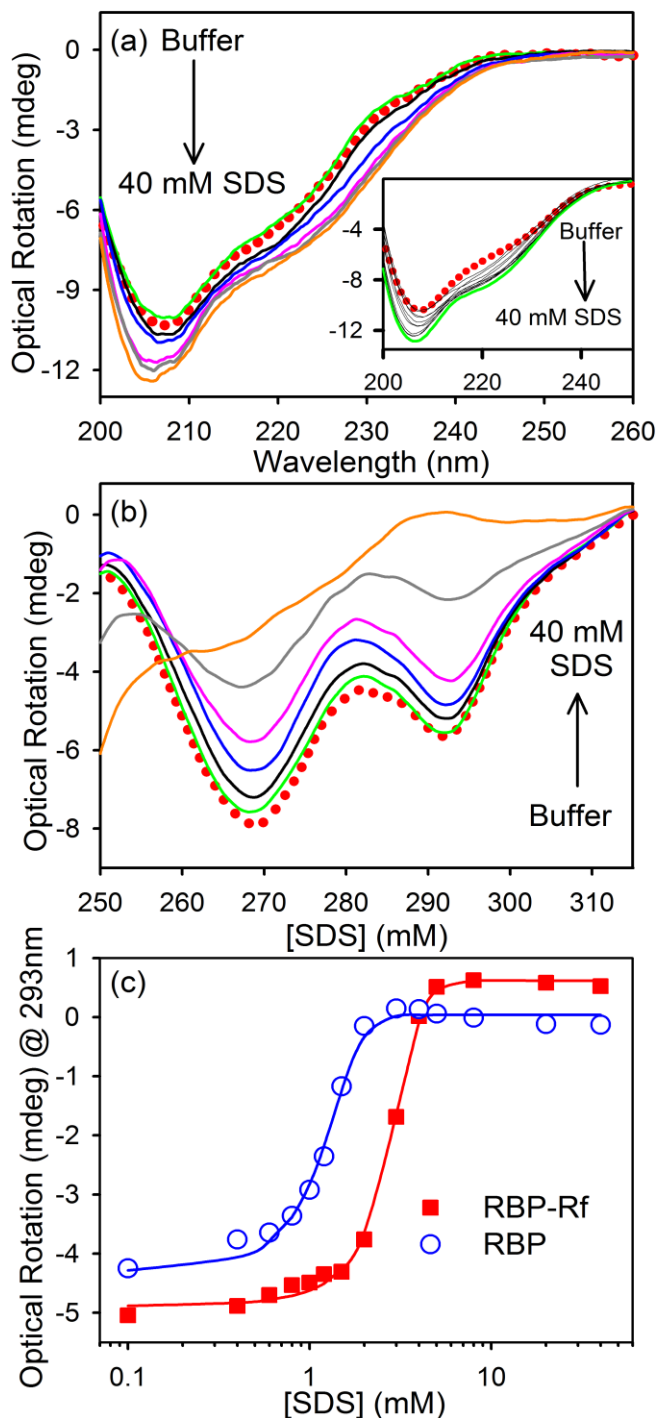


**Figure 7.2:** (a) Far-UV CD spectra of RBP-Rf complex at various concentrations of SDS. Inset shows the Far-UV CD spectra of RBP at various concentrations of SDS. (b) Near-UV CD spectra of RBP-Rf complex at different concentrations of SDS. (c) Optical rotation of RBP (at 293 nm; triangle) and RBP-Rf (at 293 nm; square) at different concentrations of SDS.

**Table 7.2: Percentages of  $\alpha$ -helix,  $\beta$ -structure and random coil of RBP; RBP-Rf complex in buffer and in different concentrations of SDS.**

<b>System</b>	<b><math>\alpha</math> Helix (%)</b>	<b>Anti-parallel (%)</b>	<b>Parallel (%)</b>	<b><math>\beta</math> turn (%)</b>	<b>Random Coil (%)</b>
<b>RBP</b>	27.5	11.1	9.8	18.5	33.1
<b>RBP+Rf</b>	27.8	11.2	9.7	18.8	32.5
<b>0.2 SDS</b>	27.2	11.3	9.9	18.7	32.9
<b>0.4 SDS</b>	29.2	10.9	9.4	18.6	31.9
<b>0.6 SDS</b>	29.8	10.7	9.3	18.5	31.7
<b>0.8 SDS</b>	28.4	10.9	9.6	18.5	32.6
<b>1.0 SDS</b>	30.6	10.4	9.1	18.5	31.4
<b>1.2 SDS</b>	30.8	10.5	9.1	18.4	31.2
<b>1.5 SDS</b>	32.2	10.1	8.8	18.4	30.5
<b>2.0 SDS</b>	32.9	9.9	8.7	18.3	30.2
<b>3.0 SDS</b>	32.5	10.0	8.7	18.5	30.3
<b>4.0 SDS</b>	32.1	10.3	8.9	18.6	30.1
<b>5.0 SDS</b>	33.5	9.9	8.5	18.3	29.8
<b>8.0 SDS</b>	33.8	9.8	8.5	18.4	29.5
<b>20.0 SDS</b>	32.4	10.2	8.7	18.4	30.3
<b>40.0 SDS</b>	33.4	9.9	8.6	18.4	29.7

Near-UV CD spectrum of protein explores contribution from aromatic amino acid residues and reveals the tertiary structure of proteins. The observed near-UV CD spectrum of RBP-Rf in buffer shows a distinct peak at 268 nm along with a shoulder in the 290 nm region (Figure 7.2b). The signal around 268 nm originates from tyrosine, whereas that in the 290 nm region is due to the tryptophan (Trp) residue of the protein. With gradual addition of SDS to RBP-Rf complex, the intensity of signal around 268 and 290 nm regions get reduced. As the concentration of added SDS goes beyond 3 mM the CD spectrum gets significantly distorted. The change in the 268 nm regions signifies perturbation to tyrosine, whereas that in the 290 nm regions indicates a drastic change in the Trp containing domain which is consistent with the steady-state and time-resolved studies. The protein itself also loses its tertiary structure in the presence of SDS (Figure 7.2c). However, the loss of tertiary structure of RBP occurs at ~3 mM SDS in the presence of Rf and ~1.5 mM SDS in the absence of Rf (Figure 7.2c). This suggests that Rf bound RBP has enhanced stability against molecular crowding environment compared to RBP itself. This is in agreement with the steady-state emission measurement where transition point for denaturation is higher for RBP-Rf complex compared to RBP without Rf (Figure

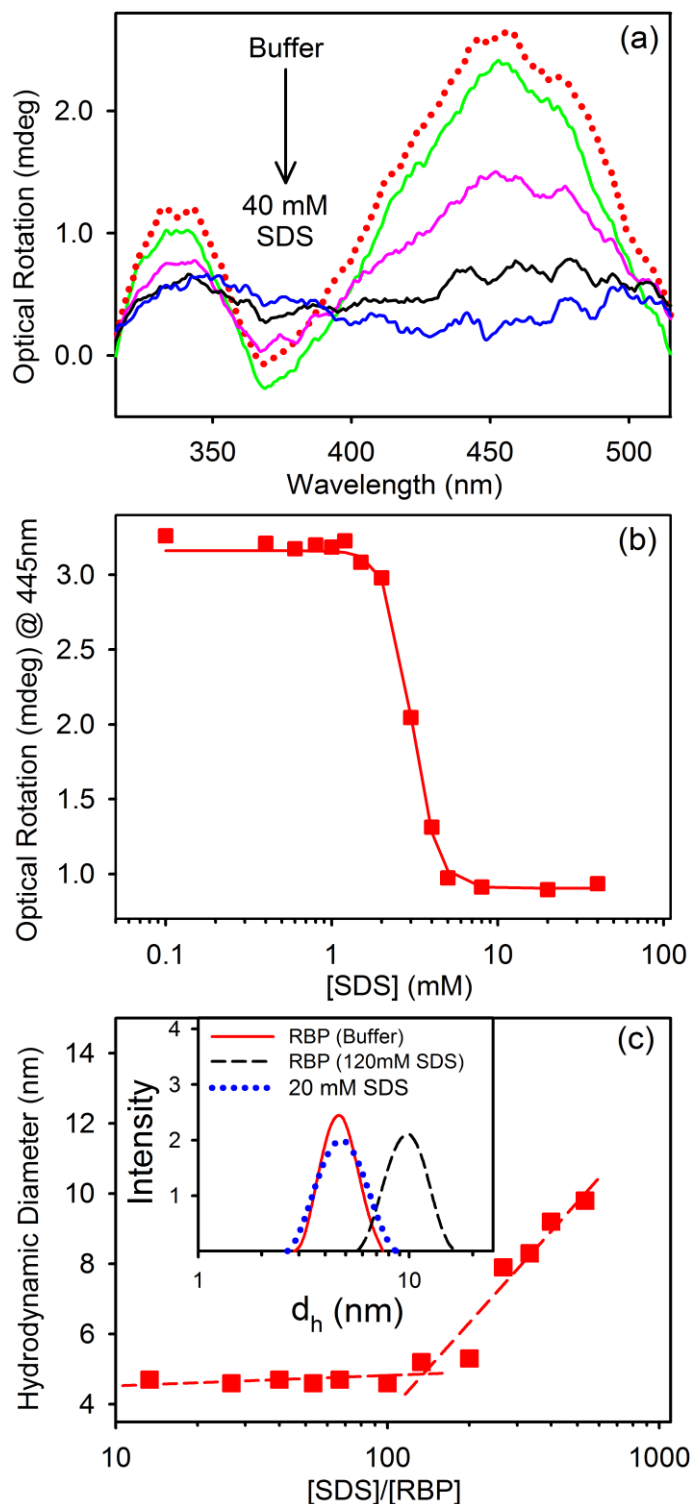


**Figure 7.3:** (a) Visible CD spectra of RBP-Rf complex at various concentrations of SDS. (b) Optical rotation values at 445 nm of RBP-Rf complex at various concentrations of SDS. (c) Hydrodynamic diameter of RBP at different SDS concentrations. Broken lines are guide to eye. Typical DLS signals for 20 mM SDS, RBP in buffer and 120 mM SDS concentration are shown in the inset.

7.1c). Previously it was found that Rf binding renders enhanced thermal stability of RBP, as manifested by a change in the denaturation temperature from 60.8 °C for RBP to 72.8 °C for RBP-Rf complex [31]. Loss in tertiary structure of the protein results in the expulsion of the vitamin from the binding site of RBP as evident from visible CD and absorption measurement (discussed in next paragraph). Rf either in buffer or in SDS does not show any appreciable optical activity in visible region. However upon binding with RBP, a set of strong CD bands appear in the visible region as shown in Figure 7.3a. The band positioned at ~445 nm is due to the  $\pi$ - $\pi^*$  transition, whereas those at 370 nm and 340 nm are attributed to a second  $\pi$ - $\pi^*$  and n- $\pi^*$  transitions, respectively [32]. These strong CD bands suggest that Rf is rigidly packed in the binding cleft and rotation of the ribose moiety is completely hindered. With increasing concentration of SDS, the CD signals in visible region get weaker and eventually disappear above ~3 mM SDS indicating the loss of binding capacity of the protein (Figure 7.3b). Further confirmation comes from the absorption spectra of RBP-Rf complex in the presence of different concentration of SDS (Figure 7.4). It is evident from the Figure 7.4a, c that addition of SDS leads to a considerable blue shift of the absorption maximum. The shoulder at ~490 nm which is characteristic of Rf binding progressively disappears forming an isobestic point at ~473 nm indicating the loss of vitamin binding capacity of RBP (Figure 7.4a). To get a clear picture of the disappearance of the 490 nm peak we deconvolute the absorption spectra (Figure 7.4b). RBP-Rf complex shows three absorption peak whereas in presence of 40 mM SDS RBP-Rf complex has only two maxima confirming the loss of binding capacity of vitamin in crowded environments.

To check whether the loss of tertiary structure of RBP as evidenced from near-UV CD is due to its unfolding, we perform DLS measurement. Inset of Figure 7.3c depicts the DLS measurements of SDS micelle; RBP in buffer and RBP in the presence of SDS. As evident from the figure, hydrodynamic diameter ( $d_H$ ) of RBP in buffer is comparable to that of SDS micelle. Thus we could not get both the peaks (protein and micelle) individually. Figure 7.3c shows the change in the hydrodynamic diameter of RBP at different SDS concentrations. As evident from the figure, hydrodynamic diameter of RBP in buffer is 4.7 nm which increases to 5.2 nm at ~2 mM SDS concentration and afterwards

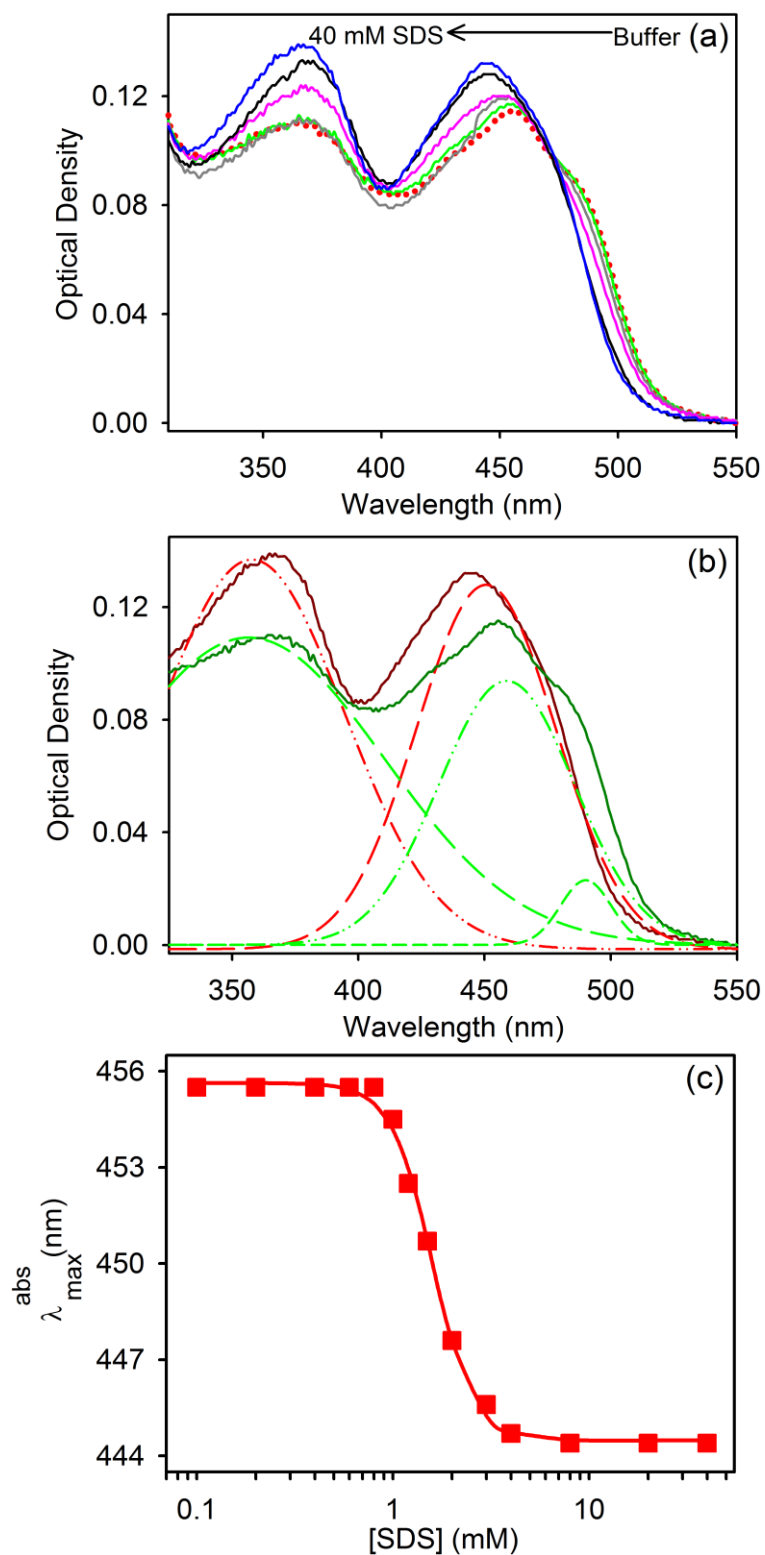


**Figure 7.4:** (a) Absorption spectra of RBP-Rf complex at different concentrations of SDS. (b) The deconvolution of absorption spectra of RBP-Rf complex at two different SDS concentrations (0 mM (green) and 40 mM (red)). (c) The shift in absorption peak of Rf in RBP-Rf complex as a function of SDS concentrations.

the size increases linearly with increasing SDS concentration. Practically there is no change in the size of RBP before CMC which supports the “cross linking hypothesis” as discussed earlier. Thus the interaction of SDS and RBP is found to be weak and only with  $[\text{SDS}]/[\text{RBP}] \geq 130$  the protein starts unfolding (Figure 7.3c). As large excess of SDS (in the form of micelles) is needed to initiate the unfolding, the interaction between SDS and RBP is assumed to be nonspecific in nature. Some other proteins like Cardiotoxin exhibits similar resistance [33], while a number of other water-soluble proteins are easily denatured by SDS [34, 35]. The observed weak interaction might be due to the acidic nature of RBP which holds an overall negative charge at physiological pH. Thus excess of SDS as micellar crowding agent is needed to initiate the hydrophobic interaction with the protein interior and consequent unfolding of the protein. Since RBP unfolds in the presence of excess of SDS and losses its tertiary structure as well as its vitamin binding capacity while there is an insignificant change in secondary structure, it seems that it adopts an intermediate structure in the presence of SDS. Previous studies by Alen et al. [36] on guanidium hydrochloride (GndHCl) denaturation of RBP concluded that the unfolding process consists of two steps with two transitions (i.e., a three-state model) and possibility of an intermediary molten globule state. Further confirmation to this fact comes from spectroscopic measurements. It has been shown earlier that tryptophan emission of RBP suffers 10-12 nm red shifts on complete denaturation indicating the exposure of Trp from the interior of the protein towards a more polar aqueous environment [21, 36]. In the present study, however, we find that tryptophan residue of RBP does not show any peak shift even at the highest concentration of SDS used (40 mM) either in the absence or in the presence of Rf. This affirms that SDS denatures RBP partially to an intermediate molten globular state in which RBP retains almost all of its secondary structure, however, loses its tertiary structure which in turn is unable to hold Rf and hence stops ET between the protein and vitamin.

Quenching of RBP fluorescence upon Rf binding has commonly been believed to be a result of efficient Förster resonance energy transfer (FRET) from excited Trp to Rf [21]. Based on the overlap of protein fluorescence and Rf absorption Li et al. calculated the Förster's parameter  $R_0$  to be 3 Å [21]. However, Choi et al. suggested that the quenching

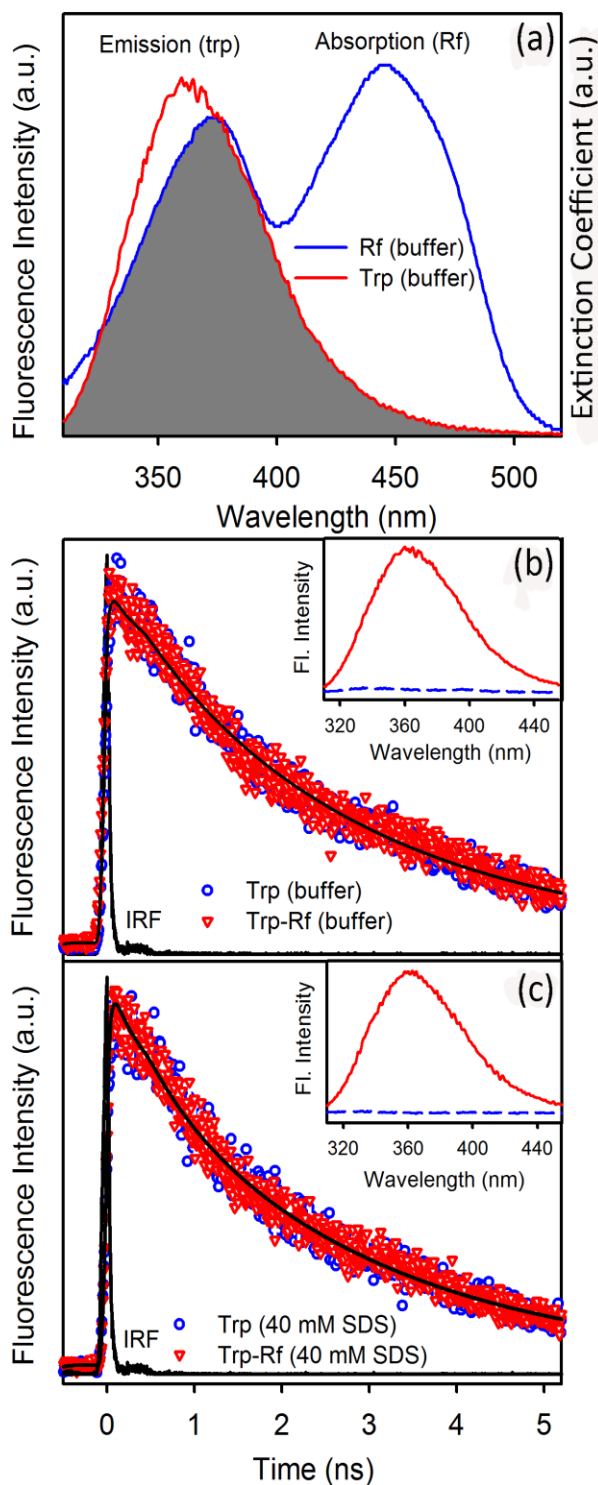


**Figure 7.5:** (a) Spectral overlap of fluorescence emission of L-tryptophan and absorption spectrum of Rf in buffer. (b) Fluorescence decay transients of L-tryptophan ( $\lambda_{ex} = 300$  nm) in the absence and presence of Rf in buffer. Corresponding steady-state emission spectra are shown in the inset. (c) Fluorescence decay transients of L-tryptophan ( $\lambda_{ex} = 300$  nm) in the absence and presence of Rf in 40 mM SDS. Corresponding steady-state emission spectra are shown in the inset.

of RBP fluorescence upon binding of Rf is due mainly to the ground-state stacking interaction between a tryptophan residue at the binding site and the quinoxaline portion of Rf, and not due to FRET [37]. However, the distance of five Trp varies from 4 to 12 Å approximately as calculated from the distances provided by Monaco et al. [27]. Based on the overlap of protein fluorescence and Rf absorption and assuming random orientation of acceptor and donor dipoles and taking quantum yield of the tryptophan in the protein RBP to be 0.06, we calculate Förster distance ( $R_0$ ) to be 23 Å. The energy transfer efficiency is found to be ~56% using Equation 2-46b. The distance between Trp and Rf is calculated to be 22 Å which is considerably higher than the acceptable distance of 4-12 Å. In order to find out whether there is possibility of energy transfer from L-Trp molecule to Rf, we perform steady-state as well as time-resolved experiment. It is important to mention here that the concentration of Rf (acceptor) is higher than that of L-Trp (donor) and also is equal to the micellar concentration. Although there is a huge quenching of L-Trp steady-state emission in buffer as well as in 40 mM SDS (inset of Figure 7.5b, c respectively), the lifetime of tryptophan does not suffer any change in these systems (Figure 7.5). This clearly indicates that the quenching is static in nature. Thus possibility of FRET between L-Trp and Rf is ruled out. However, both steady-state and time-resolved measurement of tryptophan residue of RBP-Rf complex (Table 7.1) shows quenching indicating that quenching is not completely static in case of RBP-Rf complex as suggested by Choi et al. [37]. It is important to note that both static and dynamic quenching require molecular contact between the fluorophore and the quencher. Also a distance of 4-12 Å between tryptophan residue of RBP and Rf molecule indicates a low possibility of FRET between them since for efficient FRET the donor-acceptor distance must be within  $0.5 R_0$  to  $1.5 R_0$  [38]. Based on these experimental findings we suggest that quenching of protein fluorescence upon Rf binding might be either static or combined dynamic and static but not due to FRET. However, the detailed description of quenching is out of the scope of the present work.

### **7.3. Conclusion:**

In this work, we have provided an experimental evidence of the effects of molecular/macromolecular crowding in the biochemical reaction by using a simple model

system. We have studied the ultrafast ET dynamics of Rf in RBP. For molecular/macromolecular crowding agent we have used SDS surfactant. It has been found that the extent of ultrafast electron transfer (ET) between Rf and RBP decreases with the addition of SDS molecules. Beyond 1 mM SDS concentration ET eventually stops as revealed from picosecond-resolved fluorescence measurement indicating loss of vitamin binding capacity of RBP. We have confirmed that the secondary structure of RBP strengthens in presence of molecular crowding agents due to cross-linking. However, its tertiary structure collapses in the presence of SDS as observed from CD measurements. These observations indicate that the loss of binding capacity of RBP above 1.5 mM of SDS (below CMC where SDS exists as monomer) concentration is due to collapse of its tertiary structure. These characteristics also indicate that in presence of crowding environments RBP changes from native (N) to a molten globular like intermediate state (I) which retains its secondary structure but loses its tertiary structure. We also suggest that quenching of tryptophan emission of RBP in presence of Rf is not due to FRET as established previously rather a combination of dynamic and static quenching. Hence, our results suggest that ET rate from tryptophan(s) to Rf in the RBP *in vivo* is slower, considering that the intracellular milieu is crowded in nature.

## References

- [1] R.J. Ellis, Macromolecular crowding: Obvious but underappreciated, *Trends Biochem. Sci.* 26 (2001) 597.
- [2] A.B. Fulton, How crowded is the cytoplasm?, *Cell* 30 (1982) 345.
- [3] S.B. Zimmerman, S.O. Trach, Estimation of macromolecule concentrations and excluded volume effects for the cytoplasm of *Escherichia coli*, *J. Mol. Biol.* 222 (1991) 599.
- [4] R.J. Ellis, A.P. Minton, Cell biology: Join the crowd, *Nature* 425 (2003) 27.
- [5] A.P. Minton, How can biochemical reactions within cells differ from those in test tubes?, *J. Cell Sci.* 119 (2006) 2863.
- [6] A.P. Minton, Macromolecular crowding, *Curr. Biol.* 16 (2006) R269.
- [7] S.B. Zimmerman, A.P. Minton, Macromolecular crowding: Biochemical, biophysical and physiological consequences, *Annu. Rev. Biophys. Biomol. Struct.* 22 (1993) 27.
- [8] B. van den Berg, R. Wain, C.M. Dobson, R.J. Ellis, Macromolecular crowding perturbs protein refolding kinetics: Implications for folding inside the cell, *EMBO J.* 19 (2000) 3870.
- [9] B. van den Berg, R.J. Ellis, C.M. Dobson, Effects of macromolecular crowding on protein folding and aggregation, *EMBO J.* 18 (1999) 6927.
- [10] V.N. Uversky, E. M. Cooper, K.S. Bower, J. Li, A.L. Fink, Accelerated  $\alpha$ -synuclein fibrillation in crowded milieu, *FEBS lett.* 515 (2002) 99.
- [11] N. Tokuriki, M. Kinjo, S. Negi, M. Hoshino, Y. Goto, I. Urabe, T. Yomo, Protein folding by the effects of macromolecular crowding, *Protein Sci.* 13 (2004) 125.
- [12] A. Christiansen, Q. Wang, A. Samiotakis, M.S. Cheung, P. Wittung-Stafshede, Factors defining effects of macromolecular crowding on protein stability: An in vitro/in silico case study using cytochrome c, *Biochemistry* 49 (2010) 6519.
- [13] D. Tsao, N.V. Dokholyan, Macromolecular crowding induces polypeptide compaction and decreases folding cooperativity, *Phys. Chem. Chem. Phys.* 12 (2010) 3491.
- [14] D. N. Beratan, J. N. Onuchic, Protein electron transfer, Bios Scientific Publishers, Oxford., 1996.

- [15] V. Balzani, *Electron transfer in chemistry*, Wiley-VCH, Weinheim, Germany, 2001.
- [16] F. Muller, *Chemistry and biochemistry of flavoenzymes*, CRC Press, Boca Raton, FL, 1991.
- [17] W.P. Winter, E.G. Buss, C.O. Clagett, R.V. Boucher, The nature of the biochemical lesion in avian renal riboflavinuria—II. The inherited change of a riboflavin-binding protein from blood and eggs, *Comp. Biochem. Physiol.* 22 (1967) 897.
- [18] C.V. Murty, P.R. Adiga, Pregnancy suppression by active immunization against gestation-specific riboflavin carrier protein, *Science* 216 (1982) 191.
- [19] D.P. Zhong, A.H. Zewail, Femtosecond dynamics of flavoproteins: Charge separation and recombination in riboflavine (vitamin B-2)-binding protein and in glucose oxidase enzyme, *Proc. Natl. Acad. Sci. USA* 98 (2001) 11867.
- [20] N. Mataga, H. Chosrowjan, Y. Shibata, F. Tanaka, Y. Nishina, K. Shiga, Dynamics and mechanisms of ultrafast fluorescence quenching reactions of flavin chromophores in protein nanospace, *J. Phys. Chem. B* 104 (2000) 10667.
- [21] T.M. Li, J.W. Hook, H.G. Drickamer, G. Weber, Effects of pressure upon the fluorescence of the riboflavin binding protein and its flavin mononucleotide complex, *Biochemistry* 15 (1976) 3205.
- [22] R.P. Simonsen, G. Tollin, Structure-function relations in flavodoxins, *Mol. cell. biochem.* 33 (1980) 13.
- [23] A.K. Shaw, S.K. Pal, Activity of subtilisin carlsberg in macromolecular crowding, *J. Photochem. Photobiol. B* 86 (2007) 199.
- [24] A. Lee, S.K.Y. Tang, C.R. Mace, G.M. Whitesides, Denaturation of proteins by SDS and tetraalkylammonium dodecyl sulfates, *Langmuir* 27 (2011) 11560.
- [25] S. Rakshit, R. Saha, P.K. Verma, R.K. Mitra, S.K. Pal, Ultrafast electron transfer in riboflavin binding protein in macromolecular crowding of nano-sized micelle, *Biochimie* 94 (2012) 2673.
- [26] M.R. Eftink, In *methods of biochemical analysis*, Suelter, C. H. ed., John Wiley and Sons, New York, 1991.
- [27] H.L. Monaco, Crystal structure of chicken riboflavin-binding protein, *EMBO J.* 16 (1997) 1475.

- [28] E.L. Gelamo, C.H.T.P. Silva, H. Imasato, M. Tabak, Interaction of bovine (BSA) and human (HSA) serum albumins with ionic surfactants: Spectroscopy and modelling, *Biochim. Biophys. Acta, Protein Struct. Mol. Enzymol.* 1594 (2002) 84.
- [29] J.R. Winkler, Long-range electron transfer in biology, John Wiley & Sons, Ltd, 2006.
- [30] G. Markus, F. Karush, Structural effects of the interaction of human serum albumin with sodium decyl sulfate<sup>1</sup>, *J. Am. Chem. Soc.* 79 (1957) 3264.
- [31] M. Wasylewski, Binding study of riboflavin-binding protein with riboflavin and its analogues by differential scanning calorimetry, *J. Protein Chem.* 19 (2000) 523.
- [32] A. Galat, Interaction of riboflavin binding protein with riboflavin, quinacrine, chlorpromazine and daunomycin, *Int. J. Biochem.* 20 (1988) 1021.
- [33] A. Galat, C. Yang, E.R. Blout, Circular dichroism study of the unfolding-refolding of a cardiotoxin from Taiwan cobra (*Naja naja atra*) venom, *Biochemistry* 24 (1985) 5678.
- [34] E.R. Blout, L. Visser, Elastase. II. Optical properties and the effects of sodium dodecyl sulfate, *Biochemistry* 10 (1971) 743.
- [35] E.L. Gelamo, M. Tabak, Spectroscopic studies on the interaction of bovine (BSA) and human (HSA) serum albumins with ionic surfactants, *Spectrochim. Acta A* 56 (2000) 2255.
- [36] S. Allen, L. Stevens, D. Duncan, S.M. Kelly, N.C. Price, Unfolding and refolding of hen egg-white riboflavin binding protein, *Int. J. Biol. Macromol.* 14 (1992) 333.
- [37] J.-D. Choi, D.B. McCormick, The interaction of flavins with egg white riboflavin-binding protein, *Arch. Biochem. Biophys.* 204 (1980) 41.
- [38] B. Valeur, J.C. Brochon, New trends in fluorescence spectroscopy, Springer Press, Berlin, 2001.

# Chapter 8

## Exploration of Environmental Dynamics and Enzymatic Activity in Nanoscopic Confinement

### 8.1. Introduction:

The role of hydration in enzyme activity has been a longstanding unresolved problem in molecular biophysics [1-3]. To understand the molecular basis of the role of water in protein function, several studies have been done to correlate a relation between enzyme activity and hydration level. Most of the studies so far aimed at elucidating the role of water in enzyme function have utilized hydrated protein powders, films or in gas phase [4-7]. For instance, Daniel et al., examined the enzyme activity of pig liver esterase (PLE) at hydration level of 3 ( $\pm 2$ ) molecules of water per molecule of enzyme and suggested that neither hydration nor fast anharmonic dynamics (100 ps) are required for enzyme function [1, 2, 8]. It was also concluded in the study that involvement of faster dynamics very much depends on the specific requirement of the enzyme for its function. For example, the function of light-driven proton pump protein bacteriorhodopsin exhibits a strong correlation with dynamical transition and its range from 0.1 to a few hundred picoseconds [9-11]. Studies of lysozymes powders equilibrated with water in air have shown that catalysis reaction occurs at a hydration level below the monolayer water coverage (0.2 g of water per gram of enzyme) [12]. However, the way of importance of dynamics at the molecular level is difficult to achieve from a single experiment and is clearly missing in contemporary literature. Also, the use of enzyme powder complicates the measurement of enzyme activity, particularly at low catalytic activities. Thus, any correlation among enzyme hydration, dynamics, and activity is still not clear. A convenient way to study the water dynamics and enzyme activity is through encapsulation in reverse micelle (RM), because of the precise control of water loading properties ( $w_0 = [\text{water}]/[\text{surfactant}]$ ) in the system. In earlier studies from this group, the efficacy of the RM environment to study protein in controlled hydration has been demonstrated [13, 14]. Here, we have studied both enzymatic activity and water dynamics of Subtilisin *Carlsberg* (SC) and have correlated

the observed catalytic function with water dynamics. SC is an alkaline serine protease with a well-known three dimensional crystal structure [15], widely used as an additive in commercial laundry products [16]. The structure of the enzyme is retained in presence of wide variety of organic solvent and remains catalytically active even at low water content [3, 7]. Therefore, both the enzymatic activity and water dynamics of the protein can be studied over a wide range of the RM hydration. In the present work, we have measured the activity of the protein using N-CBZ-Gly-Gly-Leu p-nitroanilide as a substrate. For solvation dynamics study, we have used 3-(dansylamino)phenylboronic acid (DB) as a solvation probe. The use of DB as a solvation probe lies in the fact that it is a potent serine protease inhibitor [17]. Therefore, it is easy to monitor the change in hydration in the active site of the protein. Circular dichroism (CD) measurements have been performed to check the secondary structure of the encapsulated protein with different degrees of hydration. From the detailed analysis of the temperature dependent solvation dynamics, we have calculated activation energy barrier ( $E_{act}$ ) between free and bound type of water present in the solvation shell of the protein and the strength of the hydrogen bonds.

## **8.2. Results and Discussion:**

### **8.2.1. Modulation of Environmental Dynamics at the Active Site and Activity of an Enzyme Under Nanoscopic Confinement: Subtilisin *Carlsberg* in Anionic AOT Reverse Micelle [18]:**

RM is a tiny aqueous droplet, surrounded and stabilized by a monolayer of surfactant molecules, and dispersed in a water immiscible organic solvent. Addition of proteins in the RM causes encapsulation of the protein inside the aqueous core of the RM [13]. Figure 8.1 shows DLS spectra of the RM with different degrees of hydration in the presence and absence of the protein, SC. Similar peak position of spectra confirms the complete encapsulation of protein inside the RM core. However, hydrogen bonding properties of interfacial water is distinct from bulk water. Therefore, it is expected that the confined water molecules of the RM will affect the conformational properties of the encapsulated

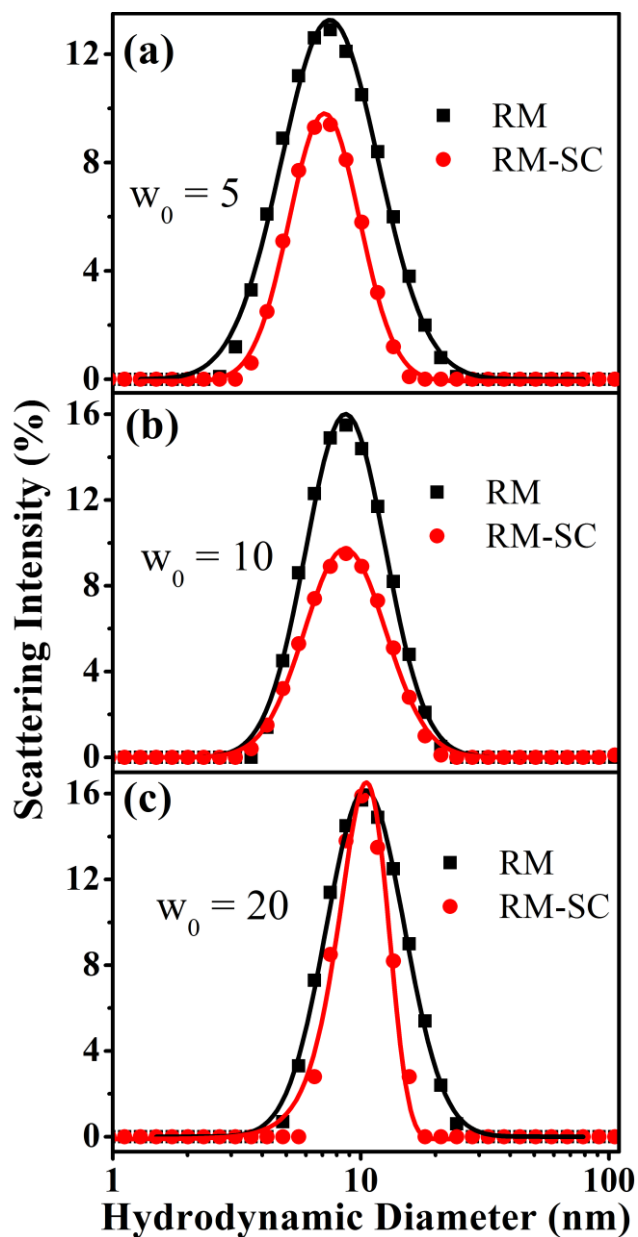


*Figure 8.1: (a-c) Dynamics light scattering spectra of reverse micelle in presence and absence of the enzyme, Subtilisin Carlsberg. The solid lines are guide to the eye.*

protein as well. To quantitatively compare our results with the expectation, we have monitored the conformational change of the protein using far-UV CD spectra. A comparison of the CD structure of free and encapsulated protein is shown in Figure 8.2a. A change in CD structure of the encapsulated protein is observed relative to the free protein in buffer. Appearance of two minima at 208 and 222 nm is indicative of the helical content of the protein. Thus the protein undergoes a significant increase in  $\alpha$ -helicity when

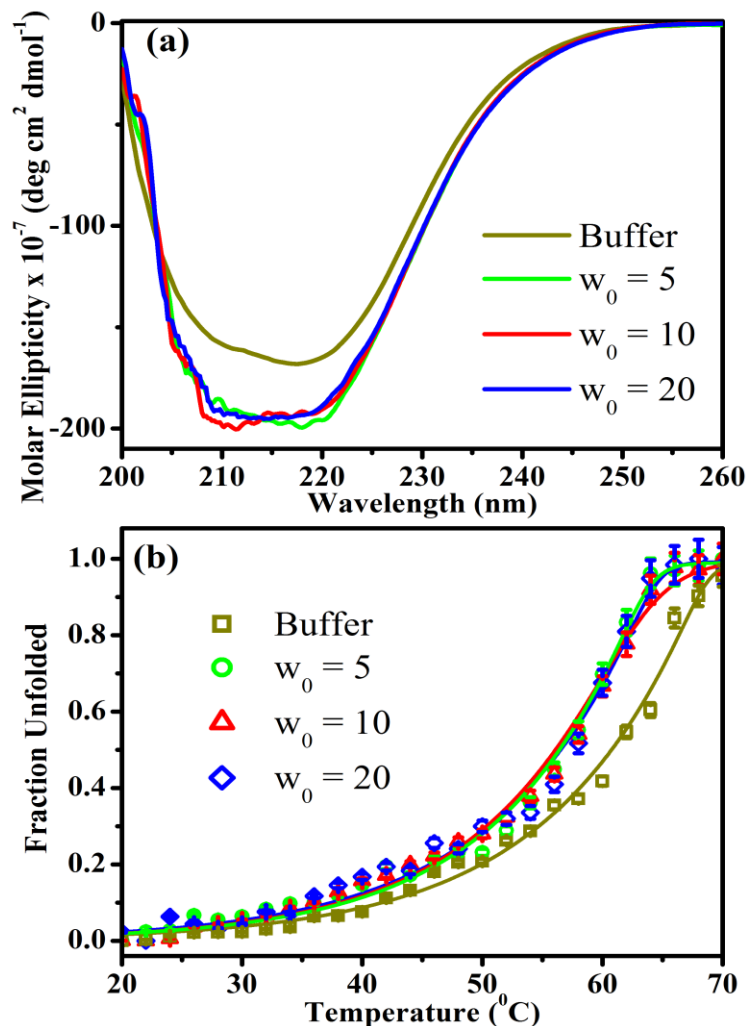


**Figure 8.2:** (a) Far- UV CD spectra of Subtilisin Carlsberg (SC) at various  $w_0$  values. (b) Fraction of unfolded protein in buffer and encapsulated in reverse micelle of various  $w_0$  values, as a function of temperature. The estimated error in measurement is about 2%.

introduced into AOT RM compared to that in aqueous buffer solution. Analysis of the spectra by CDNN/K2D analysis indeed reveals that  $\alpha$ -helix content of SC increases after encapsulation in AOT RM (Table 8.1, 8.2). As shown in Table 8.1, the content of  $\alpha$ -helix,  $\beta$ - sheet,  $\beta$ -turn and random coil structure of SC in aqueous buffer are 33.6, 17.5, 17.3 and 31.6% respectively, which are in excellent agreement with that calculated from the X-ray structure [19] and the report of Griebenow using Fourier transform infrared (FTIR) spectroscopy [20]. However, after encapsulation of protein in RM the  $\alpha$ -helix content increases from 33.6% in aqueous solution to 41.1% in the AOT RM. We have noted that the estimation of  $\alpha$ -helix content depends on the analysis software used (Table 8.1, 8. 2).

**Table 8.1: Percentages of  $\alpha$ -helix,  $\beta$ -structure,  $\beta$ -turn and random coil of SC in buffer and in RM of different degrees of hydration, calculated from CDNN analysis with standard error of ~2%.**

System	$\alpha$ -Helix (%)	Antiparallel (%)	Parallel (%)	$\beta$ -turn (%)	Random Coil (%)
Buffer	33.60	8.85	8.65	17.30	31.60
$w_0 = 5$	41.14	7.25	7.25	16.48	27.88
$w_0 = 10$	41.74	7.17	7.17	16.40	27.52
$w_0 = 20$	40.00	7.40	7.40	16.50	28.70

**Table 8.2: Percentages of  $\alpha$ -helix and  $\beta$ -sheet (parallel and antiparallel) of SC in buffer and in RM of different degrees of hydration, calculated from K2D analysis with standard error of ~2%.**

System	$\alpha$ -Helix (%)	Antiparallel (%)	Parallel (%)
Buffer	24	15	61
$w_0 = 5$	32	16	52
$w_0 = 10$	32	16	51
$w_0 = 20$	32	16	51

The increased helical content of the protein SC in RM is not surprising given the fact that in the RM confinement, most of the water molecules are hydrogen bonded to the negatively charged sulfosuccinate head groups of the AOT molecules leaving very few water molecules to interact with the protein SC. Therefore, the extent of hydrogen bonding between the amide group of the protein and water molecules decreases, consequently interhelical hydrogen bonds in such an environment are strengthened. Similar results are also observed for other proteins in surfactant solutions [21-25]. However, the molar ellipticity remains unaltered with increasing the  $w_0$  values indicating the positioning of SC near the surface of the RM. In order to obtain more insight on the stability of the protein due to confinement effect, the thermal unfolding transition experiments are carried out. As shown in Figure 8.2b, the thermal unfolding curves obtained by recording CD signal of the encapsulated protein at 222 nm exhibit different thermal melting behaviors (~58 °C) than that of the free protein (64 °C) in aqueous solution. This destabilization may arise due to the geometrical confinement effect of the RM, as RM is reported to have two opposing effects on helical structure: stabilization due to backbone dehydration and destabilization due to geometrical confinement [25], where the latter appears to be dominating in our experiment. However, as shown in Figure 8.2 and Tables 8.1, 8.2, after encapsulation there is no such change either in  $\alpha$ -helix content or in thermal stability of the protein with increasing degrees of hydration.

Figure 8.3a shows enzymatic activity of the protein SC in the AOT RM with various degrees of hydration ( $w_0$ ) within the structural integrity of the protein in the nanoenvironments. The estimated specific activity (Figure 8.3b; Table 8.3) is found to be increased with increasing degree of hydration. Scheme 8.1 shows the mechanistic pathways for the hydrolysis of the substrate CBZ-GGL-pNA by SC. Briefly, in the first step the nucleophile (Ser-221) attacks the substrate to form an acyl-enzyme intermediate followed by deacylation in the second step. In the final step, water act as a nucleophile which hydrolyzes the ester bond between the substrate and Ser-221 of the enzyme to form

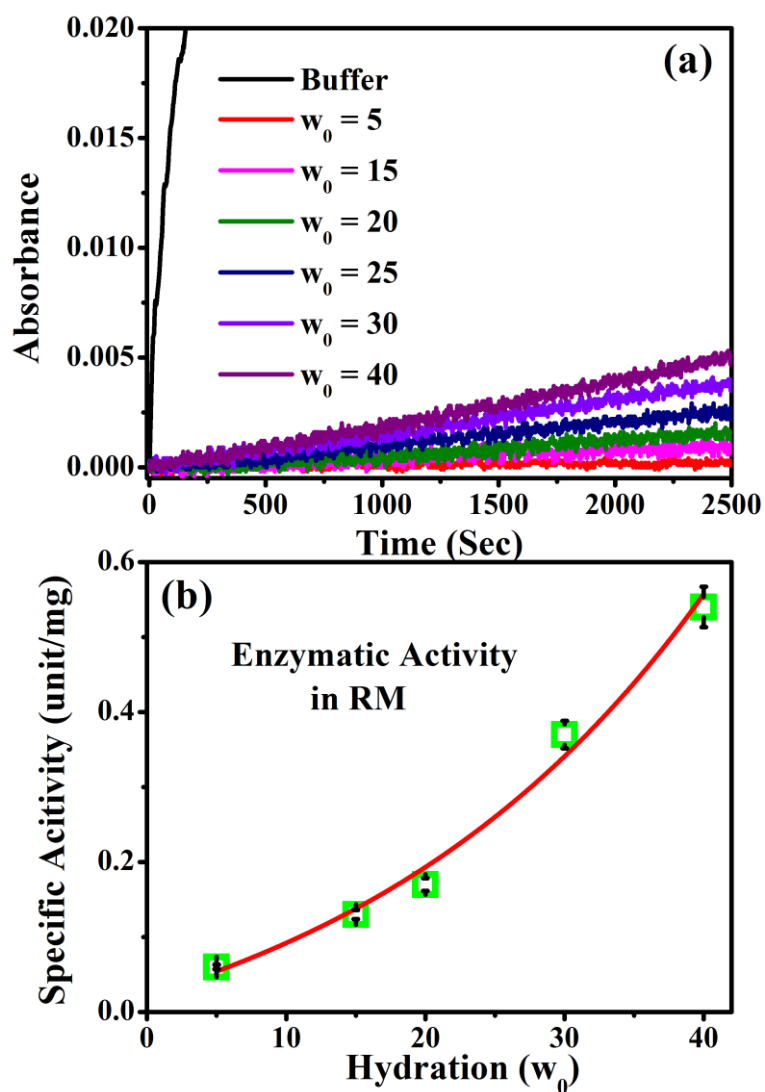
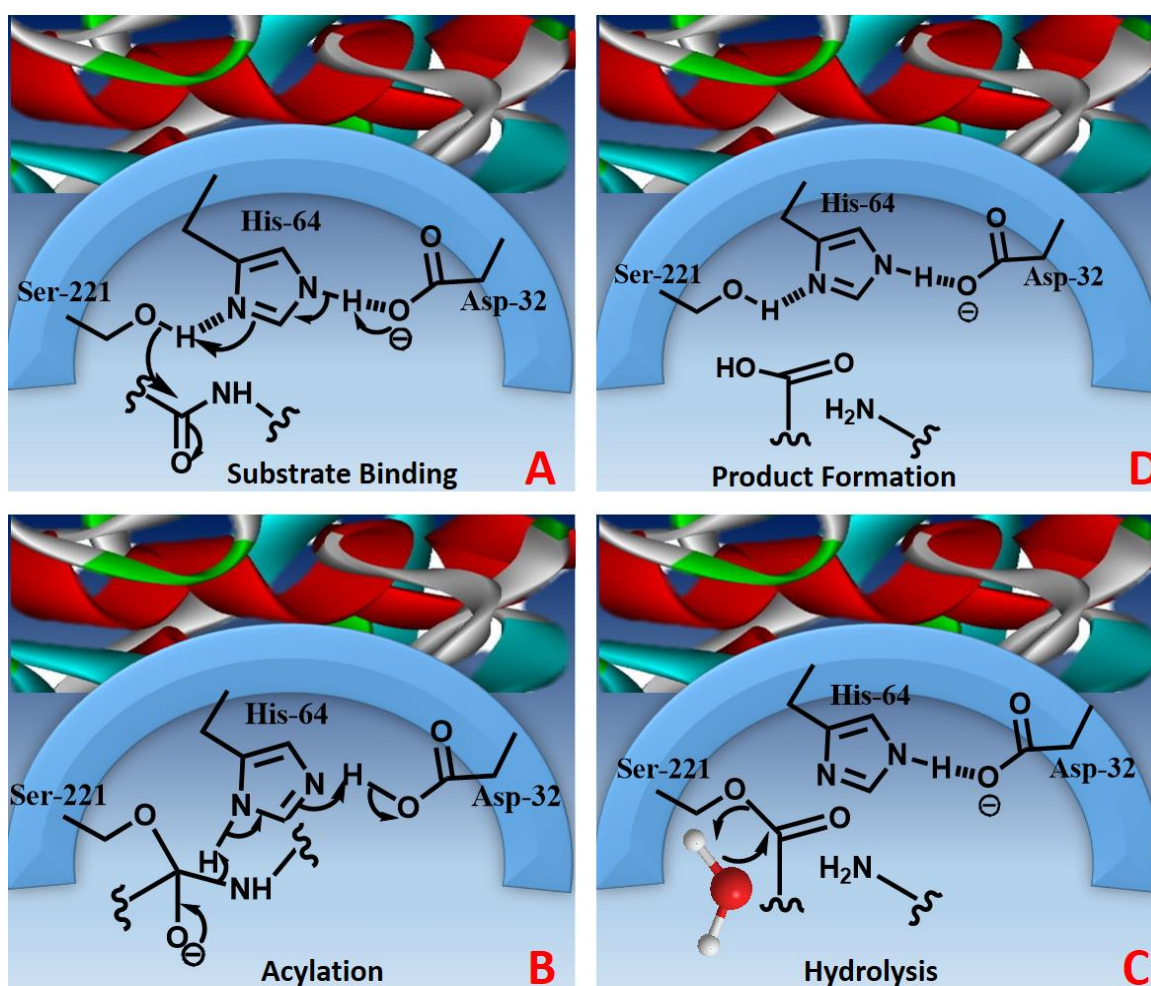


Figure 8.3: (a) Enzymatic activity of SC in buffer and in RM with different  $w_0$  values. (b) Change in specific activity of SC with changing  $w_0$  values of the AOT RM. Solid line is guide to the eye. The estimated error in measurement is about 3%.

**Table 8.3: Comparison of Specific Activity in units/mg of SC in buffer and in RM with different  $w_0$  values with standard error of ~5%.<sup>a</sup>**

System	Specific Activity (units/mg)
Buffer	14.87
$w_0 = 5$	0.06
$w_0 = 15$	0.12
$w_0 = 20$	0.17
$w_0 = 30$	0.39
$w_0 = 40$	0.54

<sup>a</sup> According to vendor (Sigma-Aldrich) one unit of SC will hydrolyze casein to produce color equivalent to 1.0  $\mu$ mole (181  $\mu$ g) of tyrosine per min at pH 7.5 at 37 °C (color by Folin-Ciocalteu reagent). The specific activity of the native SC is 7-15 units/mg



**Scheme 8.1: Schematic representation of the mechanistic pathway for substrate hydrolysis by the enzyme SC. In the first step the nucleophile (Ser-221) attacks the substrate (CBZ-GGL-pNA) to form an acyl-enzyme intermediate followed by deacylation in the second step. In the final step water acts as nucleophile which hydrolyzes the ester bond between the substrate and Ser-221 of the enzyme to form the final hydrolysis products.**

the final hydrolysis products. The distinct difference in enzymatic activity of the protein even at higher  $w_0$  values compared to bulk buffer again suggests the positioning of the enzyme near the surface of the RM. In order to correlate the change of enzymatic activity of the protein with water dynamics at the active site, we have used time-dependent fluorescence Stokes shift (TDFSS) method using the fluorescence behavior of the enzyme inhibitor, DB, attached to the active site of the enzyme. Figure 8.4b shows the fluorescence decay transients of SC-DB adduct in the RM of  $w_0 = 5$  at three selected wavelengths at room temperature. The decay transients at the blue end (430 nm) can be fitted tri-exponentially with the time components of 180 ps (47%), 1.03 ns (44%) and 4.10 ns (9%), whereas, at the extreme red wavelength (590 nm) the transient shows rise components of 480 ps and 1.95 ns along with a decay component of 10 ns. The presence of faster decay components at the blue end and rise component at the red wavelength in contrast to the

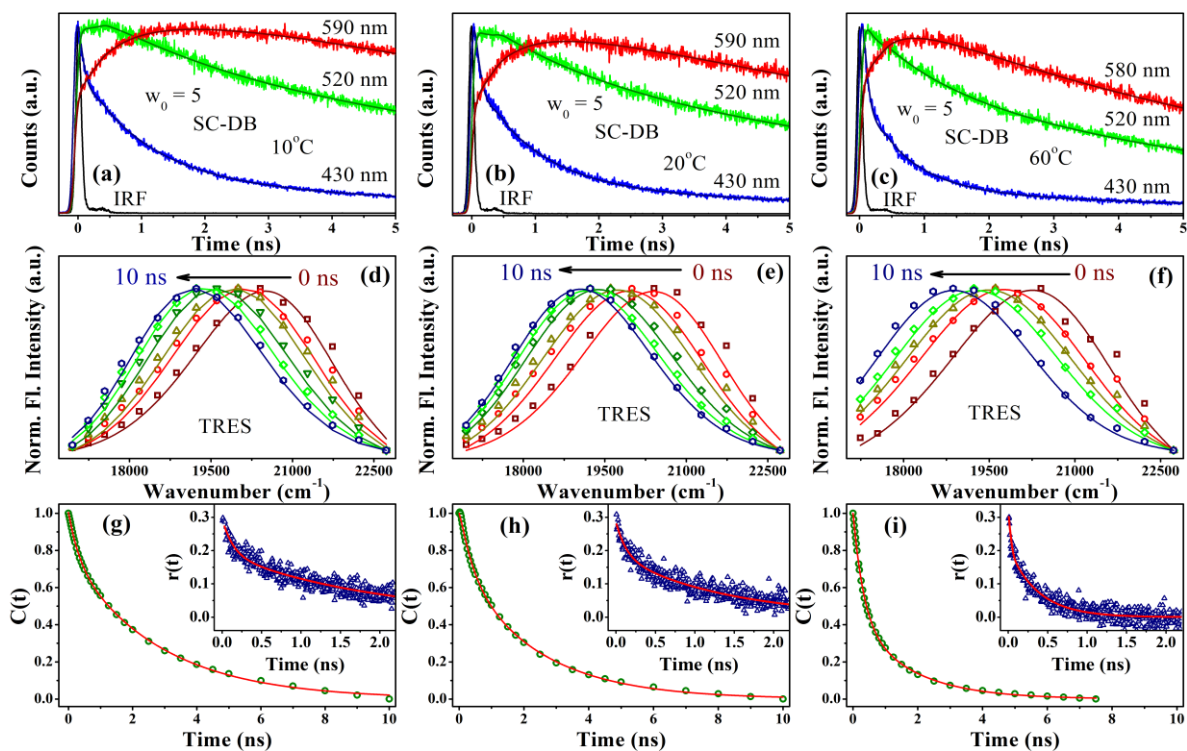


**Figure 8.4:** (a-c) Fluorescence decay transients of 3-(dansylamino)phenylboronic acid bound to *Subtilisin Carlsberg*, encapsulated within AOT reverse micelle of  $w_0 = 5$  at different temperatures. (d-f) and (g-i) are the corresponding time-resolved emission spectra (TRES) and solvent correlation function,  $C(t)$  respectively. The corresponding anisotropy decay profiles,  $r(t)$  are shown in the inset of Figure of (g-i). The estimated error in measurement is about 2%.

protein in aqueous solution is indicative of slower solvation of the probe in the encapsulated protein. From these decay transients, we construct the time-resolved emission spectra (TRES) as shown in Figure 8.4e, which is associated with a significant dynamical Stokes shift of  $1350 \text{ cm}^{-1}$  in 10 ns. Following TRES, we have constructed the solvent correlation function,  $C(t)$  using equation 2-14. The temporal decay of the  $C(t)$  shows biexponential decay with time constants of 410 ps and 2.35 ns (Figure 8.4h and Table 8.4). Previous theoretical [26] and experimental [27-30] studies on hydration at bio-interfaces have revealed that the interfacial waters are hydrogen bonded to the biomolecular interface and show slower dynamics than that of bulk water. The slow components in solvation dynamics may be due to several reasons, for example, self-diffusion of probe (DB),

**Table 8.4: Time constants for  $C(t)$  and  $r(t)$  of SC in RM using DB as fluorescent probe, at various temperatures with standard error of  $\sim 5\%$ .<sup>a</sup>**

$w_0$	Temp. (°C)	Em. peak (nm)	Solvation Time Constants					$E_{act}$ (kcal $mol^{-1}$ )	Rotational Time Constants			
			$a_1$	$\tau_1$ (ns)	$a_2$	$\tau_2$ (ns)	$\langle \tau_{av} \rangle$ (ns)		$a_1$	$\tau_1$ (ns)	$a_2$	$\tau_2$ (ns)
5	10	508	0.23	0.32	0.77	2.78	2.23	3.3±0.02	0.35	0.13	0.65	1.95
	20	512	0.30	0.41	0.70	2.35	1.77		0.34	0.12	0.66	1.39
	30	515	0.23	0.25	0.77	1.33	1.08		0.23	0.11	0.77	0.75
	40	517	0.52	0.42	0.48	2.10	1.23		0.29	0.06	0.71	0.59
	50	518	0.54	0.37	0.46	1.75	1.00		0.32	0.05	0.68	0.48
	60	519	0.56	0.32	0.44	1.69	0.92		0.36	0.02	0.64	0.38
10	10	518	0.51	0.63	0.49	2.90	1.75	3.4±0.02	0.07	0.29	0.16	1.82
	20	520	0.70	0.58	0.30	3.19	1.37		0.07	0.12	0.18	0.94
	30	523	0.71	0.45	0.29	2.20	0.96		0.08	0.16	0.14	0.10
	40	525	0.70	0.38	0.30	2.10	0.89		0.07	0.16	0.14	0.91
	50	526	0.74	0.30	0.26	2.30	0.82		0.10	0.15	0.13	0.64
	60	526	0.69	0.26	0.31	1.80	0.74		0.11	0.24	0.09	0.67
20	10	524	0.49	0.37	0.51	1.65	1.02	3.5±0.02	0.09	0.22	0.17	1.42
	20	527	0.58	0.29	0.42	1.37	0.74		0.10	0.21	0.15	1.23
	30	528	0.61	0.24	0.39	1.19	0.60		0.12	0.18	0.13	1.06
	40	529	0.69	0.22	0.31	1.12	0.50		0.10	0.11	0.14	0.66
	50	529	0.74	0.20	0.26	1.02	0.42		0.12	0.10	0.13	0.53
	60	529	0.73	0.20	0.26	1.00	0.41		0.15	0.12	0.09	0.61

<sup>a</sup>  $\tau_i$  represents the time constants,  $a_i$  represents its relative contribution, and  $\langle \tau_s \rangle$  is the average solvation time constant.

tumbling of the protein, local relaxation of the protein matrix, and dynamic exchange between bound and free water. The minimal change in time-dependent full width half-maxima in TRES (Figures 8.4-8.6), suggests the insignificant contribution from self-diffusion of the probe in the solvation response [31]. Tumbling motion or reorientation of the entire protein molecule causes time scale of around 10-100 ns, which is markedly higher than time components realized for DB in SC (Table 8.4) [31]. Therefore, in the present study, the origin of the slow component might be due to the collective contribution from both the bound type water as well as from the segmental motion of the protein residues. As the probe DB resides into the enzyme pocket of the protein, hence there should be a contribution from the protein residue. Similar result is also reported earlier by Sahu et. al [32] where they showed slow solvation time component (4.5 ns) for ANS bound to BSA. We have also studied the solvation dynamics of the encapsulated protein at

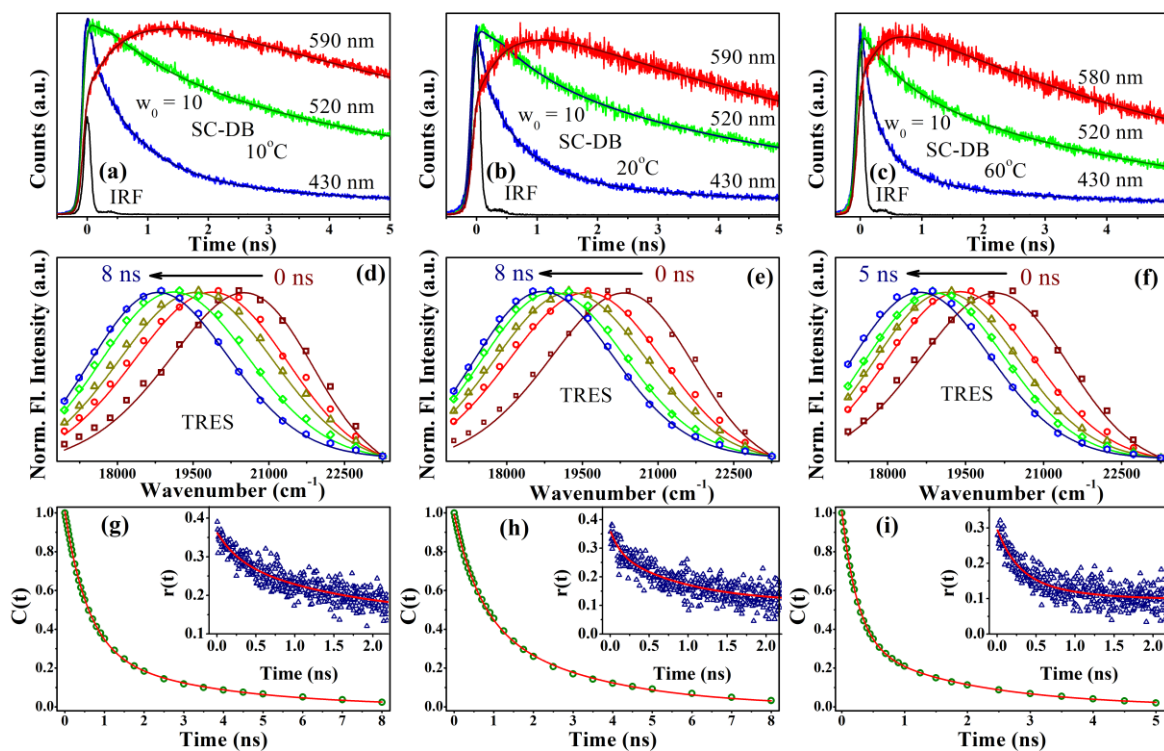


**Figure 8.5:** (a-c) Fluorescence decay transients of 3-(dansylamino)phenylboronic acid bound to Subtilisin Carlsberg, encapsulated within AOT reverse micelle of  $w_0 = 10$  in different temperatures. (d-f) and (g-i) are the corresponding time-resolved emission spectra (TRES) and solvent correlation function,  $C(t)$  respectively. The corresponding anisotropy decay profiles,  $r(t)$  are shown in the inset of panels g-i. The estimated error in measurement is about 2%.

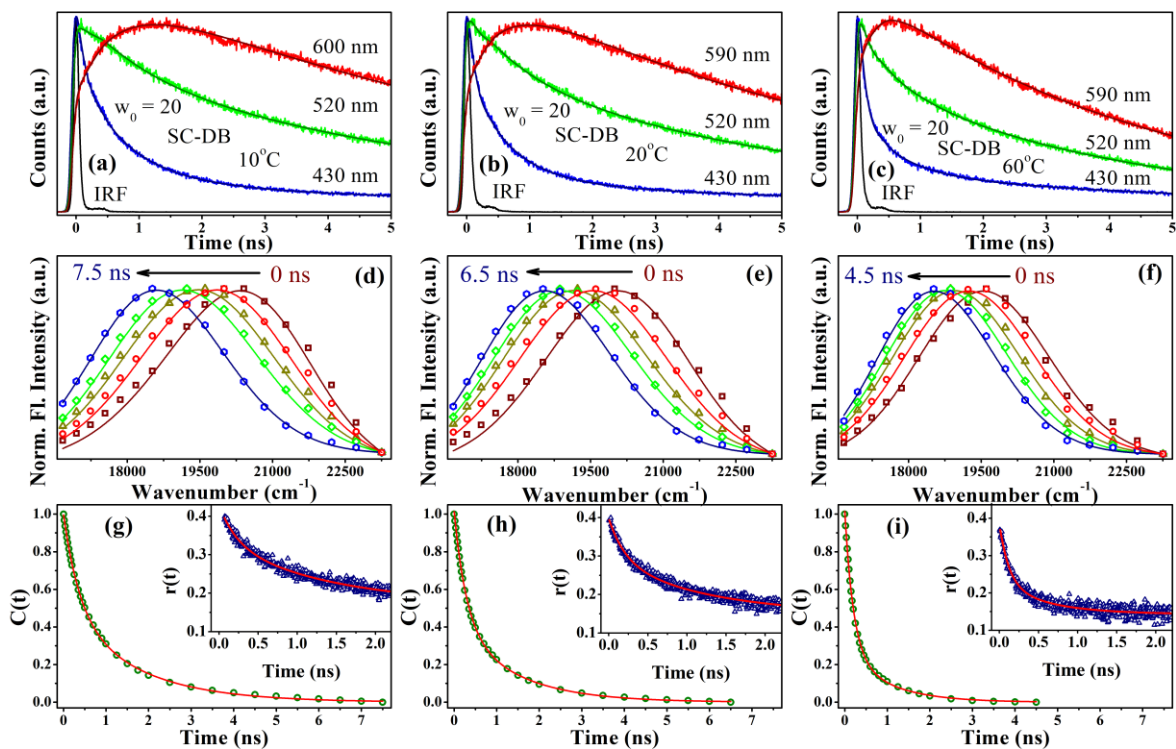


**Figure 8.6:** (a-c) Fluorescence decay transients of 3-(dansylamino)phenylboronic acid bound to Subtilisin Carlsberg, encapsulated within AOT reverse micelle of  $w_0 = 20$  in different temperatures. (d-f, g-i) Corresponding TRES and  $C(t)$ , respectively. The corresponding anisotropy decay profiles,  $r(t)$  are shown in the inset of panels g-i. The estimated error in measurement is about 2%.

different temperatures. Figure 8.4 shows the temperature-dependent solvation dynamics study at three representative temperatures (10, 20, and 60 °C) of the protein in the AOT RM at  $w_0 = 5$ . With an increase in temperature, the average solvation time constant,  $\langle\tau_s\rangle$  ( $= \sum_i a_i \tau_i$ ) becomes faster (Table 8.4) revealing increased flexibility of the protein with associated interfacial water at higher temperature. The increased flexibility of the protein at higher temperature is also reflected from the faster rotational anisotropy data of the probe at higher temperature (inset, Figure 8.4g-i). Figure 8.5, 8.6 shows the dynamics at the active site of the protein in the AOT RM in higher degree of hydration ( $w_0 = 10$  and 20) at different temperatures. It is clear from the studies that with increase in  $w_0$ , the solvation dynamics at a particular temperature becomes faster attributing less confinement effect with increasing  $w_0$  [33, 34].

In order to study the role of the protein in the slower dynamics of solvation at the active site, in a series of control experiments we have investigated the solvation dynamics of the RM without protein, using the probe DB (Figures 8.7-8.9; Table 8.5). The observed solvation time constants are quite similar to the previous studies in AOT RM systems and are attributed to the interfacial bound type and free type water molecules, respectively [35]. The dependency of average solvation time constant in different degrees of hydration ( $w_0$ ) and in different temperatures is found to be similar to those at the active site of the protein in the AOT RM, however, in a different way as shown in Figure 8.10. From the temperature- induced acceleration of solvation dynamics of water in encapsulated protein and free RM, we have calculated the free energy of activation from bound to free water molecules using multishell continuum model proposed by Bagchi et al. [26] Briefly, the water molecules at the interface comprise two components: one is “free water” and the other is attached to the biomolecule by a strong hydrogen bond and rotates only in a

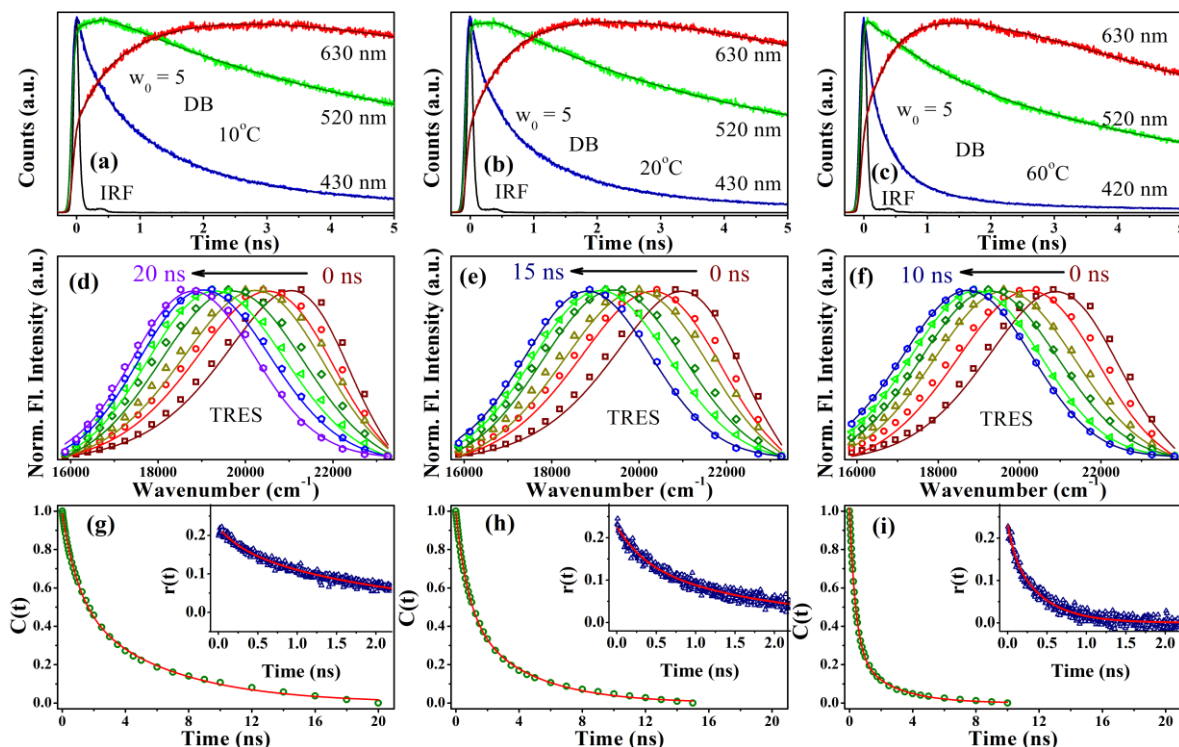


**Figure 8.7:** (a-c) Fluorescence decay transients of 3-(dansylamino)phenylboronic acid in AOT reverse micelle of  $w_0 = 5$  in different temperatures as a control study. (d-f, g-i) Corresponding TRES and  $C(t)$ , respectively. The corresponding anisotropy decay profiles,  $r(t)$  are shown in the inset of panels g-i. The estimated error in measurement is about 2%.

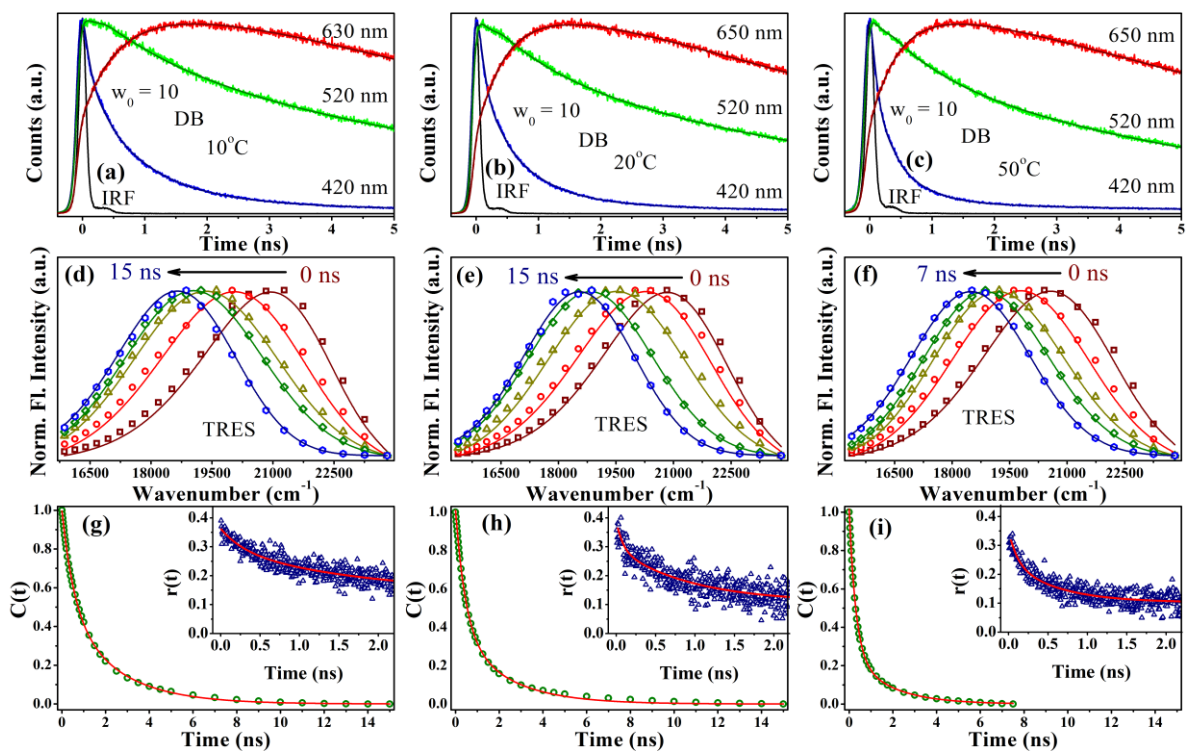


**Figure 8.8:** (a-c) Fluorescence decay transients of 3-(dansylamino)phenylboronic acid in AOT reverse micelle of  $w_0 = 10$  in different temperatures as a control study. (d-f) Corresponding TRES and  $C(t)$ , respectively. The corresponding anisotropy decay profiles,  $r(t)$  are shown in the inset of panels g-i. The estimated error in measurement is about 2%.

coupled fashion with the slowly rotating biomolecule. The latter species is termed “bound water” and there is always a dynamic exchange between the free and bound water. The energetic of this bound to free type transition of water molecules with temperature is assumed to be governed by an Arrhenius type of activation energy barrier crossing model [26, 36, 37] as follows:

$$k_{\text{bf}} \approx \frac{1}{\langle \tau_s \rangle} = A \exp\left(\frac{-E_{\text{act}}}{RT}\right) \quad (8-1)$$

where  $\langle \tau_s \rangle$  represents the average solvation time constant,  $k_{\text{bf}}$  is the rate constant for bound-to-free water conversion,  $A$  is the pre-exponential factor, and  $E_{\text{act}}$  is the corresponding activation energy for the transition process. Plot of  $\ln(1/\langle \tau_s \rangle)$  vs.  $1/T$  produces good linear fits (Figure 8.11) with corresponding activation energy values of 3.3, 3.4, and 3.5 kcal mol<sup>-1</sup> for protein encapsulated in  $w_0 = 5, 10$  and 20 RMs, respectively, whereas activation energy values for free RM are 4.0, 4.3, and 5.0 kcal mol<sup>-1</sup> respectively.

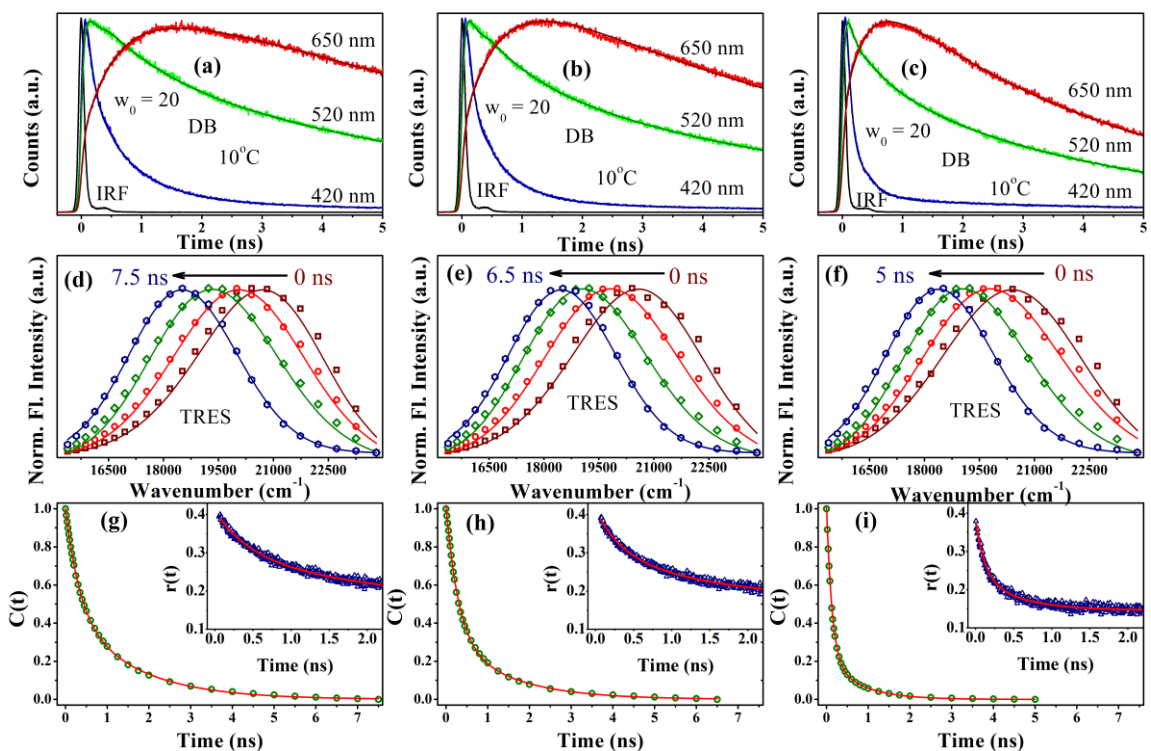


**Figure 8.9:** (a-c) Fluorescence decay transients of 3-(dansylamino)phenylboronic acid in AOT reverse micelle of  $w_0 = 20$  in different temperatures as a control study. (d-f) Corresponding TRES and  $C(t)$ , respectively. The corresponding anisotropy decay profiles,  $r(t)$  are shown in the inset of panels g-i. The estimated error in measurement is about 2%.

**Table 8.5:** Time constants for solvent correlation function,  $C(t)$  and rotational time constants,  $r(t)$  of DB in RM at various temperatures with standard error of  $\sim 5\%$ .<sup>a</sup>

$w_0$	Temp. (°C)	Em. peak (nm)	Solvation Time Constants					$E_{act}$ (kcal mol <sup>-1</sup> )	Rotational Time Constants			
			$a_1$	$\tau_1$ (ns)	$a_2$	$\tau_2$ (ns)	$\langle \tau_{av} \rangle$ (ns)		$a_1$	$\tau_1$ (ns)	$a_2$	$\tau_2$ (ns)
5	10	508	0.45	1.03	0.55	5.83	3.66	3.5±0.02	0.22	0.30	0.78	2.16
	20	512	0.52	0.78	0.48	3.97	2.33		0.36	0.36	0.64	1.82
	30	516	0.66	0.72	0.34	4.09	1.87		0.47	0.34	0.53	1.58
	40	518	0.65	0.52	0.35	2.39	1.18		0.25	0.15	0.75	0.71
	50	519	0.71	0.44	0.29	2.49	1.03		0.24	0.06	0.76	0.47
	60	520	0.73	0.39	0.27	2.36	0.92		0.25	0.08	0.75	0.41
10	10	520	0.49	0.56	0.51	2.32	1.46	4.3±0.04	0.07	0.29	0.16	1.84
	20	523	0.61	0.45	0.39	2.20	1.13		0.09	0.08	0.19	0.94
	30	526	0.74	0.40	0.26	2.05	0.83		0.11	0.11	0.14	1.04
	40	527	0.74	0.31	0.26	1.68	0.66		0.07	0.17	0.13	0.94
	50	528	0.74	0.30	0.26	1.75	0.67		0.11	0.11	0.14	0.60
20	10	526	0.52	0.33	0.48	1.54	0.91	5.0±0.08	0.11	0.44	0.14	2.21
	20	529	0.67	0.29	0.33	1.42	0.66		0.10	0.32	0.14	1.50
	30	531	0.72	0.22	0.28	1.27	0.51		0.12	0.23	0.13	1.17
	40	532	0.75	0.17	0.25	1.08	0.40		0.14	0.16	0.12	0.87
	50	533	0.79	0.16	0.21	0.96	0.33		0.13	0.14	0.11	0.64
	60	533	0.79	0.13	0.21	0.78	0.27		0.14	0.12	0.09	0.53

<sup>a</sup>  $\tau_i$  represents the time constants,  $a_i$  represents its relative contribution, and  $\langle \tau_{av} \rangle$  is the average solvation time constant.

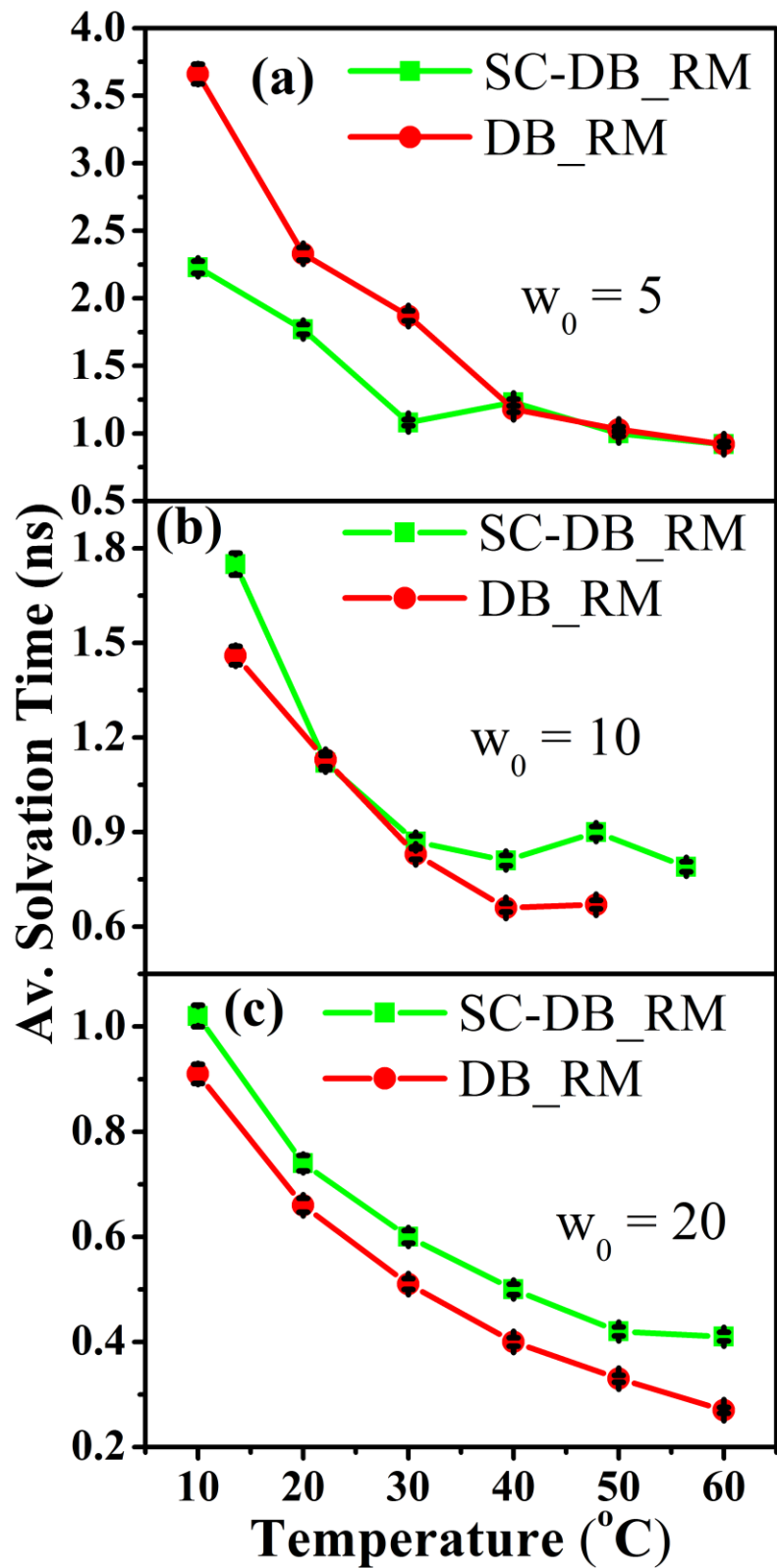


Figure 8.10: Comparison of the average solvation time constant of free 3-(dansylamino)phenylboronic acid and bound to Subtilisin Carlsberg encapsulated within reverse micelle of different  $w_0$  values. The estimated error in measurement is about 2%.

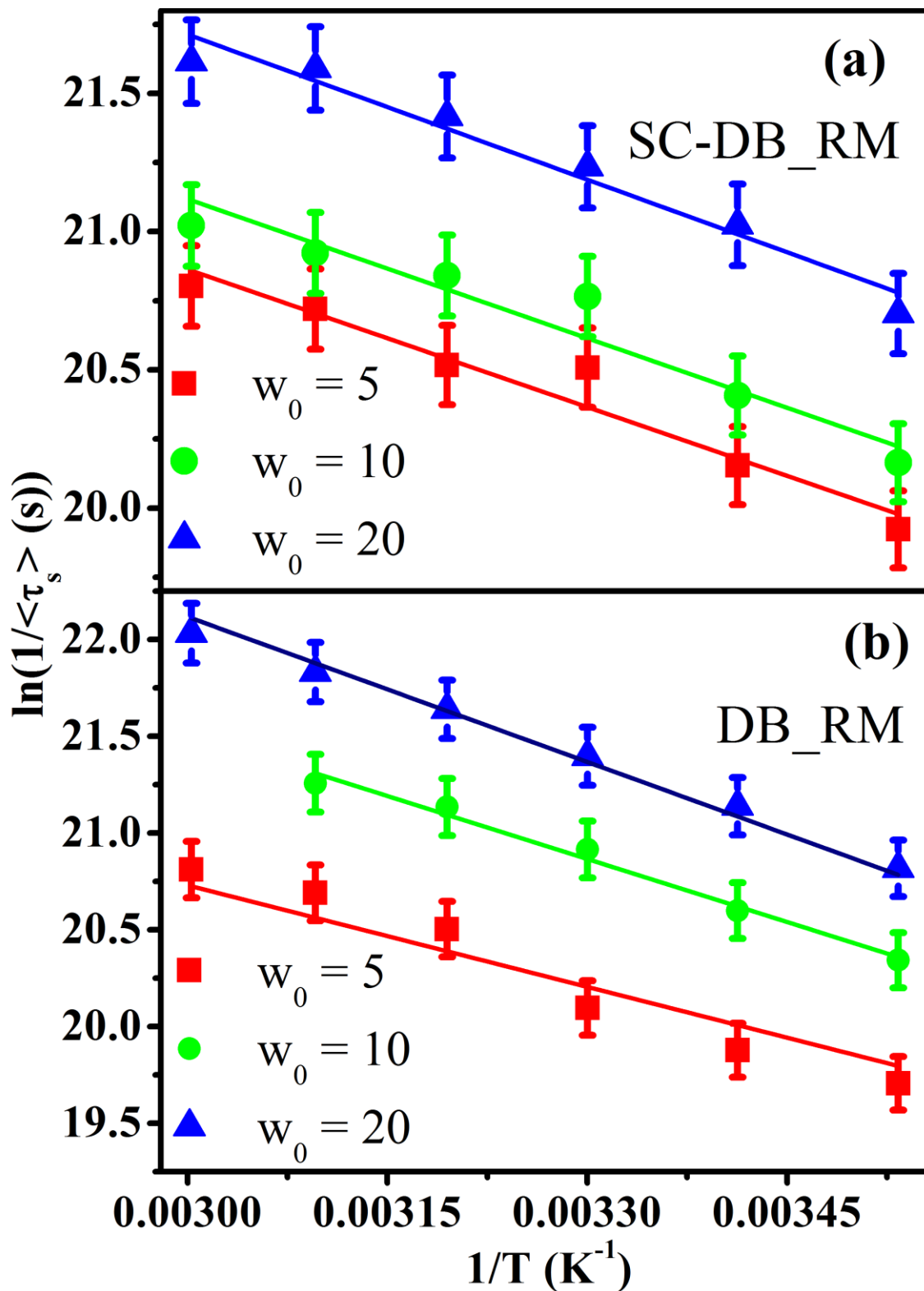
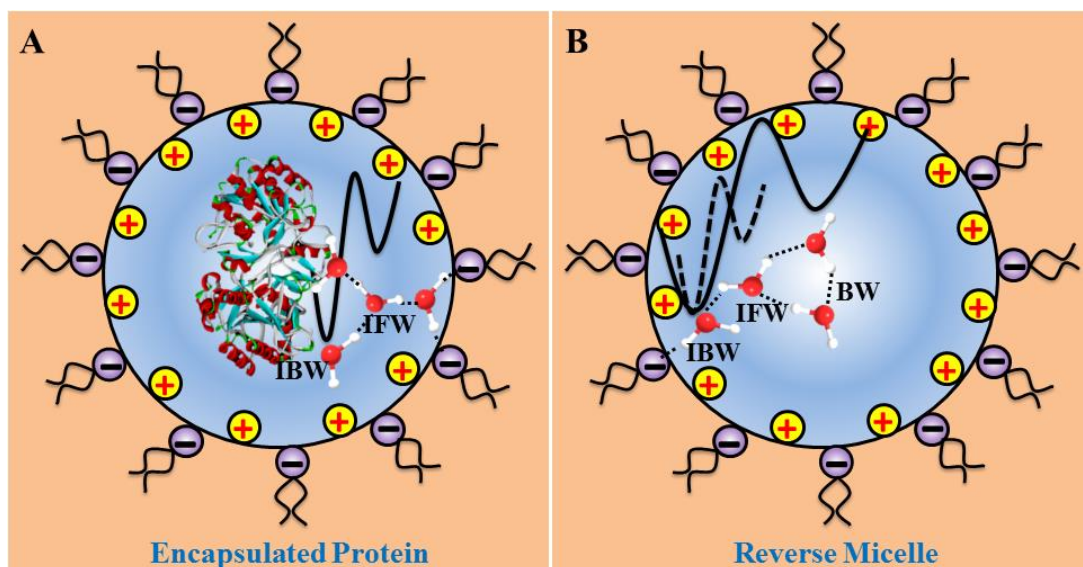


Figure 8.11: Plot of  $\ln(1/\tau_s)$  against  $1/T$  for for AOT/i-Oc RM with  $w_0 = 5, 10,$  and  $20$  in presence (a) and absence (b) of the enzyme, SC. Straight lines are fitting of the experimental data using equation 8-1 (see text). The estimated error is about 1%.



**Scheme 8.2:** Schematic representation of the different types of water molecules namely interfacial bound water (IBW, water molecules hydrogen bonded to protein surface or AOT head groups), interfacial free water (IFW, water molecules hydrogen bonded to IBW) and bulk type water (BW), respectively. For encapsulated protein there are mainly two types of water molecules irrespective of the hydration number due to hydration sharing by both protein and surfactant head group. Thus, the activation energy ( $E_{act}$ ) is almost same. However for RM, with increasing hydration number ( $\geq 10$ ) bulk type (BW) of water molecules generates. Therefore, the activation energy ( $E_{act}$ ) increases (see text).

The observed  $E_{act}$  values for protein free RM are in good agreement with our previous result using C500 as solvation probe [38]. It has to be noted that energy barrier calculated for  $w_0 = 5$  is relatively lower and this could be because at  $w_0 = 5$  RM has only two types of water molecules namely interfacial bound water (IBW, water molecules hydrogen bonded to protein surface or AOT head groups) and interfacial free water (IFW, water molecules hydrogen bonded to IBW) (Scheme 8.2A, B) and this type of conversion is associated with an energy barrier of 2.4-4 kcal mol<sup>-1</sup> [39]. However, for the higher  $w_0$  values ( $\geq 10$ ), the RM water pool is formed and the probe senses a transition from IBW to bulk type (BW) water molecules (Scheme 8.2B) that is associated with a higher energy barrier of 7–8 kcal mol<sup>-1</sup> [40]. However, in the encapsulated protein there is only two types of water molecules (IBW and IFW) as shown in Scheme 8.2A, and bulk type water is not formed even at higher  $w_0$  values due to the competitive sharing of hydration water between the protein and surfactant molecules. This makes the  $E_{act}$  value to be remain same at all the  $w_0$  values of the encapsulated protein, although  $\langle \tau_s \rangle$  changes due to the increased fraction of interracially free water (IFW) at higher  $w_0$  values. Thus the dynamics and energetics of

water molecules at the active site of the enzyme is correlated with the degree of hydration and differentiated from the free reverse micelle.

### **8.3. Conclusion:**

In conclusions, the study presented here investigates the structure, function and dynamics of SC in AOT RM. The solvation dynamics at the active site of the enzyme becomes faster with increasing  $w_0$  values of the AOT RM. The observed acceleration of faster dynamics is due to increased content of interfacial free type (IFW) of water molecules at higher  $w_0$  values. CD result suggests the helical content of the protein to be increased in AOT RM compared to free aqueous buffer, which remains unaltered by changing  $w_0$  values. However, the enzymatic activity is found to be increased with increasing water content in the RM. The genesis of the observation appears to stem from the hydrolysis characteristics of the reaction between CBZ-GGL-pNA and SC, where water act as nucleophile (Scheme 8.1). Faster hydration dynamics at the active site of the enzyme with increasing water content causes an increase in local polarity around the active site due to the hydration of polar and charged groups. The increase in polarity increases the active site flexibility, which in turn facilitates the hydrolysis reaction. The increased activity of the enzyme at higher hydration also supports the fact that global structural intactness is not an accurate indication of the active site flexibility. The temperature dependent hydration dynamics supports the general view that the mobility of the water molecules in protein surface or RM increases with temperature due to the transition of surface bound water to free water at elevated temperature, which is also revealed by the Arrhenius type of energy barrier crossing model. The result presented here establish the fact that hydration dynamics has an important role on the functionality of an enzyme.

## References

- [1] R.M. Daniel, R.V. Dunn, J.L. Finney, J.C. Smith, The role of dynamics in enzyme activity, *Annu. Rev. Biophys. Biomol. Struct.* 32 (2003) 69.
- [2] M. Lopez, V. Kurkal-Siebert, R.V. Dunn, M. Tehei, J.L. Finney, J.C. Smith, R.M. Daniel, Activity and dynamics of an enzyme, pig liver esterase, in near-anhydrous conditions, *Biophys. J.* 99 (2010) L62.
- [3] R. Affleck, Z.F. Xu, V. Suzawa, K. Focht, D.S. Clark, J.S. Dordick, Enzymatic catalysis and dynamics in low-water environments, *Proc. Natl. Acad. Sci. USA* 89 (1992) 1100.
- [4] F. Létisse, S. Lamare, M.D. Legoy, M. Graber, Solid/gas biocatalysis: An appropriate tool to study the influence of organic components on kinetics of lipase-catalyzed alcoholysis, *Biochim. Biophys. Acta* 1652 (2003) 27.
- [5] P.A. Lind, R.M. Daniel, C. Monk, R.V. Dunn, Esterase catalysis of substrate vapour: Enzyme activity occurs at very low hydration, *Biochim. Biophys. Acta* 1702 (2004) 103.
- [6] M. Graber, M.P. Bousquet-Dubouch, N. Sousa, S. Lamare, M.D. Legoy, Water plays a different role on activation thermodynamic parameters of alcoholysis reaction catalyzed by lipase in gaseous and organic media, *Biochim. Biophys. Acta* 1645 (2003) 56.
- [7] A. Zaks, A.M. Klivanov, Enzymatic catalysis in nonaqueous solvents, *J. Biol. Chem.* 263 (1988) 3194.
- [8] R.M. Daniel, J.C. Smith, M. Ferrand, S. Héry, R. Dunn, J.L. Finney, Enzyme activity below the dynamical transition at 220 K, *Biophys. J.* 75 (1998) 2504.
- [9] J. Fitter, R.E. Lechner, N.A. Dencher, Picosecond molecular motions in bacteriorhodopsin from neutron scattering, *Biophys. J.* 73 (1997) 2126.
- [10] U. Lehnert, V. Réat, M. Weik, G. Zaccai, C. Pfister, Thermal motions in bacteriorhodopsin at different hydration levels studied by neutron scattering: Correlation with kinetics and light-induced conformational changes, *Biophys. J.* 75 (1998) 1945.
- [11] M. Ferrand, A.J. Dianoux, W. Petry, G. Zaccai, Thermal motions and function of bacteriorhodopsin in purple membranes: Effects of temperature and hydration studied by neutron scattering, *Proc. Natl. Acad. Sci. USA* 90 (1993) 9668.

- [12] A. Rupley John, P.H. Yang, G. Tollin, Thermodynamic and related studies of water interacting with proteins, *ACS. Symp. Ser.* 127 (1980) 111.
- [13] R. Biswas, S.K. Pal, Caging enzyme function:  $\alpha$ -chymotrypsin in reverse micelle, *Chem. Phys. Lett.* 387 (2004) 221.
- [14] R. Saha, S. Rakshit, P.K. Verma, R.K. Mitra, S.K. Pal, Protein–cofactor binding and ultrafast electron transfer in riboflavin binding protein under the spatial confinement of nanoscopic reverse micelles, *J. Mol. Recognit.* 26 (2013) 59.
- [15] R. Bott, M. Ultsch, A. Kossiakoff, T. Graycar, B. Katz, S. Power, The three-dimensional structure of bacillus amyloliquefaciens subtilisin at 1.8 Å and an analysis of the structural consequences of peroxide inactivation, *J. Biol. Chem.* 263 (1988) 7895.
- [16] D.R. Durham, Utility of subtilisin GX as a detergent additive, *J. Appl. Microbiol.* 63 (1987) 381.
- [17] R. Smoum, A. Rubinstein, V.M. Dembitsky, M. Srebnik, Boron containing compounds as protease inhibitors, *Chem. Rev.* 112 (2012) 4156.
- [18] S. Rakshit, R. Saha, S.K. Pal, Modulation of environmental dynamics at the active site and activity of an enzyme under nanoscopic confinement: Subtilisin carlsberg in anionic AOT reverse micelle, *J. Phys. Chem. B* (2013) doi.org/10.1021/jp4061494.
- [19] D.J. Neidhart, G.A. Petsko, The refined crystal structure of subtilisin carlsberg at 2.5 Å resolution, *Protein Eng.* 2 (1988) 271.
- [20] K. Griebenow, A.M. Klibanov, Can conformational changes be responsible for solvent and excipient effects on the catalytic behavior of subtilisin carlsberg in organic solvents?, *Biotechnol. Bioeng.* 53 (1997) 351.
- [21] M.S. Celej, M.G. D'Andrea, P.T. Campana, G.D. Fidelio, M.L. Bianconi, Superactivity and conformational changes on alpha-chymotrypsin upon interfacial binding to cationic micelles, *Biochem. J.* 378 (2004) 1059.
- [22] M.I. Viseu, T.I. Carvalho, S.M.B. Costa, Conformational transitions in  $\beta$ -lactoglobulin induced by cationic amphiphiles: Equilibrium studies, *Biophys. J.* 86 (2004) 2392.
- [23] S.M. Andrade, T.I. Carvalho, M.I. Viseu, S.M.B. Costa, Conformational changes of  $\beta$ -lactoglobulin in sodium bis(2-ethylhexyl) sulfosuccinate reverse micelles, *Eur. J. Biochem.* 271 (2004) 734.

- [24] S. Rakshit, R. Saha, P.K. Verma, R.K. Mitra, S.K. Pal, Ultrafast electron transfer in riboflavin binding protein in macromolecular crowding of nano-sized micelle, *Biochimie* 94 (2012) 2673.
- [25] S. Mukherjee, P. Chowdhury, F. Gai, Tuning the cooperativity of the helix–coil transition by aqueous reverse micelles, *J. Phys. Chem. B* 110 (2006) 11615.
- [26] N. Nandi, B. Bagchi, Dielectric relaxation of biological water, *J. Phys. Chem. B* 101 (1997) 10954.
- [27] J.K.A. Kamal, T. Xia, S.K. Pal, L. Zhao, A.H. Zewail, Enzyme functionality and solvation of subtilisin carlsberg: From hours to femtoseconds, *Chem. Phys. Lett.* 387 (2004) 209.
- [28] S.K. Pal, J. Peon, A.H. Zewail, Biological water at the protein surface: Dynamical solvation probed directly with femtosecond resolution, *Proc. Natl. Acad. Sci. USA* 99 (2002) 1763.
- [29] S.K. Pal, A.H. Zewail, Dynamics of water in biological recognition, *Chem. Rev.* 104 (2004) 2099.
- [30] P.K. Verma, S. Rakshit, R.K. Mitra, S.K. Pal, Role of hydration on the functionality of a proteolytic enzyme  $\alpha$ -chymotrypsin under crowded environment, *Biochimie* 93 (2011) 1424.
- [31] K. Bhattacharyya, B. Bagchi, On the origin of the anomalous ultraslow solvation dynamics in heterogeneous environments, *J Chem Sci* 119 (2007) 113.
- [32] K. Sahu, S.K. Mondal, S. Ghosh, D. Roy, P. Sen, K. Bhattacharya, Temperature dependence of solvation dynamics and anisotropy decay in a protein. ANS in bovine serum albumin, *J. Chem. Phys.* 124 (2006) 124909.
- [33] A. Amararene, M. Gindre, J.Y. Le Huerou, C. Nicot, W. Urbach, M. Waks, Water confined in reverse micelles: Acoustic and densimetric Studies, *J. Phys. Chem. B* 101 (1997) 10751.
- [34] G. Carlstroem, B. Halle, Water dynamics in microemulsion droplets. A nuclear spin relaxation study, *Langmuir* 4 (1988) 1346.
- [35] P.K. Verma, A. Makhal, R.K. Mitra, S.K. Pal, Role of solvation dynamics in the kinetics of solvolysis reactions in microreactors, *Phys. Chem. Chem. Phys.* 11 (2009) 8467.

- [36] S. Rakshit, R. Saha, A. Chakraborty, S.K. Pal, Effect of hydrophobic interaction on structure, dynamics, and reactivity of water, *Langmuir* 29 (2013) 1808.
- [37] S. Rakshit, R. Saha, P.K. Verma, S.K. Pal, Role of solvation dynamics in excited state proton transfer of 1-naphthol in nanoscopic water clusters formed in a hydrophobic solvent, *Photochem. Photobiol.* 88 (2012) 851.
- [38] R.K. Mitra, S.S. Sinha, S.K. Pal, Temperature-dependent solvation dynamics of water in sodium Bis(2-ethylhexyl) sulfosuccinate/Isooctane reverse micelles, *Langmuir* 24 (2008) 49.
- [39] S. Pal, S. Balasubramaian, B. Bagchi, Temperature dependence of water dynamics at an aqueous micellar surface: Atomistic molecular dynamics simulation studies of a complex system, *J. Chem. Phys.* 117 (2002) 2852.
- [40] S. Sen, S. Mukherjee, A. Halder, K. Bhattacharyya, Temperature dependence of solvation dynamics in a micelle. 4-Aminophthalimide in triton X-100, *Chem. Phys. Lett.* 385 (2004) 357.

# List of Publications

## (Peer-Reviewed Journals)

1. **S. Rakshit**, R. Saha, A. Singha, Z. S. A. Seddigi and S. K. Pal  
“Protein Molecular Interaction, Co-solubilisation of Organic Pollutants and Ecotoxicity of a Potential Carcinogenic Fuel Additive MTBE in Water”, *J. Mol. Liq.* 180 (2013) 235.
2. **S. Rakshit**, R. Saha, A. Chakraborty and S. K. Pal  
“Effect of Hydrophobic Interaction on Structure, Dynamics and Reactivity of Water”, *Langmuir*, 29 (2013) 1808.
3. **S. Rakshit**, R. Saha, P. K. Verma and S. K. Pal  
“Role of Solvation Dynamics in Excited State Proton Transfer of 1-Naphthol in Nanoscopic Water Clusters Formed in a Hydrophobic Solvent”, *Photochem. Photobiol.*, 88 (2012) 851.
4. **S. Rakshit**, N. Goswami and S. K. Pal  
“Slow Solvent Relaxation Dynamics of Nanometer Sized Reverse Micellar Systems Through Tryptophan Metabolite, Kynurenine”, *Photochem. Photobiol.*, 88 (2012) 38.
5. **S. Rakshit**, R. Saha, P. K. Verma, R. K. Mitra and S. K. Pal  
“Ultrafast Electron Transfer in Riboflavin Binding Protein in Macromolecular Crowding of Nano-Sized Micelle”, *Biochimie*, 94 (2012) 2673.
6. **S. Rakshit**, S. R. Saha, R and S. K. Pal  
“Modulation of Environmental Dynamics at the Active Site and Activity of an Enzyme Under Nanoscopic Confinement: Subtilisin Carlsberg in Anionic AOT Reverse Micelle”, *J. Phys. Chem. B*, DOI: 10.1021/jp4061494 (2013).

- 7.\* R. Saha<sup>#</sup>, P. K. Verma<sup>#</sup>, **S. Rakshit**, S. Saha, S. Mayor and S. K. Pal  
 (#contributed equally)  
 “Light Driven Ultrafast Electron Transfer in Oxidative Redding of Green Fluorescent Proteins”, *Sci. Rep.*, 3, (2013) 1580.
- 8.\* R. Saha, **S. Rakshit**, R. K. Mitra and S. K. Pal  
 “Microstructure, Morphology and Ultrafast Dynamics of a Novel Edible Microemulsion”, *Langmuir*, 28 (2012) 8309.
- 9.\* R. Saha, **S. Rakshit**, D. Majumdar, A. Singha, R. K. Mitra, and S. K. Pal  
 “Nanostructure, Solvation Dynamics and Nano-Templating of Plasmonically Active SERS Substrate in Reverse Vesicles”, *J. Nanopart. Res.*, 15 (2013) 1576.
- 9\* R. Saha, **S. Rakshit**, P. K. Verma, R. K. Mitra and S. K. Pal  
 “Protein-Cofactor Binding and Ultrafast Electron Transfer in Riboflavin Binding Protein under the Spatial Confinement of Nanoscopic Reverse Micelles”, *J. Mol. Recognit.*, 26 (2013) 59.
- 10.\* R. Saha, **S. Rakshit**, R and S. K. Pal  
 “Molecular Recognition of a Model Globular Protein Apomyoglobin by Synthetic Receptor Cyclodextrin: Effect of Fluorescence Modification of the Protein and Cavity Size of the Receptor in the Interaction”, *J. Mol. Recognit.*, DOI: 10.1002/jmr.2301 (2013).
- 12.\* S. Batabyal, **S. Rakshit**, S. Kar, and S. K. Pal  
 “An Improved Microfluidics Approach for Monitoring Real-Time Interaction Profiles of Ultrafast Molecular Recognition”, *Rev. Sci. Instrum.*, 83 (2012) 043113.
- 13.\* P. K. Verma, **S. Rakshit**, R. K. Mitra and S. K. Pal  
 “Role of Hydration on the Functionality of a Proteolytic Enzyme Alpha-Chymotrypsin Under Crowded Environment”, *Biochimie*, 93 (2011) 1424.

\* Not included in the thesis.